

Pyridyltriazole-containing Compounds as Zinc-
responsive MRI Contrast Agents and
Luminescence Probes

Thesis Submitted for the Degree of
Doctor of Philosophy
at the University of Leicester

by
Adhitiyawarman

Department of Chemistry
University of Leicester
September 2018

Pyridyltriazole-containing Compounds as Zinc-responsive MRI Contrast Agents and Luminescence Probes

Adhitiyawardman

Abstract

Magnetic resonance imaging (MRI) is a versatile imaging modality in modern clinical applications. The use of MRI started to be more powerful since the invention of smart contrast agents, which can selectively respond to a specific stimulus such as a metal ion. This study was focused on GdDO3A-based complexes designed to be zinc-responsive MRI contrast agents by exploiting a new pyridyltriazole moiety as an active arm for a zinc(II) chelator. This active arm was designed to have a coordination displacement ability to give a switch-on MR signal. A series of pyridyltriazole containing compounds were synthesized and examined sequentially.

The primary compound containing pyridyltriazole **LnC2** ($q = 0$) exhibited no response towards zinc(II). Modification by changing the binding orientation of the pyridyltriazole, **LnC4** had reduced the steric hindrance allowing one coordination site for water ($q = 1$); however, it still did not show any change in signal to the presence of zinc(II). Increasing the distance between the active arm and the lanthanide centre *via* additional carbon linkers (**LnC5** and **LnC6**) gave complexes an open-structure ($q = 2$). This structure also had low affinity toward zinc(II) and did not provide a switch on response to the MR signal. Addition of a hydroxyl functional group to the pyridyltriazole (**LnC7**) did not change its coordination mode ($q = 2$). Incorporation of a carboxylic acid group (**LnC8**) provided coordination to give a $q = 1$ complex. Furthermore, it exhibited coordination displacement in response to zinc(II), by modulating its hydration number to give a “switch on” MR signal; the relaxivity increased by 30% from 6.5 to 8.6 mM⁻¹s⁻¹ as a response to one equivalent of zinc(II). Elongation of the linker by replacing it with the tri- and tetra-ethylene glycol (**LnC9** and **LnC10**) changed their relaxivity in response to zinc(II) which was assumed to be a result of a different coordination mode.

A series of emissive lanthanide complexes with high fluorescence quantum yields were also synthesized as luminescence probes namely; a click-ready complex (**TbC1**), water soluble complexes (**TbC2a**, **TbC2b**), a polymerizable complex (**TbC2c**), a dimer complex (**TbC2-dimer**), tridentate ligand complexes (**Tb/Eu(27)**₃, **Tb/Eu(32b)**₃) and a complex potential for dual-modal fluorescence/MR imaging probe (**Tb(GdC8)**₃).

Acknowledgements

Firstly, I would like to thank to Allah the mighty god for his blessing, mercy and forgiveness. My sincerest gratitude goes to both of my project supervisor Dr Mark P. Lowe and Dr Sandeep Handa for all of their excellent ideas, supports and concerns, I appreciate you for being my supervisors. Many thanks to Prof. Paul Cullis for his advice, thought and time. I also want to thank to Dr Gerry Griffith for NMR experiments, Mr Kuldip Singh for X-ray crystallography and Mr Mick Lee for mass spectrometry analyses.

Secondly, for my parents, family and relatives, I am truly grateful for your dedication and support. A massive thank you for my wife Nurul Hidayah for her love and support during the hardest part of my study, I am so blessed to have you in my life. You have been supportive through this difficult time. Special for my beloved daughter Tia and my son Fatan, everything I do is for your future.

Thirdly, for all of the Ph.D group members, Adil, Vicki, Nada, Sarab and Lucy thank you for awarding me the excellent friendship and help, as well as to all of the synthetic lab members I have worked with over the past few years. Finally, I would like to acknowledge the Ministry of Research, Technology and Higher Education, Directorate General of Resources for Research, Technology and Higher Education, Republic of Indonesia for funding.

Abbreviations

°C	Degrees Centigrade
a.u.	Arbitrary units
B_0	External magnetic field
br	Broad
CT	Computed tomography
Cyclen	1,4,7,10-tetraazacyclododecane
d	Doublet
DCM	Dichloromethane
dd	Doublet of doublets
ddd	Doublet of doublet of doublets
DMSO	Dimethylsulfoxide
DO3A	1,4,7-tris(carboxymethyl)-1,4,7,10-tetraazacyclododecane
DOTA	1,4,7,10-tetraazacyclododecane-1,4,7,10-tetraacetic acid
EDTA	Ethylenediaminetetraacetic acid
eq	Equivalent
ESI	Electrospray Ionisation
ESMS	Electrospray Mass Spectrometry
<i>et al.</i>	<i>et alii</i> (and others)
EtOAc	Ethyl Acetate
EtOH	Ethanol
g	Gram
h	Hour
HEPES	4-(2-Hydroxyethyl)-1-piperazineethanesulfonic acid
HOMO	Highest Occupied Molecular Orbital
HPLC	High-Performance Liquid Chromatography
HSA	Human Serum Albumin
Hz	Hertz
I	Intensity
I	Spin quantum number
ICT	Internal Charge Transfer
<i>in situ</i>	In the reaction mixture
ISC	Inter System Crossing
K	Kelvin
LFSE	Ligand Field Stabilisation Energy
LUMO	Lowest Unoccupied Molecular Orbital
μ	Magnetic moment
μ .w.	Microwave
M	Molar
m	Multiplet
m.p.	Melting point
m/z	Mass to charge ratio
MALDI	Matrix Assisted Laser Desorption Ionisation
MeCN	Acetonitrile
MeOH	Methanol
mg	Milligram
min	Minute
mL	Millilitre

mM	Millimolar
mmol	Millimole
MRI	Magnetic Resonance Imaging
NaAsc	Sodium Ascorbate
nm	Nanometre
NMR	Nuclear Magnetic Resonance
PEG	Polyethylene Glycol
PET	Positron Emission Tomography
ppm	Part per million
q	Number of inner sphere water molecule
q	Quartet
quin	Quintet
R_1/R_2	Longitudinal/Transverse relaxation rate
r_1	Relaxivity
s	Second
s	Singlet
S_0	Singlet ground state
S_1	Singlet excited state
SPECT	Single Photon Emission Computed Tomography
Φ	Fluorescence quantum yield
τ_m	Residence lifetime of a water molecule coordinated to the metal ion
τ_R	Molecular reorientation time
t	triplet
T_1	Longitudinal relaxation time
T_2	Transverse relaxation time
tBuDO3A	1,4,7-tris(tert-butoxycarbonylmethyl)-1,4,7,10-tetraazacyclododecane
TFA	Trifluoroacetic acid
TLC	Thin Layer Chromatography
TMS	Tetramethylsilane
UV	Ultra Violet
<i>via</i>	By means of
<i>vs</i>	versus
γ	Gyromagnetic ratio
ϵ	Extinction coefficient
λ	Lambda (wavelength)

Table of Content

Abstract	i
Acknowledgements	ii
Abbreviation	iii
Index of Compounds	xii
Chapter 1	1
General Introduction	1
1.1 Imaging	1
1.2 Imaging Modalities	1
1.3 Magnetic Resonance Imaging (MRI)	3
<i>1.3.1 History and Basic Principle of MRI</i>	3
<i>1.3.2 Longitudinal Relaxation or Spin-Lattice Relaxation (T1)</i>	9
<i>1.3.3 Transverse Relaxation or Spin-Spin Relaxation (T2)</i>	12
1.4 MRI Contrast Agent	15
<i>1.4.1 Gadolinium-based Contrast Agent and Relaxivity</i>	15
<i>1.4.2 Inner-, Second- and Outer-sphere Water Molecules</i>	17
<i>1.4.3 Strategies for Increase Relaxivity</i>	18
<i>1.4.4 Dipole-dipole (Dipolar) Relaxation</i>	19
<i>1.4.5 Smart Contrast Agent</i>	20
<i>1.4.6 Application of MRI</i>	21
1.5 Luminescence Emission Spectroscopy	21
<i>1.5.1 Fundamental Properties of Photoluminescence</i>	22
<i>1.5.2 Stokes Shift</i>	24
1.6 Lanthanides	25
<i>1.6.1 Chemistry and Coordination Properties of Lanthanides</i>	25
<i>1.6.2 Lanthanide Luminescence</i>	26
1.7 Click Chemistry	27
<i>1.7.1 Click Chemistry in Drug Discovery</i>	29
1.8 Zinc in the Human Body	30
<i>1.8.1 Zinc as an Essential Element</i>	30
<i>1.8.2 Zinc and Diseases</i>	31
1.9 Project Outline	32
<i>1.9.1. Design Rationale</i>	32

1.9.2. Aims of Project	34
1.10 Theses Outline.....	34
Chapter 2	36
Synthesis of Zinc-responsive MRI Contrast Agent	36
2.1 Background.....	36
2.1.1 Zinc Chemical Properties	36
2.1.2 Zinc in Biological Systems	38
2.1.3 Zinc-responsive Probes.....	39
2.1.4 Zinc-responsive MRI Contrast Agents	40
2.1.5 Designing Zinc-responsive MRI Contrast Agent	44
2.2 Synthesis of the First Model Complexes (LnC1 and LnC2).....	46
2.3 Synthesis of Modified Complexes	53
2.3.1 Synthesis of LnC3 and LnC4.....	53
2.3.2 Synthesis of LnC5 and LnC6.....	61
2.3.3 Synthesis of LnC7 and LnC8.....	67
2.3.4 Synthesis of LnC9 and LnC10.....	73
2.4 Summary and Conclusion.....	77
Chapter 3	79
Photophysical Properties and Zinc-responsive Studies.....	79
3.1 Background.....	79
3.2 Luminescence Properties of Europium and Terbium.....	79
3.3 Antenna Sensitization.....	81
3.5 Photophysical Changes by Zinc Complexation	84
3.6 Photophysical Studies.....	85
3.6.1 Photophysical Properties of Model Complexes (LnC1 and LnC2).....	86
3.6.2 Photophysical Properties of LnC3 and LnC4.....	93
3.6.3 Photophysical Properties of LnC5 and LnC6.....	97
3.6.4 Photophysical Properties of LnC7 and LnC8.....	104
3.6.5 Photophysical Properties of LnC9 and LnC10.....	114
Chapter 4	119
High Emissive Lanthanide Complexes in Molecular Labelling	119
4.1 Introduction	119
4.2 Lanthanides and Molecular Imaging	120
4.3 Synthesis of Highly Emissive Tb Complexes.	125
4.3.1 Synthesis of TbC1 and TbC2	126

4.3.2	Synthesis of <i>TbC2a</i> , <i>TbC2b</i> and <i>TbC2c</i>	130
4.3.3	Synthesis of <i>TbC2-dimer</i>	133
4.3.4	Synthesis of <i>Tb(27)₃</i> and <i>Tb(32b)₃</i>	135
4.3.5	Synthesis of a Trimer <i>Tb(GdC8)₃</i> as a Dual Modal Fluorescence-MR Imaging Agent	142
4.4	Summary and Conclusion	144
Chapter 5	145
Conclusions and Future Work	145
5.1	Conclusions	145
5.1.1	Synthesis of Zinc(II)-responsive MRI Contrast Agents and Their Examination	145
5.1.2	Potential Emissive Probes for Molecular Labelling.....	151
5.2	Future Work	153
Chapter 6	157
Experimental	157
6.1	Materials	157
6.2	Chromatography Studies	157
6.3	Spectroscopy Studies	157
6.3.1	NMR Spectroscopy Studies	157
6.3.2	UV-Vis and Fluorescence Spectroscopy Studies	157
6.3.3	Mass Spectroscopy Studies	158
6.3.4	Crystallography Studies.....	158
6.3.5	Relaxation-time Measurements.....	158
6.4	General Synthetic Methods	159
6.4.1	Sonogashira Reactions.....	159
6.4.2	Chlorination Reactions	159
6.4.3	The DO3A's Fourth Arm Attachments.....	159
6.4.4	Macrocycle's tert-Bu Deprotection Reactions.....	160
6.4.5	TMS Deprotection Reactions	160
6.4.5.1	Procedure 1	160
6.4.5.2	Procedure 2	160
6.4.6	Click Reactions	160
6.4.6.1	Procedure 1	160
6.4.6.2	Procedure 2	161
6.4.6.3	Procedure 3	161
6.4.6.4	Procedure 4.....	161

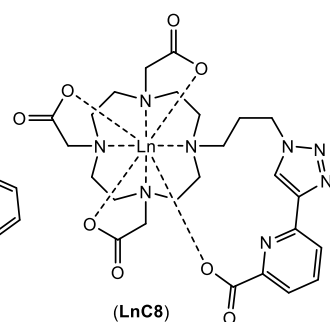
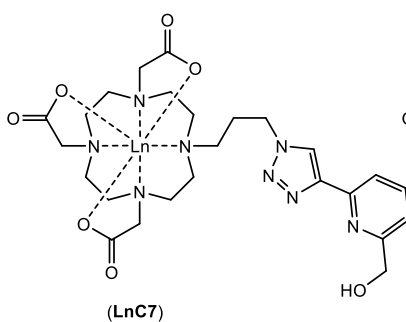
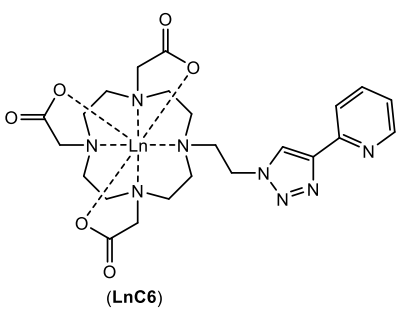
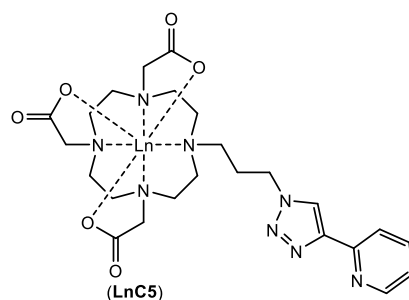
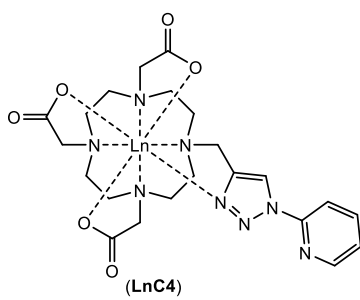
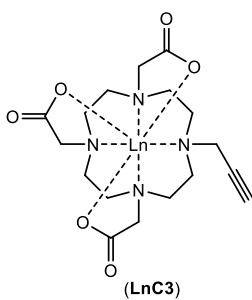
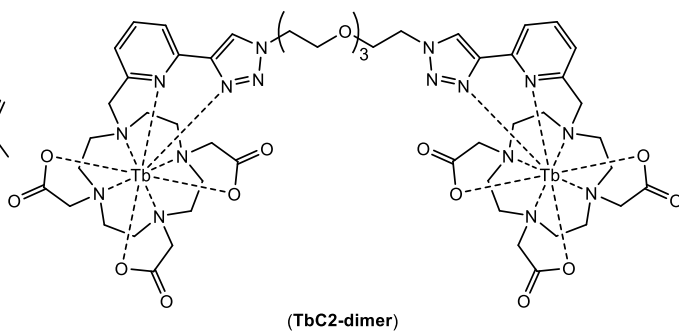
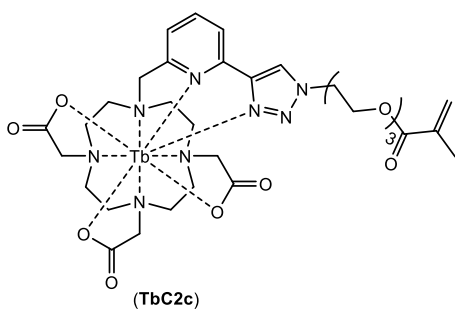
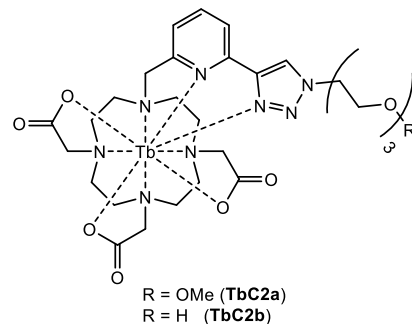
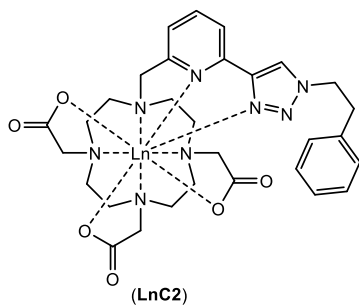
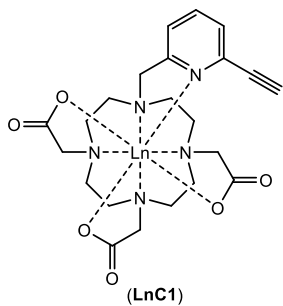
6.4.7	Synthesis of Azides	161
6.4.7.1	Procedure 1	161
6.4.7.2	Procedure 2	162
6.4.8	Tosylation Reactions	162
6.4.9	Lanthanide Complexation	162
6.4.9.1	Procedure 1	162
6.4.9.2	Procedure 2	162
6.5	Synthetic Compounds	163
6.5.1	Synthesis of tri- <i>tert</i> -butyl 2,2',2''-(1,4,7,10-tetraazacyclododecane-1,4,7-triyl)triacetate (1)	163
6.5.2	Synthesis of (6-((trimethylsilyl)ethynyl)pyridin-2-yl)methanol (2).....	164
6.5.3	Synthesis of 2-(chloromethyl)-6-((trimethylsilyl)ethynyl)pyridine (3)	164
6.5.4	Synthesis of tri- <i>tert</i> -butyl 2,2',2''-(10-((6-ethynylpyridin-2-yl)methyl)-1,4,7,10-tetraazacyclododecane-1,4,7-triyl)triacetate (4)	165
6.5.5	Synthesis of 2,2',2''-(10-((6-ethynylpyridin-2-yl) methyl)-1,4,7,10-tetraazacyclododecane-1,4,7-triyl)triacetic acid (C1)	165
6.5.6	Synthesis of EuC1	166
6.5.7	Synthesis of TbC1	166
6.5.8	Synthesis of GdC1	166
6.5.9	Synthesis of (6-ethynylpyridin-2-yl)methanol (5)	167
6.5.10	Synthesis of (6-(1-phenethyl-1 <i>H</i> -1,2,3-triazol-4-yl)pyridin-2-yl)methanol (6).....	167
6.5.11	Synthesis of 2-(chloromethyl)-6-(1-phenethyl-1 <i>H</i> -1,2,3-triazol-4-yl)pyridine (7)	168
6.5.12	Synthesis of tri- <i>tert</i> -butyl 2,2',2''-(10-((6-(1-phenethyl-1 <i>H</i> -1,2,3-triazol-4-yl)pyridin-2-yl)methyl)-1,4,7,10-tetraazacyclododecane-1,4,7-triyl)triacetate (8)	168
6.5.13	Synthesis of 2,2',2''-(10-((6-(1-phenethyl-1 <i>H</i> -1,2,3-triazol-4-yl)pyridin-2-yl)methyl)-1,4,7,10-tetraazacyclododecane-1,4,7-triyl)triacetic acid (C2)	169
6.5.14	Synthesis of EuC2	169
6.5.15	Synthesis of TbC2	169
6.5.16	Synthesis of Tb2a	170
6.5.17	Synthesis of Tb2b	170
6.5.18	Synthesis of TbC2c	170
6.5.19	Synthesis of tri- <i>tert</i> -butyl 2,2',2''-(10-(prop-2-yn-1-yl)-1,4,7,10-tetraazacyclo dodecane-1,4,7-triyl)triacetate (9).....	171

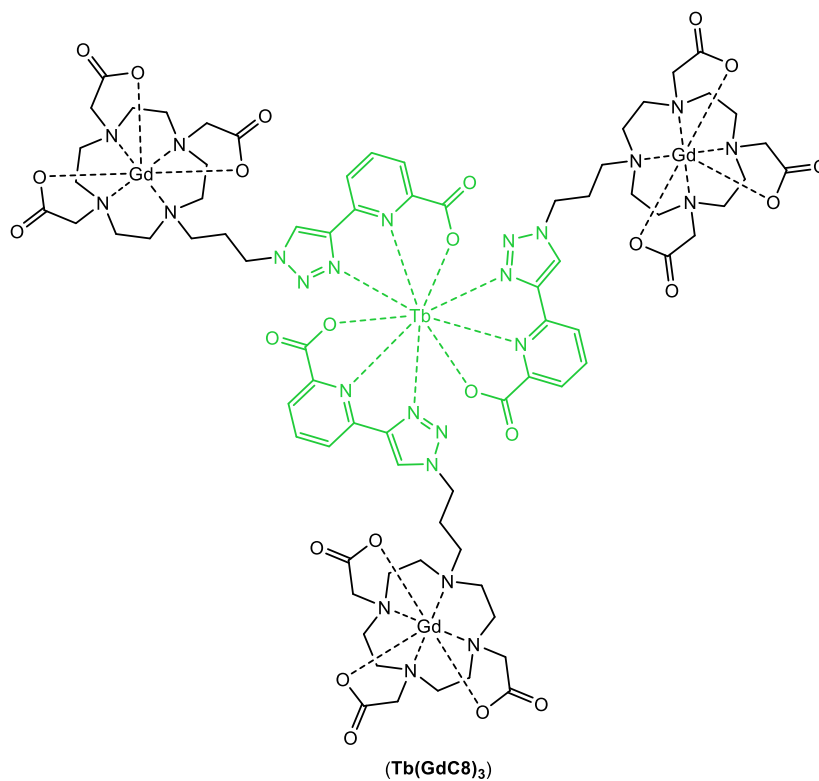
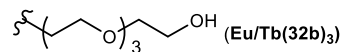
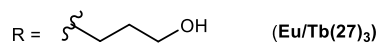
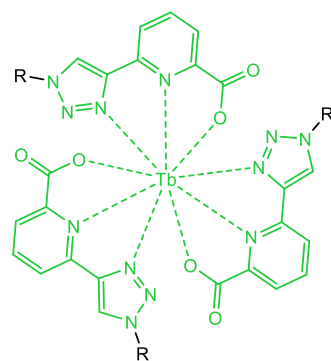
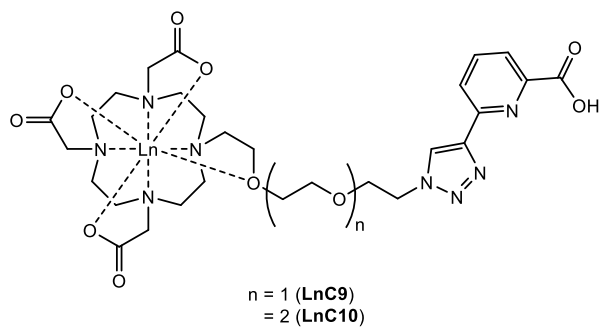
6.5.20	Synthesis of 2,2',2''-(10-(prop-2-yn-1-yl)-1,4,7,10-tetraazacyclododecane-1,4,7-triyl)triacetic acid (C3)	171
6.5.21	Synthesis of EuC3	172
6.5.22	Synthesis of 2-azidopyridine (10)	172
6.5.23	Synthesis of (1-(pyridin-2-yl)-1H-1,2,3-triazol-4-yl)methanol (11)	172
6.5.24	Synthesis of 2-(4-(chloromethyl)-1H-1,2,3-triazol-1-yl)pyridine (12)	173
6.5.25	Synthesis of tri-tert-butyl 2,2',2''-(10-((1-(pyridin-2-yl)-1H-1,2,3-triazol-4-yl)methyl)-1,4,7,10-tetraazacyclododecane-1,4,7-triyl)triacetate (13)...	173
6.5.26	Synthesis of 2,2',2''-(10-((1-(pyridin-2-yl)-1H-1,2,3-triazol-4-yl)methyl)-1,4,7,10-tetraazacyclododecane-1,4,7-triyl)triacetic acid (C4).....	174
6.5.27	Synthesis of EuC4	174
6.5.28	Synthesis of TbC4	175
6.5.29	Synthesis 3-(4-(pyridin-2-yl)-1H-1,2,3-triazol-1-yl)propan-1-ol (14)	175
6.5.30	Synthesis of 2-(1-(3-chloropropyl)-1H-1,2,3-triazol-4-yl)pyridine (15) .	175
6.5.31	Synthesis of tri-tert-butyl 2,2',2''-(10-(3-(4-(pyridin-2-yl)-1H-1,2,3-triazol-1-yl)propyl)-1,4,7,10-tetraazacyclododecane-1,4,7-triyl)triacetate (16)	176
6.5.32	Synthesis of 2,2',2''-(10-(3-(4-(pyridin-2-yl)-1H-1,2,3-triazol-1-yl)propyl)-1,4,7,10-tetraazacyclododecane-1,4,7-triyl)triacetic acid (C5).....	177
6.5.33	Synthesis of EuC5	177
6.5.34	Synthesis of 2-(4-(pyridin-2-yl)-1H-1,2,3-triazol-1-yl)ethan-1-ol (17)...	178
6.5.35	Synthesis of 2-(1-(2-chloroethyl)-1H-1,2,3-triazol-4-yl)pyridine (18a)..	178
6.5.36	Formation of 2-(1-vinyl-1H-1,2,3-triazol-4-yl)pyridine (elimination by-product)	179
6.5.37	Synthesis of 2-(4-(pyridin-2-yl)-1H-1,2,3-triazol-1-yl)ethyl 4-methylbenzene sulfonate (18b)	179
6.5.38	Synthesis of tri-tert-butyl 2,2',2''-(10-(2-(4-(pyridin-2-yl)-1H-1,2,3-triazol-1-yl)ethyl)-1,4,7,10-tetraazacyclododecane-1,4,7-triyl)triacetate (19) ..	180
6.5.39	Synthesis of 2,2',2''-(10-(2-(4-(pyridin-2-yl)-1H-1,2,3-triazol-1-yl)ethyl)-1,4,7,10-tetraazacyclododecane-1,4,7-triyl)triacetic acid (C6).....	180
6.5.40	Synthesis of EuC6	181
6.5.41	Synthesis 2-(((tert-butyldimethylsilyl)oxy)methyl)-6-ethynylpyridine (20).....	181
6.5.42	Synthesis of 3-(4-(6-(((tert-butyldimethylsilyl)oxy)methyl)pyridin-2-yl)-1H-1,2,3-triazol-1-yl)propyl 4-methylbenzenesulfonate (21).....	182
6.5.43	Synthesis of 3-(4-(6-(((tert-butyldimethylsilyl)oxy)methyl)pyridin-2-yl)-1H-1,2,3-triazol-1-yl)propyl 4-methylbenzenesulfonate (22).....	182
6.5.44	Synthesis of tri-tert-butyl 2,2',2''-(10-(3-(4-(6-(hydroxymethyl)pyridin-2-yl)-1H-1,2,3-triazol-1-yl)propyl)-1,4,7,10-tetraazacyclododecane-1,4,7-triyl)triacetate (23)	183

6.5.45	Synthesis of 2,2',2''-(10-(3-(4-(6-(hydroxymethyl)pyridin-2-yl)-1H-1,2,3-triazol-1-yl)propyl)-1,4,7,10-tetraazacyclododecane-1,4,7-triyl)triacetic acid (C7).....	184
6.5.46	Synthesis of EuC7	184
6.5.47	Synthesis of ethyl 6-bromopicolinate (24).....	185
6.5.48	Synthesis of ethyl 6-((trimethylsilyl)ethynyl)picolinate (25).....	185
6.5.49	Synthesis of ethyl 6-ethynylpicolinate (26).....	186
6.5.50	Synthesis of ethyl 6-(1-(3-hydroxypropyl)-1H-1,2,3-triazol-4-yl)picolinate (27).....	186
6.5.51	Synthesis of Eu/Tb(27)₃	187
6.5.52	Synthesis of ethyl 6-(1-(3-chloropropyl)-1H-1,2,3-triazol-4-yl)picolinate (28).....	187
6.5.53	Synthesis of tri-tert-butyl 2,2',2''-(10-(3-(4-(6-(ethoxycarbonyl)pyridin-2-yl)-1H-1,2,3-triazol-1-yl)propyl)-1,4,7,10-tetraazacyclododecane-1,4,7-triyl)triacetate (29).....	188
6.5.54	Synthesis of 2,2',2''-(10-(3-(4-(6-(ethoxycarbonyl)pyridin-2-yl)-1H-1,2,3-triazol-1-yl)propyl)-1,4,7,10-tetraazacyclododecane-1,4,7-triyl)triacetic acid (C8).....	189
6.5.55	Synthesis of EuC8	189
6.5.56	Synthesis of GdC8	190
6.5.57	Synthesis of Tb(GdC8)₃	190
6.5.58	Synthesis of 2-(2-(2-(2-hydroxyethoxy)ethoxy)ethyl 4-methylbenzenesulfonate (30a).....	191
6.5.59	Synthesis of 2-(2-(2-(2-(2-hydroxyethoxy)ethoxy)ethoxy)ethyl 4-methylbenzene sulfonate (30b).....	191
6.5.60	Synthesis of 2-(2-(2-(2-(tosyloxy)ethoxy)ethoxy)ethyl methacrylate (30c)..	192
6.5.61	Synthesis of ((oxybis(ethane-2,1-diyl))bis(oxy))bis(ethane-2,1-diyl) bis(4-methylbenzenesulfonate) (30d).....	192
6.5.62	Synthesis of 2-(2-(2-(2-methoxyethoxy)ethoxy)ethyl 4-methylbenzenesulfonate (30e).....	193
6.5.63	Synthesis of 2-(2-(2-(2-azidoethoxy)ethoxy)ethan-1-ol (31a).....	193
6.5.64	Synthesis of 2-(2-(2-(2-(2-azidoethoxy)ethoxy)ethoxy)ethan-1-ol (31b).....	193
6.5.65	Synthesis of ethyl 6-(1-(2-(2-(2-(2-hydroxyethoxy)ethoxy)ethyl)-1H-1,2,3-triazol-4-yl)picolinate (32a).....	194
6.5.66	Synthesis of ethyl 6-(1-(2-(2-(2-(2-(2-hydroxyethoxy)ethoxy)ethoxy)ethyl)-1H-1,2,3-triazol-4-yl)picolinate (32b).....	194
6.5.67	Synthesis of Eu/Tb(32b)₃	195
6.5.68	Synthesis of ethyl 6-(1-(2-(2-(2-(2-chloroethoxy)ethoxy)ethyl)-1H-1,2,3-triazol-4-yl)picolinate (33a).....	195

6.5.69 Synthesis of ethyl 6-(1-(2-(2-(2-(2-chloroethoxy)ethoxy)ethoxy)ethyl)-1H-1,2,3-triazol-4-yl)picolinate (33b)	196
6.5.70 Synthesis of tri-tert-butyl 2,2',2''-(10-(2-(2-(2-(4-(6-(ethoxycarbonyl)pyridin-2-yl)-1H-1,2,3-triazol-1-yl)ethoxy)ethoxy)ethyl)-1,4,7,10-tetraazacyclododecane-1,4,7-triyl)triacetate (34a)	197
6.5.71 Synthesis of tri-tert-butyl 2,2',2''-(10-(2-(2-(2-(2-(4-(6-(ethoxycarbonyl)pyridin-2-yl)-1H-1,2,3-triazol-1-yl)ethoxy)ethoxy)ethoxy)ethyl)-1,4,7,10-tetraazacyclododecane-1,4,7-triyl)triacetate (34b)	198
6.5.72 Synthesis of C9	199
6.5.73 Synthesis of C10	199
6.5.74 Synthesis of EuC9	200
6.5.75 Synthesis of GdC9	200
6.5.76 Synthesis of EuC10	201
6.5.77 Synthesis of TbC10	201
6.5.78 Synthesis of GdC10	202
Chapter 7	203
References	203
Chapter 8	213
Appendix	213
8.1 X-ray Crystallography	213
8.2 HPLC Analyses	228
8.3 Mass Spectrometry Analyses	229
8.4 Courses and Conferences	232

Index of Compounds





Chapter 1

General Introduction

1.1 Imaging

Imaging techniques have attracted much attention during the last three decades replacing the old traditional time consuming *in vitro* bioassay. Since the first imaging of an organ performed in 1950 by Benedict Cassen *via* a rectilinear scanner,¹ imaging is considered as the best non-invasive approach to investigate what exactly happens inside the cells, tissues, organs or body parts of a living organism. It is mainly conducted in order to understand the processes or to study the structural and functional properties of living systems² in the course of metabolism or the synthetic pathway of a particular metabolic process. The imaging information informs clinicians on how to deal with abnormal systems which are derived from certain diseases. However, the way to get a precise image that contains valid information is not an easy task. Some imaging modalities can work by exploiting the native substances on natural systems which are detectable by the instrument, such as the presence of hydrogen, bubbles, divergence in tissue density (bone). In fact, not all imaging instruments can do such things, the majority of advanced instrumentation needs special probes that can visualize the presence, location, distribution, shape, or concentration of specific substances. In most cases, the development of imaging techniques is simultaneously accompanied by the development of powerful probes that can enhance its basic ability to provide full information about the objects being investigated.

1.2 Imaging Modalities

There are a number of imaging modalities that can be utilized to “see” biological complexities inside living systems for treatment of diseases. Generally, they can be divided into imaging with a high radiation energy including X-rays, computed tomography (CT), positron emission tomography (PET), single photon emission computed tomography (SPECT)^{3,4} and imaging with a low radiation energy comprising optical imaging (OI), ultra sound (US) and magnetic resonance imaging (MRI).⁵

X-rays, discovered by Roentgen, are high energy electromagnetic waves that can be absorbed differentially by tissues to produce “shadows”. The CT imaging technique is slightly more advanced than X-ray. CT produces a three-dimensional anatomic image by

tomography (imaging by section).¹ PET imaging began in the 1950s and is considered as a sensitive technique used in neurology and cardiology. It exploits the emission from the radionuclide which is attached to the agent administered into the body.⁶ SPECT was developed by Keyes in 1976,¹ it uses gamma emitters instead of positron emitters, which are produced prior to use and are attached to carriers such as peptides.⁶

Fluorescence microscopy, including confocal fluorescence microscopy (CFM) and fluorescence lifetime imaging microscopy (FLIM) is an OI technique suitable for biological sample investigation.⁷ This technique provides various visible/NIR emitters to see the organs or tissues differences. US employs high sound frequencies between 1 to 20 MHz which can be used for imaging and as a therapeutic tool. US waves are emitted to a biological tissue, then the reflected sound is detected and displayed as an image.¹ MRI applies a powerful magnetic field and radio wave frequency to obtain full description of living organism. The properties of these main imaging modalities are summarized in Table 1.1.

Table 1.1: Common imaging modalities and its properties.^{7, 1}

Technique	Resolution	Depth	Scan Time	Sensitivity	Agents	Primary use
MRI	50-100 10^{-6} m	No limit	min-h	$\sim 10^{-6}$ M	Gd, Fe_nO_m	Versatile, high soft tissue contrast, cancer, cardiovascular
CT	50 10^{-6} m	No limit	min	$\sim 10^{-6}$ M	Iodine, AuNP	Lung and bone, blood clots
Ultrasound	50 10^{-6} m	mm-cm	min	High	Microbubbles Air, C_3F_8 , SF_6 , C_4F_{10}	Vascular and interventional
PET	1-2 mm	No limit	min	$\sim 10^{-12}$ M	^{18}F , ^{11}C , ^{15}O , ^{13}N , ^{64}Cu , ^{76}Br , ^{68}Ga	Versatile
SPECT	1-2 mm	No limit	min	$\sim 10^{-10}$ M	^{99m}Tc , ^{111}In , ^{67}Ga , ^{123}I , ^{131}I	Labelled antibodies
Fluorescence microscopy	nm	mm	s	$\sim 10^{-8}$ M	Fluorophores	Cell work, image-guided surgery

These kinds of techniques are advantageous due to their non-invasive nature, allowing the study of abnormalities inside biological systems. Nonetheless, they have their own imperfection. X-rays for example have a limitation dose due to the use of ionizing radiation. CT obtains a low quality image over soft tissue and its intense X-ray exposure on a single examination make it unsuitable for use over a long period.¹ PET and

SPECT on the other hand, have the lack of an anatomical reference frame and again the safety concern because the use of ionization radiation.¹ OI has limited tissue penetration and potentially has phototoxicity due to the interaction between fluorescence dye and the light used. US also has poor penetration through bone or air and has poor resolution. MRI has a long imaging time and is considered as an expensive technique with low sensitivity. Although, no individual imaging modality is well suited to all aspects of structure and function, MRI is a promising technique that is applied without hazardous radiation, offering spatial resolution.

1.3 Magnetic Resonance Imaging (MRI)

Magnetic resonance imaging is a powerful method in modern clinical application which is being used on a daily basis in disease diagnosis. MRI is able to detect the physiological changes by providing non-invasive anatomical structure in high resolution.⁸ This method has the same principles as NMR analysis in chemistry laboratories, in fact MRI in medical application relies mainly on the presence of water protons inside biological systems, which contain a high concentration of water (approximately 90 M protons in tissue⁹) that can provide observable signal.⁸ The term of “MR imaging or MRI” is used instead of “NMR imaging” due to the negative connotation of “nuclear”.

1.3.1 History and Basic Principle of MRI

The nuclear magnetic signal was first discovered independently by two research groups led by F. Bloch and E. M. Purcell in 1946, who were awarded the Nobel Prize for Physics in 1952.¹⁰ While, MRI was developed by an American chemist Paul Lauterbur from the State University of New York in 1973. By this invention he shared the Nobel Prize in Physiology or Medicine with Peter Mansfield in 2003.¹¹

MRI is a NMR experiment conducted in a living organism. All basic concepts which are relevant to NMR remain unchanged. As previously stated, it relates to the properties of the nuclei particles namely protons and neutrons. These particles are in a constant rotation and have an angular momentum (P) and a magnetic moment (μ) just like a tiny magnet bar (Fig. 1.1). Thus, they are influenced by any given magnetic field and electromagnetic waves. However, only nuclei containing an odd number of protons or neutrons have spin characteristics and magnetic properties (Table 1.2). Hydrogen is

one of these nuclei containing only a single proton; it has a nuclear spin quantum number $I = 1/2$.

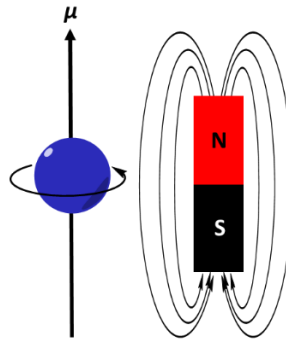


Figure 1.1: Rotating proton inducing the magnetic moment acts as a small magnet.

In the presence of the external magnetic field, there will be interaction between the proton's magnetic moment and the external magnetic field. This interaction splits the energy into two different levels (α - and β -states). The α -state is considered as the lowest energy, achieved when its magnetic moment is parallel (aligned) with the external magnetic field. On the contrary, the β -state is the highest energy when its magnetic moment is opposed (unaligned) to the external magnetic field as illustrated in Fig. 1.2.

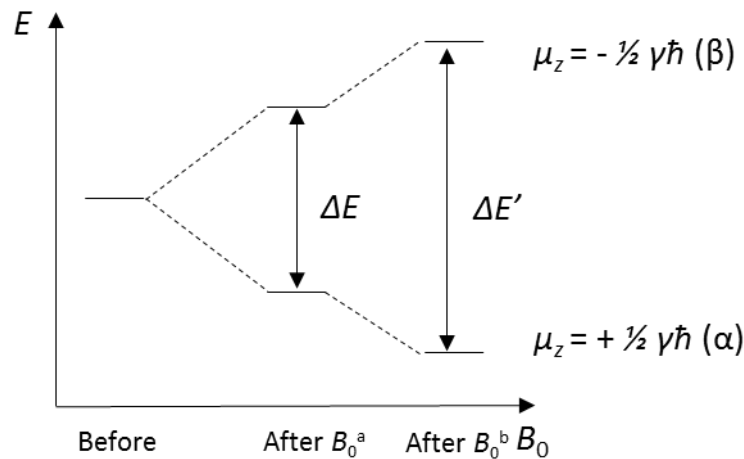


Figure 1.2: Proton's energy level splitting in an external magnetic field B_0 .

The energy gap between two energy states is proportional to the magnitude of the external magnetic field B_0 . The correlation between nuclear magnetic moment and the angular momentum is defined as in Eqn 1.1.

$$\mu = \gamma P \quad (1.1)$$

According to quantum theory, angular momentum and nuclear magnetic moment are quantized. The angular momentum in the z direction is given in Eqn 1.2.

$$P_z = \hbar m_l \quad (1.2)$$

Where, \hbar equals to $h/2\pi$ and m_l is the magnetic quantum number (Eqn. 1.3) which characterizes the corresponding stationary state of the nucleus.

$$m_l = I, I-1, I-2, \dots, -I \quad (1.3)$$

These magnetic quantum numbers are related to the spin quantum number, I . The total number of energy levels is thus equal to $2I + 1$. Therefore, since the proton has a spin quantum number $1/2$, there are two possible spin states for proton ($m_l = +1/2$ and $m_l = -1/2$). The magnitude of the magnetic moment of the z direction is achieved following the Eqn. 1.1 and 1.2.

$$\mu_z = \gamma P_z = \gamma \hbar m_l = \pm \gamma \hbar I = \pm \frac{1}{2} \gamma \hbar \quad (1.4)$$

Thus, proton can be pictured as a magnetic dipole which could have parallel and anti-parallel orientations as illustrated in Fig. 1.3.¹²

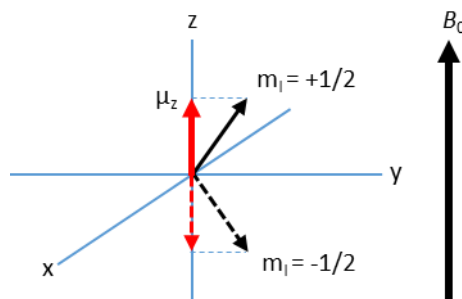


Figure 1.3: Two possible orientations of m_l about the z-axis.¹²

The energy differences between α and β states in an external magnetic field B_0 which coincides to the z axis are expressed in Eqn. 1.5.

$$\Delta E = 2\mu_z B_0 = \gamma \hbar B_0 \quad (1.5)$$

Theoretically, the energy of the spins is minimized when the individual magnetic moment is aligned with the external magnetic field. In fact, most of the nuclei are not aligned with the external magnetic field due to the thermal motion energy. This energy is higher than the energy of interaction between a nuclear magnetic moment and the external applied field. It makes the magnetic moments of the individual spin have different orientations.

As a result, the net alignment is magnetized and represented as a bulk magnetization. This magnetization is a vector quantity, thus containing a magnitude and a direction.¹³

The distribution of protons between the ground state and an excited state is given by the Boltzmann relation (Eqn. 1.6).

$$\frac{N_{\alpha}}{N_{\beta}} = e^{\left(\frac{-\Delta E}{kT}\right)} = e^{\left(\frac{-\gamma h B_0}{2\pi kT}\right)} \approx 1 - \frac{-\gamma h B_0}{2\pi kT} \quad (1.6)$$

Where, N_{α} and N_{β} are the number of nuclei in the ground and excited states respectively. ΔE is the energy different between them, while h is the Planck's constant (6.626×10^{-34} J.s), k is the Boltzmann constant (1.3805×10^{-23} J.K⁻¹) and T is the absolute temperature (K).¹²

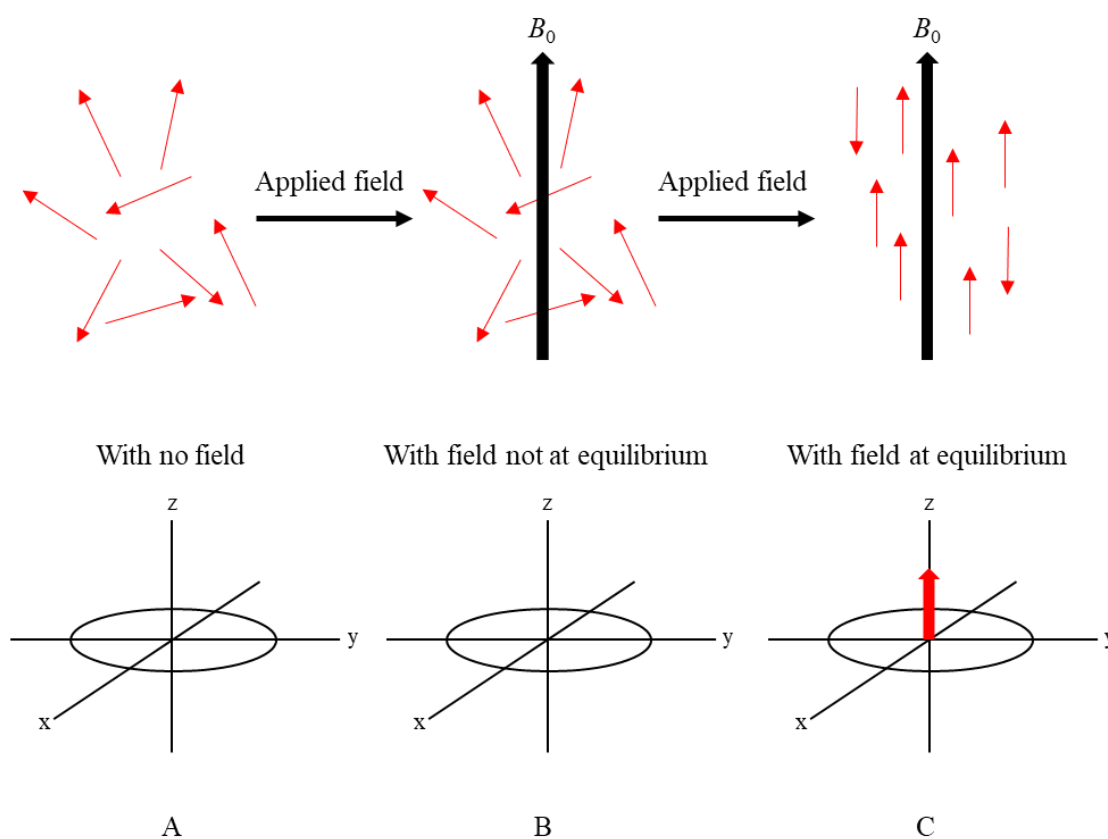


Figure 1.4: The magnetic moment and its net magnetization. A) With no external magnetic field. B) Once external magnetic field applied. C) After a sufficient time at equilibrium.¹³

Under normal conditions, the magnetic moments point in a random direction with no net magnetization (Fig. 1.4A). When the external magnetic moment is applied there is an energetic preference for moments to be aligned with the external magnetic field. Even though there is still no bulk magnetization being formed at the initial application of the

external field (Fig. 1.4B), after a sufficient interval of time the magnetic moments start to align parallel to the external magnetic field (Fig. 1.4C). At this equilibrium, the bulk magnetization vector is aligned along z-axis.

The strong external magnetic field also induces the second proton's turning motion which is independent to its actual rotation. The magnetic dipole in a homogeneous magnetic field B_0 experiences a torsional moment that attempts to align it with the direction of the field.¹² As a result, the proton's magnetic moment rotates around the z axis parallel to the external magnetic field with a constant angle elevation. These phenomena are called precession as illustrated in Fig. 1.5.

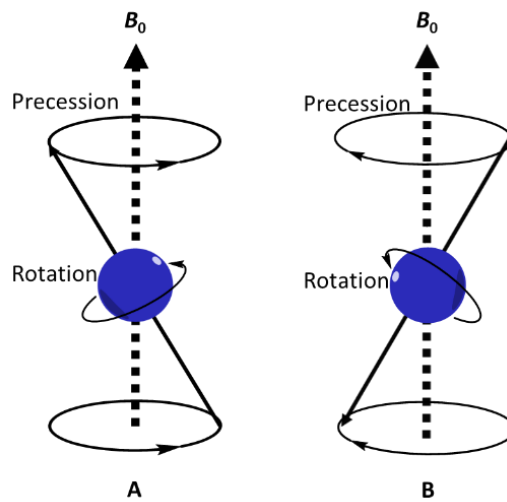


Figure 1.5: The rotation motion of the proton's magnetic moment around its z-axis parallel (A) and anti-parallel (B) to the applied external magnetic field B_0 .

The precession frequency is known as Larmor frequency (ω_0) which is proportional to the applied magnetic field strength expressed by Eqn. 1.7 and 1.8.

$$\omega_0 = -\gamma B_0 \text{ in rad s}^{-1}. \quad (1.7)$$

$$\nu_0 = -\gamma B_0 / 2\pi \text{ in Hz}. \quad (1.8)$$

Where, B_0 is the magnitude of the external magnetic field, γ is the gyromagnetic ratio equal to $-eg/2m$ (with m is the mass of precessing system while g is g-factor of the system), which is a constant characteristic of the particular nucleus (Table 1.2).¹³

Table 1.2; NMR properties of common nuclides.¹⁴

Isotope	Natural abundance (%)	Protons	Neutrons	I	Magnetic moment ($\mu' = \mu / \mu_N$)	Gyromagnetic ratio (γ) (10^7 rad T ⁻¹ s ⁻¹)	Resonance frequency (MHz*)
¹ H	99.985	1	0	1/2	2.7928456	26.752196	100.000
¹³ C	1.100	6	7	1/2	0.702411	6.72828	25.150
¹⁵ N	0.366	7	8	1/2	-0.283189	-2.712621	10.140
¹⁷ O	0.038	8	9	5/2	-1.89380	-3.62808	13.562
¹⁹ F	100	9	10	1/2	2.628867	25.18147	94.129
²⁹ Si	4.67	14	15	1/2	-0.55529	-5.3190	19.883
³¹ P	100	15	16	1/2	1.13160	10.8394	40.518

*For a magnetic field of 2.34866 T in which ¹H resonates at 100.000 MHz.

The magnetic moment contains the z- and xy-components creating magnetization to their own axis. However, all spinning nuclei which rotate parallel to the B_0 have their net magnetization on the z-positive but not in the z-negative axis (Fig. 1.6. (left)). On the other hand, there is no net magnetization on the xy-axis (Fig. 1.6 (right)) due to dephasing process of the spinning nuclei which could point to different direction. As illustrated at Fig. 1.6 (left), the magnetization on the y-positive axis of one proton spinning at this direction is cancelled by the magnetization of another spinning proton on the opposite direction (y-negative axis). The number of protons spinning around z-axis aligned to B_0 direction (precession) are higher (lower energy) than those to the opposite direction. As a result, there is a net magnetization on the z-positive axis (Fig. 1.6 (middle)).

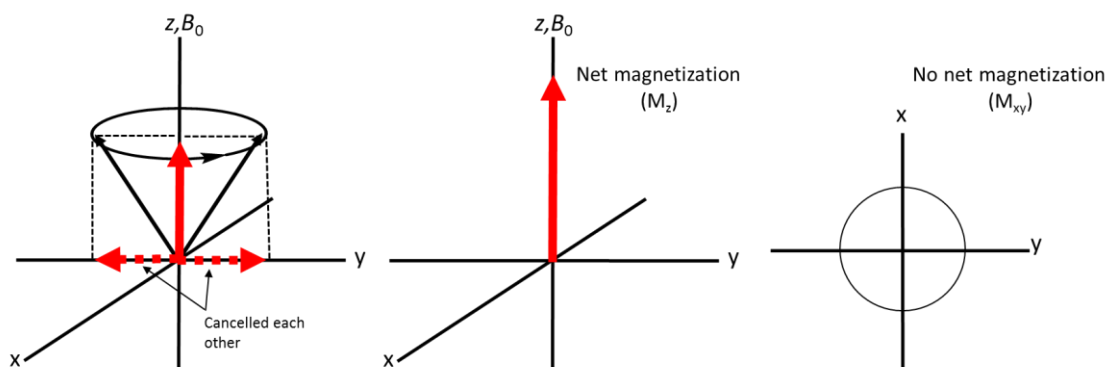


Figure 1.6. The precessing motion creating a vector containing z- and xy-axis magnetization. This figure shows two spinning protons around the z-axis on the opposite direction (left), they have net magnetization on the z-axis, M_z (middle) and have no net magnetization on the xy-axis, M_{xy} (right).

The magnetization is a total value from all protons aligned and unaligned to B_0 . In other words, the net magnetization on the z-axis is as a result of the sum of all protons aligned with B_0 deducted by all protons unaligned to B_0 as depicted at Fig. 1.7.

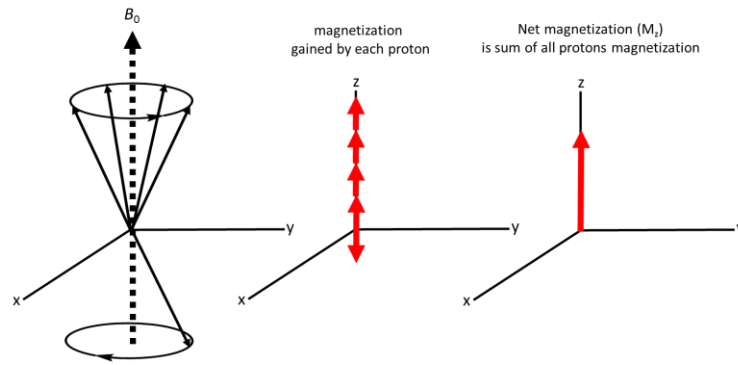


Figure 1.7: The net magnetization as a sum of all precessing protons.

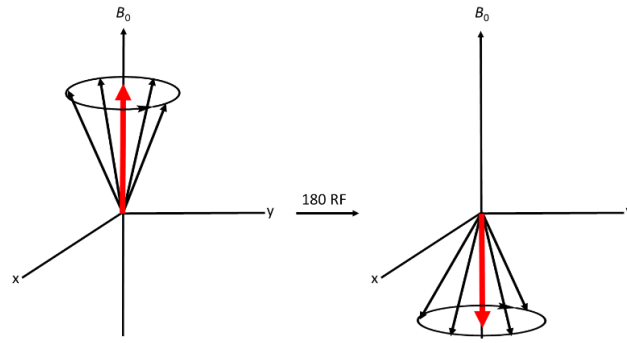
The time required to recover from the excitation process is the relaxation time. This relaxation time is crucial in order to get contrast in MR images. In addition, the divergence of water content presents differences in intensity. The biological environmental differences caused by a disease¹⁵ also contribute to the observed intensity, consequently give a contrast between tissue. This is because the relaxation time varies in different environments. Based on that, a greater differentiation of signals among tissues exhibits a clearer image. Relaxation times can be divided into longitudinal (spin-lattice) relaxation time T_1 and transverse (spin-spin) relaxation time T_2 with the rate of relaxation given as $1/T_1$ and $1/T_2$ or R_1 and R_2 respectively.

1.3.2 Longitudinal Relaxation or Spin-Lattice Relaxation (T_1)

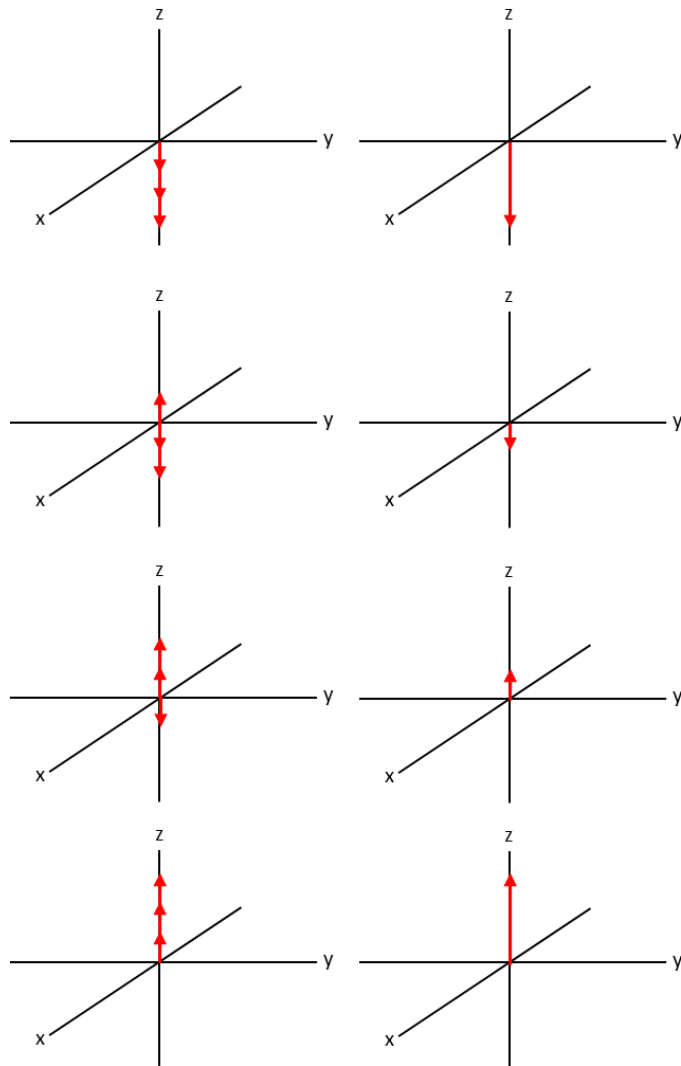
As discussed in the previous section, by absorption of a specific RF pulse, the net magnetization flips to the opposite direction of the external magnetic field (higher energy). After the RF pulse has stopped, it gradually relaxes back to its initial position by releasing its energy. The time required for magnetization to reach 63% of its maximum is designated as longitudinal or spin-lattice relaxation time. The T_1 relaxation also means restoration of the Boltzmann equilibrium along the z-axis which can be calculated following Eqn. 1.9 or 1.10.

$$M_z = M_{z0} \left[1 - e^{\left(-\frac{t}{T_1}\right)} \right] \text{ for } 90^\circ \text{ RF pulse} \quad (1.9)$$

$$M_z = M_{z0} \left[1 - 2e^{\left(-\frac{t}{T_1}\right)} \right] \text{ for } 180^\circ \text{ RF pulse} \quad (1.10)$$



(A)



(B)

Figure 1.8: T_1 relaxation processes showing A). The net magnetization after 180 RF pulse. B). From top to down on the left-hand side is showing the orientation of magnetic moment to each proton during the relaxation, and from top to down on the right-hand side is showing the net magnetization.

Where, M_{z0} is the net magnetization along z-axis at equilibrium while M_z is the net magnetization along z-axis at certain time t .

Fig. 1.8 illustrates the T_1 relaxation after being exposed to a 180° RF pulse. The net magnetization on the z component decreases gradually and at one point it becomes zero before it starts to increase again on their initial direction. In practice, modulation of net magnetization on the z-axis cannot be identified due to its static motion (lack of magnetic field alteration). The magnetic moment on the transverse magnetization on the other hand, provides a readable signal as a result of the turning motion of the net magnetization on the transverse plane which can be further transformed to FID signal as illustrated at Fig. 1.9.

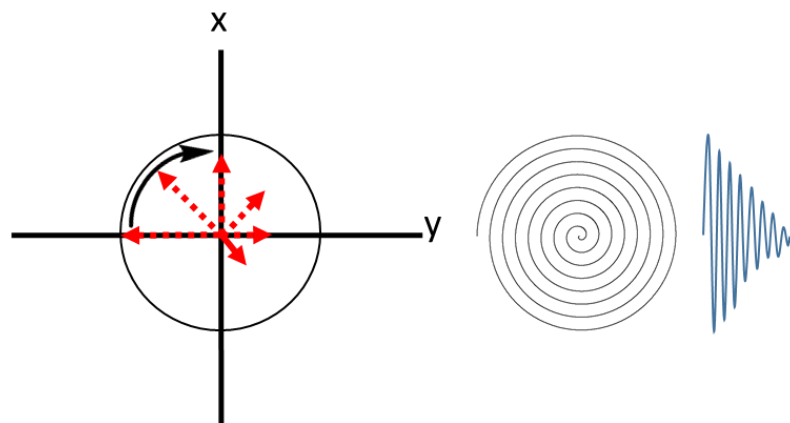


Figure 1.9: The net magnetization diminishment on the xy-axis (left), creating spiral-like track (middle) to produce a FID signal (right) during the T_1 relaxation experiment

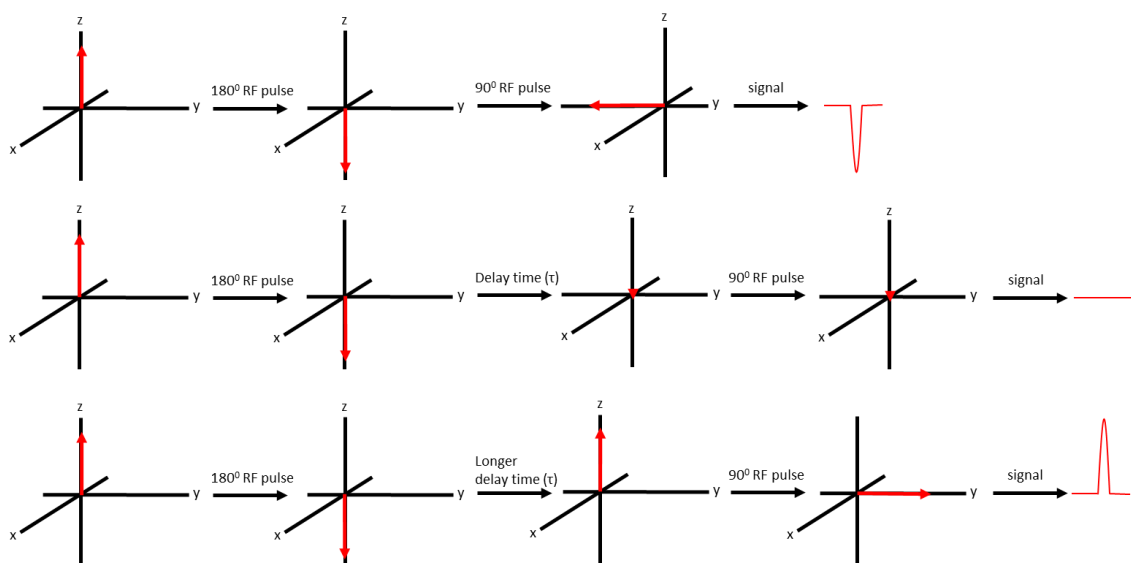


Figure 1.10: Inversion recovery experiment using sequence 180° and 90° RF pulses by varying the delay time (τ).¹²

There are some methods that can be used for measuring T_1 relaxation by manipulation of the magnetization direction. The most common method is called as inversion recovery experiment. In measuring longitudinal relaxation time (T_1), this method exploits two RF pulses (180° and 90°) which are applied in different interval or delay times. The complete process is illustrated at Fig. 1.10. The first step is started by applying the 180° RF pulse that transforms M_z to $-M_z$. After a delay time, the second 90° RF pulse is applied to transform it to an observable M_{xy} in which FID is acquired then transformed to a peak. The experiment is repeated for several different delay times. The experimental results are then fitted by the exponential function described at Eqn. 1.9 to give a T_1 relaxation curve as in Fig. 1.11. The differences between relaxation time (short and long T_1) give contrast to the image when the correct delay time τ is chosen.

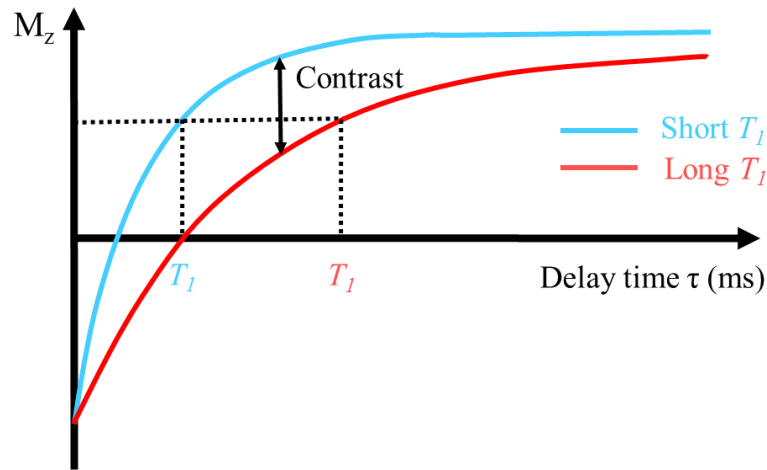


Figure 1.11: Curve fitting profile of the inversion recovery experiment using 180° and 90° RF pulses applied in different delay time showing short (blue line) and long (red line) T_1 .

1.3.3 Transverse Relaxation or Spin-Spin Relaxation (T_2)

In addition to the z -magnetization there is also magnetization in the x, y plane called transverse or xy -magnetization (M_{xy}), which can be generated by certain techniques. When the 90° RF pulse applied to the net magnetization on z -axis is aligned with B_0 , the net magnetization direction will be switched to the xy plane. This 90° RF pulse will switch half of the z -axis component to the opposite direction providing a relatively similar amount for both aligned and unaligned protons. In addition, the 90° RF pulse also puts the spinning protons in similar phase (coherence) causing the net magnetization on the xy -axis as illustrated at Fig. 1.12.

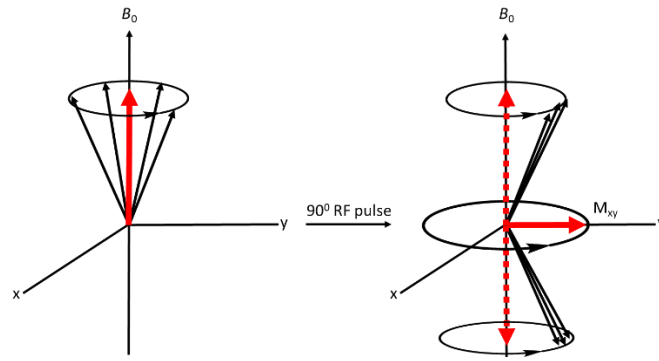


Figure 1.12: The 90° pulses switch the M_z to the M_{xy} .

Once the 90° RF pulse is switched off, T_2 relaxation starts to occur. Over time, they gradually lose their phase coherence, reducing their transverse magnetization (M_{xy}). Different to T_1 relaxation, there is no energy exchanged from nuclei to the lattice, but from nuclei to nuclei. Therefore, it is called spin-spin relaxation.

An important mechanism for transverse relaxation is based on an energy transfer within the spin system. Any transition of a nucleus between its spin states changes the local field at nearby nuclei at the correct frequency to stimulate a transition in the opposite direction.¹² Fig. 1.13 is a good illustration of transverse relaxation process after exposure to a 90° RF pulse. The top figure from left to right shows the phase coherence diminishment of spin protons. As a result, the value of M_{xy} as shown at the bottom, decreases during the relaxation.

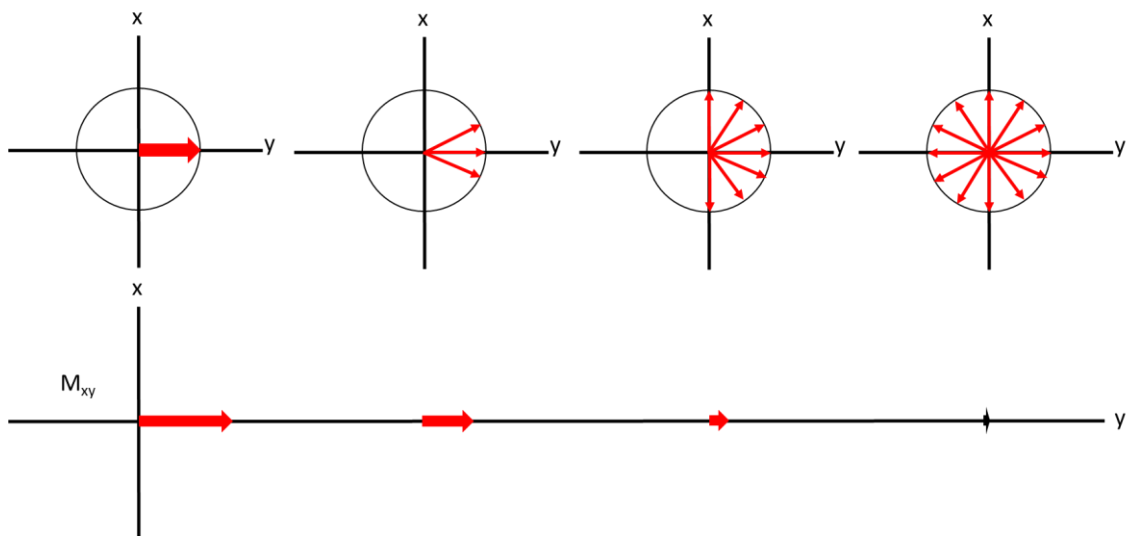


Figure 1.13: Showing the xy-axis after a 90° RF pulse showing the dephasing process on the xy-axis (top) and its net magnetization (bottom).

The common method for measuring T_2 relaxation is pioneered by Erwin Hahn, thus called as Hahn echo. He used two 90° RF pulses which is applied by a specific time delay. This method was then modified by Carr and Purcell by replacing the second two 90° RF pulses by an 180° RF pulse providing much more accurate results. The entire step is shown in Fig. 1.14.

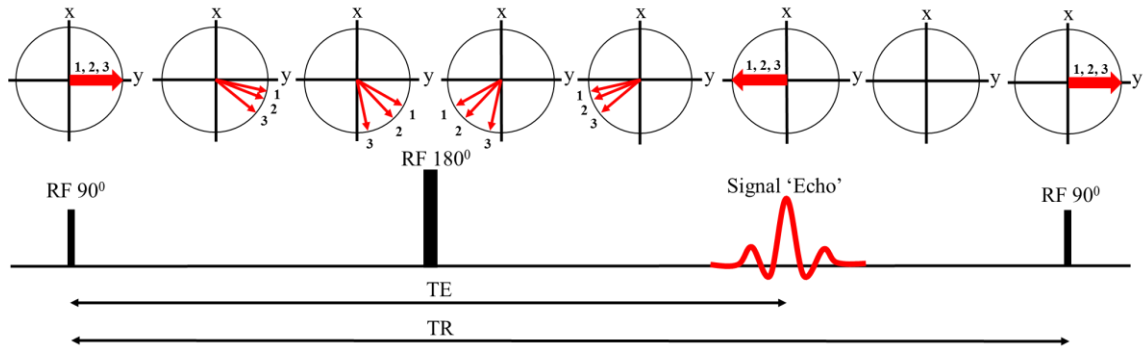


Figure 1.14: Spin echo experiment to determine the T_2 relaxation. The top figure from left to right is showing the magnetization alteration around xy plane during the applying 90° and 180° RF pulses with an interval delay time to get the signal echo as shown in the bottom figure.

The xy plane (transverse) magnetization, M_{xy} is produced when a 90° pulse has been applied to the M_z which aligns with B_0 . The local magnetic inhomogeneity causes some spins to slow down and some other speed up (spin rate of $1 < 2 < 3$). As a result, the M_{xy} decreases gradually by the time. Before the signal completely disappears, an 180° RF pulse is applied. This causes the exchange of position between the slower and the faster spins. At one point, they will reunite as their initial time at which the echo signal is acquired.

Both of these relaxation mechanisms (T_1 and T_2) can be weighted in the MRI scan to illustrate differences between tissues. However, most MRI analyses use weighted differences in T_1 relaxation.¹⁶ Although the dependency of the signal intensity of MRI relies on both water concentration and relaxation times (for T_1 and T_2)⁸, it seems that the relaxation time is the only factor that can be manipulated in MRI (impossible to change the water content). Therefore, in many MRI experiments, contrast agents are used for shortening the relaxation rate to increase signal intensities.

1.4 MRI Contrast Agents

The dependency of MRI signal intensity on proton relaxation rate leads to the strategy of shortening the relaxation time of water protons by the addition of probes called contrast agents. Contrast agents are paramagnetic substances that are capable of enhancing relaxation rates of water protons in tissues, organs or blood to give better contrast so that more observable or detectable images are achieved. Contrast agents have properties that shorten T_1 and T_2 . Based on this, they can be classified as: T_1 contrast agents, a group that shorten T_1 more than T_2 , *i.e.* the longitudinal relaxation rate ($1/T_1$) is greater than transverse relaxation rate ($1/T_2$); or T_2 contrast agents that act in the opposite way. T_1 contrast agents increase the signal intensity, while T_2 contrast agents decrease it. T_1 contrast agents are known as positive contrast agents, for example paramagnetic gadolinium-based contrast agents, while T_2 contrast agents is defined as negative contrast agent such as ferromagnetic iron oxide particles.⁹ T_1 contrast agents generally have transverse relaxivity (r_2) and longitudinal relaxivity (r_1) ratio (r_2/r_1) of 1-2 while T_2 agents have 10 or more.¹⁷

The presence of a Gd(III) complex increases the longitudinal ($1/T_1$) and transverse ($1/T_2$) relaxation rates of water protons by roughly similar amounts. Thus, a Gd(III) complex is better visualized by T_1 -weighted imaging, due to the similar effect of transverse and longitudinal relaxivities which increases the ratio of $1/T_1$ more than $1/T_2$ in tissue.¹⁷

1.4.1 Gadolinium-based Contrast Agent and Relaxivity

In three decades, the use of gadolinium as a contrast agent has become a routine clinical application. The choice to Gd(III) is due to its seven unpaired electrons and their associated fluctuating magnetic field that can interact with water protons and speed up their relaxation. Compared to other lanthanides such as dysprosium(III) and holmium(III) which have larger magnetic moments, Gd(III) has a symmetric S -ground state which is a more hospitable environment for electron spins, leading to a much slower electronic relaxation rate (long electron spin relaxation time $\sim 10^{-9}$ s).¹⁸ This places the fluctuating magnetic field associated with Gd(III) more in tune with proton Larmor frequency, the fluctuation within Dy, Ho is much higher and less in tune with the proton Larmor frequency. There are some requirements for contrast agents such as; low toxicity, fast clearance, water solubility, in solution they should have a low osmotic potential,¹⁸ and

must be thermodynamically and kinetically stable to ensure long-term stability to avoid any transmetallation of Gd(III).¹⁹

In addition to its excellent character as the best relaxation agent, gadolinium(III) is considered as a toxic metal if present inside the body at the doses administrated. This is due to its ionic radius being nearly equal to calcium(II) leading to competition reactions,²⁰ which can cause problems with metabolic or signalling processes.²¹ Fortunately, its toxicity can be avoided by using chelating agents, which make it safe for clinical use. Many chelating agents have been used; however, multidentate ligands are preferred to form thermodynamically and more importantly kinetically stable complexes.

The contribution of a contrast agent in increasing an MR signal is expressed as relaxivity (r), which is defined as the capability of a contrast agent to increase the relaxation rate per unit concentration (presented in units of $\text{mM}^{-1}\text{s}^{-1}$).¹⁷ The correlation between relaxivity and relaxation rate is derived from the Eqn. 1.11.

$$\frac{1}{T_{i,obs}} = \left(\frac{1}{T_{i,d}}\right) + \left(\frac{1}{T_{i,p}}\right) = \left(\frac{1}{T_{i,d}}\right) + (r_i[CA]) \quad \text{for } i = 1, 2 \quad (1.11)$$

Where, r_i represents the relaxivity, that is the amount of increase in $1/T_1$ or $1/T_2$ per millimolar of contrast agent. In other words, r_i gives a scale to the effectiveness of a contrast agent in decreasing the relaxation time of surrounding water proton. Therefore, larger r_1 values will provide brighter images, while for larger r_2 values, more darker images are obtained.²² The observed relaxation rate is expressed by $(1/T_{i,obs})$. While $(1/T_{i,d})$ and $(1/T_{i,p})$ correspond to the relaxation rate in the absence of contrast agent (diamagnetic contribution) and the relaxation rate caused by contrast agent (paramagnetic contribution). Based on the Eqn. 1.11, r_i can be determined by plotting $(1/T_{i,obs})$ versus $[CA]$, in which r_i is expressed as its slope. The paramagnetic contribution is derived from all coordination waters as formulated in Eqn. 1.12.

$$\frac{1}{T_{i,p}} = \left(\frac{1}{T_i}\right)_{inner} + \left(\frac{1}{T_i}\right)_{2nd} + \left(\frac{1}{T_i}\right)_{outer} \quad \text{for } i = 1, 2 \quad (1.12)$$

Where, $(1/T_i)_{inner}$, $(1/T_i)_{second}$, and $(1/T_i)_{outer}$ correspond to the relaxation rate contributed by inner-, second and outer water molecules. These types of water molecules will be discussed in the following section.

1.4.2 Inner-, Second- and Outer-sphere Water Molecules

The bulk water surrounding the contrast agent can be classified into three different types namely inner-, second- and outer-sphere water molecules as presented at Fig. 1.15. The inner-sphere water molecules are the main contributor to the relaxation rate, they interact directly with the paramagnetic metal ion. The second-sphere is classified as water molecules that are indirectly bound to the paramagnetic metal ion, they contribute by hydrogen bonding to the ligand, *e.g.* to ligand carboxylate groups. While, all other water closely diffusing molecules are considered as outer-sphere water. The second- and the outer-sphere are considered to have a smaller contribution (although GdDOTA has a similar contribution between inner- and outer sphere waters) to the relaxation rate.²⁰

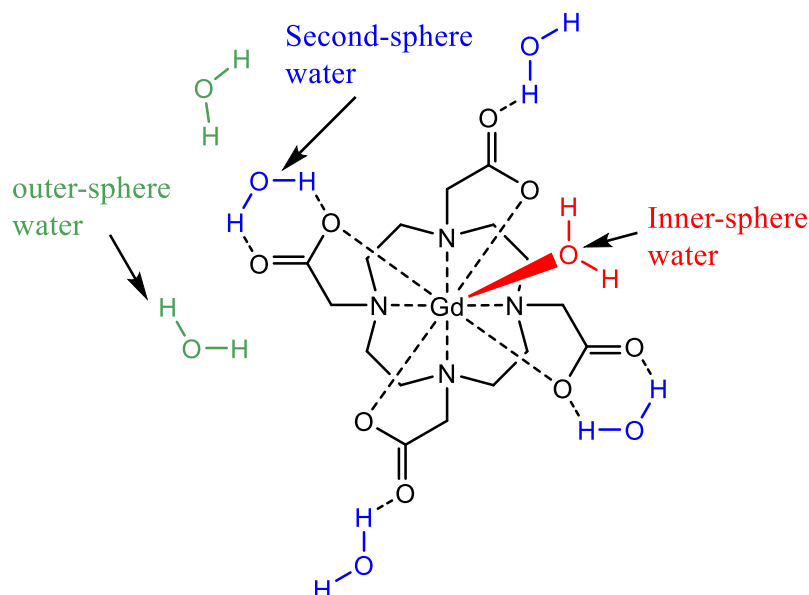


Figure 1.15: Different classes of water associated with Gd(III)-based contrast agent. Inner-sphere (directly bonded to paramagnetic metal), second-sphere (coordinated indirectly) and the outer-sphere water.¹⁷

The longitudinal relaxation ($1/T_1$) contributed to by inner-sphere waters and the paramagnetic metal ion is expressed by Eqn. 1.13.

$$\left(\frac{1}{T_1}\right)_{inner} = \frac{[CA]q}{55.56(\tau_m + T_{1,m})} \quad (1.13)$$

Where, [CA] is molar concentration of paramagnetic complex, q is number of bound water molecules, T_{1m} is longitudinal relaxation time of bound water molecules and τ_m is the water exchange lifetime. The inner-sphere relaxivity is clearly increased by the increasing of the hydration number, however, practically the number of inner-sphere

waters is limited to one or two molecules in order to maintain the thermodynamic stability and/or the kinetic inertness of the complex.

Second-sphere relaxation takes place on the water molecules indirectly coordinated to the paramagnetic metal ion. Its contribution is not easily calculated due to a short τ_m and unknown quantity of the second-sphere water molecules as well as its Gd-H distance.¹⁷ The actual mechanism of the outer-sphere relaxation is not completely understood. Outer-sphere relaxation has received less attention because of the lower contribution to the total relaxivity and the difficulty in exerting control over it. The contribution of second- and outer-sphere can be estimated by examination of $q = 0$ complexes. For this reason, many studies have been conducted to manipulate or to control the inner-sphere water molecules in order to develop contrast agent for certain applications.

1.4.3 Strategies to Increase Relaxivity

Based on the Solomon-Bloembergen theory there are three aspects contributing to relaxivity namely: hydration number (q), rotational correlation time (τ_R) and the residence life time (τ_m). As illustrated in Fig. 1.16, the relaxation depends on the longitudinal relaxation time (T_{1m}) of inner-sphere water molecules, rotational correlation time (τ_R) and residence lifetime (τ_m) of the bound water molecules.²³

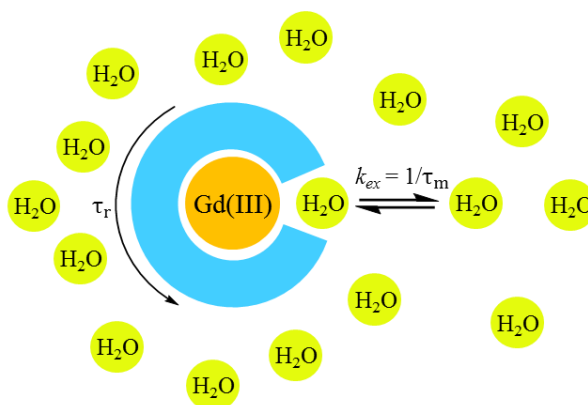


Figure 1.16: Water relaxation model of inner-sphere water exchange mechanism with surrounding outer sphere water molecules.¹⁸

In addition, according to Eqn. 1.13, the relaxivity can be increased in two ways. First, it is clear that increasing q will increase the relaxivity. However, it reduces the gadolinium coordination sites available to the ligand and therefore the complex

thermodynamic stability will decrease simultaneously. The presence of small ligands such as bicarbonate and phosphate can also potentially occupy the coordination site.⁹ Second, the relaxivity will increase with smaller τ_m values. By lowering the residence lifetime, the water exchange rate to its surrounding contrast agent water will increase, therefore more waters are relaxed per second. On the other hand, the relaxivity will decrease if the water exchange rate becomes too fast. This is because the interaction between water and the contrast agent is not long enough. In addition, τ_R also plays an important role in relaxivity. The relaxivity will increase by lengthening the rotational correlation time.²⁰ It provides sufficient time for coupling between proton and the paramagnetic metal ion (Gd(III)). However, this factor only really works well in lower applied magnetic field (0.5-3T). The rotation or tumbling rate can be reduced by increasing the molecular weight or increasing the size of contrast agent such as through dimerization, polymerization or by additional hydrophobic moieties that can interact with protein or lipid. The water exchange rate and the rotational diffusion are temperature dependent, thus so is the relaxivity.⁹ Controlling q , rotational correlation time and lifetime, allows optimum dipole-dipole interaction between paramagnetic metal ion (Gd(III)) and surrounding water molecules.

1.4.4 Dipole-dipole (Dipolar) Relaxation

As mentioned in the previous section, lanthanide ions such as Gd(III) can decrease the relaxation time *via* a dipolar mechanism.⁹ This mechanism is believed to occur to both T_1 and T_2 relaxation which are affected by four main factors namely: types of spins, distance, angle and relative motion between them. As tiny bar magnets which has two poles (dipoles), protons will interact each other through space. In addition, which is most important, there is also interaction between electrons and protons, which is more powerful than a proton-proton interaction as a result of their massive gyromagnetic ratio. Thus, Gd(III) that contains seven unpaired electrons is very effective in relaxing water protons. Dipole-dipole interaction is much stronger over short distances and is decreased by a factor of $1/r^6$. The angle between two spins affects the dipolar interaction by a factor of $3 \cos^2\theta - 1$, in which its value becomes zero at $\theta \approx 54.7^\circ$. The type of relaxation depends on the spin movement, for a frequency similar to the Larmor frequency, T_1 relaxation is preferred, while slow movement causes predominantly T_2 relaxation.

1.4.5 Smart Contrast Agents

During the last 20 years, smart contrast agents (also known as a responsive or activated contrast agents) attract much attention.^{8,24,25,26} This class of contrast agents respond only to specific stimuli, and it is believed that these will increase the “power” of MRI during disease diagnosis. Several types of smart contrast agents have been reported that act differently based on their mechanism of action. First, contrast agents that can bind to the stimuli in a reversible way. These contrast agents are also called reversible MRI contrast agents. For example (DOPTA-Gd) which responds selectively towards calcium(II) (Fig. 1.17 (left)).²⁷ This type of contrast agent can be used detect the fluctuation of calcium ions inside the body. The second type are contrast agents that cannot return to their initial condition. These agents are called as irreversible MRI contrast agents such as Yb-DO3A-oAA that responds specific to nitric oxide (Fig. 1.17 (right)).²⁸ There have been some reports of smart contrast agents that respond to biological activities such as enzymes,^{29, 30} blood-brain barrier,²⁴ pH,^{31,32} gene expressions^{33,34} hypoxia,³⁵ adenosine³⁶, temperature³⁷ and metals.^{27, 38, 39}

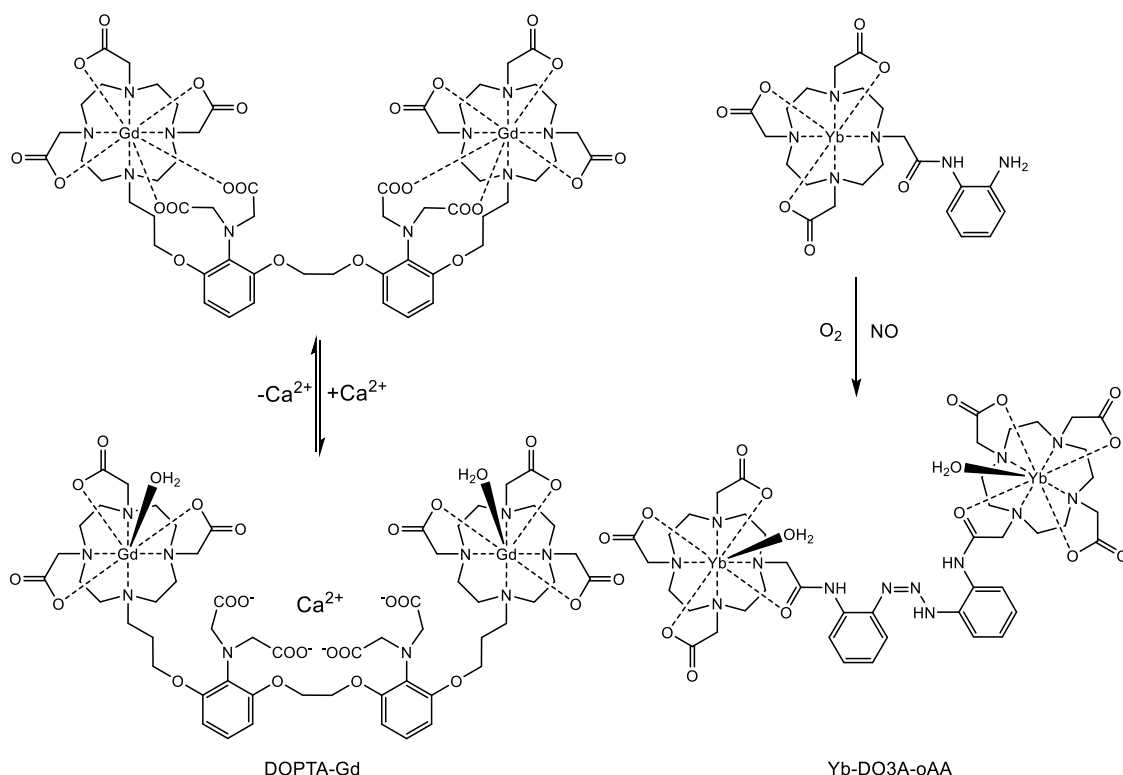


Figure 1.17: Examples of smart MRI contrast agents that respond to specific stimuli reversibly (left)²⁷ and irreversibly (right).²⁸

Since they are designed to be responsive to specific stimuli, selectivity is the most substantial aspect when building a strategy to achieve the desired probe. Several factors including donor type, number of donors, cavity size, and geometry play an important role. Inactivity in the presence of any other metals, potential interference from both small- and macro-organic molecules should be considered.⁸ The most significant aspect is that it should meet the fundamental criteria, namely: high water solubility, low toxicity and an ability to image both intra and extra cellular spaces.⁸ Nowadays, research on gadolinium (Gd)-based contrast agents is increasing.

1.4.6 Application of MRI

The use of MRI technique expands to cover many applications, not just to give physiological images, it can also provide other information such as identification of a specific metal and reaction of interest in living biological systems by a relevant contrast agent.^{8,40} This is because the non-invasive, non-radiative and relatively safe technique can be applied in living organisms.⁴¹ To support such development, multimodal techniques have been widely applied, which are able to eliminate their own individual weakness to provide a powerful analysis method. The intention has been to combine modalities during the last decade. For example, the combination of luminescence imaging and MRI, in which luminescence imaging is capable of giving acceptable image; however, a lack of good penetration to a deep tissue; while MRI has better penetration to give whole body images although in a relatively lower resolution.⁴¹ A contrast agent can be designed to have the ability to accumulate in a specific place such as in a cancer cell by attaching it to a target vector. For example a tumor-targeted MRI contrast agent cycloalkane-based cyclic RGD (Arg-Gly-Asp) peptide which conjugated with GdDOTA has a high affinity to U87MG glioblastoma.⁴² Many studies have been conducted to combine an MRI contrast agent to certain moieties that can be used in other modalities.^{41,43} It has been extended to many purposes in showing anatomical features, such as liver,⁴⁴ tumor,⁴⁵ drug delivery,⁴⁶ and blood flow. Moreover, MRI contrast agents can be used to detect the abundance of certain metal ions such as Fe, Ca, Zn, Cu.^{47,48,49,50,51}

1.5 Luminescence Emission Spectroscopy

Luminescence emission spectroscopy is becoming one of the most promising techniques in biology and medicine. Luminescence spectroscopy can detect very low concentrations 10^{-10} to 10^{-12} M, much lower than e.g. absorption spectroscopy and NMR

spectroscopy, at least 10^{-8} M and 10^{-5} M respectively.⁵² The term of “luminescence” was first introduced in 1888 by Wiedemann for characterizing the light which is not derived from heat radiation.⁵³ Luminescence is a process of emission of light by a substance that could be caused by chemical reaction, absorption of energy or friction. Luminescence induced by photoexcitation is known as photoluminescence which can be divided into fluorescence and phosphorescence. These processes are differentiated by their electronic pathways. Fluorescence refers to a shorter-lived emission process which occurs once energy is absorbed (between 10^{-9} to 10^{-7} seconds). While phosphorescence occurs over much longer times (between 10^{-6} to 10^2 seconds). Details of these processes are described in the following section.

1.5.1 Fundamental Properties of Photoluminescence

When a substance absorbs energy (light), the electron on its ground state (S_0) will be excited to their excited state (S_1 , S_2 , etc.), this process occurs very quickly ($\sim 10^{-15}$ seconds). The energy absorbed is quantized (discrete) following Planck’s law expressed in the Eqn. 1.14.

$$E = nh\nu = nh \frac{c}{\lambda} \quad (1.14)$$

Where, E is the energy, h is the Planck’s constant (6.624×10^{-34} mkg s^{-1}), ν is the frequency, c is the speed of light (3×10^8 ms $^{-1}$), n is the positive integer and λ is the wavelength. According to this Planck’s law, the energy of photon is directly proportional to the wavelength.

In addition, each energy level (S_0 and S_1) contains different vibrational or rotational energy levels (ν_0 , ν_1 , ν_2 , etc.), in which, at room temperature, most molecules occupy the lowest vibrational level. As a consequence, excitation can occur from the ground state to any vibration energy levels of the excited state, for example from ground state at lowest vibration energy level (S_0, ν_0) to excited state at third vibration energy level (S_1, ν_3). There are two different kinds of excited states: singlet excitation state when electron spin may remain oriented as before, and triplet state when its orientation changes and has the same direction as that of the remaining electron from the former pair. The energy level of the triplet excited state is slightly lower than its singlet state. Molecules can arrive in triplet states only by intersystem crossing (non-radiative process) from a singlet state and not from the ground state. The presence of rotational energy levels

associated with each vibrational level increase the number of possible absorption bands. Therefore, broad absorption spectra are always observed for most fluorophores.

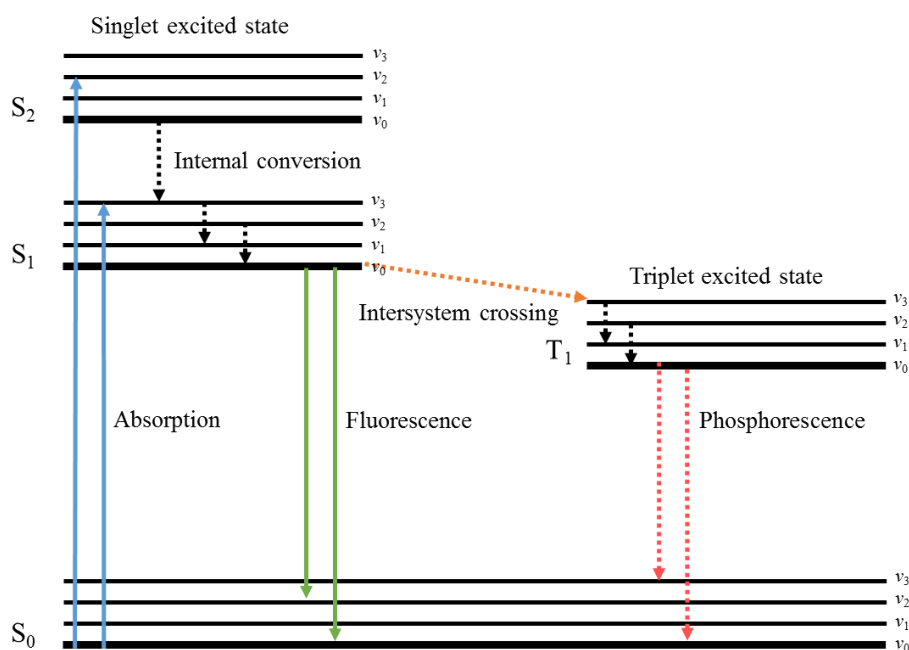


Figure 1.18: Jablonski diagram visualizing absorption and luminescence processes.

Once energy is absorbed and the electron is excited from ground state (S_0) to the excited state (S_1), the electron then falls to the lowest vibration energy level in the excited state by collision then several processes could occur. The first process is called internal conversion (IC), in which the electron will relax from lowest vibrational level of the upper state to a higher vibrational level of a lower excited state by emitting heat to its surrounding (about 10^{-12} s). The transition energy between vibrational energy levels is more efficient when their vibrational wave functions overlap to each other, which is known as the Franck-Condon principle. When the electrons reach the lowest vibrational level of the first excited state, there are two possible mechanisms that take place namely: fluorescence or phosphorescence. It is called fluorescence, when the electron returns from the lowest vibrational level of the singlet excited state to any vibration levels on its ground state by emitting energy (photon) (this process varies from 5×10^{-9} s for many organic crystalline materials and up to 2 s for the lanthanide chelates). Another process is a non-radiative pathway called inter-system crossing (ISC), which occurs due to the feasibility of transitions between the excited singlet-state (S_1) and the excited triplet-state (T_1). The electron in the singlet excited state could be transferred to the triplet excited state before it then relaxes to its ground state by emitting energy. The transition between lowest triplet

excited state (T_1) to its ground state (S_0) are spin-forbidden, thus the rate constant is lower than fluorescence. This is termed as “phosphorescence” which has a very long lifetime (typically 10^{-3} s).⁵² The absorption and luminescence processes can be visualized using Jablonski diagram (Fig. 1.18) which is named from a Polish physicist Alexander Jablonski.

1.5.2 Stokes Shift



Figure 1.19: Electronic absorption and emission bands.

In most fluorophores, the vibration of energy levels for both ground and excited states are similar. This is because the absorption process does not perturb the shape of molecule significantly. Furthermore, the fluorescence emission always takes place from the lowest vibrational level of the first excited state. Therefore, they produce the similar profile/shape as in absorption, like a mirror image as presented at Fig. 1.19.⁵⁴

The energy emitted by a fluorophore in the fluorescence process is always lower than that of absorption and even lower in phosphorescence. This means that the emission bands are situated at longer wavelengths. The gap between absorption and emission wavelengths is known as Stokes Shift, which was firstly observed in 1852 by Sir George Stokes.⁵⁵ The Stokes shift is originated by the rapid relaxation of excited electrons to the lowest vibrational energy of first excited state. Besides, as presented in Fig. 1.19, the transition between excited state and the higher vibrational energy level of the ground state also contributes to the loss of some emission energy which is converted to vibration. In addition to that, the solvent orientation effect, excited-state reactions, complex formation, and resonance energy transfer can also contribute to the Stokes shift. As a result, its magnitude varies from a few, up to hundreds of nanometres.

1.6 Lanthanides

Lanthanide originates from a Greek word *Lanthaneien* meaning “lying hidden”.⁵³ Lanthanides are also known as rare earth elements although they are not scarce.⁵⁶ Lanthanides have luminescence properties except La and Lu (Gd has a very high excited state generally inaccessible). Resembling the *d*-block elements which are characterized by incompletely filled *d*-orbitals, lanthanides have incompletely filled *f*-orbitals. In addition, the uncommon energy level arrangements of the lanthanides make them have different patterns of electron configuration compared to main group and *d*-block elements. For instance, Ce has electron configuration [Xe] $6s^2 5d^1 4f^1$, while addition one electron as in Pr has electron configuration [Xe] $6s^2 4f^3$, moreover in Gd the configuration changes due to the preferable of half-filled electron configuration [Xe] $6s^2 5d^1 4f^7$, while Tb has the electron configuration of the previous pattern [Xe] $6s^2 4f^9$. Most of lanthanide elements have 3+ oxidation states in aqueous solution and are paramagnetic as a consequence of their unpaired electrons.⁵⁷

1.6.1 Chemistry and Coordination Properties of Lanthanides

The *f*-orbitals in lanthanides lie deeper and are shielded from their environment by filled *5s*, *5p* and/or *6s* orbitals. This means that the *4f* orbitals do not directly participate in chemical bonding. This also explains the similarities in chemical properties of the lanthanide ions which lead to difficulty in separation on their early discovery.⁵⁶ The emission process is not affected by the surrounding matrix and the ligand field, resulting in sharp, line-like emission bands.⁵⁶ The *f-f* transitions are formally forbidden by the spin and Laporte rule providing long excited state lifetime (milli- to micro-second) or six times longer than common organic fluorophores.^{56,58,59} The coordination properties occur mainly through ionic interaction and have very weak covalent character. Therefore, the complex stereochemistry is affected by the steric hindrance of its ligands. Lanthanides are highly electropositive elements, and the trivalent ions (Ln^{3+}) are considered as the most stable ions and behave as hard Lewis acids. Thus, in designing a chelating ligand, the hard base-containing ligands are the most preferred.⁵⁷

Lanthanides have relatively large ionic radii which substantially decrease with increasing atomic number. This “contraction” is derived by the increasing charge density.^{56,58} Thus, the coordination properties of lanthanides are significantly influenced by the ionic radii. In fact, they could have up to 12 coordination number, however 8 and

9 are the most common number.⁵⁷ A strong coordinating ligand is required for tailoring highly stable complexes due to the large hydration enthalpies. Furthermore, the complex stability is increased by large favourable entropic effects generated by multidentate ligands (macrocyclic effect).⁵⁷

1.6.2 Lanthanide Luminescence

Electronic transitions in lanthanide ions are generated from electronic transitions inside $4f$ orbitals. Typical luminescence for lanthanide ions is not affected considerably by their surroundings. As mentioned before, this is because the $4f$ orbitals of lanthanide elements are shielded from the environment by filled $6s$ and $5p$ orbitals, as a result, their spectroscopic and magnetic properties are not affected by the environment. Although the differences in coordination geometry can have clear different in Eu(III) spectra. The transitions within the $4f$ states are parity forbidden, but due to mixing with allowed transitions, like the $4f-5d$ transitions, they do occur. As a result of their shielded f orbital and their forbidden transition character, they have low absorption coefficients and have long luminescence lifetimes, which ranging from microseconds (as in Yb and Nd) up to several milliseconds (as in Eu and Tb).^{7, 53} Fig. 1.20 shows partial energy levels of lanthanide(III) ions.

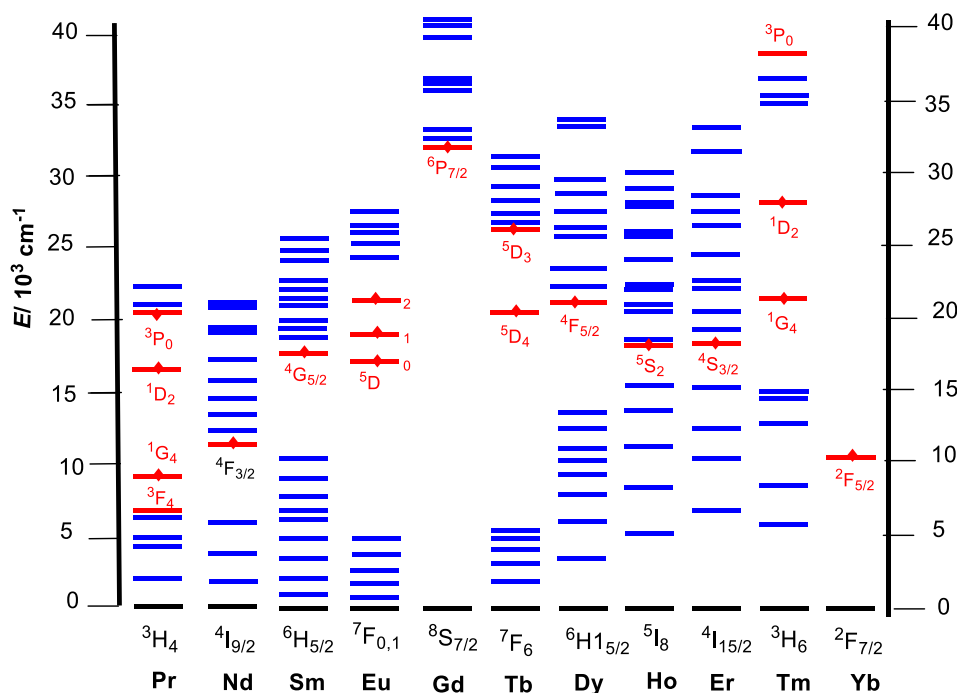
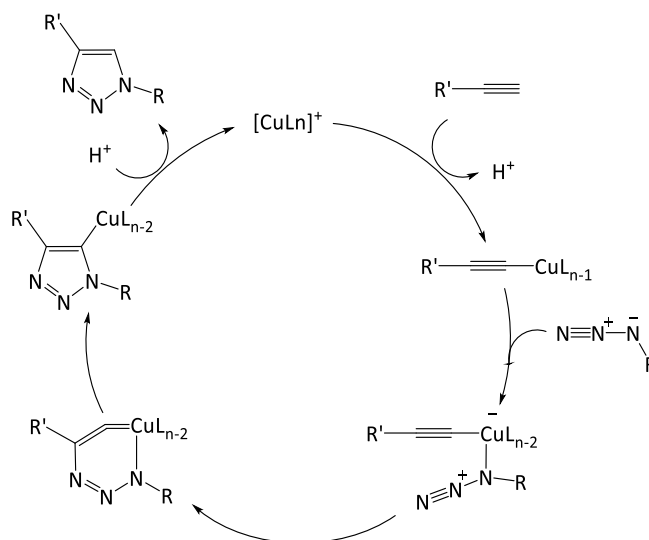


Figure 1.20: Partial energy diagrams for the lanthanide(III) aqua ions. The main luminescent levels are drawn in red, while the fundamental level is indicated in blue.⁵³

Similar to the organic luminescence probes, lanthanide luminescence probes usually display a large Stokes shift with narrow emission peaks,⁵³ and also have a long-emission lifetime, but are relatively insensitive to photobleaching compared to organic fluorophores since the lanthanide ions are good quenchers of the triplet state.⁶⁰ Ligand field splitting of Ln(III) ground and excited states is significantly lower, which is commonly lower than 200 cm^{-1} or 2.5 kJ mol^{-1} .^{56,61} These values are much lower compared to those in transition metals.

There are three types of transition that can occur in lanthanide ions, namely: ligand to metal charge transfer (LMCT), $4f-5d$ and intraconfigurational $4f-4f$.⁶² The first two take place at higher energy. As mentioned previously, the $f-f$ transitions are forbidden. The parity allowed magnetic dipole transitions (MD) are allowed in the free lanthanide ion, $\Delta L = 0$ and $\Delta J = 0, \pm 1$, but $J = 0$ to $J = 0$ is forbidden.⁵⁶ The electric dipole (ED) transition mostly occurs in absorption and emission, $\Delta L, \Delta J < 6; 2, 4, 6$, if J or $J' = 0$; $J = 0$ to $J' = 0$ is forbidden. The interaction between lanthanide ions and their environment allows the mixing of electronic states of opposite parity into $4f$ wave functions causing ED transition to be partly allowed. This called induced ED transition.⁶²

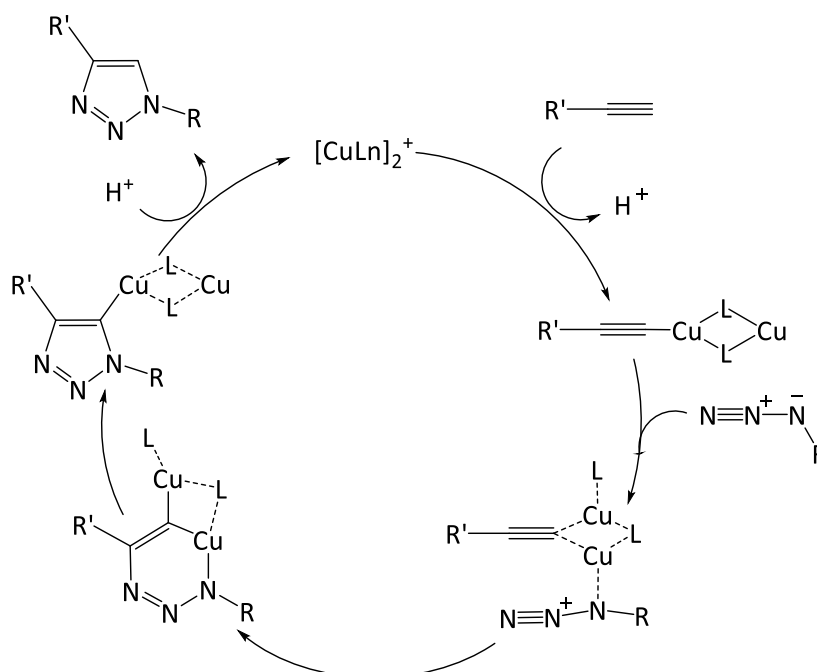
1.7 Click Chemistry



Scheme 1.1: Proposed mechanism for copper(I) catalyzed cycloaddition.⁶³

“Click chemistry” is a well-known phrase coined by Sharpless and co-workers, which defines a reaction which has: selectivity with a wide variety of starting materials and benign solvents; is high-yielding, clean with no significant by products; insensitive

to the reaction environment such as water and oxygen; unaffected by the nature of the functionalized groups being combined with each other; and has a simple purification process.⁶⁴ The Cu(I)-catalysed azide-alkyne 1,3-dipolar cycloaddition (CuAAC) is one such reaction. It became popular in the 1960s when Huisgen and colleagues investigated to study the reaction.⁶⁵ The CuAAC was first published by Meldal⁶⁶ and Sharpless⁶⁷ groups separately in 2002. The first proposed mechanism of this reaction (regioselective 1,4-triazole) is illustrated in Scheme 1.1.



Scheme 1.2. Proposed binuclear mechanism of CuAAC reaction based on DFT calculation.⁶⁸

The reaction is initiated by the complex formation of the copper catalyst through a π -electron with the alkyne bond, which is followed by deprotonation of the terminal alkyne bond to form a Cu-acetylide intermediate species. The copper then binds to the azide forming a copper-azide-acetylide species. The following step has highest energy barrier (based on computational studies) which determines the rate of the reaction.⁶³ In this step, the distal nitrogen of the azide attacks the C-2 carbon of the acetylide to form unusual a six-membered copper(III) metallacycle which is followed by a ring contraction to form the triazolyl-copper derivative (this intermediate was confirmed through X-ray by Nolte *et al.*⁶⁹). The last step is proteolysis to release the copper catalyst and triazole product.⁶³ This reaction works well at room temperature by using a copper(I) catalyst which is generated *in situ* by copper(II) sulphate with sodium ascorbate as a reducing

agent. The triazole product might constitute one or two species in the transition state.⁶⁵ Recently, there were reports of some new proposed mechanisms of click reaction involving two copper(I) species in their intermediate.^{70, 71, 72} One of them is presented at Scheme 1.2. This mechanism is believed to be more favourable kinetically.⁷¹ Low molecular weight organic azide with ((C+O)/N) ratio lower than 3 should not be isolated due to their explosive potential.

After the conventional Sharpless-Fokin catalyst ($\text{CuSO}_4/\text{NaAsc}$), there are a number of catalysts being investigated to catalyse some harsh reactants such as 2-azidopyridine which is relatively inert to be “clicked” by the conventional CuSO_4 method. The most recently used are namely Ru, Ag, Au, Ir, Ni, Zn, Ln.^{73, 74} In addition, click reaction can be conducted with other techniques in order to optimize the reactions condition for instance by microwave irradiation^{75, 76} (which gives a shorter reaction time, mostly has high yields and clean reactions), ultrasound (as a green source of energy to give decrease reaction time and side reaction),^{77, 65} Click reactions can also be done in one pot reactions,^{78, 79, 80} or even copper-free click reactions^{81, 82} and solvent-free click reactions.^{83, 84} Due to its reaction condition flexibility, the use of click chemistry spreads in different areas such as: bioconjugation,⁸⁵ polymer,⁸⁶ material science,⁸⁷ radiopharmaceuticals,⁸⁸ glycoscience⁶⁵ and drug discovery.⁸⁹

1.7.1 Click Chemistry in Drug Discovery

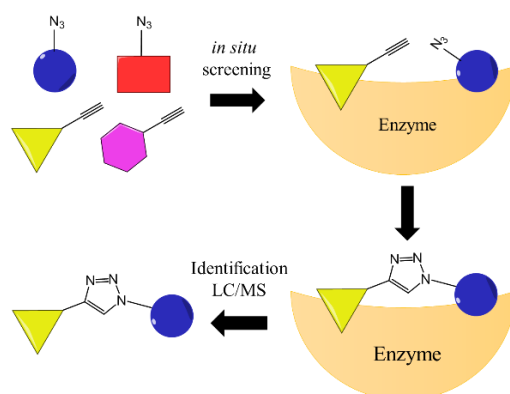


Figure 1.21: Screening test in drug developments.

The recent approach to the drug development is to synthesise commercial drug analogues⁹⁰ or is based on screening of extra- and intracellular molecular targets (Fig. 1.21).⁹¹ The process involves attaching or combining several structures to reach the target compound. In this case click chemistry is a powerful method or tool for simple to complex molecule construction to form triazole containing linkers. In addition, the mild reaction

conditions and in most cases both reactant and product functional groups do not interact with functional biomolecules are considered as the advantages of this reaction. 1,2,3-triazole is a well-known scaffold which is present in active compound performing antimicrobial, antiviral, antitumor or anti-HIV activities.^{90, 91}

The *in situ* click reaction is also used in sensor, labelling and imaging agents. The click reaction meets the demand required in developing such probes. Its fast reaction is characteristic, mild reaction conditions, high selectivity and yield are the main factors considered. Many studies conducted following this approach have analysed different targets namely chromosome and genetic,⁹² nucleic acids and proteins,⁹³ live mammalian cell,⁹⁴ RNA transcription,⁹⁵ cell surface glycoprotein and HER2 kinase.⁹⁶

1.8 Zinc in the Human Body

The necessity of zinc(II) in the human body was noticed over 50 years ago after the case of zinc(II) deficiencies were found in Shiraz, Iran.^{97, 98} Zinc(II) is the second most abundant transition-metal ion found in the human body after iron.⁹⁹ It presents as a divalent ion and spreads around human body either tightly bound in proteins or as mobile pools which exist in certain mammalian organs such as in liver,¹⁰⁰ brain and pancreas which are carefully regulated.⁹⁹ As an intracellular element, 30-40% of zinc(II) is located in nucleus, 50% is in cytoplasm, organelles and specialized vesicles and cell membrane.¹⁰¹ 2-3 g of total zinc(II) is found in adults and only about 0.1% - 0.75% of it is required to be administrated from food on a daily basis in order to renew it.^{98, 101}

1.8.1 Zinc as an Essential Element

Many studies reports zinc(II)'s contribution to several biological processes in metabolism, and it also has a significant role in enzyme regulation, structure and function, neural signal transmission, and gene expression. The significant role for zinc(II) is as a structural cofactor in metalloproteins.⁹⁹ Many hydrolytic enzymes contain zinc(II) ion in the active site, since zinc(II)-bound water or hydroxide are excellent nucleophilic agents. For example, in the catalytic centre of human carbonic anhydrase II (CAII) zinc(II) is coordinated by three histidine residues and a water molecule.¹⁰² Zinc(II) ions are also concentrated in nerve tissues in high quantity (0.1–0.5 mM for brain tissue),¹⁰³ which is located in membrane-enclosed synaptic vesicles as a signalling molecule.¹⁰⁰ It is also believed to have antioxidant properties, but not in the same sense as vitamin E. It reduces

oxidative stress and enhances the activity and levels certain anti-oxidant enzymes and proteins, whilst significantly reducing lipid peroxidation.^{104,105} Zinc(II) is also involved in glucose and lipid metabolism, where it reduces glucose absorption and synthesis, on the other hand promoting glucose metabolism and storage. It plays an important role in the normal functioning of the islet cells of the pancreas.¹⁰⁴ Zinc(II) is one of several essential metals which participate in maintaining the immune cells such as B-cells and T-cells to prevent inflammation.¹⁰⁶ The intracellular free zinc(II) in these cells is involved in signalling events.⁹⁷ Zinc(II) has been ascribed as a factor in increased resistance against tumours.¹⁰⁷ Zinc(II) participates in metabolism processes, transmission and regulation of genetic information, storage, synthesis and action of peptide hormones and structural maintenance of chromatin and biomembranes.¹⁰¹ Nowadays, more than a thousand transcription factors and more than 300 enzymes are known to require zinc(II) for their activities.⁹⁷ In addition, zinc(II) is considered as an important element in cell growth, DNA synthesis, RNA transcription, cell division, and cell activation. Most of zinc(II) is found in liver, kidney, bones, muscle, brain, with the highest in prostate and a part of the eyes.¹⁰⁰

1.8.2 Zinc and Diseases

The abundance of zinc(II) inside the body can be an indicator related to some diseases, the disruption of which is associated with a number of disease states including: types I and II diabetes, Parkinson's disease, epilepsy, amyotrophic lateral sclerosis, Guam ALS-Parkinsonism dementia, hypoxia-ischemia and certain cancers.^{108, 109, 110} A high level of zinc(II) is observed in Alzheimer's disease (the zinc(II) ions released during neuro transmission may induce galvanization of beta-amyloid (A β) plaques) inside the plaques formed of patients.¹⁰⁹ *In vivo* experiments in the mice proves that the zinc(II) excess is a risk factor for Alzheimer's disease pathological processes.¹¹¹ The presence of (A β) plaques in the brain is among the pathological hallmark of AD in which the accumulation of zinc(II) is identified in (A β) plaques.¹¹¹

There is also correlation between zinc(II) and cardiovascular disease in which the decrease in the level of zinc(II) associates with increased cardiovascular diseases.¹¹² Recently, zinc(II) is recognized as an important factor in the regulation of apoptosis.¹¹³ The level of zinc(II) in cancer cells is upregulated by zinc(II) transfer proteins, inhibiting the zinc(II) depletion which is known to induce cell death *via* apoptosis or necrosis.¹⁰⁰

Cancer cells have upregulated zinc(II) levels which allow them to survive.¹⁰⁰ The zinc(II) deficiency may arise from disruption to some structure and function to a fatal problem or even the death. Zinc(II) deficiency is associated with a range of pathological states including skin change, slowed growth, delayed wound healing, hypogonadism and brain development disorder.¹⁰⁰ Zinc(II) deficiencies can be caused by malabsorption syndrome and other gastrointestinal disorders, chronic liver and renal diseases, cystic fibrosis, pancreatic insufficiency, rheumatoid arthritis and other chronic conditions.¹⁰⁰ Zinc(II) deficiency also takes place in intestinal malabsorption syndromes such as acrodermatitis enteropathica, sprue and cystic fibrosis.⁹⁸ Prostate cancer and diabetes is linked to zinc(II) deficiency.⁸ In both type-1 and type-2 diabetes many studies have been conducted to explain the molecular mechanisms underlying the action of zinc(II). In which the involvement of zinc(II) in the insulin storage structure was discovered firstly in 1930s.¹¹⁴ Today, it is known that there is a relationship between zinc(II) and insulin hormone. It is present in β -cells of the pancreas as a hexamer consisting of two zinc(II) ions which can be released into the portal venous system at the time of β -cell de-granulation.¹¹⁵

1.9 Project Outline

1.9.1. Design Rationale

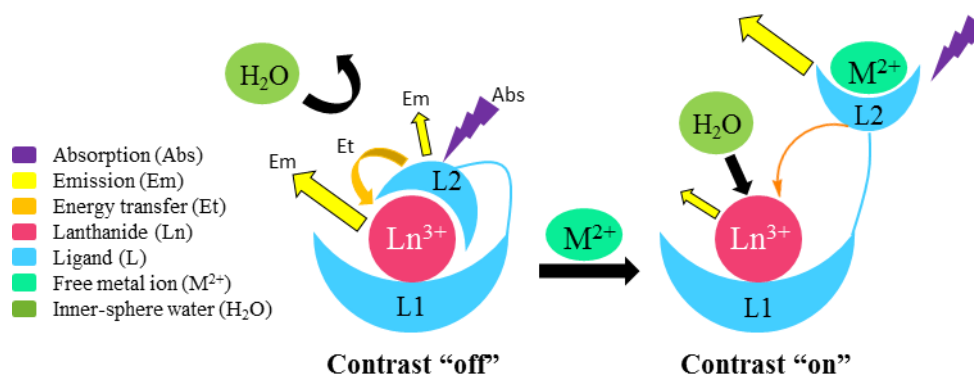


Figure 1.22: The binding model hypothesized of targeted zinc(II)-responsive MRI contrast agent in the absence and presence of zinc(II) (M^{2+}) including the predicted emission alteration.

The importance of zinc(II) in many biological processes increases the necessity of special methods for zinc(II) investigation. As mentioned before, the silent spectroscopic property of zinc(II) makes it difficult to 'see'. Since MRI technique relies only on water's proton relaxation signal, the use of a zinc(II)-responsive contrast agent is considered as a powerful method to investigate this "invisible" essential metal ion. The design of a zinc(II)-responsive contrast agent in this project is illustrated in Fig. 1.22.

Briefly, it consists of three main parts, namely the paramagnetic metal ion, main-ligand and one side-ligand or arm which is active in response to the zinc(II).

This model has proven to be effective in producing such smart probes (this will be discussed in Chapter 2). Therefore, by following this model this research focused on the design of gadolinium-based MRI contrast agents and luminescence probes which respond to the presence of free zinc(II) ions. This probe is a complex compound containing ring-closed DO3A macrocycle as the main ligand (L1) to hold the paramagnetic metal ion, gadolinium(III) (Ln). This complex is attached by a pyridyltriazole-containing ligand as an active arm (L2) that is expected to bind reversibly between the paramagnetic ion and the targeted zinc(II) ion (M^{2+}) to produce an opened-closed structure.

The complex properties and its behaviour in response to zinc(II) ion was studied by exploiting the pyridyltriazole moiety which behaves as an active arm and an antenna (explained at section 3.3) simultaneously. As an antenna, it has a capability to capture the energy given in this case in the form of light. Then it can either emit the energy and return to the ground state or transfer it to any lower energy levels around it through the triplet state. In fact, gadolinium(III) as a paramagnetic metal ion used in this contrast agent has an emissive state which lies at a higher energy level. Thus, the energy captured by the antenna cannot be transferred to its emissive state. On the other hand, certain lanthanides such as terbium(III) and europium(III) have a relatively lower emissive state than the triplet state of pyridyltriazole and most of the other organic antennae. Therefore, energy transfer to these lanthanides is possible. The occurrence of this energy transfer is shown by the emission bands typical for the corresponding lanthanide. The study of the emission properties is very important in designing a smart contrast agent in order to understand the coordination condition (such as to calculate the hydration number) or the active arm behaviour (such as the emission alteration due to different coordination environments). These were used as an early sign to examine the complex response towards targeted zinc(II) ion. Based on this reason, the europium complex analogues on each targeted complex were always be synthesized prior to their main targeted gadolinium(III) complexes.

The proposed mechanism for the targeted compound as illustrated in Fig. 1.22 is as follows: the pyridyltriazole-containing arm (L2) will coordinate to metal centre (Ln^{3+})

through N pyridyl's atom or N triazole's atom *etc.* Consequently, there are no water molecules bound to Ln^{3+} (hydration number $q = 0$), thus they exhibit poor contrast. In the presence of a free divalent metal ion (M^{2+}) in this case is zinc(II), the coordination of pyridyltriazole to Ln^{3+} is expected to be displaced by M^{2+} . This allows water molecules to enter the Ln^{3+} coordination sphere and “switch on” the contrast. In addition, by complexation to Zn^{2+} , pyridyltriazole is also expected to change its emission properties. This has potential to be used in other applications such as fluorescence imaging. In order to achieve good selectivity toward Zn(II), some studies to modify the pyridyltriazole active arm (L2) by additional functional groups such as carboxylate (-COOH) or hydroxide (-OH) are also reported.

1.9.2. Aims of Project

This project was intended to design a zinc-responsive MRI contrast agent with a “switch-on” effect in relaxivity *via* modulation of the hydration number (q) upon zinc(II) ion binding. The contrast agent was developed by using a common Gd-DO3A-based main ligand with a new pyridyltriazole-based structure as a zinc(II) chelator and an active arm. Through this project, the influence of distance between pyridyltriazole scaffold and the lanthanide centre by varying the length of its carbon linker was also studied. In addition, different functional groups were used to observe the coordination affinity towards a lanthanide centre and the zinc(II) target. The influence of distance and functional group will be analysed by observing their luminescence properties. Lastly, this project was also purposed to exploit the potential compounds to be used as luminescence probes.

1.10 Theses Outline

This first chapter presents the general background on its main aspects relating to the topics involving in this work. First, the history of invention and development MRI, mechanism, including the basic principles of MRI technique. Second, the luminescence spectroscopy principle and its application. Third, the essential of biological zinc(II) and its correlation to sever diseases. Chapter 2 describes all aspects relating to the synthetic chemistry used to synthesis the target compounds. The active arm pyridyltriazole was manipulated by switching its structure orientation, changes to the linker or by modification of its side functional groups. Chapter 3 discusses the photophysical properties of the compounds designed as zinc-responsive MRI contrast agents. Chapter 4 exhibits unexpected findings related to emissive fluorescence analogous compounds,

which were originally intended to be used to study the complex properties. Chapter 5 provides a summary of the whole study in synthesizing zinc-responsive contrast agent. Chapter 6 presents the synthesis and analysis methods used along with details characterization of all synthesized compounds.

Chapter 2

Synthesis of Zinc-responsive MRI Contrast Agent

2.1 Background

The development of zinc(II) probes is considered indispensable due to the importance of zinc(II) as a key factor in many severe diseases as discussed in the Chapter 1. Although the information relating the correlation between disease and either high or low concentration zinc(II) is very limited,¹¹⁶ zinc(II) probe development is essential for disease investigations, understanding mechanisms and functions, pathological studies and finally for medication purposes. Zinc(II) probes are commonly designed by mimicking the zinc(II) binding motif which is present in nature, such as amino acid in proteins (enzymes) of a living organism. The zinc(II) active site contains specific ligands (structures) that bind through complexation. Thus, understanding the zinc(II) active sites and zinc(II) chemical properties are required to study its behaviour throughout complexation in order to build zinc(II) probes.

2.1.1 Zinc Chemical Properties

Zinc is found at the end of the first-row transition metals, it has a full d shell (d^{10}) and behaves as a diamagnetic metal. This filled d -shell induces its silent properties (no $d-d$ transition) with respect to spectroscopic analysis. It is considered as a borderline acid along with some other divalent first-row transition metals such as iron(II), cobalt(II), nickel(II), and copper(II).^{117,118} Therefore, it interacts with both soft and hard Lewis bases. Zinc does not undergo redox reactions due to its closed d shell and only has one oxidation state +2, although its complexes could facilitate a redox reaction through certain mechanisms without changing its oxidation state.¹¹⁹ Zinc(II) is considered as a stable ion in biological media and it is available in constant flux.¹⁰¹ In addition, zinc(II) complexes have no ligand field stabilisation energy (LFSE) which leads to geometric flexibility in its coordination geometry.¹⁰⁸ The coordination geometry of zinc(II) is derived primarily by electrostatic and steric interaction between zinc(II) ion and the coordinating ligand.¹²⁰ The possible geometries of zinc(II) are illustrated in Fig. 2.1.¹²¹

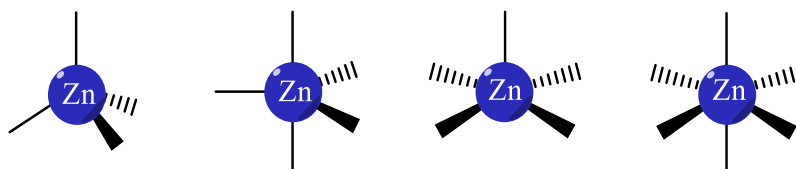


Figure 2.1: Common coordination geometries zinc(II) configuration (from left to right; tetrahedral, trigonal bipyramidal, square pyramidal, octahedral).

According to the Irving–Williams series, the binding experienced by zinc(II) ions is stronger compared to manganese(II) and iron(II) when presented with similar environmental conditions.¹²² Their complex stabilities are presented as follow.¹²³



Interaction between alkali metal ions in water is different from that of transition metals. The alkali metal ions such as Na(I) and Mg(II), bind to water molecules purely through an electrostatic interaction, while transition metals such as zinc(II) have some covalent character, which is confirmed by its heat of solvation energy about -500 kcal/mol. In solution, zinc(II) is solvated by six water molecules, in which each water molecule contributes about -80 kcal/mol which is equal to covalent binding energy of Zn-O.¹²⁰

In addition, zinc(II) aquo complex is considered as a Brønsted acid due to the proton dissociation when dissolved in water to give the aquo-hydroxo complex as presented in Fig. 2.2.

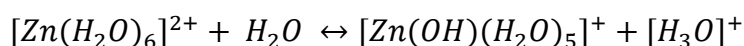


Figure 2.2: Proton dissociation of zinc(II) aquo complex.

Where, $[\text{H}_3\text{O}]^+$ can be calculated by the Henderson-Hasselbalch equation (Eqn. 2.1) to give a pK_a of 9.05 for hydrolysis of this hexaaquo complex. Zinc chloride and other zinc salts of strong acids behave as weak acids which can be calculated through Eqn 2.2 by the assumption that the concentration of $[\text{H}_3\text{O}]^+$ and $[\text{Zn}(\text{OH})_5\text{H}_2\text{O}]^+$ are similar.¹²⁰

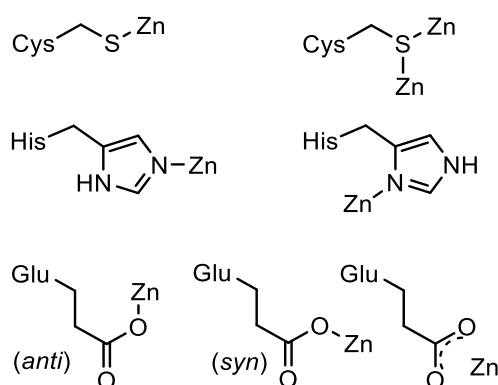
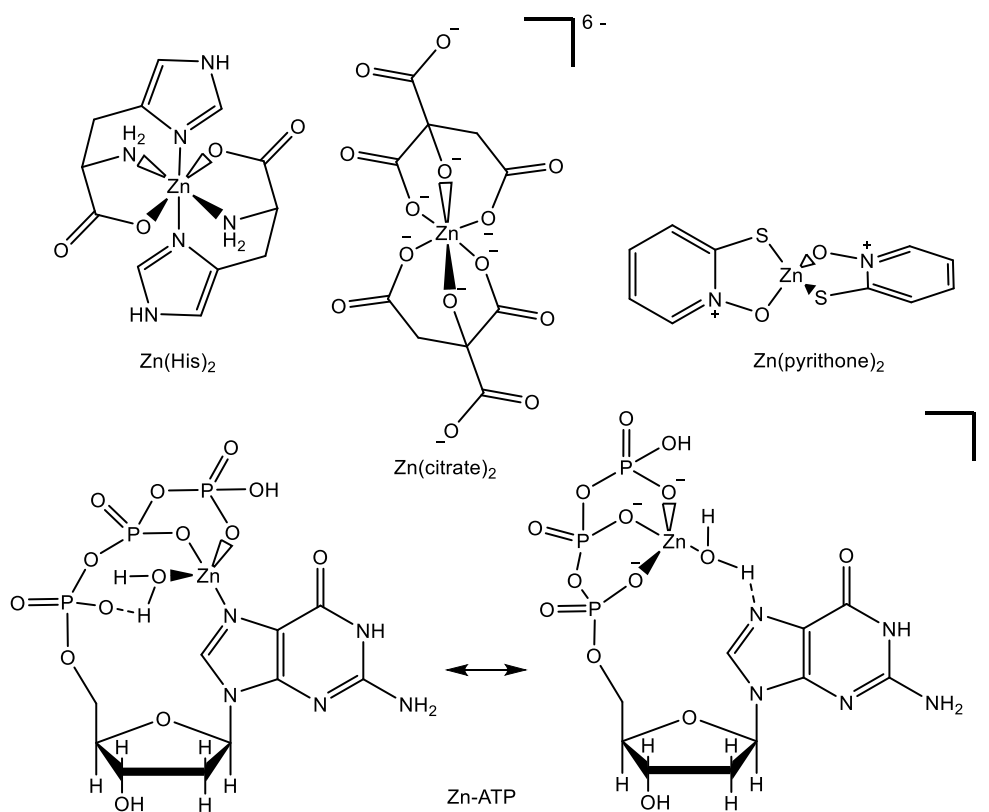
$$[\text{H}_3\text{O}]^+ = K_{a1} \frac{[\text{Zn}(\text{H}_2\text{O})_6]^{2+}}{[\text{Zn}(\text{OH})(\text{H}_2\text{O})_5]^+} \quad (2.1)$$

$$\text{pH} = 0.5\text{pK}_{a1} - 0.5\log(C_s) \quad (2.2)$$

Where, (C_s) is roughly the zinc total concentration. According to this equation, it is known that when the pH is reduced the $[\text{Zn}(\text{H}_2\text{O})_6]^{2+}$ is increased. However, this pH calculation also depends on the chemical composition of the zinc salt.

2.1.2 Zinc in Biological Systems

As discussed in Section 1.7, zinc(II) is present in the human body either tightly bound to proteins (in which it is believed that it will remain in its position during the lifetime of the protein) or as a mobile pool (which binds reversibly through both association and dissociation), which enables zinc(II) regulation such as transporting, transferring, sensing, signalling and storing. Therefore, the first factor to understand is its coordination preference. In nature, zinc(II) is found in proteins bound through certain amino acids such as histidine (His), aspartate (Asp), glutamate (Glu) and cysteine (Cys) (Fig. 2.3).¹²²

Figure 2.3: Zinc binding fashion of certain amino acids.¹²²Figure 2.4: Zinc binding models of naturally occurring small molecules.¹²⁰

Zinc(II) can bind with three to six of these amino acids which can come from up to 4 different proteins with a varied binding motif. This variation is believed to be a consequence of no LFSE.¹²⁰ This is the most important factor in zinc(II) coordination chemistry which allows for a dynamic coordination number of the zinc(II) ion in interactions with different substrates (ligands).¹²⁰

The characteristics of zinc(II) coordination chemistry are the key point to be studied regarding the design of a zinc(II) chelator. The bonding to zinc(II) in proteins could occur *via* sulphur, oxygen and nitrogen donor atoms from these amino acids. Some reports show the zinc(II) binding motif with some small molecular ligands such as pyridithione, citrate, histidine and to a larger ligand such as ATP (Fig. 2.4).¹²⁰ Accordingly, these three kinds of donor atoms (oxygen, nitrogen and sulphur) are an important consideration in designing a zinc-responsive probe.

2.1.3 Zinc-responsive Probes

The first reported zinc-responsive probe was derived from a quinoline containing compound to be used in fluorescence imaging.^{124,125} This compound naturally has low solubility in water, moderate quantum yield and is excited in the UV range (300-400 nm). There are some zinc(II) sensors known today (Fig. 2.5), such as **ZPP1** and **ZPP3** which can be used to calculate quantitatively zinc(II) released from Min6 cells.¹²⁶ Modified structures of these probes (**ZP1B** and **ZP3B**) have improved their sensitivity to the micromolar range. They contain coordinating and non-coordinating picolyl groups which are used to detect zinc(II) containing granules in Min6 insulinoma cells.¹²⁶ Some zinc(II) sensors are based on Coumarin derivatives such as **ZnIC** and **A7**. **ZnIC** is used for imaging exogenous zinc(II) in HEK293 cells,¹²⁷ while compound **A7** was used in RAW264 cells.¹²⁸ Both are sensitive to picomolar concentration, have moderate selectivity and emission spectra in the visible region. Another example of zinc(II) sensors is **FQ1**, which exhibits an intense zinc-induced emission, but has low water solubility and selectivity.¹²⁹ In addition, **ICPBCZin**, a zinc(II) sensor which has two carboxylate groups has a nanomolar selectivity.¹³⁰ **AQZ** is another example of sensor which showing a ratiometric fluorescence with a good selectivity toward zinc(II).¹³¹

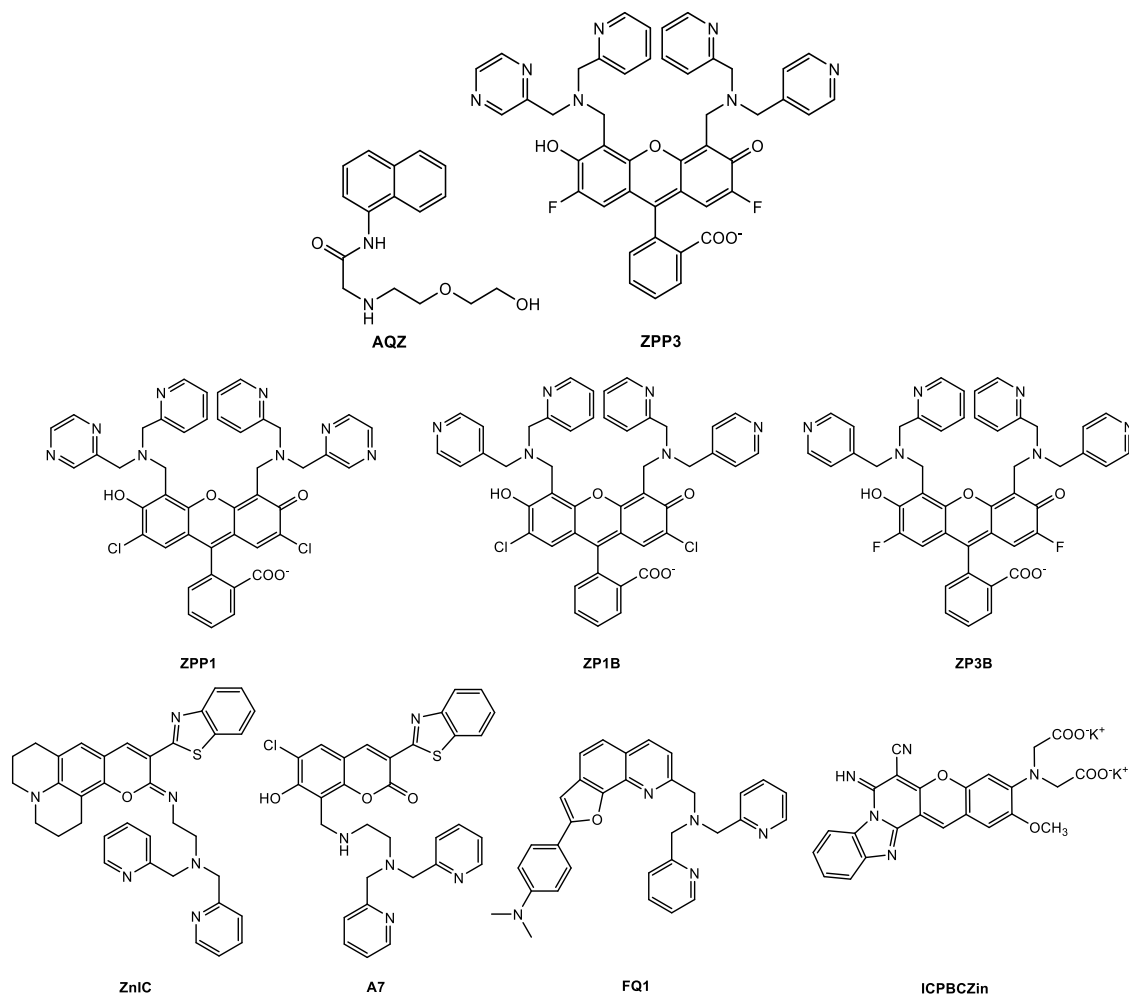


Figure 2.5: Structures of some literature reported zinc-responsive probes.^{126, 127, 128, 129, 130, 131}

A general mechanism of action of the majority of these zinc(II) sensors relies on a quenching mechanism *via* photo-induced electron transfer or intramolecular charge transfer, in the metal-free state of the molecule.¹³² During the ligand coordination to Zn, the electron transfer deactivation pathway is largely prohibited upon binding, at the same time more extended pi-conjugation is formed so that their luminescence exhibits significant enhancement and induces a red-shift.⁴¹ These mechanisms will be discussed more detail in Chapter 3. In the other words, the occurrence of zinc-ligand binding is observable through their photophysical properties by transformations of either or both of their absorption, emission or changes to their quantum yield.

2.1.4 Zinc-responsive MRI Contrast Agents

The MRI technique could participate in many biological investigations by using a smart contrast agent. These contrast agents are designed to be selectively responsive to

a specific target as previously explained in Section 1.4.5. One application is to detect endogenous biological metals including zinc(II) ion.⁸ By combination of the MRI technique and a responsive contrast agent, many biochemical events in living organisms can be investigated. The design of such smart contrast agents (in this case zinc-responsive MRI contrast agents) could be simply performed by a combination of a zinc-responsive probe with a paramagnetic metal complex, as it has been discussed in Section 1.4.1, in which majority of them are based on gadolinium. Zinc-responsive MRI contrast agent can be classified to several groups according to their mechanisms, namely: probes that change rotational tumbling time which correlates with water exchange rate; those that change the number of coordinating inner-sphere water molecules; and/or multimeric compounds.

Fig. 2.6 shows some reported zinc-responsive MRI contrast agents, made responsive through a change in rotational tumbling in response to the presence the free zinc(II) ion. **Gd-DOTA*di*BPEN** for example, in response in the presence of zinc(II), it shows enhanced relaxivity by 20% from 5.0 ± 0.1 to 6.0 ± 0.1 $\text{mM}^{-1} \text{s}^{-1}$ (at 37°C, pH 7.6, 0.1 M Tris buffer and 23 MHz) in response to 2 equivalents of added zinc(II) (Gd:Zn/1:2) and it also shows selectivity toward zinc(II) over sodium(I), potassium(I), calcium(II) and magnesium(II), but not over copper(II).¹¹⁶ **GdDOTA-*di*BPYREN** which is slightly different from **Gd-DOTA*di*BPEN** has the relaxivity 4.2 ± 0.1 $\text{mM}^{-1} \text{s}^{-1}$ in the absence of zinc(II), which is increased to 6.9 ± 0.2 $\text{mM}^{-1} \text{s}^{-1}$ upon the addition of 2 equivalents of zinc(II) (37°C, pH 7.6, 0.1 M Tris buffer, 23 MHz). It has the same modulation as its similar compound (**Gd-DOTA*di*BPEN**), in the presence human serum albumin its relaxivity increased from 8.4 ± 0.2 to 15.3 ± 0.4 $\text{mM}^{-1} \text{s}^{-1}$ selective over calcium(II) and magnesium(II) but again gave the same response with copper(II).¹³³ There are a couple of dual-modal zinc-responsive MRI contrast agents and luminescence imaging probes derived from Gd-DO3A-based contrast agents. The first compound contains an amidoquinoline moiety (**GdDOTA*AA*QA**). The relaxivity value of this compound raised from 4.2 to 6.6 $\text{mM}^{-1} \text{s}^{-1}$ (57% higher) during the addition of a half equivalent of zinc(II) ion (measured at 25°C, 9.4 T) although the hydration number remained unchanged.¹³⁴ The second compound carrying 8-sulfonamidoquinoline group (**GdDOTA*SA*QA**) which increased its relaxivity from 3.8 to 5.9 $\text{mM}^{-1} \text{s}^{-1}$ (55% enhancement at 25°C, HEPES buffer 100 mM pH 7.2, 23 MHz) upon the addition of 0.5 equivalent zinc(II) ion. In

addition to that it has no significant movement during the addition other biological metal ion such as magnesium(II), iron(II), iron(III) and calcium(II).⁴¹

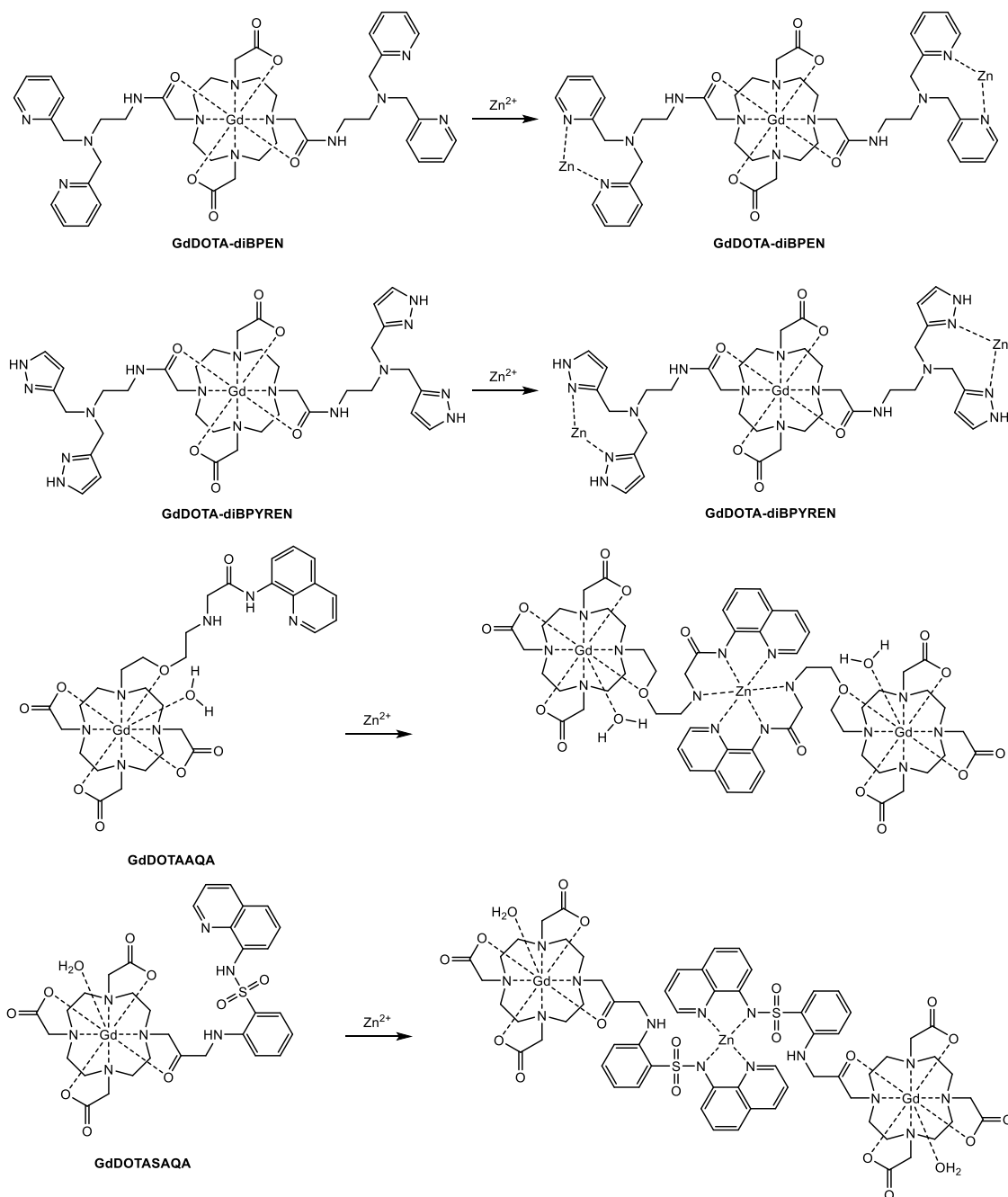


Figure 2.6: Zinc responsive MRI contrast agents based on modulation of their rotational tumbling. ^{116, 133, 134, 41}

Fig. 2.7 shows zinc-responsive contrast agents which rely on a change in the number of inner-sphere waters. **Gd-daa3** is a Gd-DO3A-based contrast agent containing an iminodiacetate active group for $Zn(II)$ binding. The relaxivity increased by 73% from 2.3 to 5.1 $mM^{-1}s^{-1}$ in response to zinc(II) and increased even more (from 5.8 to 7.7 mM^{-1}

$^1\text{s}^{-1}$) in the presence of both zinc(II) and human serum albumin (at 37°C , HEPES buffer and 60 MHz). It enhanced the relaxivity by increasing the hydration number q as shown in luminescence lifetime experiments with **Tb-daa3**.¹³⁵ On the other hand, its related compound **Gd-apa3**, which has one pyridine and one acetate group, increased the relaxivity by 103% in a response to Zn^{2+} .¹³⁶ These two probes are selective for zinc(II) over sodium(I), potassium(I), calcium(II) and magnesium(II). However, **Gd-daa3** has some response to copper(II). Another GdDO3A-based zinc-responsive contrast agent in this group is **GdL1**. It also contains a carboxylate moiety as their active arm. The relaxivity of this compound increased from 3.8 to $6.6 \text{ mM}^{-1} \text{ s}^{-1}$ (310K, 1.4 T, 0.1M MOPS buffer pH 7.4) upon the addition of 1 equivalent zinc(II) ion and have no significant changes with sodium(I), potassium(I), magnesium(II), calcium(II) and copper(II).⁴⁹

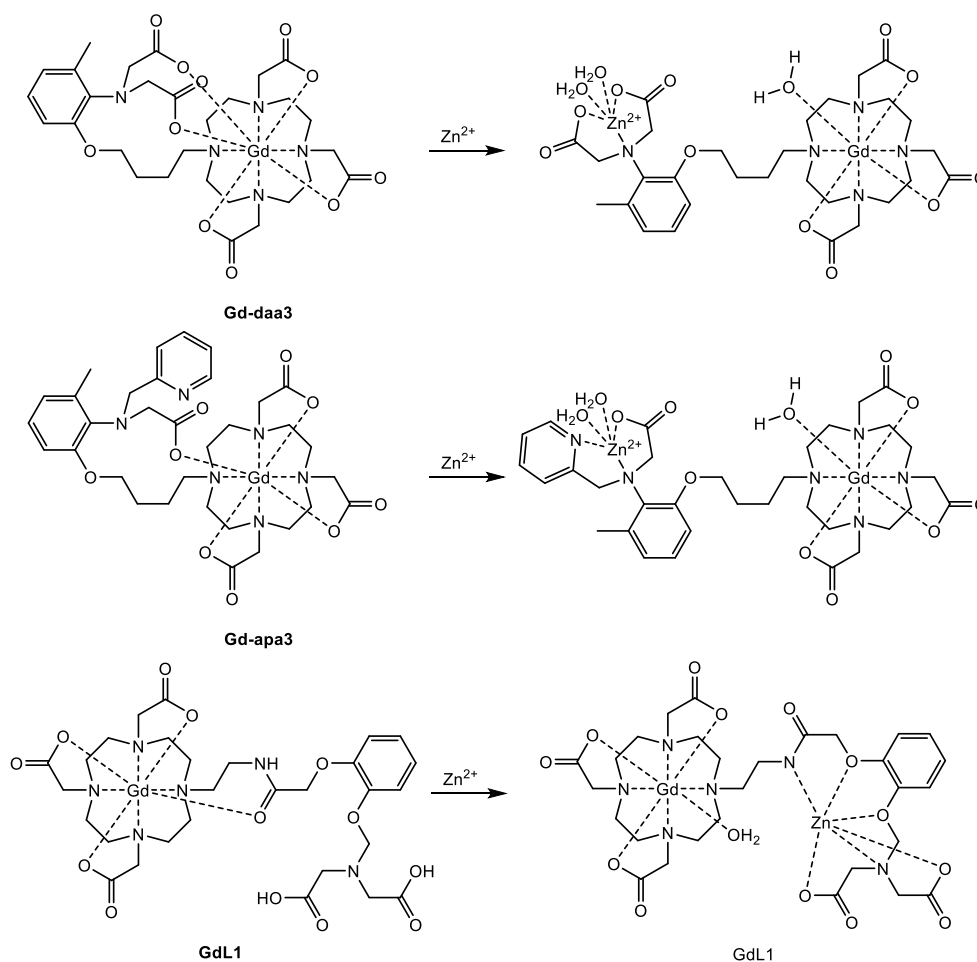


Figure 2.7: Zinc responsive MRI contrast agents based on the modulation of their hydration number.^{135, 136, 49}

Based on these examples, both carboxylate and amine groups cannot be omitted when designing a zinc-responsive MRI contrast agent. The active arm must consist of at

least one of these functional groups. In addition, there are some other factors that should be considered during the development of zinc-responsive MRI contrast agent to get an “ideal” probe. These important factors will be discussed in the following section.

2.1.5 Designing a Zinc-responsive MRI Contrast Agent

There were some reported zinc(II) probes described in the previous section, generally the probes consist of several parts which are combined with their own function to construct a zinc-responsive probe. The common mechanism of a metal-responsive MRI contrast agent is illustrated in Fig. 2.8.^{8, 137}

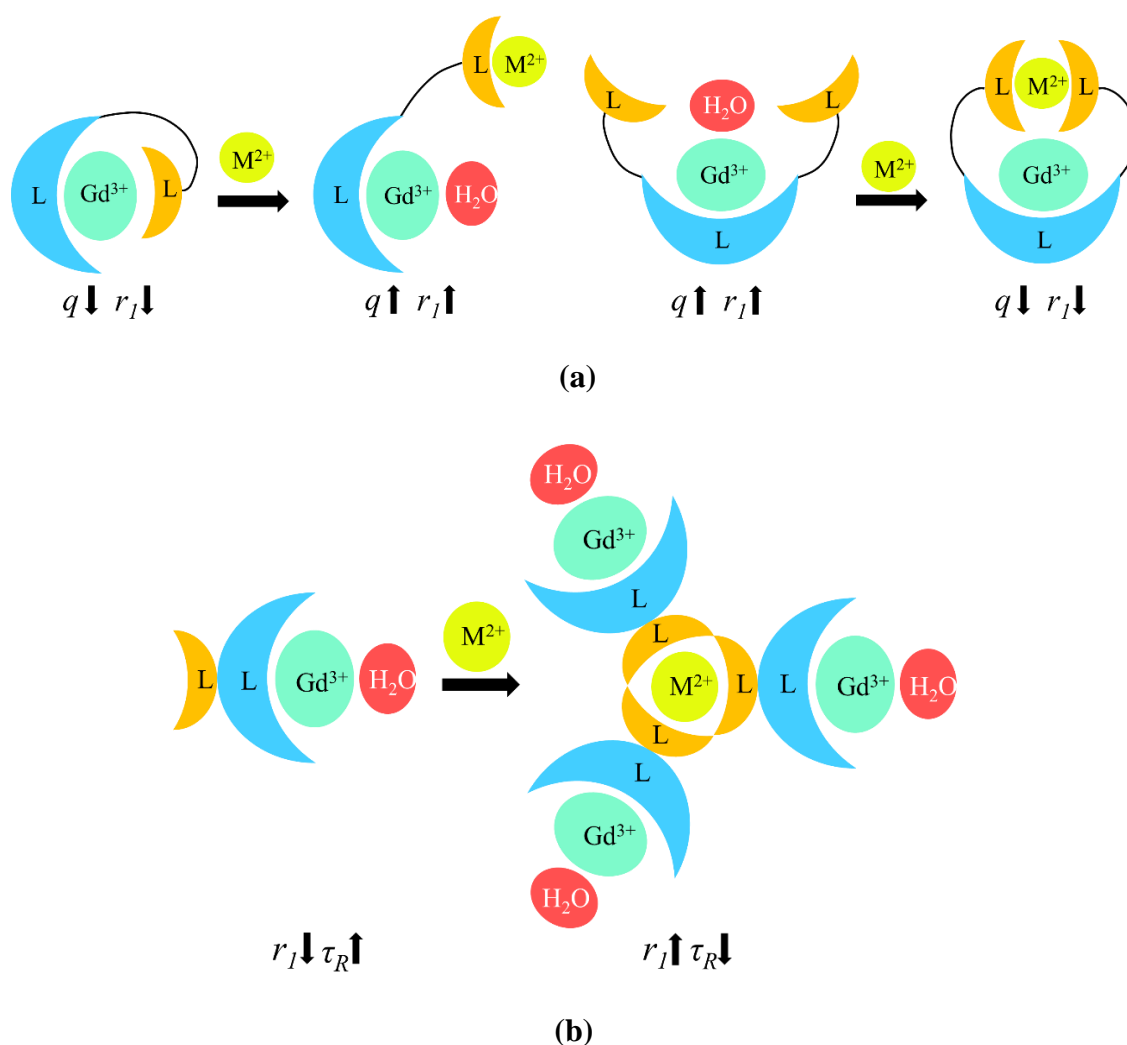


Figure 2.8: MR-based metal ion sensing *via* modulation of (a) q or (b) τ_R .

Increasing the hydration number leads to a high relaxivity, but decreases the thermodynamic stability and/or kinetic inertness.¹⁷ Macrocyclic ligands with eight coordination sites (such as DOTA, $\log K_{ML}$ 25.3) and seven coordination sites (such as in

DO3A, $\log K_{ML}$ 23.8) which contain one and two water molecules respectively are considered as excellent ligands that have sufficient thermodynamic stability and kinetic inertness to be suitable for *in vivo* applications.¹³⁸ In addition, the macrocyclic ligands will significantly reduce the paramagnetic lanthanide (gadolinium(III)) toxicity, facilitate distribution in tissues and increase the efficiency of gadolinium(III) during shortening relaxation time.¹³⁸ The kinetic inertness of macrocyclic ligands toward dissociation also has been tested in many reports providing good results, as well as its chemical inertness toward transmetallation processes.¹³⁸

Another mechanism of metal-activated probes is the manipulation of the rotational correlation time (τ_R) in which the relaxivity is enhanced in accordance to a slow τ_R (Fig. 2.8 (b)).^{8, 137} Reduction to the τ_R (slowing the movement) can be easily done by increasing the molecular weight or bulk structure through dimerization or polymerization. However, this is usually followed by reducing its water solubility and low cell permeability (poor uptake). Furthermore, the attachment of a specific binding site that can interact with protein such as HSA will also reduce τ_R significantly. These model MRI contrast agents can comprise one or two active arms which contain a specific active site that has capability to interact with the targeted ions either reversibly or irreversibly. Formation of this active site is a challenging process. Both the lanthanide metal centre and the active arm properties should be considered in order to achieve the expected properties such as the complex stability and responsivity in the presence and in the absence of targeted zinc(II) ions.

Accordingly, due to the Lewis acidity character of lanthanides and strong electrostatic interactions, the suitable ligands for complexation are Lewis base such as carboxylic and amine groups.⁵⁸ In this project, the cyclen backbone will be used as the main ligand. A cyclen-based ligand like DOTA and DO3A form very stable complexes with lanthanides. The cyclen's ring which contains four nitrogen atoms is an ideal size (fit in size) to hold the paramagnetic lanthanide ion.⁵⁸ In addition, the investigation of pyridyltriazole moieties as a ligand or a metal chelator have been conducted in the Lowe group during the last decade. Therefore, this study is intended to develop a zinc responsive contrast agent by exploiting a GdDO3A-based contrast agent containing a pyridyltriazole moiety as a zinc(II) chelator. This pyridyltriazole is generated through a click chemistry reaction.

2.2 Synthesis of Model Complexes (LnC1 and LnC2)

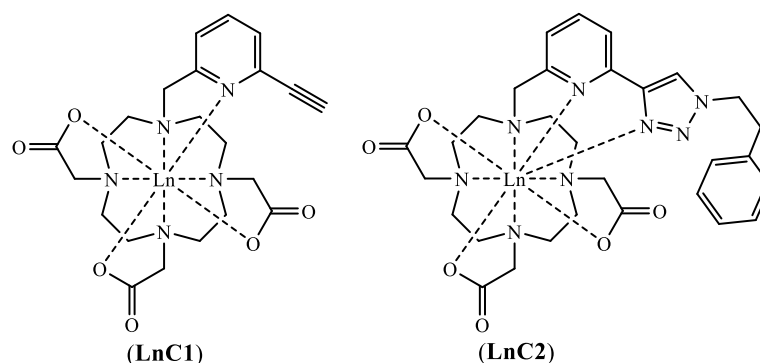
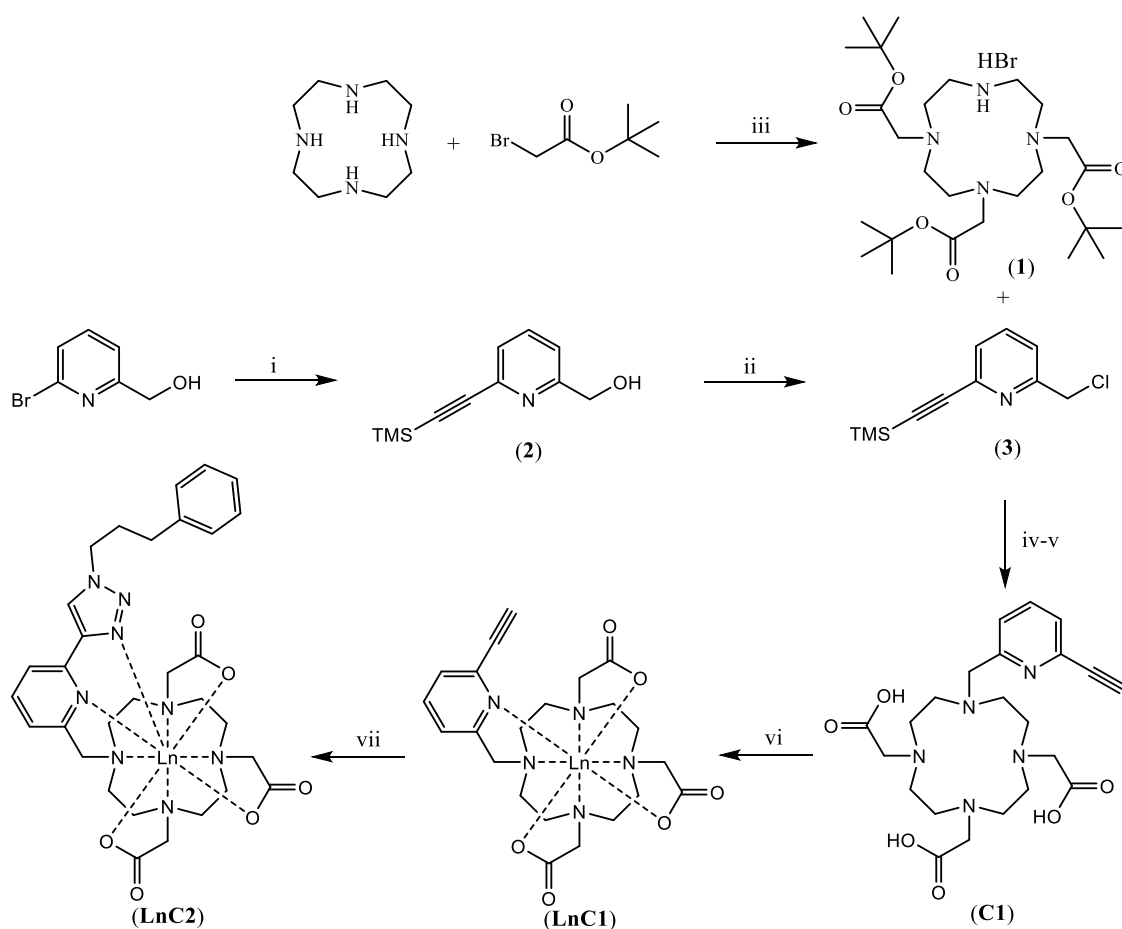


Figure 2.9: LnDO3A-based model complexes (**LnC1** and **LnC2**) for zinc-responsive MRI Contrast agent (Ln = Eu, Gd, Tb).

The project to develop a zinc-responsive MRI contrast agent commenced by synthesizing a pyridyltriazole ligand which is attached as an active arm to a multidentate DO3A-based main ligand. To achieve this purpose, different synthetic routes were explored using various approaches, which aimed to find the best synthetic pathway to achieve the desired compound. Any possible efficient alternative routes were also explored and examined to provide a comparative method. In this report, the first model complexes are presented in Fig. 2.9. Lanthanide compounds (**LnC1** and **LnC2**) are based on the DO3A (**1**) core. In these model complexes, DO3A appended with an active arm pyridine, in which the pyridine ring is connected directly to the main ligand DO3A. The alkyne group in **LnC1** can be further converted to a triazole ring with any azide bearing compound to form pyridyltriazole containing compounds, the complex **LnC2** is shown with a pendant ethyl benzene group.

The synthetic pathway to **LnC1** complex contains several steps, as shown in Scheme 2.1. The first step is to synthesise the cyclen core tBuDO3A (**1**). It was synthesized from the reaction of cyclen with *tert*-Butyl bromoacetate through an alkylation reaction in the presence of sodium acetate as a base (sodium acetate accelerates the reaction deprotonation of N-cyclen) in DMA solvent. This reaction was conducted following a previously published method¹³⁹ and was carried out at room temperature for 5 days and monitored by mass spectroscopy (MS). By maintaining the molar ratio quantitatively, a low reaction temperature and a weak base, the tri-N-alkylated product can be formed preferentially. It is precipitated as a bromium salt by addition of KBr, which is favoured rather than in the form of a free base due to the ease of product separation from mono-, di-, or tetra-alkylated byproduct through precipitation, thus a high

purity product was obtained.¹³⁹ The tri-alkylated product was precipitated as a white solid by adjusting the pH at 9 with additional of sodium carbonate to the reaction mixture. This alkylation reaction followed S_N2 mechanism is an exothermic reaction, thus the temperature of system increased during the initial addition of reactants. The temperature for this reaction was controlled to <30 °C to minimize the formation of byproduct especially tetrasubstituted macrocycle, tBuDOTA. Mass spectrometry (MS) analysis showed a peak at *m/z* 515 [M+H]⁺ indicating the formation of the desired product. ¹H NMR spectra of **1** is consistent with the literature.¹³⁹

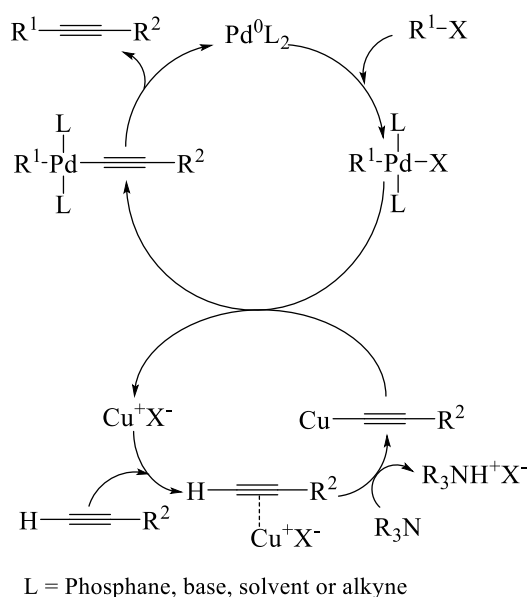


Scheme 2.1: Synthetic route to **LnC1** and **LnC2** i) TMS-acetylene, Pd(PPh₃)₂Cl₂, CuI, EtN₃, 50°C, 1 h. ii) SOCl₂, DCM, rt, 3 h. iii) DMA, NaOAc, KBr, 0-rt, 5 days. iv) K₂CO₃, MeCN, reflux. v) DCM:TFA (1:1). vi) LnCl₃.6H₂O, H₂O pH 6.4, (Ln = Eu, Gd, Tb). vii) CuSO₄, NaAsc, NaN₃, (2-bromoethyl) benzene.

Compound **2** was synthesized through a Sonogashira cross-coupling reaction by using (6-bromopyridin-2-yl)methanol and ethynyltrimethylsilane (TMS-acetylene). Sonogashira cross-coupling is a popular procedure for alkynylation of alkenyl or aryl halides including both primary and secondary alkyl halides, since it was introduced by

Sonogashira and Hagihara in 1975.¹⁴⁰ This method has become an important tool in the development of chemistry natural products, pharmaceuticals, and material sciences,¹⁴⁰ although it has disadvantages due to environmentally unfriendly base amine solvent and the copper salt which is difficult to recover.¹⁴⁰

The sonogashira reaction was catalysed by $\text{Pd}(\text{PPh}_3)_2\text{Cl}_2$ with CuI as a co-catalyst, the reaction was carried out under N_2 atmosphere, since the sensitivity of the intermediate copper acetylides generated *in situ*, the presence of oxidative agents including air leads the formation of the homocoupling product of the terminal alkyne.¹⁴⁰ Thus, the flask was degassed after the (6-bromopyridin-2-yl)methanol was charged to the flask along with both catalysts. In addition, to prevent the formation of homocoupling product, the alkyne was added slowly to the reaction mixture by syringe.¹⁴¹ Although the exact mechanism of Sonogashira coupling reaction remains unrevealed, in general, there are two catalytic routes believed take place simultaneously during the entire reaction as presented at Scheme 2.2.



Scheme 2.2: Catalytic cycle of the Sonogashira Coupling reaction.

Through the first Pd-cycle, the formation of the palladium complex is conducted through fast oxidative addition of $\text{R}^1\text{-X}$ to $\text{Pd}(0)\text{L}_2$. $\text{Pd}(0)\text{L}_2$ is formed by reduction of palladium (II) complexes ($\text{Pd}(\text{PPh}_3)_2\text{Cl}_2$) by using triethyl amine, in which electron donor from the triethyl amine reduces the paladium(II) species *via* σ -complexation-dehydropalladation-reductive elimination. In the second Cu-cycle, the π -alkyn-Cu complex is formed by the copper(I) salt (CuI) before the triethylamine which acts as a

base, abstracts the terminal alkyne's proton to form a Cu acetylide species. This is generally accepted in Cu-cycle formation, although the details of the mechanism still poorly understood.¹⁴⁰ The next step determines the rate of the reaction, it is the combination of the Pd- and Cu-cycles through a transmetalation step to form $R_1PdL_2(-C\equiv CR^2)$ species followed by tran/cis isomerization and reductive elimination to give coupled product ($R_1-C\equiv C-R_2$) and the initial catalyst.

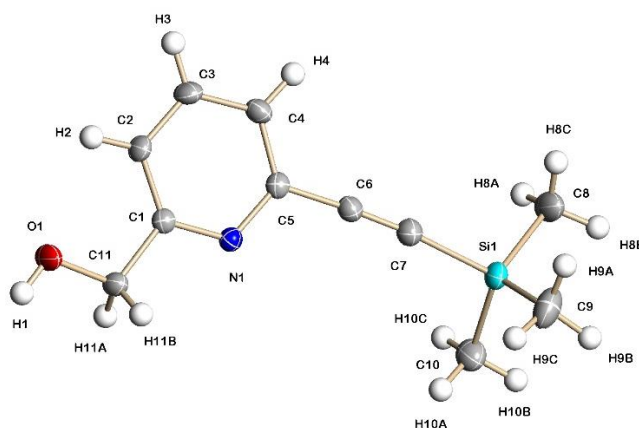
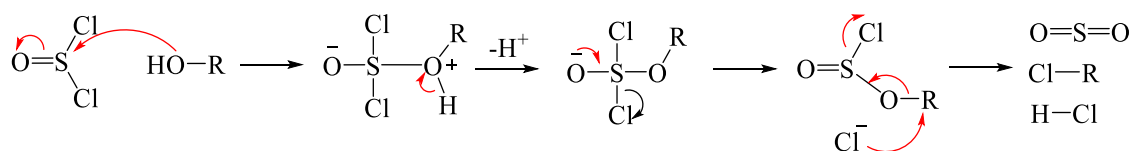


Figure 2.3: An Ortep representation of the crystal structure of (6-((trimethylsilyl)ethynyl)pyridin-2-yl)methanol (**2**).

The 1H NMR spectrum (in $CDCl_3$) showed a typical singlet peak corresponding to $-Si(CH_3)_3$ of the product at δ 0.28 supported by MS analysis showed a peak at m/z 206 for $[M+H]^+$. Crystallization was achieved in EtOAc and x-ray crystal structure was obtained as illustrated at Fig. 2.3.



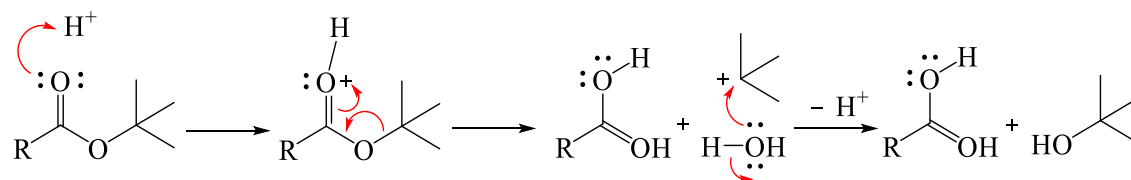
Scheme 2.3: The chlorination mechanism for alcohol group.

Chlorination of the compound **2** was performed using $SOCl_2$ in DCM. An excess amount of $SOCl_2$ was used to ensure reaction completion. This is an exothermic reaction, so that it was chilled in an ice bath once these two reactants were mixed. The mechanism of this reaction is illustrated at Scheme 2.3. The chlorination reaction was initiated by an alcohol attack to the $SOCl_2$ by releasing HCl , followed by cleavage of RO bond to form SO_2 gas. The excess of $SOCl_2$ was then neutralized by $NaHCO_3$. 1H NMR spectroscopic (in $CDCl_3$) analysis showed no typical peak corresponding to $-OH$ at $\sim \delta$ 3.47, furthermore, the ^{13}C NMR spectrum indicated a large shift of the adjacent carbon from δ 64.5 ($-CH_2OH$) to 45.9 ($-CH_2Cl$) ppm. This indicated that the $-OH$ has been converted to

-Cl. The MS analysis also confirmed the formation of chlorinated product with a peak at m/z 224 $[M+H]^+$ with a characteristic chloride isotope pattern.

The formation of compound **4** (see Chapter 6) was performed by reacting compounds **1** and **3** in MeCN in the presence K_2CO_3 . This fourth alkylation reaction of DO3A requires higher temperature and a stronger base, thus K_2CO_3 was chosen instead of NaOAc. The reaction was accomplished within 24 hours, by heating at reflux in MeCN. In addition to its property as a base, K_2CO_3 can also remove the TMS protecting group from the alkyne simultaneously. Nevertheless, if it does not remove it to completion, it still can be achieved later by addition of an aqueous solution of K_2CO_3 in methanol. The reaction completion was confirmed by the presence of a peak at m/z 630 for $[M+H]^+$ indicating the formation of compound **4**.

Compound **C1** was formed by removing the *tert*-butyl protecting group through acid-catalysed hydrolysis reaction by TFA in DCM. The mechanism of this reaction was illustrated at Scheme 2.4. This reaction exploits moisture in the air in order to trap the *t*-butyl cation to generate *tert*-butanol, thus this reaction was performed in an open atmosphere.



Scheme 2.4: Acid hydrolysis in removing *tert*-Butyl protecting group.

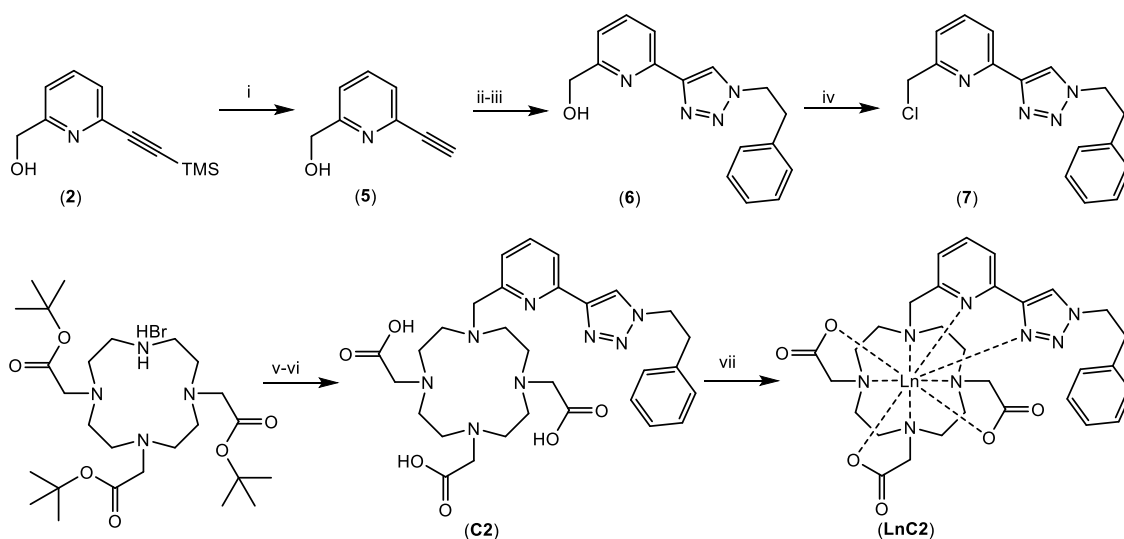
The *tert*-Butyl alcohol by-product is easily removed under reduced pressure along with the remaining TFA. Removing the protecting groups changes the polarity of product significantly. Its polarity increases since the functional groups are transformed from esters to carboxylic acids, which makes the product water soluble and no longer soluble in most organic solvents. The MS analysis showed a peak at m/z 462 $[M+H]^+$ indicating the formation of the desired product.

The synthesis of the lanthanide complexes was performed by reacting the ligand (**C1**) with the corresponding lanthanide salts ($LnCl_3 \cdot 6H_2O$). This entire complexation reaction process was carried out at three different pH values. Firstly, the formation of lanthanide complex was conducted at pH 6, at this pH the lanthanide presence as a free ion in the solution so that it can be complexed, then the pH was increased to pH 10 to

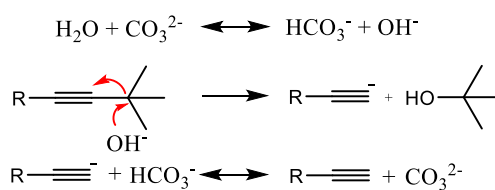
separate the remaining free lanthanide ion. At this pH the lanthanide ion will precipitate as $\text{Ln}(\text{OH})_3$. This can be easily separated by filtration through celite. Finally, the pH was neutralized to pH 7. The presence of unreacted lanthanide was then tested by xylenol orange buffered solution at pH 5. At below pH 6 xylenol orange has absorption maxima at 434 nm and independent to the pH.¹⁴² Any changes to the colour of xylenol orange indicate the presence of free lanthanide ions in the solution due to the rearrangement of conjugated double bonds of xylenol orange after complexation to this metal. The MS analyses of **EuC1**, **TbC1** and **GdC1** showed peaks at m/z 634 $[\text{M}+\text{Na}]^+$, 640 $[\text{M}+\text{Na}]^+$, 639 $[\text{M}+\text{Na}]^+$ respectively, with the typical characteristic isotope pattern.

LnC1 complex was used to prepare **LnC2** complex through copper-catalysed Huisgen 1,3-dipolar cycloaddition. **LnC1** was 'clicked' with (2-azidoethyl)benzene as a model compound in order to determine the optimum condition for synthesis, before using a more water-soluble substituent such as polyethylene-glycol. (2-bromoethyl)benzene was converted to (2-azidoethyl)benzene *via* reaction with sodium azide, before it was reacted with **LnC1**. This reaction was conducted at room temperature by employing a copper(I) catalyst which was generated *in situ via* reduction of a copper(II) sulphate with sodium ascorbate as the reducing agent. The mechanism of this reaction was illustrated in Section 1.7. The MS analyses showed peaks at m/z 759 $[\text{M}+\text{H}]^+$ and 787 $[\text{M}+\text{Na}]^+$ for **EuC2** and **TbC2** respectively. All of these **LnC2** complexes were then purified *via* elution through a column containing the non-ionic Amberlite XAD-16 resin. This is a resin that absorbs and releases ionic species through hydrophobic and polar interaction to remove the copper catalyst and the remaining reducing agent.

A second synthetic route to prepare **LnC2** is outlined at Scheme 2.5. In this route, the pyridyltriazole was synthesized separately before being attached to the main ligand DO3A-*t*-Bu. The first step on this route was the elimination of TMS protecting group of compound **2** through a base catalytic hydrolysis process to form compound **5** (Scheme 2.6). The ¹H NMR analysis of **5** showed a singlet peak at δ 3.10 correlated to hydrogen on the terminal alkyne and the absence of TMS group at δ 0.28. Accurate mass spectrometry analysis confirmed the desired product with m/z 134 as $[\text{M}+\text{H}]^+$.



Scheme 2.5: Alternative synthetic route for the formation of **LnC2**. i) $\text{K}_2\text{CO}_3(\text{aq})$ 1 M, MeOH. ii) (2-bromoethyl)benzene, NaN_3 , MeOH:H₂O (1:3), rt 24 h. iii) $\text{CuSO}_4 \cdot 5\text{H}_2\text{O}$ NaAsc, rt 24 h. iv) SOCl_2 , DCM, 0°C - rt 24 h. v) K_2CO_3 , MeCN, reflux 24 h. vi) TFA:DCM (1:1), rt. vii) $\text{LnCl}_3 \cdot 6\text{H}_2\text{O}$, H₂O pH 6.4.



Scheme 2.6: Base catalysed TMS deprotection mechanism.

It was then subjected to the copper(I)-catalyzed Huisgen 1,3-dipolar cycloaddition with (2-azidoethyl)benzene which is generated *in situ* as previously explained, to produce the ‘clicked’ compound **6** in which obtained as a white solid. This compound was confirmed by ¹H NMR spectroscopic analysis which showed a typical singlet peak at δ 7.85 for the hydrogen on the triazole ring. The MS analysis confirmed the formation of desired product with m/z 281 $[\text{M}+\text{H}]^+$. It was then chlorinated (using the same mechanism as in the synthesis of compound **3**) to give compound **7**. It was confirmed by MS analysis with m/z 299 and 321 for $[\text{M}+\text{H}]^+$ and $[\text{M}+\text{Na}]^+$ respectively. Attachment to **1** to form compound **8** followed by deprotection of the carboxylates to form compound **C2**. MS analysis confirmed the formation of these compounds (m/z 777 $[\text{M}+\text{H}]^+$ for **8** and 609 $[\text{M}+\text{H}]^+$ for **C2**). The final step was the formation of **LnC2** complexes through the same conditions used in the formation of **LnC1**. The MS analysis confirmed the formation of these lanthanide complexes giving the expected calculated isotope pattern; **EuC2** and **TbC2** obtained peaks at m/z 781 $[\text{M}+\text{Na}]^+$ and 787 $[\text{M}+\text{Na}]^+$ respectively. The benefit of this second route is that it produced a relatively pure compound compared to the first

route, which only contains NaCl as an impurity without any copper catalyst or remaining ascorbic acid reductant.

The preliminary studies of the photophysical properties in response to the targeted metal ion showed that neither **LnC1** nor **LnC2** complexes were demonstrated the fundamental properties required of a zinc-responsive MRI contrast agent, *i.e.* no significant changing in photophysical properties observed in response to zinc(II) ion. All of the photophysical and metal responsive examination results of these complexes will be discussed in Chapter 3. To bypass this limitation, further structure modification was required in order to change their properties.

2.3 Synthesis of Modified Complexes

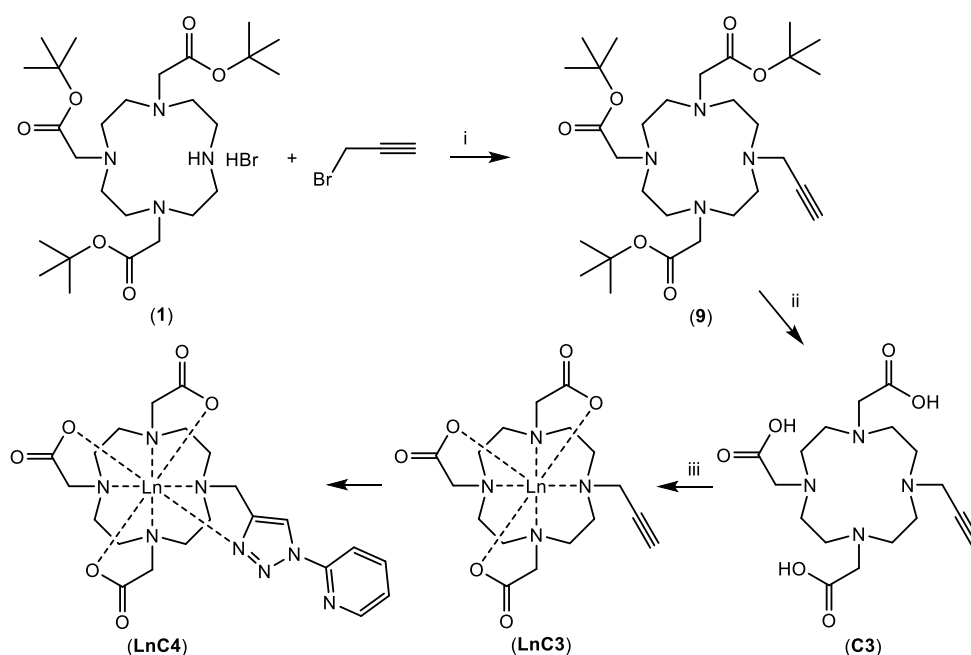
Compound **LnC2** was unresponsive towards zinc(II), due to the structure imperfection. It is considered that the potential donor atoms (nitrogen) on the active arm are isolated inside the closed structure bind to the lanthanide centre. Therefore, preventing it from interacting with the surroundings, in this case in the presence of the free metal ion. For this reason, the design of the first model was modified to increase the probability of the potential donor atoms being able to interact with the target free metal ions. This leads to the first modification of **LnC2** complex as described sequentially in the following sections.

2.3.1 Synthesis of **LnC3** and **LnC4**

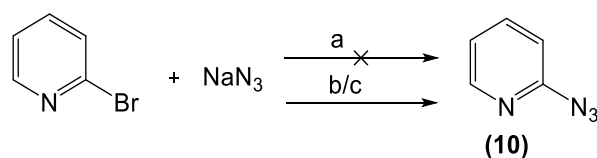
The first modification was achieved by simply swapping the position of the pyridyltriazole active arm *i.e.* attaching to DO3A *via* the triazole of the pyridyl. It was believed that this would increase the chance of coordination displacement from the lanthanide centre to the target metal ion, since this active arm is much more exposed to its environment. To this purpose, the intermediate **LnC3** and the target **LnC4** complexes were synthesized as depicted at Scheme 2.7.

LnC4 is a lanthanide complex containing a slightly different pyridyltriazole compared to **LnC2**. In addition, it was attached to DO3A in a reverse way. The synthesis of **LnC3** and **LnC4** was conducted using similar routes as for the formation of **LnC1** and **LnC2**. The first step was to synthesis compound **9** by reacting **1** with propargyl bromide in the presence of K₂CO₃ in acetonitrile. Compound **9** was confirmed by accurate mass

spectroscopy with m/z 553 for $[M+H]^+$.¹⁴³ ^1H NMR spectroscopy analysis showed a singlet peak at δ 2.17 indicating the terminal-alkyne proton of compound **9** along with typically broad resonances for the cyclen's ring hydrogens. The *tert*-Butyl protecting groups were then removed in DCM:TFA to give proligand **C3** as a brown oil with m/z 385 corresponding to $[M+H]^+$. The formation of **LnC3** was carried out under the same conditions as the formation of previous lanthanide complexes. The successful formation of **EuC3** complex was indicated by accurate mass spectroscopy with m/z 557 for $[M+Na]^+$.¹⁴³



Scheme 2.7: Synthetic route of **LnC3** and **LnC4**. i) MeCN, K_2CO_3 , rt. ii) TFA:DCM (1:1). iii) $\text{LnCl}_3 \cdot 6\text{H}_2\text{O}$, H_2O pH 6.4.

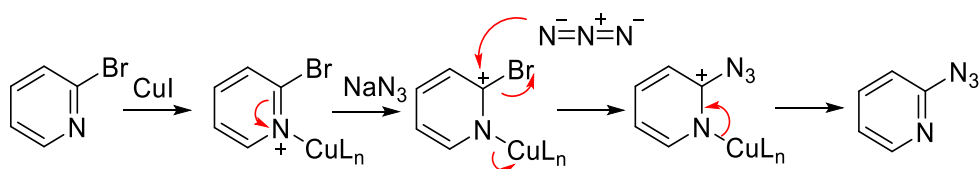


Scheme 2.8: a) $\text{H}_2\text{O}:\text{tBuOH}$ (1:1), 24h (0%). b) CuI, NaAsc, $\text{MeOH}:\text{H}_2\text{O}$ (7:3), reflux 20h (100%). c) CuI, NaAscorbate, μw 125°C, 1h (100%).

The first attempt to synthesis **LnC4** was reacting **LnC3** with 2-azidopyridine (**10**) by using conventional copper(I)-catalyzed Huisgen dipolar cycloaddition. However, no **EuC4** was identified when using the same conditions for formation of **EuC2** from **EuC1**. This is because compound **10**, which was intended to be generated *in situ*, did not form (Scheme 2.8 (a)). This nucleophilic substitution between sodium azide and 2-

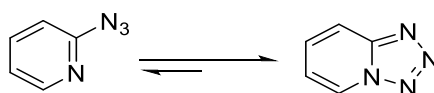
bromopyridine is harder compared to reaction with alkyl halides. To overcome this problem, compound **10** was prepared using CuI catalyst with different synthetic methods (Scheme 2.8 (b) and (c)).

The reaction took 20 hours to give 100% conversion (TLC analysis), when it was conducted by heating at reflux (b), but only takes an hour when using microwave heating at 125°C (c). The power of microwave heating has been reported to accelerate the azide formation in a short time.^{144,145,146} In addition, Cu(I) iodide, solvent system (H₂O:EtOH/3:7) and NaAscorbate is essential for perfect conversion.¹⁴⁷ The proposed mechanism of this reaction is illustrated at Scheme 2.9. The formation of 2-azidopyridine was confirmed by mass spectroscopy (ESI) with m/z 121 for [M+H]⁺. Although 2-azidopyridine has ((C+O)/N) ratio lower than 3, it is safe to be isolated and stored for months at normal condition. The ¹H NMR analysis showed comparable peaks with the literature.¹⁴⁸



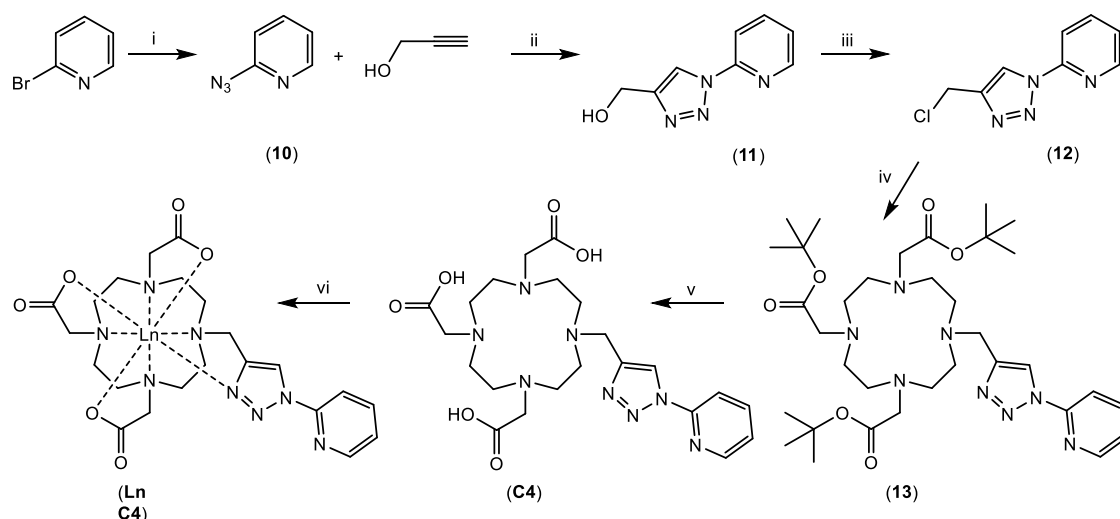
Scheme 2.9: Copper-catalyzed substitution nucleophilic in the formation of 2-azidopyridine.

However, the click reaction for formation of **LnC4** by reacting **LnC3** with compound **10** was difficult. There was no **LnC4** formed under room temperature condition and only a little product (**LnC4**) was observed by MS when it was carried out under microwave heating at 125°C. The formation of **LnC4** probably could be increased by increasing the reaction time under microwave heating. However, the formation of a ‘black-dirty’ reaction mixture makes it difficult to isolate the product. The reactivity inertness of **10** was believed to be caused by the formation of tetrazole^{149, 150} which is present in equilibrium as shown in scheme 2.10.



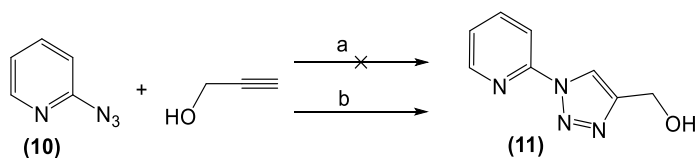
Scheme 2.10: The equilibrium of closed and opened ring of 2-azidopyridine (**10**).

Although the equilibrium of compound **10** depends on several factors including solvent, temperature and the presence of other substituents.¹⁴⁹ In general, the closed ring (tetrazole) is the main form of 2-azidopyridine.¹⁵¹



Scheme 2.11: Alternative synthetic route to the formation of **LnC4**. i) NaN_3 , CuI , NaAsc , $\text{EtOH}:\text{H}_2\text{O}$ (7:3), $\mu.w.$ 125°C . ii) CuI , NaAsc , $\text{EtOH}:\text{H}_2\text{O}$ (7:3), reflux. iii) SOCl_2 , DCM , 0°C - rt. iv) **1**, K_2CO_3 , MeCN , reflux. v) $\text{TFA}:\text{DCM}$ (1:1). vi) $\text{LnCl}_3 \cdot 6\text{H}_2\text{O}$, H_2O pH 6.4, reflux.

In order to find a better way to synthesize **LnC4**, another reaction route was conceived by preparing the pyridyltriazole separately as shown in Scheme 2.11. In general, the step was similar to the alternative route in making **LnC2**, in which the fourth arm was constructed separately before appended to the main DO3A ligand. It was started by synthesis of compound **11** by reacting 2-azidopyridine (**10**) with propargyl alcohol through copper(I)-catalyzed Huisgen 1,3-dipolar cycloaddition. Several methods were attempted with different chemicals and reaction conditions as depicted at Scheme 2.12.



Scheme 2.12: (a) $\text{CuSO}_4 \cdot 5\text{H}_2\text{O}$, NaAscorbate , $^t\text{BuOH}:\text{H}_2\text{O}$ (1:1), rt, (0%); (b) CuI , NaAscorbate , $\text{MeOH}:\text{H}_2\text{O}$ (7:3), μw 125°C 20 h.

In the first method (a), compound **10** was then reacted with propargyl alcohol through copper(I)-catalyzed Huisgen 1,3-dipolar cycloaddition. Again, the reaction was not successful using the most popular catalytic system $\text{CuSO}_4 \cdot 5\text{H}_2\text{O}/\text{NaAscorbate}$. The formation of tetrazole makes this compound relatively inert in click reaction under standard reaction conditions.¹⁵⁰

However, when using the reaction conditions as in (b), with an excess of propargyl alcohol, 2-azidopyridine was consumed completely during the reaction, although some byproducts were observed in TLC. Under these conditions, the high temperature is believed to shift the equilibrium to the left,¹⁴⁹ that makes it possible to be ‘clicked’. As

for the click reaction which was conducted under microwave condition in preparation of **EuC4** from **EuC3**, a dirty black mixture was also obtained, however due to the polarity of compound **14** which is lower compared to **EuC4**, the extraction process by using organic solvents could be employed to isolate the product (**11**).

The ^1H NMR spectrum showed a typical singlet peak at δ 8.56 correlated to the hydrogen on the triazole ring and the presence of a triplet peak at δ 2.08 (equals to 1H) indicating the presence of -OH. The formation of **11** was also confirmed by MS with m/z 177 for $[\text{M}+\text{H}]^+$. Crystallization allowed x-ray analysis as presented at Fig. 2.10.

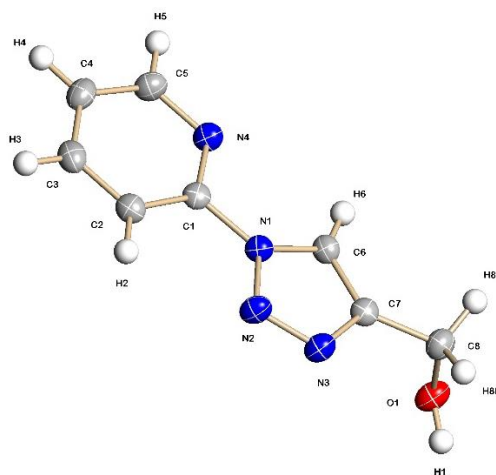
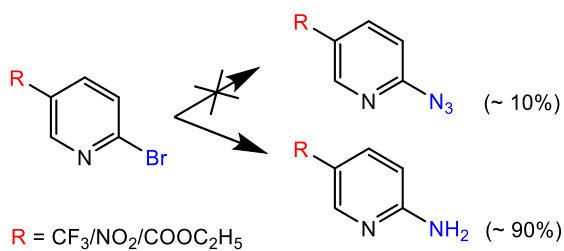


Figure 2.10: An Ortep representation of the crystal structure of (1-(pyridin-2-yl)-1H-1,2,3-triazol-4-yl)methanol (**11**).

Some attempts were made to increase the yield of the clicked product as compound **11**. The presence of an electron withdrawing group on 6 position of 2-azido pyridine, was reported to accelerate the formation of clicked product in the presence of Cu(I) acetate catalyst.¹⁵² Two different starting materials 2-bromo-5-(trifluoromethyl)pyridine and 2-bromo-5-nitropyridine were used. However, there was no azide formation when using the similar procedure to synthesize 2-azidopyridine (**10**). As presented at Scheme 2.13 the formation of amines was preferred instead of azides. These amine products were analysed by ^1H NMR spectroscopy to give spectra typical for 5-(trifluoromethyl)pyridin-2-amine as reported by Elmkaedem *et al.*¹⁵³ (Fig. 2.11) and 5-nitropyridin-2-amine as reported by Fantasia *et al.* (Fig. 2.12) respectively.



Scheme 2.13: Applying electron withdrawing groups (NO₂ and CF₃) in synthesizing the azide. Reaction conditions; NaN₃, CuI, NaAscorbate, MeOH:H₂O (7:3), reflux/mw.

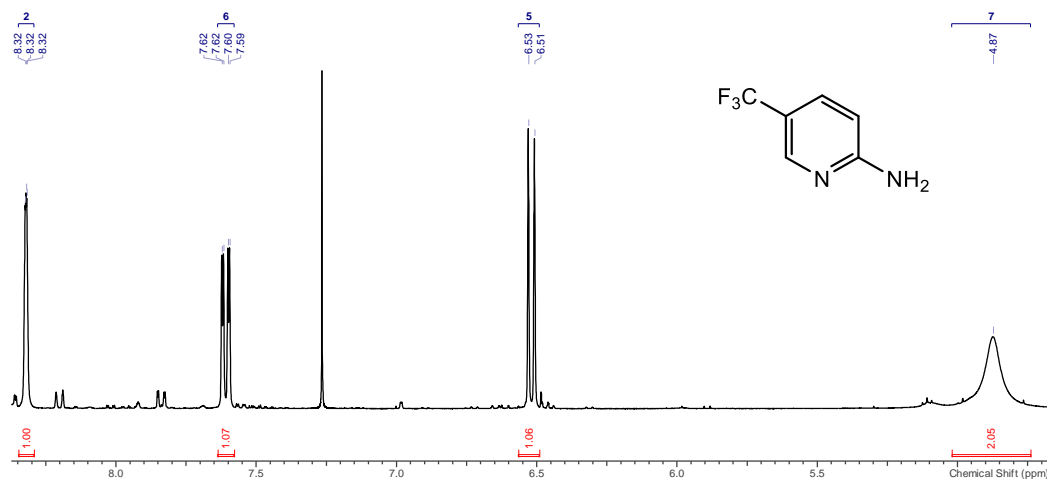


Figure 2.11: ¹H NMR (400MHz, CDCl₃) spectrum of 5-(trifluoromethyl)pyridin-2-amine.

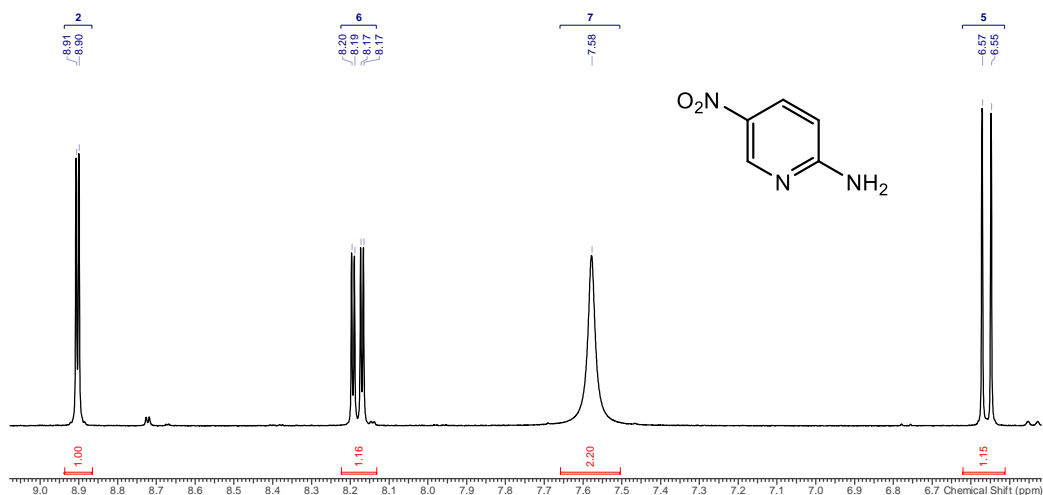
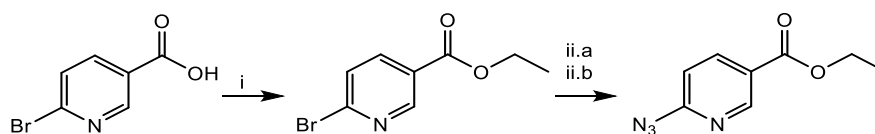


Figure 2.12: ¹H NMR (400MHz, DMSO) spectra of 5-nitropyridin-2-amine.

Another starting material containing 6-bromonicotinic acid was used. It was firstly converted to an ethyl ester by acid catalysis esterification with ethanol before finally converted to an azide as presented at Scheme 2.14. The esterification reaction provided a high yield; however, the azidification reaction provided a ten times smaller

amount of the azide product compared to the amine by-product when using the previous method as presented at Fig. 2.13.



Scheme 2.14: Synthesis route of ethyl 6-azidonicotinate; i) EtOH, H₂SO₄ conc. ii.a) NaN₃, CuI, NaAscorbate, MeOH:H₂O (7:3), reflux/ μ w. ii.b) NaN₃, DMF.

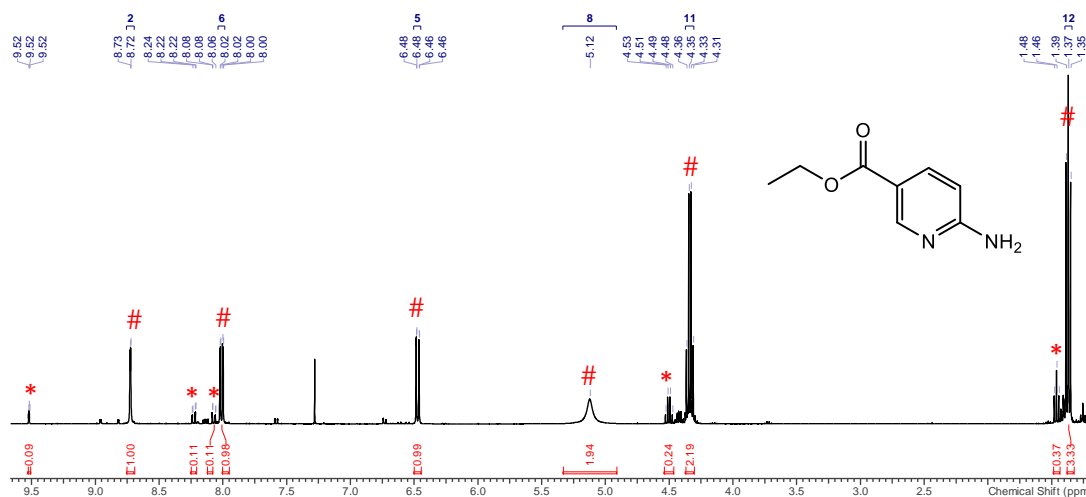


Figure 2.13: ¹H NMR (400MHz, CDCl₃) spectra of reaction mixture containing ethyl 6-azidonicotinate (marked as “*”) and ethyl 6-aminonicotinate byproduct (marked as “#”).

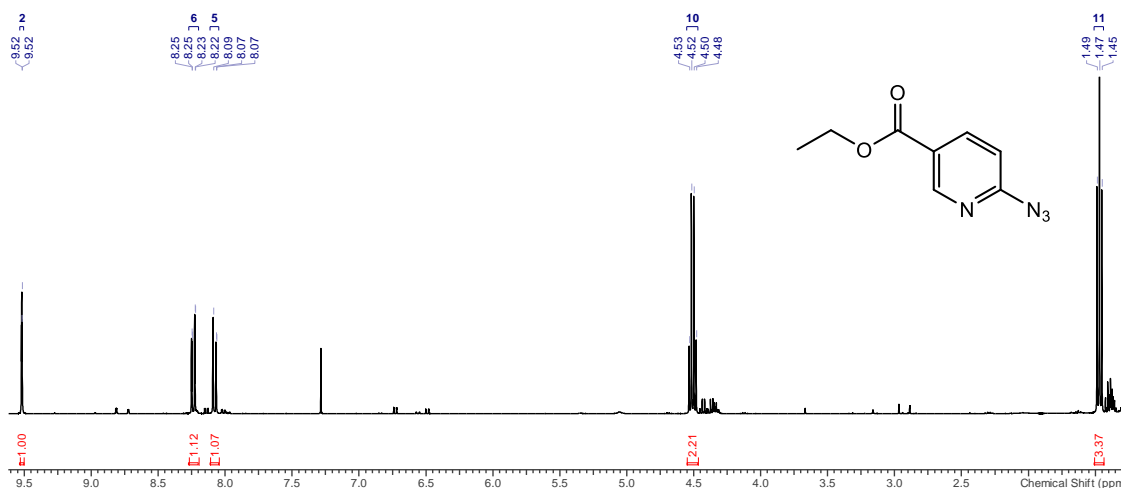
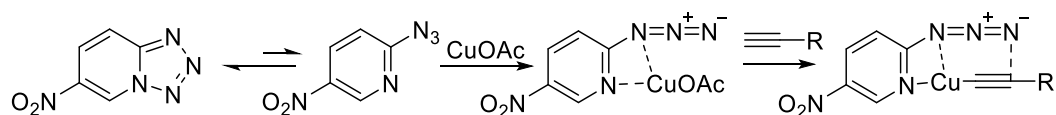


Figure 2.14: ¹H NMR (400MHz, CDCl₃) spectra of ethyl 6-azidonicotinate.

On the other hand, if the reaction was conducted in DMF as a polar aprotic solvent, the target azide was formed preferentially. The formation of 6-azidonicotinate was confirmed by ¹H NMR analysis as presented at Fig. 2.14. The use of DMF solvent makes

the isolation of the product slightly difficult. According to the literature,¹⁵² this electron withdrawing group will stabilize the opened-ring form of 2-azidopyridine that is easily complexed with the copper(I) acetate before then reacting with an alkyne as shown in Scheme 2.15.

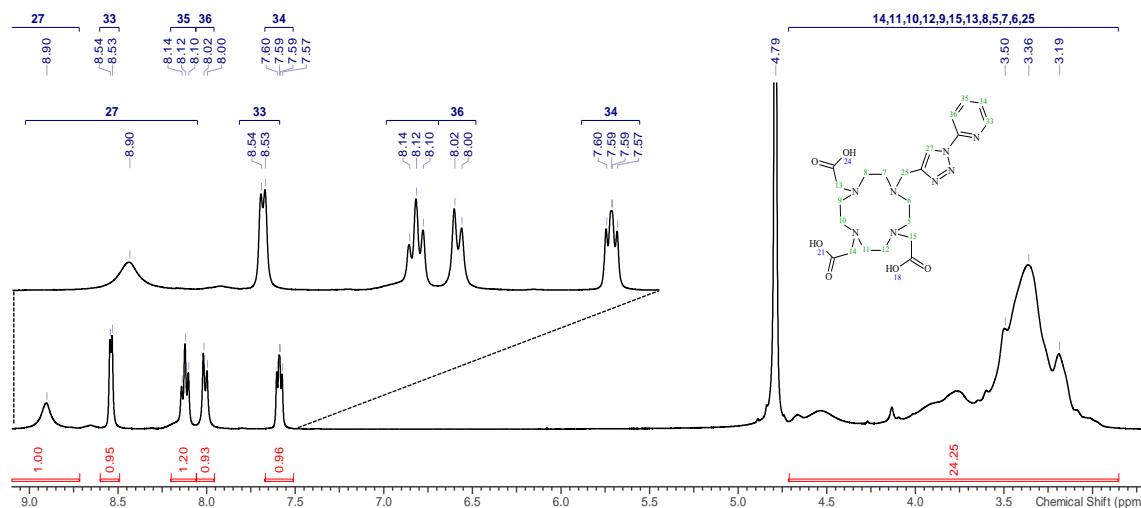


Scheme 2.15: The proposed mechanism of copper(I) acetate catalysed click reaction.¹⁵²

However, the reaction of between 6-azidonicotinate with propargyl bromide following exactly with the Zhang *et al.*¹⁵² method was unsuccessful. The reaction mixture gave a light-yellow suspension and remained unchanged which indicating the presence of $[(R-C\equiv C-Cu)_2]_n$.¹⁵² This was believed to be due to oxidation of the copper(I) acetate. These multiple failures in preparing either the azide starting material or the “clicked” product, turned the attention back to compound **11** in order to synthesise the targeted complex.

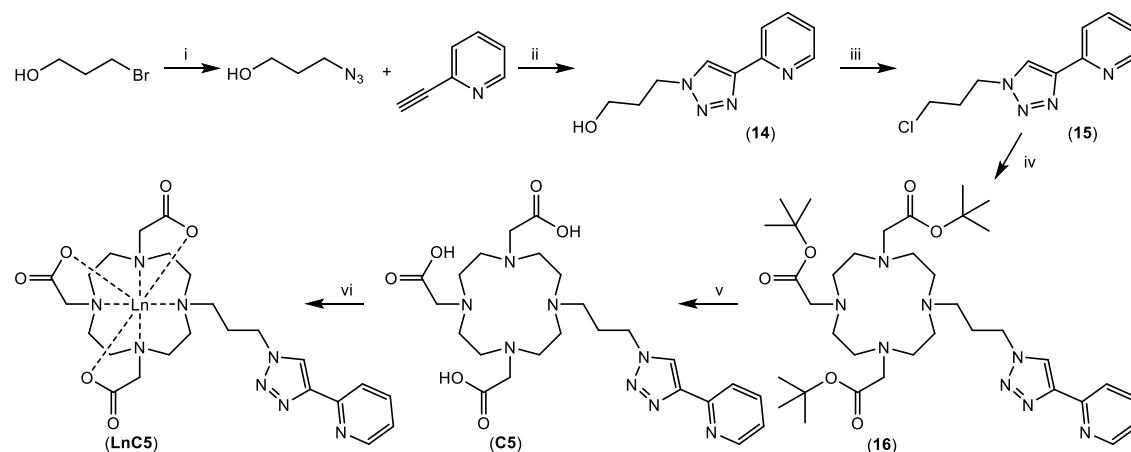
Chlorination of **11** was achieved with the same procedure explained previously, to give **12**. The ¹H NMR spectrum showed an absence of the triplet peak at δ 2.08 corresponding to -OH and a shift on its adjacent carbon from δ 61.2 to 42.4 ppm before and after chlorination respectively. MS analysis gave a peak at m/z 197 for $[M+H]^+$ with typical chlorine isotope pattern convinced the formation of **12**. The success of the formation of compound **12**, indicates that the synthetic route as shown in Scheme 2.11 is preferable in order to synthesis **EuC4**.

Compound **12** was then attached to DO3A to give compound **13**, followed by tBu-group deprotection. These two reactions were carried out using similar methods applied to the previous compounds. The ¹H NMR spectrum of **C4** is presented in Fig. 2.15. The triazole’s hydrogen (δ 8.9 ppm) is present as a broad peak which is believed to be affected by the macrocycle’s ring movements. The corresponding lanthanides europium and terbium complexes of **C4** were synthesized and analysed by MS to give m/z at 675 and 683 as $[M+Na]^+$ respectively.

Figure 2.15: ^1H NMR (400MHz, D_2O) spectra of **C4**.

The photophysical properties including metal-responsive studies are presented at Chapter 3. According to these studies, further structural modification was needed owing to indication of the occurrence coordination performed by one of the nitrogen's in the triazole ring to give a stable five-membered ring coordination between pyridyltriazole and lanthanide.

2.3.2 Synthesis of **LnC5** and **LnC6**



Scheme 2.16: Synthesis pathway of **LnC5**; i) NaN_3 , $\text{EtOH}:\text{H}_2\text{O}$ (7:3), μw , 1h. ii) $\text{CuSO}_4 \cdot 5\text{H}_2\text{O}$, NaOAc $\text{EtOH}:\text{H}_2\text{O}$ (7:3), μw , 1h. iii) SOCl_2 , DCM , rt. iv) **1**, K_2CO_3 , MeCN , reflux. v) $\text{TFA}:\text{DCM}$ (1:1), rt. vi) $\text{LnCl}_3 \cdot 6\text{H}_2\text{O}$, H_2O pH 6.4.

The synthesis of **LnC5** is proposed to give more space between the DO3A core and the pyridyltriazole active arm. Formation of **LnC5** was initiated by synthesizing compound **14**. According to previous experiments (synthesis of **LnC2** and **LnC4**), it was

decided that the formation of active arm prior to complexation was considered as the best strategy. Thus, this method was chosen to synthesise **LnC5** as presented in Scheme 2.16. Compound **14** was synthesized by reacting the 3-bromo-1-propanol with sodium azide to produce an organic azide *in situ*, followed by click chemistry with 2-ethynylpyridine through general copper(I)-catalyzed Huisgen 1,3-dipolar cycloaddition to produce **14**. The ^1H NMR spectrum showed a typical sharp singlet peak at δ 8.24 ppm which corresponds to the triazole hydrogen. Accurate mass spectrometry gave a peak at m/z 205 for $[\text{M}+\text{H}]^+$, supporting the successful formation of **14**.

The synthesis of **14** was conducted using two different methods: the first method was using conventional heating, while the second method used microwave heating. Conventional heating needed a longer reaction time, 20 hours for synthesis the azide and another 20 hours for the click reaction; whereas, microwave heating completed these two steps in just in 2 hours. However, conventional heating gave a cleaner reaction mixture compared to microwave heating. The presence of impurities can be seen through the TLC analysis of the reaction mixture.

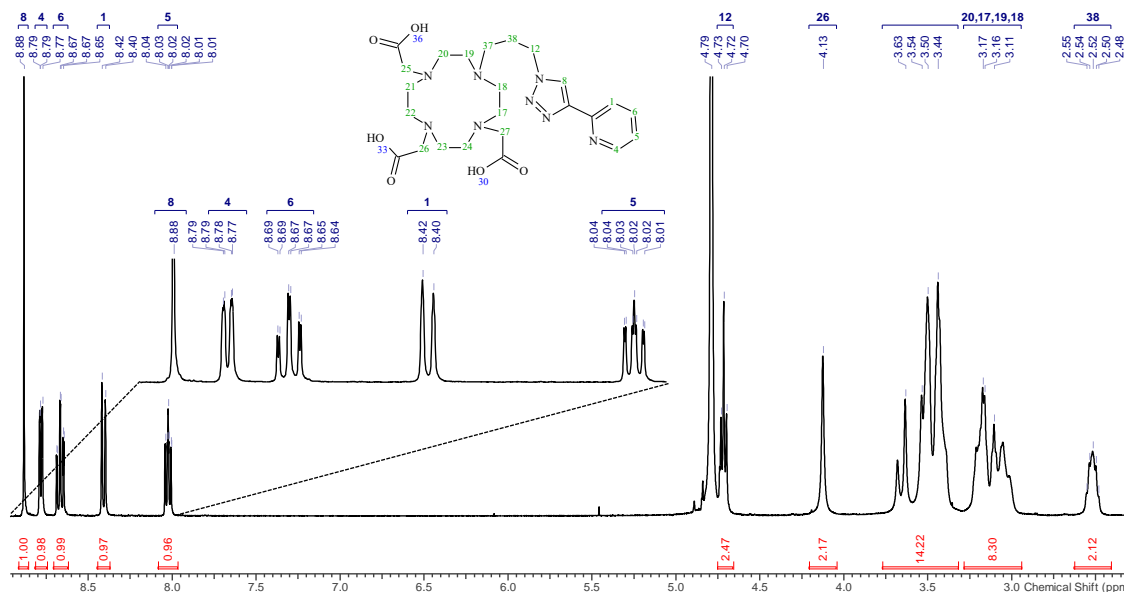
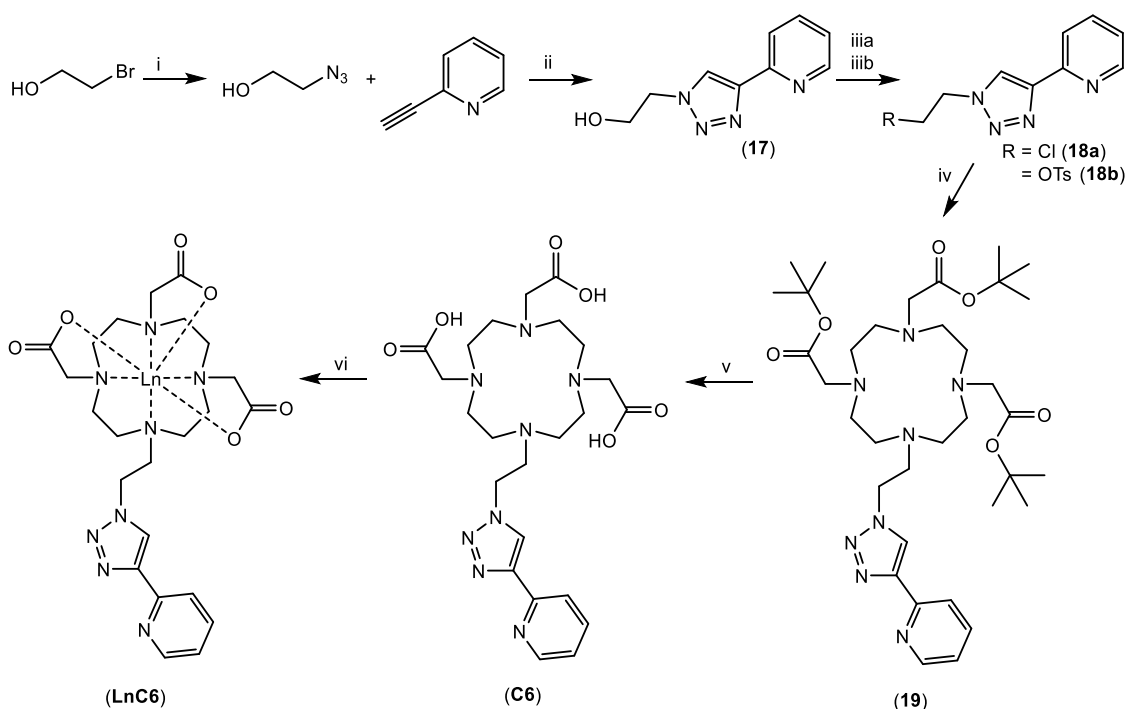


Figure 2.16: ^1H NMR (400MHz, D_2O) spectrum of **C5**.

Compound **14** was chlorinated (**15**) followed by reaction with **1** to produce **16**, following procedures used in the synthesis of **8**. Successful synthesis of **16** was confirmed by ^1H NMR spectroscopy providing the typical broad peaks of the macrocyclic ring and the corresponding peaks of the pyridyltriazole. It was confirmed by MS analysis providing a peak m/z 701 for $[\text{M}+\text{H}]^+$. Carboxylates deprotection was applied to give **C5**

with m/z 533 for $[M+H]^+$. The 1H NMR spectra of **C5** is presented at Fig. 2.16. Complexation with the appropriate lanthanides followed the same procedures as explained earlier. **EuC5** was analysed by MS to obtain a peak at m/z 703 $[M+Na]^+$, showing the characteristic europium isotope patterns.

In an attempt to reduce the distance between the active arm and DO3A, **LnC6** was synthesized. It is principally the same compound as **LnC5** with a one fewer CH_2 groups in the linking to the pyridyltriazole. The reaction route is presented at Scheme 2.17. Instead of using 3-bromo-1-propanol, 2-bromo-1-ethanol was used to produce compound **17**, via the same procedures (as for **14**) to produce a white crystalline product with m/z 213 for $[M+Na]^+$. 1H NMR spectroscopy analysis also confirmed the formation of clicked product **17**. Similarly, there were no significant obstacles during chlorination of **17** with tionylchloride in the formation of compound **18a**.



Scheme 2.17: Synthetic pathway of **LnC6**. i) NaN_3 , EtOH:H₂O (7:3), μw , 1h. ii) $CuSO_4 \cdot 5H_2O$, NaOAc, EtOH:H₂O (7:3), μw , 1h. iii) SOCl₂, DCM, rt. iii) tosyl chloride, pyridine, 0-4°C. iv) **1**, K₂CO₃, MeCN, reflux. v) TFA:DCM (1:1), rt. vi) $LnCl_3 \cdot 6H_2O$, H₂O pH 6.4.

A problem was encountered when attaching **18a** to DO3A (**1**). This reaction is usually conducted under basic conditions when attaching a fourth arm to DO3A. During the synthesis of compound **19**, the nucleophilic substitution did not run smoothly. The TLC analysis on the reaction mixture spotted the remaining starting material DO3A with

one unidentified compound even if the reaction time was increased five times longer than usual. The presence of an unexpected compound was also identified in MS analysis which containing a peak at m/z 173 for $[M+H]^+$. ^1H NMR analysis of the reaction mixture showed unexpected peaks from unknown compound in the reaction mixture. Three prominent peaks at δ 5.22, 5.75 and 7.42 gave an indication of the identity of the impurity (Fig. 2.17).

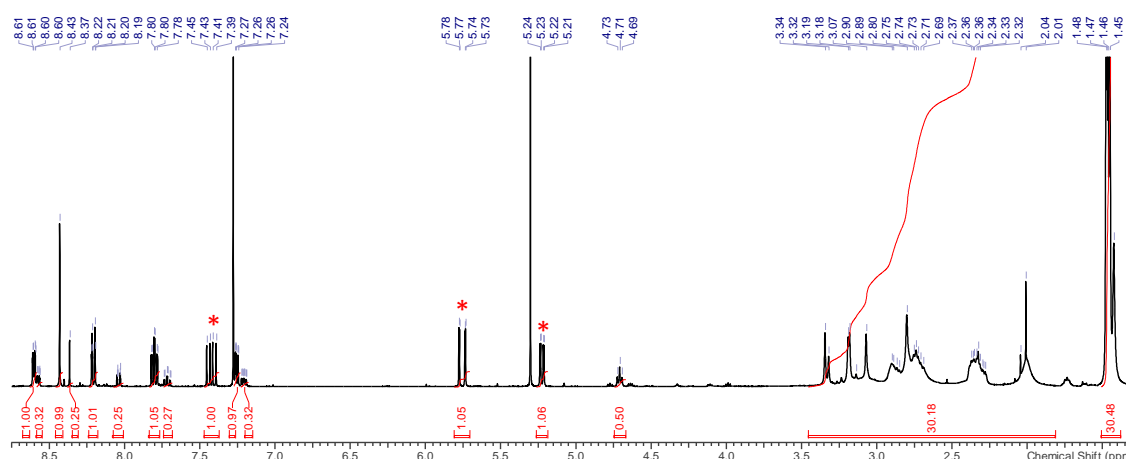


Figure 2.17: ^1H NMR (400MHz, CDCl_3) spectrum of the reaction mixture during preparation of **C6**. Three unexpected peaks are indicated with stars (*).

The peak integration values were comparable with the peaks in the aromatic region. This indicated that there was a correlation between these peaks *e.g.* the three peaks mentioned above are belong to a compound who also has peaks in the aromatic region. The isolation of this unknown compound was achieved through chromatography column, to give a yellow solid that was then recrystallized to provide a colour less crystal. The ^1H NMR spectrum of this unknown compound is shown in Fig. 2.18.

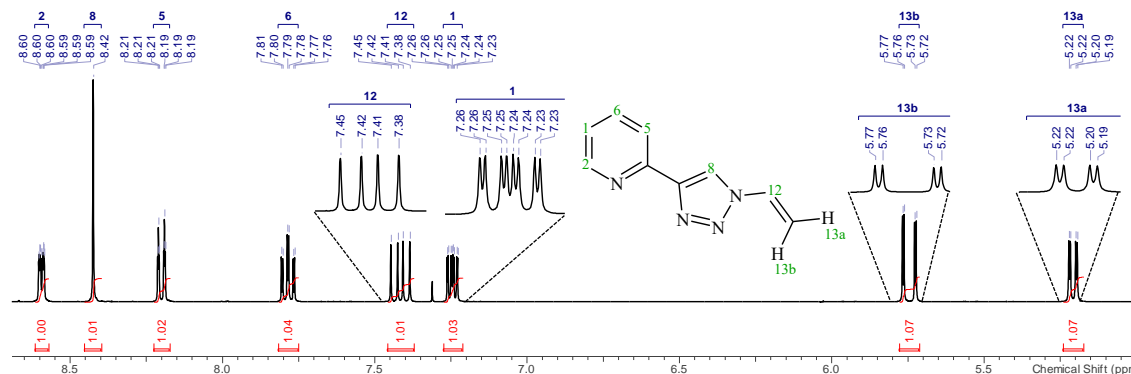


Figure 2.18: ^1H NMR spectra of elimination by-product.

The three unexpected peaks in the ^1H NMR spectrum of the reaction mixture (Fig. 2.17) correspond to this unknown compound. According to this ^1H NMR data, there are five

peaks (located in the aromatic region) similar to its starting material (compound **18a**) while two peaks (in aliphatic region) present in the starting material are missing. The three new peaks which appear at δ 5.22 (dd, $J = 9.0; 2.0$ Hz), 5.75 (dd, $J = 16.0; 2.0$ Hz) and 7.42 ($J = 16.0; 9.0$ Hz) ppm are therefore believed derived from these missing peaks.

According to this NMR data including its integration values, the formation a bimolecular elimination (E2) product as the S_N2 competitor is suggested. Also supported by MS data, the proposed structure of the unknown compound is illustrated in Fig. 2.19.

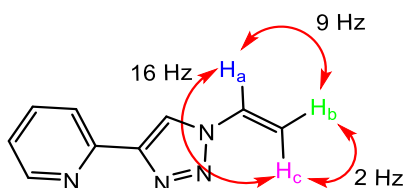
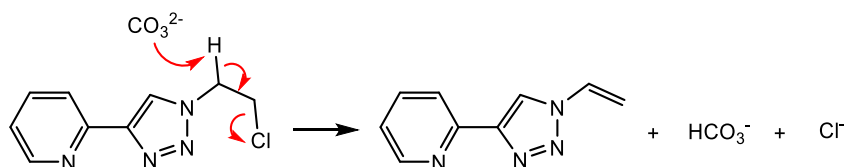
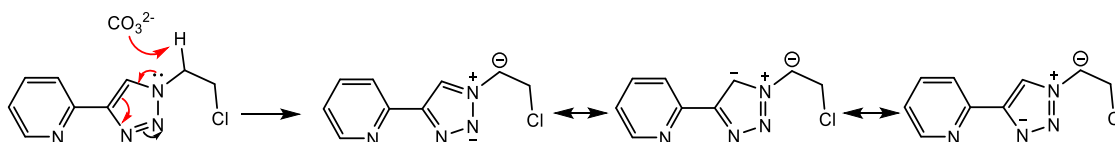


Figure 2.19: Proposed structure of “unknown” by-product.

Peaks at 5.22, 5.75 and 7.42 are predicted belong to H_b , H_c and H_a respectively, which is supported by the coupling constant analyses. Peaks at 5.22 and 5.75 ppm have a similar small coupling constant $J = 2.0$ Hz, which typical for geminal coupling of vinyl protons (usually < 3 Hz). While a larger coupling constant $J = 16.0$ Hz experienced by protons at 7.42 and 5.75 and $J = 9.0$ Hz between peak 7.42 and 5.22 ppm. This is also supported by 2D NMR analysis data. The mechanism of elimination reaction is presented at Scheme 2.18.



Scheme 2.18: Proposed mechanism of by-product formation.

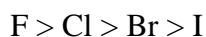


Scheme 2.19: Carbanion stabilization.

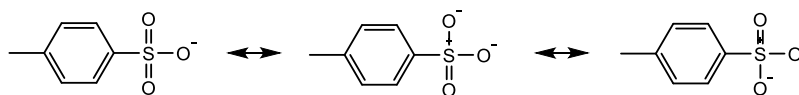
How does this elimination reaction favoured to take place with compound **18a** (two carbons) but not to **15** (three carbons)? Since both of compounds **15** and **18a** are primary alkyl halides and the nitrogen is a good nucleophile, it is believed that the steric hindrance is the main factor inducing the elimination reaction. The substitution reaction

is more difficult in **18a** compared to **15** due to the steric hindrance of the pyridyltriazole. In addition, this elimination reaction is supported by the nitrogen atom in the triazole's ring which helps to distribute the negative charge, stabilize the carbanion and it increase the acidity of the hydrogen by reducing the electron density as illustrated at Scheme 2.19.

Generally, the substitution nucleophilic bimolecular (S_N2) will always compete with the elimination reaction (E2). The elimination reaction however, produces much more molecules compared to the starting material, which means it is thermodynamically favoured because it increases entropy of the reaction. S_N2 reaction is preferred when using a strong nucleophile and in aprotic solvent, while E2 reaction tend to be take place in the presence of a strong base. In addition, a higher temperature will increase the rate of elimination more than the rate of substitution.^{154, 155} Therefore, to bypass this problem, other strategies were attempted to increase the substitution product. Firstly, running the reaction at a lower temperature; secondly, using a more concentrated solution; lastly, changing the leaving group. It has been mentioned previously that chlorine in a polar aprotic solvent behaves as a good nucleophile following this order.



Which means that in polar aprotic solvents, the leaving group with higher electronegativity will be more difficult to leave. So that the use of a better leaving group will be expected to induce the substitution pathway. To achieve this purpose, the tosylate group was chosen as a leaving group in compound **18b**. The tosylate has a bulky structure compared to chlorine, as the size increases, the ability of the leaving group to leave is increased. Furthermore, it has been known that the resonance stabilized structure increases the ability of the leaving group to leave as illustrated at Scheme 2.20.



Scheme 2.20: The electron rearrangement of tosylate.

The synthesis of compound **18b** was achieved by reaction between tosylchloride and compound **17** in pyridine solvent at a low temperature. Pyridine acts as a base during deprotonation of the reaction result. The formation of compound **18b** was confirmed by ^1H NMR spectroscopy analysis, which was showing the corresponding peaks typical for tosylate and supported by the MS data with a peak at m/z 345 for $[\text{M}+\text{H}]^+$.

The elimination product was still observed by using these approaches *e.g.* by using **18b** instead of **18a** starting material, lowering the temperature and reducing the amount of solvent. Therefore, the only strategy that was employed to scale up the substitution product was the gradient addition of the starting material (**18a/18b**) to the reaction mixture until all the starting material DO3A has been fully consumed. Compound **19** (m/z 680 $[M+H]^+$) was then purified and deprotected through the same procedure of the previous compound to give compound **C6** (m/z 519 $[M+H]^+$). The ^1H NMR spectrum of **C6** is presented at Fig. 2.20. Synthesis of the europium complex of **C6** was conducted with the general procedures of lanthanide complexation. MS analysis gave a peak with at m/z 691 $[M+Na]^+$, for **EuC6**.

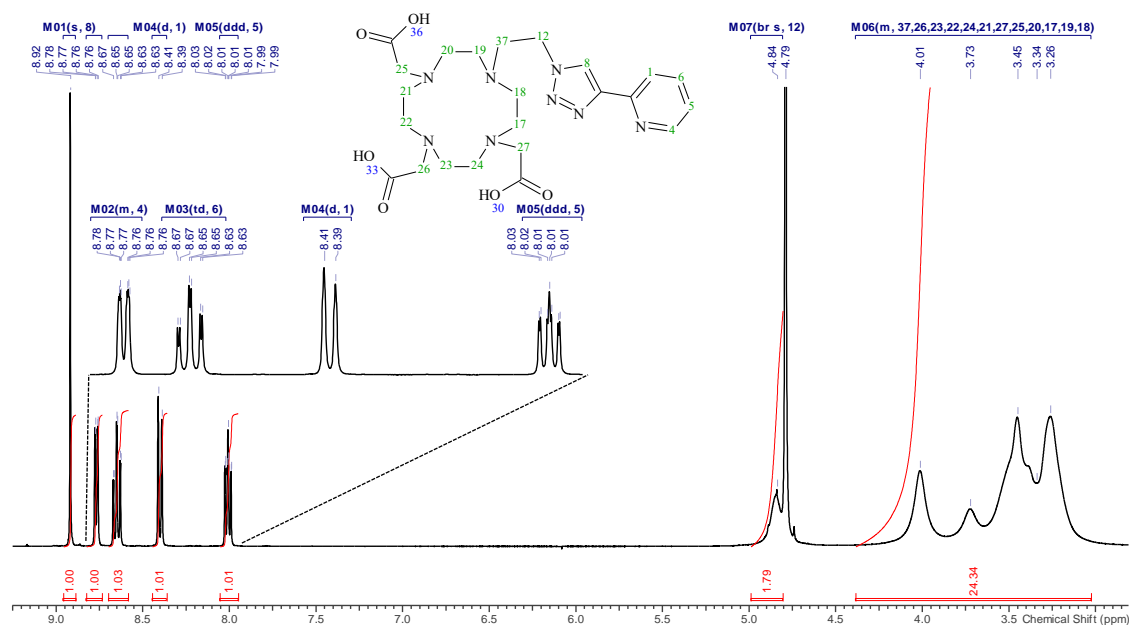


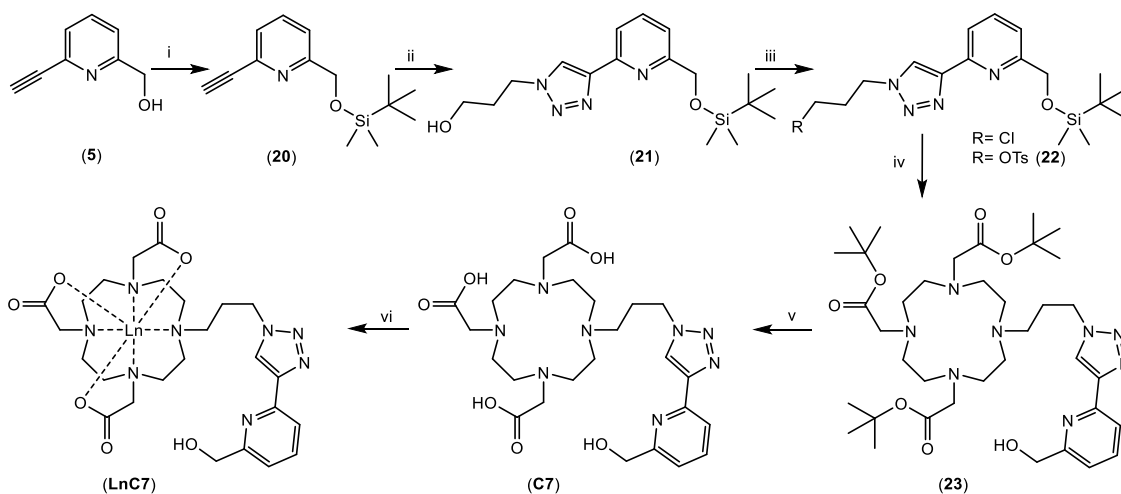
Figure 2.20: The ^1H NMR (400MHz, D_2O) spectrum of **C6**.

Photophysical properties of these two complexes (**LnC5** and **LnC6**) will be discussed at Chapter 3. The pyridyltriazole active arm for these compounds were not coordinated to the metal centre. Therefore, further modifications were required to increase its affinity for metal centre.

2.3.3 Synthesis of **LnC7** and **LnC8**

The following strategy was to attract the pyridyltriazole towards the lanthanide centre, which was initiated by additional a functional group with a good affinity. This led to the formation of **C7**, in which the pyridyltriazole active arm is attached by an $-\text{CH}_2\text{OH}$

group to form a tridentate chelator. The synthetic pathway towards this compound is illustrated at Scheme 2.21.



Scheme 2.21: Synthetic pathway of **LnC7**; i) imidazole, TBDMSCl, DCM, 0-25°C, 30 min. ii) 3-bromopropanol, NaN₃, CuSO₄·5H₂O, NaAsc, EtOH:H₂O (7:3). iii) SOCl₂, DCM, 0°C-rt / Tosylchloride, Pyridine, 0°C, 24h. iv) K₂CO₃, MeCN, reflux. v) TFA:DCM (1:1), rt, 24h. vi) LnCl₃·6H₂O, H₂O pH 6.4.

Synthesis of **LnC7** began with 6-Bromo-pyridin-2-yl methanol as a starting material. This starting material was used during the synthesis **LnC1** and **LnC2**. Thus, the synthesis procedure to get compound **5** can be seen in Section 2.2. The next step was to protect the hydroxyl group with *tert*-butyldimethylsilyl chloride (TBDMSCl). This reaction was carried out in an aprotic solvent in the presence of imidazole. ¹H NMR analysis showed no peak corresponding to -OH at $\delta \sim 3.79$ ppm instead of the presence TBS protection group at 0.96 and 0.12 ppm. This indicated that the -OH group had been protected and was supported by MS analysis, which obtaining a peak at m/z 248 for [M+H]⁺ indicating the formation of **20**. The next step was to synthesise **21** through a copper(I)-catalysed Huisgen 1,3-dipolar cycloaddition. The presence of TBDMS protecting group decreased the polarity of the click product significantly, as a result the separation process *via* SiO₂ column chromatography was relatively easy compared to the previous compound. ¹H NMR spectrum presented the typical triazole's hydrogen along with TBDMS peaks. It supported by MS data showed a peak at m/z 349 for [M+H]⁺.

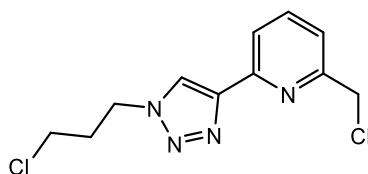


Figure 2.21: Double chlorinated by-product.

The following step was to convert the hydroxyl group to a leaving group before attaching to DO3A. The chlorination reaction was also tried to be applied for this compound. However, this reaction did not provide a clean product. The TLC analysis indicated some unidentified compounds. The MS analysis showed the presence of target compound along with a double chlorinated product as presented at Fig. 2.21. To bypass this problem, the tosylation reaction was again applied to compound **21** as a leaving group to give compound **22**. This reaction worked well under the same conditions as the previous compound. ^1H NMR (1D and 2D) analysis confirmed the formation of **22** supported by MS data providing a peak at m/z 503 for $[\text{M}+\text{H}]^+$.

Compound **22** was then introduced to DO3A following the same reaction conditions to give compound **23**. The formation of **23** was confirmed by ^1H NMR analysis supported by MS data providing a peak at m/z 845 for $[\text{M}+\text{H}]^+$. After *t*Bu-deprotection through the same acid catalysis procedure with TFA, it was purified through semi-preparation reverse-phase HPLC column chromatography to give compound **C7** as a white hygroscopic product. The ^1H NMR of **C7** is presented at Fig. 2.22.

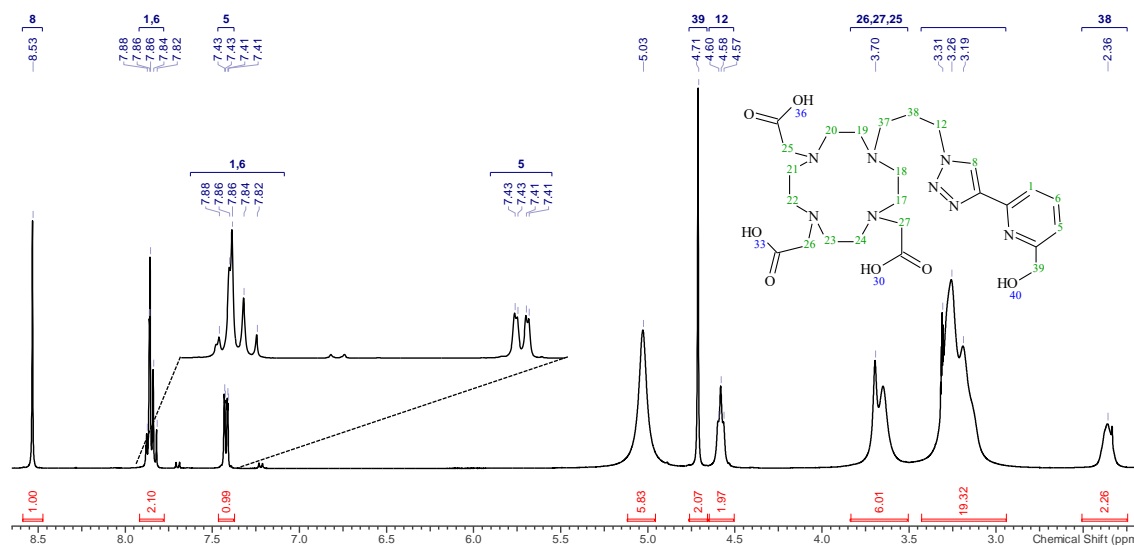
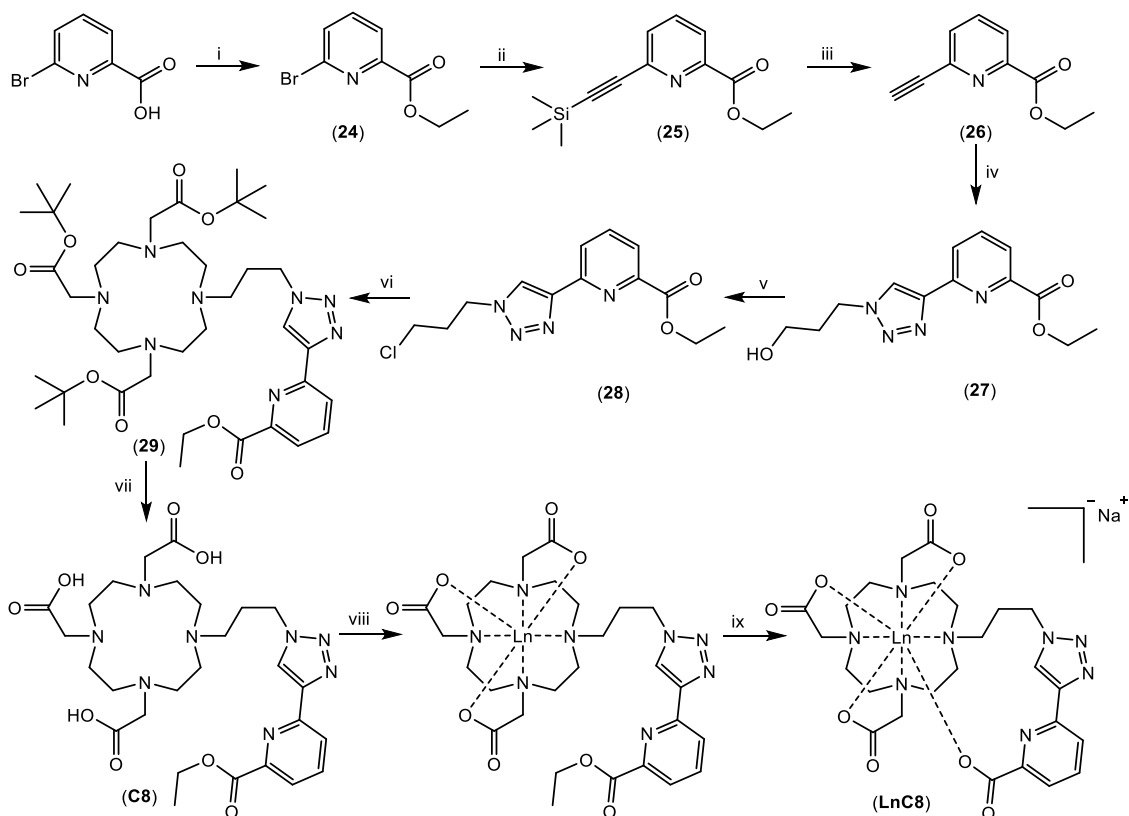


Figure 2.22: The ^1H NMR (400MHz, CD_3OD) spectrum of **C7**.

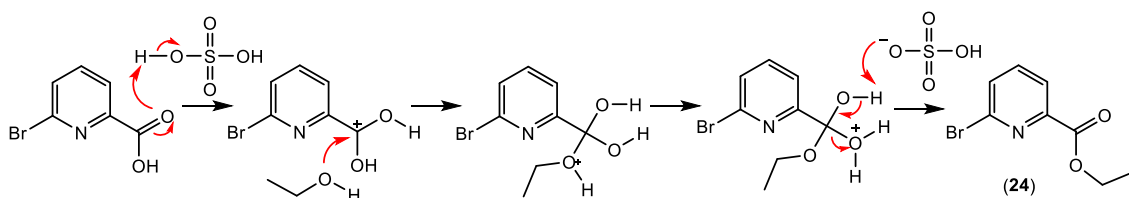
Synthesis of the europium complex of **C7** was conducted with the same general procedure of lanthanide complexation. MS analyses gave a peaks with m/z 735 $[\text{M}+\text{Na}]^+$, for **EuC7**.

The second strategy to attract the pyridyltriazole active arm was by introducing a carboxylate group to the pyridyltriazole. This functional group was successful in the

development some literature examples of zinc-responsive probes as discussed earlier in this chapter. A number of synthetic routes were attempted to give the best reaction pathway as depicted at Scheme 2.22.



Scheme 2.22: Synthetic route of **LnC8**. i) EtOH, H₂SO₄ conc. reflux, 24h. ii) TMS-acetylene, Pd(PPh₃)₂Cl₂, CuI, EtN₃, 50°C, 1 h. iii) TBAF, THF, rt, 1h. iv) 3-bromopropanol, NaN₃, CuSO₄·5H₂O, NaAsc, MeOH:H₂O (3:1), 65°C, 24h. v) SOCl₂, DCM, rt, 24h. vi) **1**, K₂CO₃, MeCN, reflux, 24h. vii) DCM:TFA (1:1), rt, 24h. viii) LnCl₃·6H₂O, H₂O pH 6.4, (Ln = Eu, Gd, Tb). ix) NaOH_(aq) pH 9, reflux.

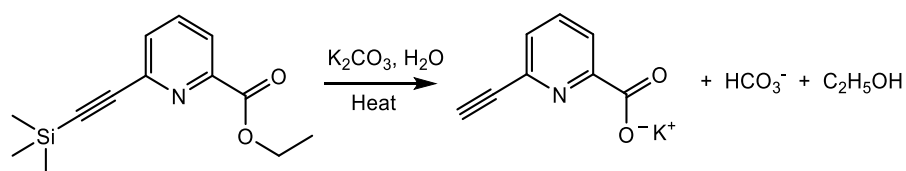


Scheme 2.23: Acid catalysis esterification reaction mechanism.

6-bromopicolinic acid was used as the starting material for the active arm. The first step was converting this carboxylic acid to an ester form. This conversion was intended to change the polarity of this starting material, thus making it easy to handle for the entire synthetic steps. Esterification reaction of 6-bromopicolinic acid and ethanol was catalysed by conc. H₂SO₄. The mechanism of this reaction is illustrated in Scheme

2.23. The ^1H NMR spectrum of compound **24** showed typical ethyl ester peaks which was supported by MS data providing a peak at m/z 230 for $[\text{M}+\text{H}]^+$. It was then charged to Sonoghasira coupling reaction by using the reaction conditions described by D'Amora *et al.* without any modification to give compound **25**.¹⁵⁶ The formation of compound **25** was confirmed by an intense peak typical to TMS on its ^1H NMR spectrum supported by MS analysis with a peak at m/z 248 for $[\text{M}+\text{H}]^+$.

This compound (**25**) was then deprotected before clicking it with an azide. The TMS deprotection was initially conducted by using the same base K_2CO_3 applied previous compound. However, the strength of this base was simultaneously induced the ester hydrolysis as shown at Scheme 2.24.



Scheme 2.24: TMS vs ester hydrolysis reaction.

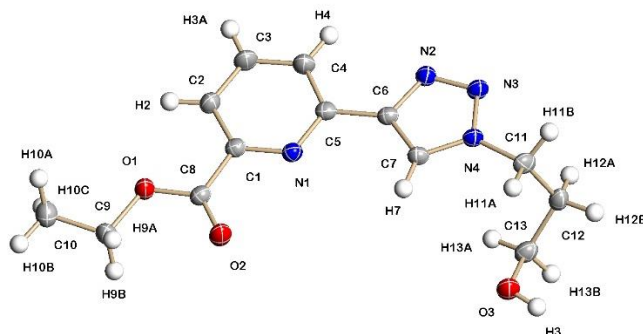


Figure 2.23: An Ortep representation of the crystal structure of ethyl 6-(1-(3-hydroxypropyl)-1H-1,2,3-triazol-4-yl)picolinate (**27**).

This hydrolysed product is a polar compound and was observed at the base line of the TLC plate. Some other bases such as caesium carbonate had been tried; however, tetra-*n*-butylammonium fluoride (tBAF) gave the best result with a relatively high yield. ^1H NMR analysis showed a typical singlet peak corresponding to alkyne. MS analysis also identified peak at m/z 176 for $[\text{M}+\text{H}]^+$. This compound was then clicked *via* copper(I)-catalysed Huisgen 1,3-dipolar cycloaddition with 3-azidopropan-1-ol which was generated *in situ* from 3-bromopropan-1-ol and sodium azide to give compound **27**. ^1H NMR analysis showed a singlet peak typical for triazole's hydrogen along with other peaks supported by its MS analysis providing peak at m/z 277 for $[\text{M}+\text{H}]^+$. This

compound was crystallized from DCM solvent to give a white-yellow crystal. Its X-ray crystal analysis is presented at Fig. 2.23.

The chlorination was applied to compound **27** to give compound **28** by using SOCl_2 . The formation of compound **28** was confirmed by ^1H NMR analysis which showed a large shift of the adjacent carbon from δ 58.7 to 41.2 ppm, supported by MS analysis providing a peak at m/z 295 for $[\text{M}+\text{H}]^+$ as well as the typical chlorine isotope pattern of compound **28**. The pendant arm was then introduced to the tBuDO3A by the similar method used to the previous compound to give compound **29**; however, due to the ethyl ester sensitivity toward basic hydrolyzation, the reaction mixture was prevented from contact with water during the extraction. ^1H NMR and MS analyses confirmed the formation of compound **29**. It was then deprotected with TFA in DCM to give **C8**. **C8** was purified using a reverse-phase HPLC providing a white hygroscopic solid with a peak at m/z 605 for $[\text{M}+\text{H}]^+$. The ^1H NMR spectrum of **C8** is presented at Fig. 2.24.

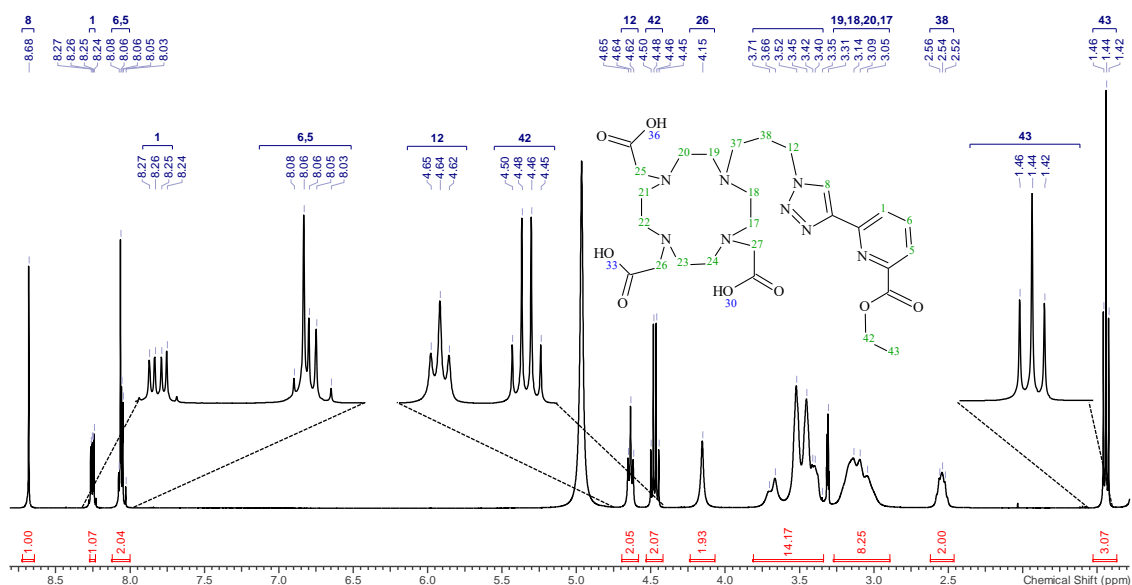


Figure 2.24. ^1H NMR (400MHz, CD_3OD) spectrum of **C8**.

Lanthanide complexation followed the usual procedure. However, the pH was strictly maintained at ~ 6.4 to preserve the ethyl ester from hydrolysis. The hydrolysis of ethyl ester would cause further lanthanide complexation by the pyridyltriazole active arm and prevent it from complexation toward targeted zinc(II) ion. In addition, there is potential to produce free lanthanide ions by metal displacement. As mentioned previously, the presence of a free lanthanide ion such as gadolinium is a danger to the health due to its toxicity.

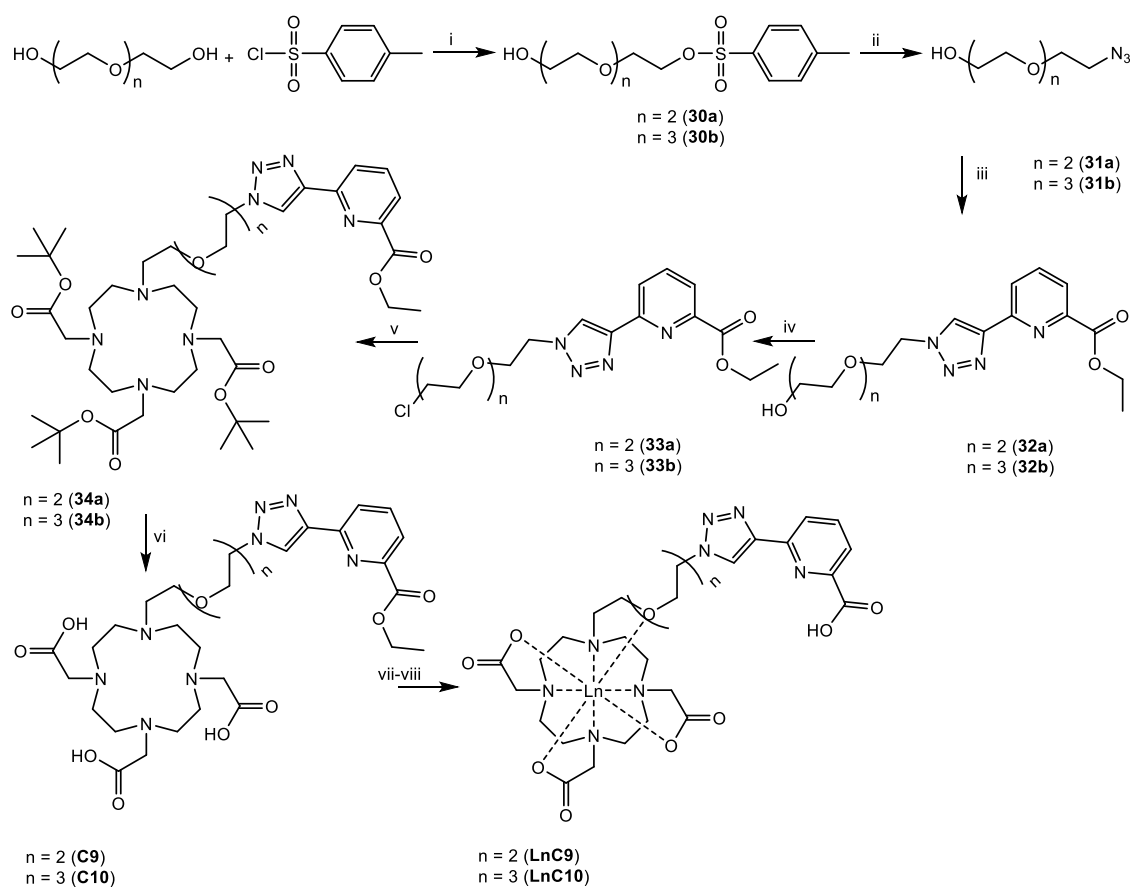
After the complexation to the corresponding lanthanides, the final stage was to activate the pendant tridentate arm by ester group hydrolyzation. The hydrolysis was conducted by heating the solution at pH 10. After the completion, the pH was then neutralized by a dilute $\text{HCl}_{(\text{aq})}$ solution. The presence of the hydrolysis by product such as ethanol was removed easily by lyophilisation to give **LnC8** containing sodium chloride as an impurity. The MS analysis of **EuC8** and **GdC8** provided a peak at m/z 727 $[\text{M}+2\text{H}]^+$ and 732 $[\text{M}+2\text{H}]^+$ respectively.

2.3.4 Synthesis of **LnC9** and **LnC10**

The next step was intended to modify the potential complex (**LnC8**) in order to achieve a zinc-responsive MRI contrast agent. In addition, this was also intended to examine its future potential applications as a dual modal probe such as fluorescence/MR imaging agent, or for use in the synthesis of multimeric contrast agents. Therefore, the first attempt was to modify the length of the linker in order to promote the active arm affinity towards the metal centre. This is to give more space between the main ligand and the active tridentate ligand by addition of more carbon linkers. Instead of using aliphatic groups, polyethylene glycol was chosen as the potential linker due to its polarity and its availability which has been used in polar substituted compounds to a wide range of applications. Literature reports suggest that the polyethylene glycol utilization increased the polarity significantly.^{157, 23} The use of triethylene- and tetraethylene glycol was expected to maintain the compound's polarity. The difference in length between these two linkers was used to investigate the coordination environment or coordination favour of the tridentate ligand. As in the previous compound (**LnC5** and **LnC6**), the further addition of carbon linker reduces the efficiency of the energy transfer between the active arm (antenna) and the lanthanide metal centre, which was observed through their lanthanide emission intensity diminishment.

The synthesis pathway of **LnC9** and **LnC10** followed the same procedure of the parent compound **LnC8**. The difference was only in the preparation of the polyethylene glycol linker. The entire synthetic pathway is presented in Scheme 2.25. The synthesis of the compounds **30a** and **30b** were conducted by using triethylene- and tetraethylene glycol starting materials. They were attached with tosylchloride leaving group by following the same procedure of tosylation which used previously to synthesis compound **22**. This tosylation reaction produced a single and a double tosylation products due to the presence

of two hydroxyl groups on both sides of the polyethoxy chain. In order to increase the selectivity toward single tosylation product of **30a** and **30b**, two procedures were used. The first procedure used one to half ratio between polyethylene glycol and tosyl chloride. In this procedure, the excess of ethylene glycol was used to ensure that all of the tosylchloride were consumed and at the same time reducing the opportunity of double tosylation reaction to occur. Indeed, this exactly followed to what has been expected, an exclusive single tosylation product resulted through this strategy along with the remaining polyethylene glycol starting material.



Scheme 2.25: Synthetic route of **LnC9** and **LnC10**; i) Pyridine, 0-4°C, 24h. ii) NaN₃, H₂O:Acetone (1:3), 75°C, 24h. iii) **26**, CuSO₄·5H₂O, NaAsc, MeOH:H₂O (3:1), 65°C, 24h. iv) SOCl₂, DCM, rt, 24h. v) **1**, K₂CO₃, MeCN, reflux, 24h. vi) DCM:TFA (1:1), rt, 24h. vii) LnCl₃·6H₂O, H₂O pH 6.4, (Ln = Eu, Gd, Tb). viii) NaOH_(aq) pH 9, reflux.

The second strategy was to apply the equivalent amount (one to one ratio) between two starting materials. The result was compared to examine the efficiency of the reaction. Increasing the quantity of the tosylchloride starting material reduced unreacted polyethylene glycol starting material but increased the double tosylation product. The presence of the double tosylation product was observed in a significant amount. There

were advantages and disadvantages between these two procedures. The first approach provided a better result in terms of purity, due to the exclusive single tosylation product. In addition, it only required separation from its corresponding polyethylene glycol starting material, which can be delayed until the following step (synthesis of azide) has conducted. Nevertheless, the total result percentage of single tosylation from this method was less than that in the second method. In contrast, although the second method produce higher percentage of result, it is essential to separate single and double tosylation product before going to the next step.

In general, both methods could be used to produce compound **30a** and **30b**. Both methods have to perform purification process either pre- or post- azidification. Therefore, the second method was preferred due to the higher reaction yield and the ease of the separation process, facilitated by their large polarity differences between single and double tosylation product. The double tosylation product was present as a white crystal while the single tosylation product as a colourless viscous liquid. ¹H NMR analyses showed typical aryl hydrogen and methyl group from the tosyl moiety to each compound **30a** and **30b**, supported by the accurate mass analysis with m/z 327 [M+Na]⁺ and m/z 349 [M+H]⁺ for **30a** and **30b** respectively.

The next step was to convert compounds **30a** and **30b** to their corresponding organic azides. This step followed the synthesis procedure reported by Mattarei *et.al.*¹⁵⁸ published previously with a little modification to the azide ratio and the reaction time. The amount of azide was minimized for environment safety reasons and to increase the effectiveness of azide starting material. The reaction performance managed to be maintained by slightly increasing the reaction time. Half the amount of azide was used to give the same reaction result. Different to the previous organic azide, this polyethylene glycol azide was safe to be separated and isolated ((C_n+O_n)/N_n ratio higher than 3), as a watery pale-yellow fluid. ¹H NMR spectroscopy analyses of **31a** and **31b** showed a large shift to both adjacent hydrogens (from $\delta \sim 4.17$ to 3.40 ppm) and carbons (from δ 69.3 to 50.7 ppm) for **31a** and **31b** respectively. It was supported by MS analyses providing a peak at m/z 198 [M+Na]⁺ and 242 [M+Na]⁺ for **31a** and **31b** respectively.

These azides were then used to synthesize **32a** and **32b** through a copper-catalyzed Huisgen 1,3-dipolar cycloaddition. The high purity azides (**31a** and **31b**) could be accurately weighed to give more precise amount compared to *in situ* preparations.

Therefore, these click reactions provided cleaner reaction results. ^1H NMR spectroscopic analyses of **32a** and **32b** showed typical peaks for triazole's hydrogen and the ethyl ester groups. MS analyses provided peaks at m/z 351 $[\text{M}+\text{H}]^+$ and 395 $[\text{M}+\text{H}]^+$ for **32a** and **32b** respectively, which confirmed the formation of the title compounds.

The chlorination process of the hydroxyl group to provide compound **33a** and **33b** required longer reaction time. The formation of these two products were analysed by MS providing peaks at m/z 369 $[\text{M}+\text{H}]^+$ and 413 $[\text{M}+\text{H}]^+$ for **33a** and **33b** respectively. ^1H NMR analyses exhibited a large shifting of the adjacent carbon from δ 61.7 to 42.8 ppm for **33a** and **33b** respectively. The attachment of these tridentate active arms was achieved in the same manner as previously employed to the main ligand DO3A. The high quality dry solvent was used to minimize ester hydrolyzation (as previously explained), since a strong base and an elevated temperature were applied in this reaction. The hydrolysis process is believed to be the main reason of the fluctuation results gained from this reaction. The ^1H NMR spectroscopic analyses showed the corresponding ethyl ester and *t*Bu protection groups. The MS analyses showed peaks at m/z 869 $[\text{M}+\text{Na}]^+$ and 913 $[\text{M}+\text{Na}]^+$ for **34a** and **34b** respectively. The *t*Bu deprotection for these compounds were achieved by using the same condition as previous compound. As mentioned previously, the ester form is much more stable in the acidic condition during deprotection. The HPLC purification provides **C9** and **C10** as a white hygroscopic solid. ^1H NMR spectrum of compound **C10** is presented at Fig. 2.25.

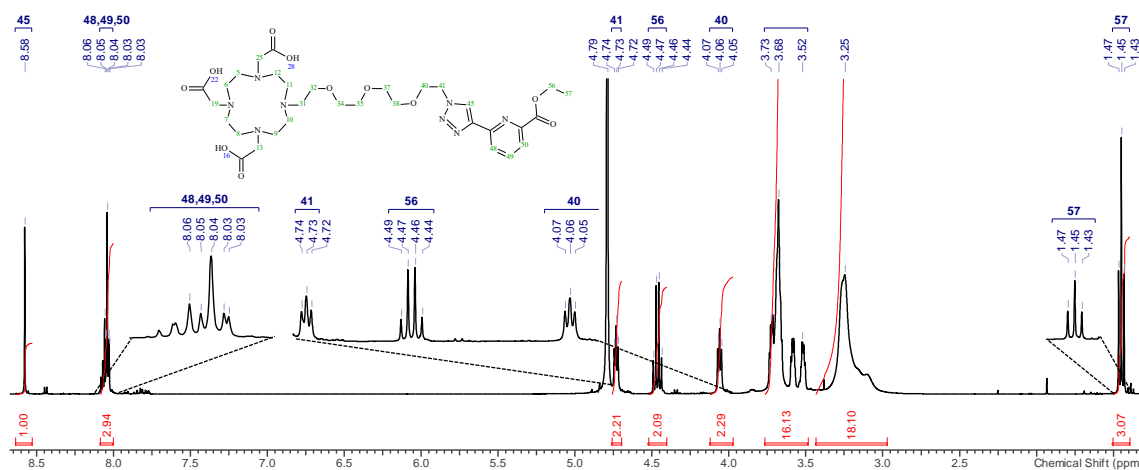


Figure 2.25: ^1H NMR (400MHz, D_2O) spectrum of **C10**.

The lanthanide complexation of these two compounds were performed in similar manner as explained to **LnC8**. The mass spectrometric analysis of the corresponding lanthanide showed peaks at 837 $[\text{M}+\text{Na}]^+$ (methyl ester form) and 850 $[\text{M}+2\text{Na}]^+$ for

EuC9 and **GdC9** respectively and at m/z 889 $[M+2Na]^+$, 895 $[M+Na]^+$ and 900 $[M+2Na]^+$ for **EuC10**, **TbC10** and **GdC10** (ester form) respectively with their typical isotope distribution pattern. For ethyl ester containing complexes, the MS analysis is not recommended to be conducted in methanol solvent due to the methyl ester formation which observed in the mass analysis result (a transesterification reaction during the sample loading in the methanol solvent or during the ionization processes is suspected).

2.4 Summary and Conclusion

The development of zinc-responsive contrast agent by exploiting pyridyltriazole-based active arm provides an alternative choice in smart MRI contrast agent developments. In general, there were two synthetic routes applied during the synthetic processes, namely by synthesizing the main lanthanide complex prior to the active arm attachment and by synthesizing the active arm separately before lanthanide complexation. Both routes basically could be applied; however, the second pathway was favoured due to its simplicity in reaction steps and purification. In addition, the lanthanide complexes provided in the first pathway (before the active arm attachment) generally lacked chromophores that makes it slightly difficult to detect during analysis process *e.g.* during purification through a semi-preparative HPLC.

The copper(I)-catalyzed Huisgen 1,3-dipolar cycloaddition (“click” reaction) succeed in providing pyridyltriazole scaffolds. However, the conventional $CuSO_4$ catalyst failed when facing 2-azidopyridine substrate to synthesise **C4**, due to the formation of closed ring, tetrazole. The use of microwave heating succeeded in clicking this “click-inert azide” although in a moderate yield. The S_N2 reaction of active arm attachments on DO3A ran smoothly facilitated by K_2CO_3 in a polar aprotic solvent MeCN, with an exception during the synthesis compound **C5**. The active arm starting material (compound **18a**) experienced a competition reaction between S_N2 and E2 mechanism as a result two different product were obtained. An attempt to increase the S_N2 product was carried out by reducing the temperature reaction and by increasing the concentration. Although, it did not completely eliminate the E2 product, the S_N2 product yield increased significantly.

The coordination affinity of the pyridyltriazole active arm toward lanthanide centre was attempted to be enhanced by additional polar functional groups namely hydroxyl and carboxylic groups as in **LnC6** and **LnC8**. These were successfully

synthesized by using different pyridine starting materials containing these groups. TBS and ester protection groups were used to protect the hydroxyl and carboxylic acid respectively during the entire synthetic steps. Polyethylene glycols were used to replace the **LnC8**'s linker. The elongation the active arm's distant succeed by this linker without disturbing the water solubility of these compounds (**LnC9** and **LnC10**).

Chapter 3

Photophysical Properties and Zinc-responsive Studies

3.1 Background

Lanthanide luminescence can be used to study structural information of the corresponding lanthanide complexes, such as their symmetry, hydration number *etc.* In addition, their luminescence lifetime is used as a sensitive tool to study changes in environment of lanthanide ions. It also can be used to study the structure and the stability of the lanthanide complexes. Moreover, the electrostatic interactions, first and second coordination sphere and ligand exchange can be investigated.¹⁵⁹ Therefore, the capability of pyridyltriazole active arms as zinc-responsive MRI contrast agents developed in this project were examined by studying their photophysical properties, including their lifetime data. Alterations to the hydration number (q) in response to a stimulus provide essential information for responsive MRI contrast agents. By comparing hydration states, the activity of a responsive MRI contrast agent can be predicted.

However, as pointed out in Chapter 1, the excited state of gadolinium lies relatively high in energy and emission is in the UV region. This makes gadolinium difficult to be excited either by direct or indirect excitation (discussed latter). On the other hand, its neighbours such as Sm, Eu, Tb and Dy possess relatively low-lying excited states in which their excited energy levels can be populated easily. Eu and Tb are considered as the most important emissive lanthanides due to their emission bands lying in the middle of the visible region, as well as their long-lived excited states. The fact that different lanthanides complexed by the same ligand are typically isostructural,¹⁶⁰ means that targeted complexes are mainly examined by using one of these emissive lanthanides and will be discussed (*i.e.* as a surrogate for gadolinium) sequentially in the following sections.

3.2 Luminescence Properties of Europium and Terbium

Lanthanide luminescence has been used in many applications, taking advantage of their unique properties to produce typical sharp emission bands and long luminescent lifetimes. As discussed in Chapter 1, the majority of lanthanides exhibit luminescence properties. Their emission spectra vary from relatively high energy as in gadolinium (emit

in UV region) to relatively low energy emission such as in Yb or Er (emit in near IR region). Europium and terbium are the most luminescent lanthanides being used due to their quantum yields, lifetimes and wavelength of emission. In addition, the energy gap between the lowest excited state and the highest ground state of Eu and Tb are relatively higher than Dy and Sm, thus they have higher emission intensity,²² i.e. they are also less quenched by the surrounding matrix through vibrational nonradiative energy transfer (such as with -OH, -CH, -NH).^{22,53,161} Although Eu and Tb experience less quenching compared to Sm and Dy, this quenching still occurs. This emission quenching can be used to estimate the number of coordinated molecule such as water. Using this phenomenon, Horrocks proposed a formulation to quantify the number of waters in a lanthanide complex by comparing the emission lifetime in H₂O and D₂O by the following equation.²²

$$q = A \left(\frac{1}{\tau_{H_2O}} - \frac{1}{\tau_{D_2O}} - B \right) \quad (3.1)$$

Where, A and B are the intrinsic properties of lanthanide(III) ions with A = 1.05 ms and 2.1 ms for europium and terbium, while B = 0. It was then revised by Parker, *et al.*, to give A = 1.2 ms and B = 0.25 ms⁻¹ for Eu, while A = 5.0 ms and B = 0.06 ms⁻¹ for Tb.¹⁶² The more waters coordinated, the more the lanthanide emission is quenched.²²

As mentioned previously, the 4*f* orbitals of the lanthanides are effectively shielded by 6*s* and 5*p* orbitals, which leads to the low extinction coefficient (ϵ) values. When incomplete 4*fⁿ* orbitals absorb electromagnetic radiation, there are three possible transitions that can occur namely: charge transfer between the lanthanide ion and the ligands, 4*fⁿ* → 4*fⁿ⁻¹*5*d* transitions and intra-4*fⁿ* transitions.¹⁵⁹ The last transition is considered as the most interesting and useful transition. The characteristic sharp absorption bands of the lanthanides are derived from this transition. Similarly, their emission spectra are sharp line-like bands and are also derived from these *f-f* transitions. The emission can occur from an excited ligand perturbed by the cation, from the excited cation perturbed by the ligand and as a consequence of non-radiative intramolecular energy transfer from the ligand excited state to the cation followed by the emission.¹⁵⁹ The occurrence of the electronic interaction and spin-orbit coupling causes the 4*fⁿ* orbitals to split resulting in the large number of electronic levels characteristic to a given lanthanide (Fig. 1.21).

The spectral lines of the europium and terbium emission that arise from the excited ⁵D₀ and ⁵D₄ to the ⁷F_J ground states transition is presented in Fig. 3.1.

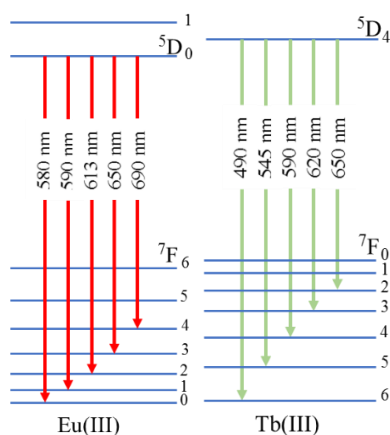


Figure 3.1: Visible Electronic emission transitions of europium(III) and terbium(III).²²

Europium has unique emission bands in the visible region at ~580 nm, ~590 nm, ~613 nm, ~650 nm, and ~690 nm, which correspond to the electronic transitions of europium emissive state (5D_0) to its ground state levels (7F_J) for $J = 0, 1, 2, 3, 4$ respectively. The europium emission bands are derived from two excited states 5D_1 and 5D_0 . However, the 5D_1 state is short-lived, thus the overall emission bands are observed mainly from 5D_0 transitions. On the other hand, terbium emission spectra are derived only from one excited state ($^5D_4 \rightarrow ^7F_J$) to give emission in the visible region at ~490 nm, ~545 nm, ~590 nm, ~620 nm and ~650 nm for $J = 6, 5, 4, 3, 2$. These specific electronic transitions are characteristic to each lanthanide emission (fingerprint). These bands are slightly influenced by properties of donor and the coordination geometry.¹⁶³ Therefore, their binding properties can be investigated by studying the luminescence and/or ratiometric analyses. The lowest lying excited states of europium (5D_0) emission and terbium (5D_4) are at 17200 cm^{-1} and 20400 cm^{-1} respectively.^{22,163} These energy levels are relatively close to the triplet excited state for certain organic chromophores allowing energy transfer processes.

3.3 Antenna Sensitization

Although the ϵ values of the lanthanides are extremely low ($\sim 1\text{-}10 \text{ M}^{-1} \text{ cm}^{-1}$),¹⁶⁰ their excited states can be populated by energy transfer from an antenna. The antenna is commonly an organic compound, which contains chromophores that promote the sensitization of the lanthanide emission. The antennae usually have high ϵ values ($\sim 10^4\text{-}10^5 \text{ M}^{-1} \text{ cm}^{-1}$).¹⁶⁰ Generally, antennae can be derived from any aromatic or hetero-aromatic containing long π -conjugated systems.¹⁶⁰ Some antennae known today such as azaxanthone, phenanthridine, and tetracycline are used as sensitizers. Most of them are

poly aromatic and heterocyclic.^{22,163} Europium was the first lanthanide sensitized *via* an antenna, when Weissman in 1942 observed the line-like emission spectra of various β -diketonate complexes by exciting the organic part with a UV light.¹⁵⁹ There were three proposed mechanisms for this energy transfer as presented at Fig. 3.2.

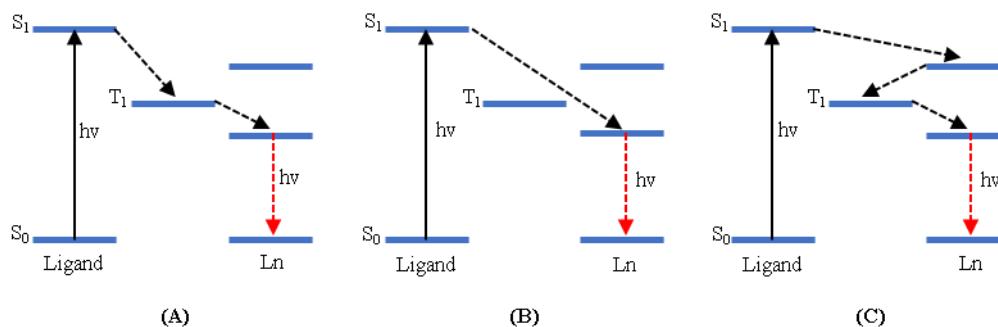


Figure 3.2: Proposed energy transfer mechanisms. (A). Energy is transferred to the Ln emissive state *via* ligand's triplet state. (B). Energy is transferred directly to the Ln emissive state. (C). Energy is transferred to Ln emissive state stepwise *via* the Ln upper emissive state and the ligand's triplet state.

The first proposed mechanism (A) was proved experimentally.¹⁵⁹ In order to transfer its energy, the energy level of the antenna's triplet state must be situated above the energy level of the lanthanide's excited state. The energy gap between the antenna's singlet and triplet states must be lower than 7000 cm^{-1} to ensure the population of the triplet state over any nonradiative relaxation (vibration) and radiative relaxation (fluorescence).²² In addition, it must also have sufficient triplet-state energy (at least 1850 cm^{-1})¹⁶⁴ or (2000 cm^{-1}) ¹⁶³ above the lanthanide's emissive state to be able to transfer and to prevent back-energy transfer from lanthanide to the antenna. The ideal antenna for imaging applications must have excitation wavelengths between 340 – 420 nm or 350 – 410 nm.¹⁶³ The lower wavelengths will potentially damage the biological media being investigated. On the other hand, it should be below 420 nm to ensure a sufficient energy gap between the antenna's triplet state and the lanthanide's excited state.²²

As mentioned previously, the lanthanide's energy levels are varied (Fig. 1.21). Gadolinium has the highest excited energy state, which lies at a remarkably higher level (${}^6\text{P}_{7/2} = 32150\text{ cm}^{-1} / 92.3\text{ kcal mol}^{-1}$)^{160,159} than common organic antennae, this makes it difficult to populate. While, europium and terbium have excited energy levels below the triplet energy levels of many organic antennae. The lowest excited energy level of europium (${}^5\text{D}_0 = 17200\text{ cm}^{-1}$) is lower than those in terbium (${}^5\text{D}_4 = 20400\text{ cm}^{-1}$), thus europium excited state is much closer to the quencher vibration energy level (such as OH

or NH) than terbium excited state. As a result, europium complexes are more susceptible to quenching than terbium.^{22,163} The energy from the antenna can be transferred to these excited states through certain mechanisms which depends on the distance between the antenna's triplet state and the lanthanide's excited state.

3.4 Energy Transfer *via* Dexter and Förster Mechanisms

The energy transfer processes are conducted *via* two different principles, Dexter and Förster mechanisms as illustrated at Fig. 3.3.

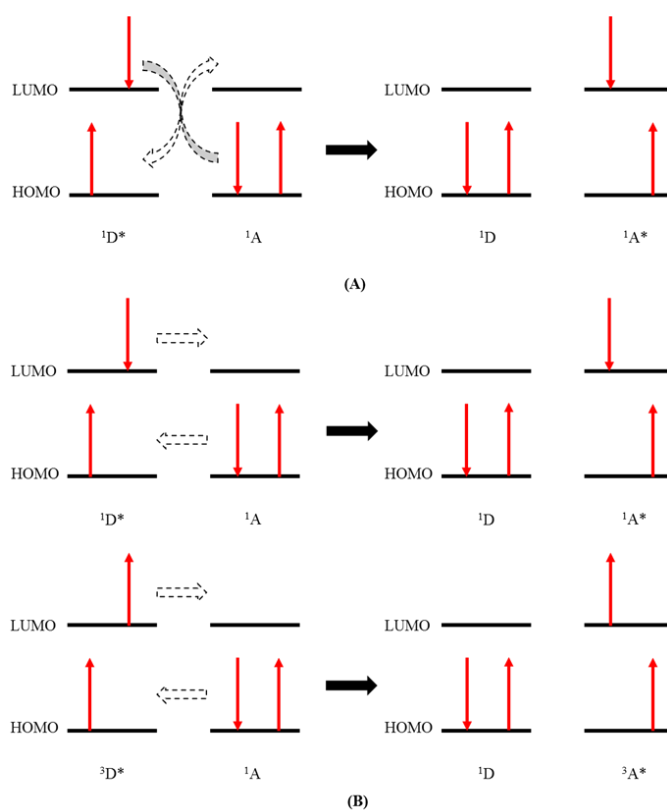


Figure 3.3: Förster and Dexter energy transfer mechanisms. A) Förster energy transfer. B) Dexter energy transfer through singlet or triplet states.

The Dexter energy transfer, which is also known as exchange mechanism, is an energy transfer process between two molecules by exchanging their electrons. This mechanism needs overlap between their orbitals, thus the excited state donor and the ground state of acceptor should be close, which typically occur within 10 Angstroms (short-range energy transfers). Its energy transfer efficiency decreases significantly with the increasing distance. The Förster energy transfer on the other hand, is known as dipole-dipole mechanism, in which the energy transfer occurs *via* dipole-dipole coupling between the antenna's triplet state and the lanthanide's $4f$ orbitals of the corresponding lanthanide.⁵³ The energy produced during relaxation of donor's excited-state electron is used to excite

the acceptor's ground-state electron, as a result, no energy is transmitted to the environment. This mechanism could be done either in singlet (S_1) or triplet (T_1) excited-states. In contrast with the Dexter mechanism, Förster mechanism is considered as a long-range energy transfer process.⁵³ The energy transfer between the antenna and the lanthanide centre can be conducted *via* Dexter and Förster energy transfer mechanisms.¹⁶⁵ The efficiency of energy transfer therefore, is a distance-dependent between antenna and the lanthanide centre (r), which follows the order of $1/r^6$.²² By decreasing the distance between the antenna and the lanthanide centre, the energy transfer efficiency will increase. Thus, lanthanide complexes containing the antennae, which is directly coordinated to the lanthanide centre, will have a higher sensitization efficiency. The energy transfer efficiency can also be increased by increasing the number of antennae.²² The heavy atom effect from chelated lanthanide makes the intersystem crossing process faster in the antenna by increasing the spin-orbit coupling.¹⁶⁶

The energy transfer efficiency from the antenna can be perturbed by changing the antenna's environment *e.g.* by coordination with certain metals such as zinc(II). This is usually followed by changing their photophysical properties *i.e.* their emission profiles. Therefore, by studying this phenomenon, the presence or rearrangement of coordination behaviour can be predicted.

3.5 Photophysical Changes by Zinc Complexation.

As was pointed out in Section 2.1, there are no $d-d$ electron transitions in zinc. The excitation process in zinc(II) complexes therefore cannot be achieved through low-lying energy charge transfer or metal-centred transitions. They usually happen *via* ligand-centred (LC) transitions or ligand-to-ligand charge transfer (LLCT).¹²¹ These processes are illustrated in Fig. 3.4.

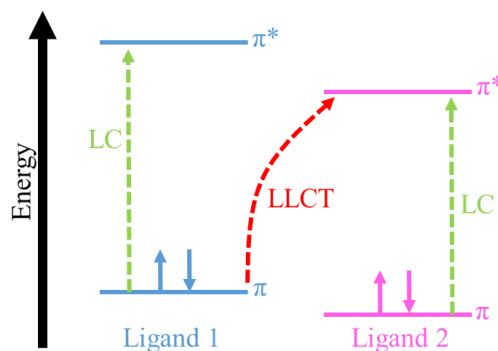


Figure 3.4: Zinc complex excitation *via* ligand-centred (LC) and ligand-to-ligand charge transfer (LLCT).

The LC transition of a zinc(II) complex occurs internally in one ligand's orbitals as marked as green dashed arrows. This process is independent from the zinc(II) metal centre. Consequently, changes in emission are induced *via* the ligand's electronic states. While, the LLCT transition involves two different ligands attached to a zinc(II) complex. This transition involves many mechanisms.¹²¹

Most of zinc(II) sensors exploit these “special” properties of zinc(II). On zinc(II) complexation, the ligand rigidity is improved and can lead to more intense ligand emission. It reduces the ligand's vibration, thus reducing the energy quenching by bond vibrations. In addition, the zinc(II) ion switches off quenching of emission *via* photoinduced electron transfer (PET) mechanisms.^{167,168,169} This process is induced by transfer lone-pair of electrons of certain atoms for example; nitrogen in pyridine to the empty orbitals of the ground state. The lone pair of electrons from this donor atom are transferred to empty ground-state orbitals of an acceptor, causing a nonradiative decay. In the presence of zinc(II) ion however, the nitrogen's lone-pair of electrons coordinate with zinc(II) and unavailable for electron transfer. The HOMO and LUMO energy levels are rearranged to such an extent, causing the energy level of the donor to lie below that of its acceptor. This rearrangement prevents the electron transfer process, thus increases the radiative decay (fluorescence), as illustrated in Fig. 3.5.

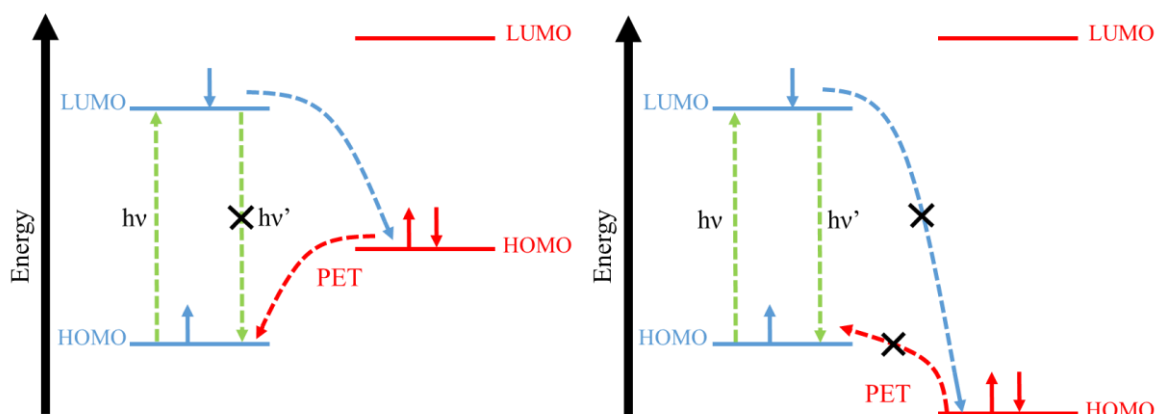


Figure 3.5: Photoinduced electron transfer (PET) (left) and inhibition mechanism induced by zinc(II) ion (right).¹²¹

3.6 Photophysical Studies

The study of targeted complexes was conducted through their emissive-lanthanide (europium or terbium) complex analogues. It was started from **LnC1** to **LnC10** consecutively, in line with the synthesis steps explained in Chapter 2. As mentioned

previously, any findings obtained on each step, were used as considerations to suggest modifications required in order to improve the properties as a zinc-responsive MRI contrast agent. The absorption and emission spectra were recorded and compared during the addition of zinc(II) or/and some other divalent biologically relevant metal ions. The conclusion drawn from the results that were obtained were then applied to their corresponding gadolinium(III) complexes because they share similar characteristics, including oxidation state and coordination properties. Finally, relaxivity measurements were conducted on those gadolinium(III) complexes that showed potential activity as a zinc-responsive MRI contrast agent.

3.6.1 Photophysical Properties of Model Complexes (**LnC1** and **LnC2**)

Photophysical studies of the first model complexes were initiated by observing the electronic absorption spectra of **EuC1** and **EuC2** (Fig. 3.6). The absorption spectra show absorption bands, that could be caused by n to π^* or π - π^* transitions. Excitation is rare for σ to σ^* transitions, because it needs such high energy. **EuC1** and **EuC2** showed two absorption maxima at $\lambda = 230$ nm; 280 nm and $\lambda = 243$ nm; 298 nm for **EuC1** and **EuC2** respectively, which correspond to n - π^* or π - π^* transitions on their pyridyl or pyridyltriazole chromophores. It was noticed that by the formation of a triazole ring in **EuC2**, the λ absorption maxima shifted about 18 nm from 280 nm (in **EuC1**) to 298 nm (in **EuC2**), which was believed due to extension the π -electron conjugation systems between pyridine and triazole ring.

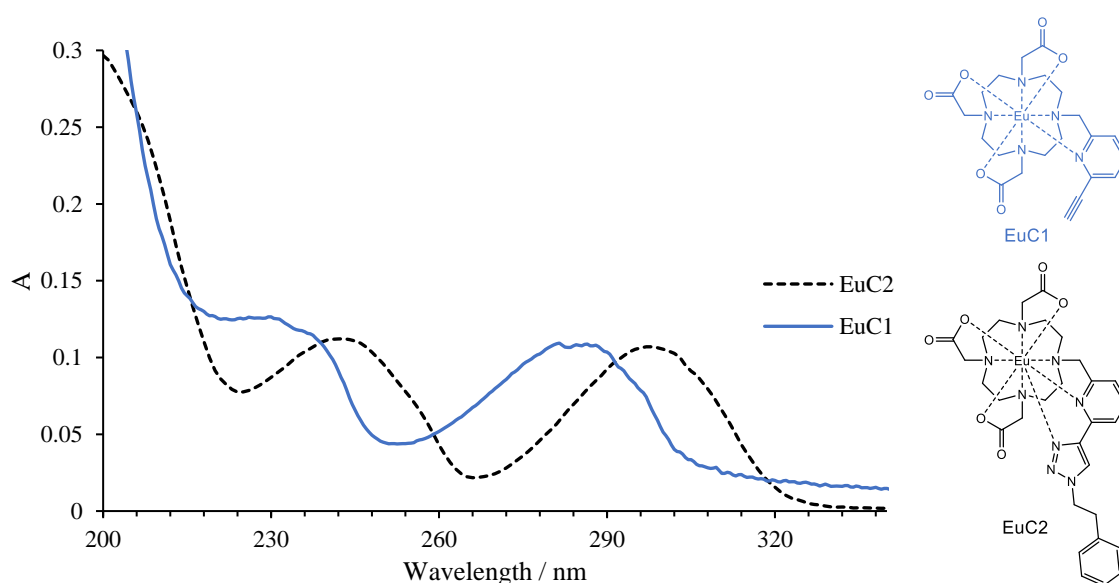


Figure 3.6: The electronic absorption spectra of **EuC1** (blue) and **EuC2** (black) in H_2O .

Luminescent emission spectra of **EuC1** and **EuC2** were observed by exciting those complexes at their λ absorption maxima. The europium emission occurs *via* energy transfer from the triplet excited state of chromophore/antenna (pyridine/pyridyltriazole) to the emissive state of the europium(III) centre. These luminescent emission spectra of the europium complexes were used to analyse their coordination environments. In which, different complexes with different coordination environments generally exhibit different luminescence lifetimes, as well as their emission spectra intensities ($\Delta J = 0-4$) (Fig. 3.7).

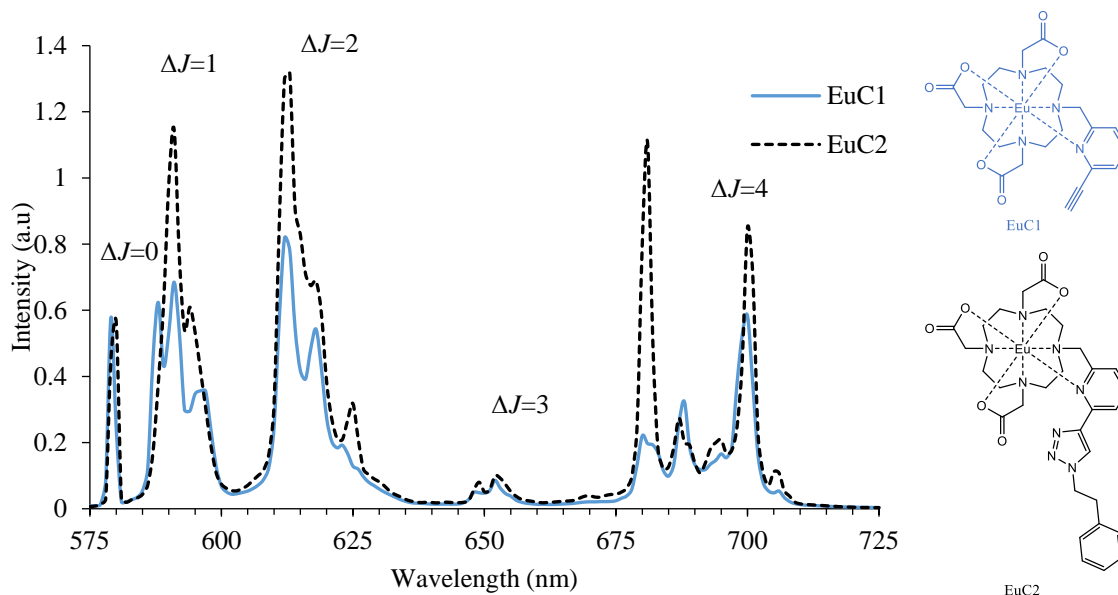


Figure 3.7: Luminescence emission spectra of (**EuC1**) (blue) and (**EuC2**) (black) (excited at 290 nm, H₂O, 298 K).

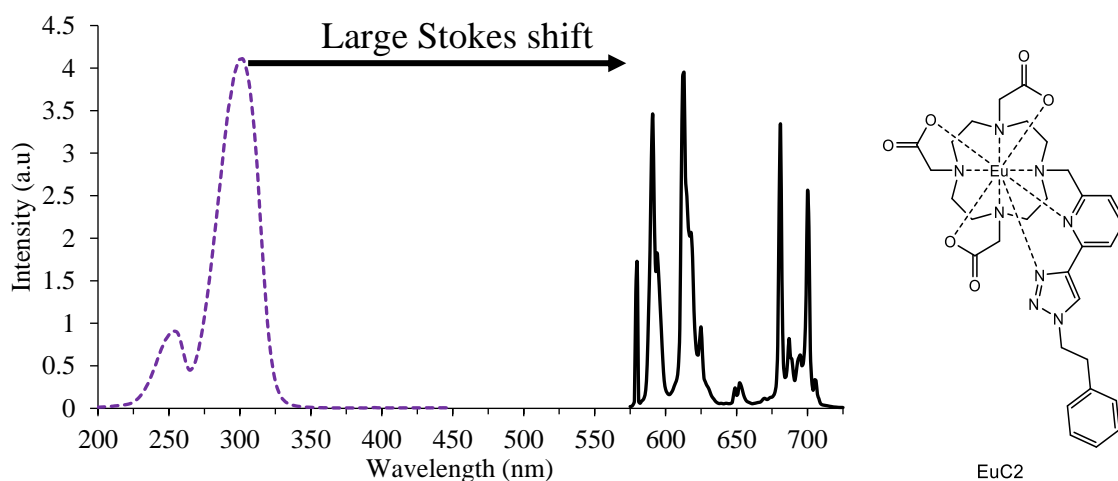


Figure 3.8: The excitation (at 617 nm) (purple) and emission (at 298) (black) spectra of **EuC2** (in H₂O, 298K).

The emission intensities of $\Delta J = 1$ and $\Delta J = 2$ transitions changed moderately from **EuC1** to **EuC2**. While, a significant change is observed in the emission intensity ratio

within the $\Delta J = 4$ transitions (at ~ 681 and ~ 700 nm) between those complexes. The luminescence spectra of **EuC1** and **EuC2** showed no emission from the pyridyl or pyridyltriazole chromophores, indicating the occurrence of an efficient energy transfer process between these antenna and the europium(III) centre *via* a ligand to metal energy transfer mechanism as presented at Fig. 3.2 (A). There is a large gap between the energy absorbed (λ_{max} absorption) and the energy emitted (λ_{max} emission). The distance between these, absorption and the emission maxima is known as Stokes shift as illustrated at Fig. 3.8. This large Stokes shift is typical for lanthanide emission *i.e.* Eu, and is beneficial for many applications.

Table 3.1: Comparison of emission intensity by pseudo direct and indirect excitation of **EuC1** and **EuC2** at two different concentrations (in H₂O pH 7 at 298K).

Complex	Intensity at 590nm Excited at 395nm (a)	Intensity at 590nm Excited at 280/298nm (b)	Ratio (b/a)	Average
EuC1	1546	102602	66.36	65.73
	1434	93358	65.10	
EuC2	868	285494	328.91	321.35
	675	211819	313.80	

EuC2 has a more intense emission compared to **EuC1**. To know this characteristic, a comparison of the emission intensities between pseudo direct (at the absorption maxima of europium) and indirect excitations (at the absorption maxima of the chromophore/antenna) at two different concentrations were measured and presented at Table 3.1. It is clear that sensitized emission from **EuC2** is approximately 5 times more emissive than **EuC1** (supported by fluorescence quantum yield data which will be discussed in Chapter 4). This suggests that the pyridyltriazole in **EuC2** is more efficient in transferring energy compared to one pyridine ring alone as in **EuC1**. This could possibly be caused by bidentate coordination from the pyridyltriazole ring making it closer to europium for more efficient energy transfer ($1/r^6$) or the lack of coordinated water (needs to be calculated) caused by steric effect. Water usually quenches the excited energy through a non-radiative decay process (vibration). In addition, a more conjugated double bond system might be lowering the singlet and triplet excited states (shown in absorption spectra, that **EuC2** absorb at longer wavelength) closer to the emissive state of europium (5D_0), which can enhance the rate of energy transfer from the antenna.

In order to build a MRI contrast agent, it is important to know how many water molecules are involved in the lanthanide coordination sites, since an active contrast agent needs at least one water molecule in their inner coordination sphere to get sufficient contrast, or it should have no water molecule to gain a switch-off effect on the desired contrast agent. There are several methods that can be used to measure the hydration number (q), one of them is by measuring the excited state lifetime of the corresponding europium(III) or terbium(III) complexes in two different solvent (H_2O and D_2O). By exploiting radiation less energy transfer from the emissive state of europium(III) to the overlapping vibration levels of O-H (in H_2O) and O-D (in D_2O) as illustrated in Fig. 3.9.

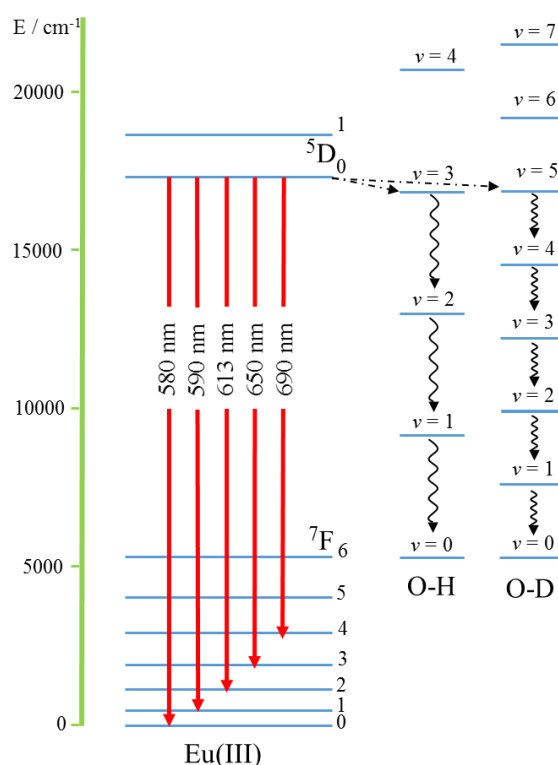


Figure 3.9: Energy level diagram of europium(III) compared to idealised vibrational energy levels of O-H and O-D oscillators. Emissive state of europium ($^5\text{D}_0$) overlaps with $v = 3$ in H_2O and $v = 5$ in D_2O . The europium emission is more efficiently quenched in H_2O than in D_2O .

The energy transfer from emissive state of europium is much more efficient to the $v = 3$ level of H_2O than $v = 5$ of D_2O , due to the Frank-Condon principle which states that the probability of vibrational state population decreases as energy increases due to poor overlap between ground and higher vibration level wavefunction. The higher in the vibrational ladder the transition is, the less probability there is of it occurring. H_2O quenches the europium emission more than D_2O as presented at Fig. 3.10, which shows the lifetime measurement of **EuC2**.

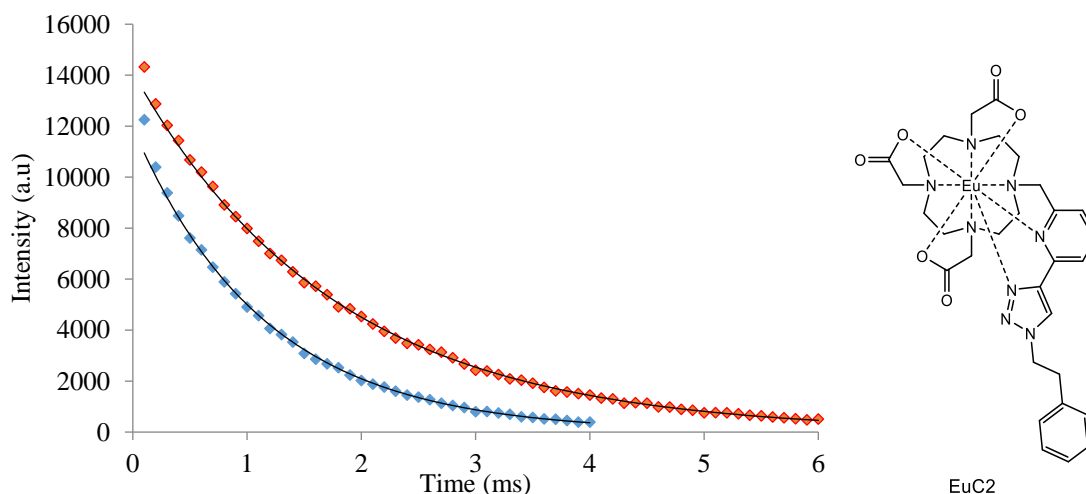


Figure 3.10: Excited state lifetime studies of **EuC2** in H₂O (blue) and D₂O (red) (at 298K).

It is clear that **EuC2** luminescence emission is shorter lived in H₂O compared to in D₂O *i.e.* it has a shorter excited state lifetime with access to non-radiative decay pathway. The lifetime measurements follow first order decay kinetics, the hydration number (q) can be calculated by using the rate constant from decay in both H₂O and D₂O as presented at Eqn. 3.1.⁵³ The first order decay constant for the depopulation of the excited state for these two complexes are summarized in Table 3.2.

Table 3.2: Summarized lifetime measurements to calculate the hydration number (q).

Complex	λ_{em}/nm	λ_{ex}/nm	$k_{H_2O}(\text{ms}^{-1})$	$k_{D_2O}(\text{ms}^{-1})$	$q(\pm 0.2)$
EuC1	591	280	1.50	0.52	0.9
EuC2	590	300	0.90	0.58	0.1

The hydration number (q) of **EuC1** is ≈ 1 , indicating that there is only one water molecule present in the inner coordination sphere of the europium centre. While, there is no such water in **EuC2**. This can be explained by two possibilities: first, the presence of the pyridyltriazole (in **EuC2**) binding in a bidentate manner to the europium centre (through the nitrogen of pyridine and one from the triazole), preventing a water molecule from coordination. The second, there is only one site coordination taken by pyridyltriazole (by pyridine's nitrogen), however the pyridyltriazole of **EuC2** blocks the coordination site by its steric hindrance. The first assumption seems acceptable since this phenomenon consistent with the significant increase in the emission intensity by increasing the coordination sites of **EuC1** (one coordination site) to **EuC2** (two coordination sites). On

the other hand, this emission enhancement could also be derived from the transformation of **EuC1** to **EuC2**, which eliminates the water molecule from the inner coordination site in **EuC2**. This makes its emission less susceptible to quenching than in **EuC1**. Thus, the second assumption is also possible. The zinc-responsive examinations however, showed an indication that the first assumption was more likely. By the fact that there was no emission enhancement during the addition of zinc(II) ion (will be discussed later) indicating that there is no free nitrogen site available for coordination toward zinc(II). The photophysical properties of **TbC1** and **TbC2** however, have special emission properties, which have potential to be used in other applications. This will be discussed in the Chapter 4.

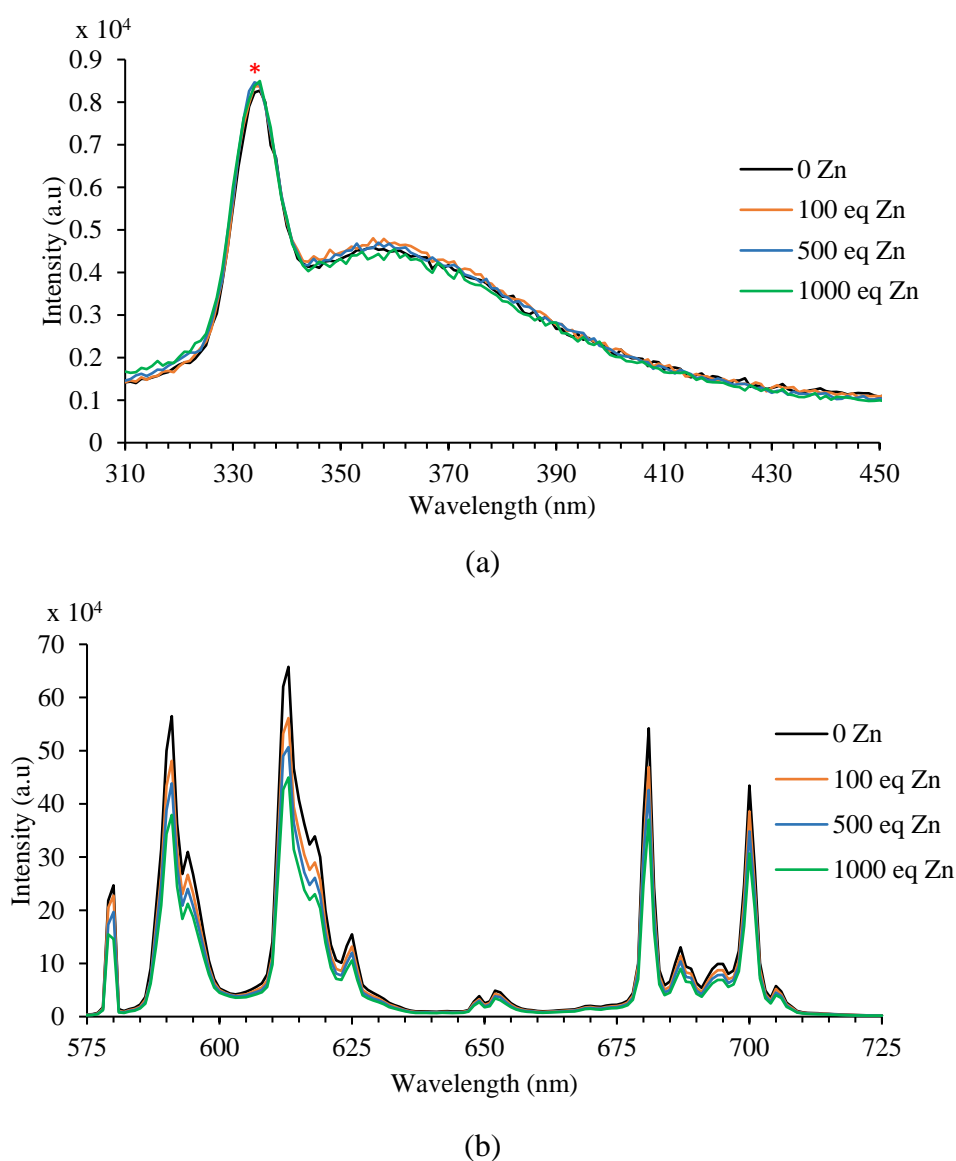


Figure 3.11: **EuC2** emission spectra in response to added zinc(II) (at 298 nm) in 50 mM HEPES buffer pH 7.4 and 0.1 M NaCl_(aq). a) Emission of the pyridyltriazole. b) Emission of the europium(III).
* = water raman peak.

The zinc-responsive examination was conducted in the 50 mM HEPES buffer pH 7.4 and over a constant ionic strength 0.1M NaCl. Overall, there was no significant change in the emission profile of **EuC2** during the addition of zinc(II) ion as presented at Fig. 3.11. There was no change in intensity emission bands observed from the pyridyltriazole, during the zinc(II) addition. Similarly, there were also no significant alteration in the europium emission (a small change is caused by dilution effects caused by zinc(II) additions). It is believed that the pyridyltriazole in **EuC2** exhibits a strong coordination binding which makes it difficult to be “opened” by such divalent metal ions.

To observe how the pyridyltriazole ligand should transform its emission spectra when it interacts with the zinc(II), the same experiment was conducted with the pyridyltriazole as an uncoordinated free arm (compound **6**). As expected, its emission increased in response with added zinc(II) as presented in Fig. 3.12.

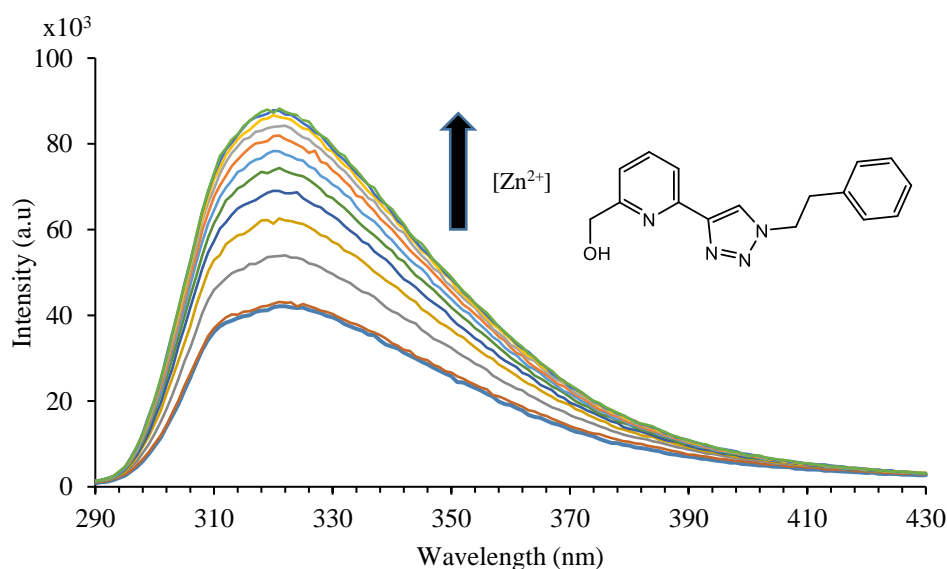


Figure 3.12: Emission profile of compound **6** (a “free” active arm) in response to added zinc(II) (in 50 mM HEPES buffer pH 7.4 and 0.1M NaCl_(aq)).

The emission profile of **GdC1** is very different to **EuC1**. It has no emission band from lanthanide centre gadolinium (there is no energy transfer processes between antenna and lanthanide centre, as in its europium complexes). As a substitute, there is an emission band from its chromophore, which is usually presented as a mirror-like spectrum between excitation and emission as presented at Fig. 3.13.

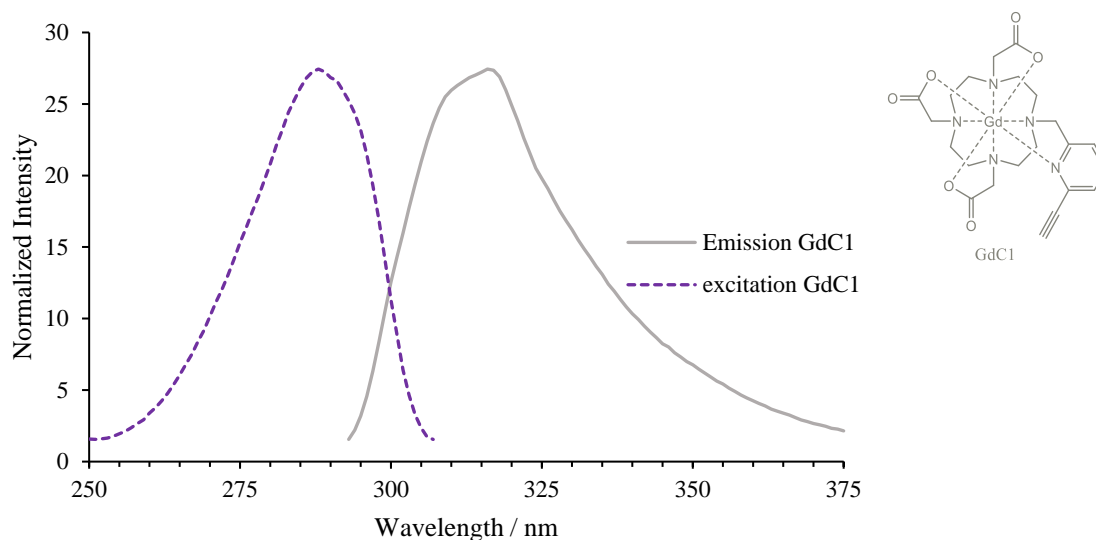


Figure 3.13: Excitation (purple) and emission (grey) spectra of **GdC1** (in H₂O at 298K). As expected, the addition of a free zinc(II) ion did not change the emission profile of either **GdC1** and **GdC2**. Based on these results, further complex modification was necessary. The coordination fashion provided a closed form, preventing it from interacting with the outer environment. Thus, by attaching an active arm in the opposite orientation, it was assumed that an “open-structure” would be provided that increase the probability of its interaction with the environment. This will be discussed in the following section.

3.6.2 Photophysical Properties of **LnC3** and **LnC4**

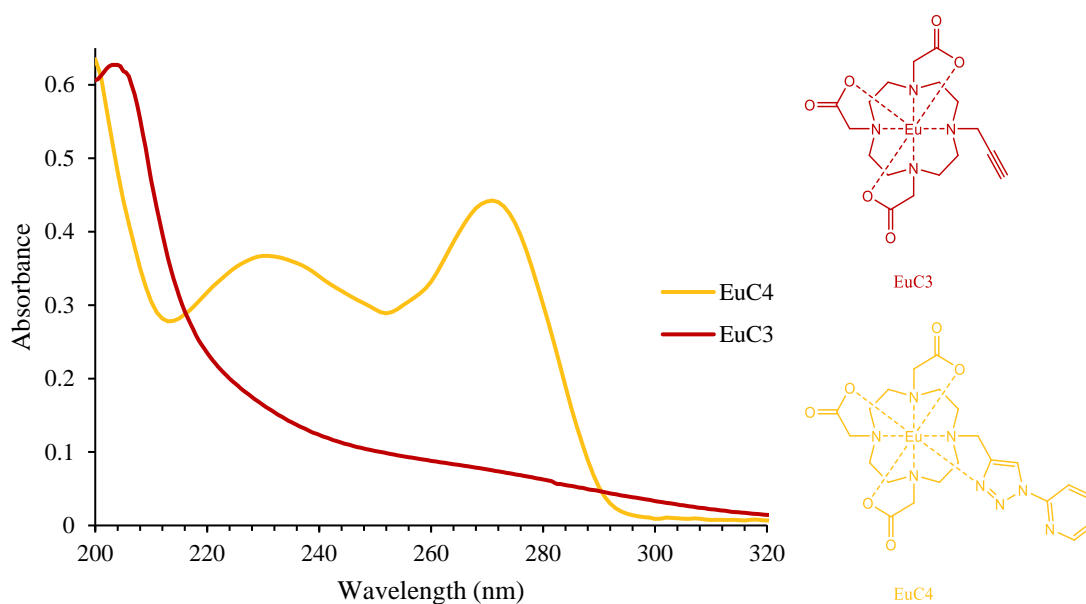


Figure 3.14: Absorption spectra of **EuC3** and **EuC4** (in H₂O at 298K).

The next principal targeted compound was **LnC4**. However, due to its importance as an intermediate compound of the synthesis process as presented in Section 2.3.1, **LnC3** will be discussed simultaneously. According to absorption measurements, there were two distinct spectra resulting from **EuC3** and **EuC4** (Fig. 3.14). There are two main absorption bands recorded for **EuC4** at ~230 nm and ~271 nm. While, there was no such absorptions observed at these wavelengths for **EuC3** complex due to the lack of chromophore.

EuC4 was excited at the absorption maxima (271 nm) of the pyridyltriazole. Energy transfer to the europium centre gives typical emission bands of europium between 575-725 nm. Luminescent emission spectra of **EuC3** was recorded by pseudo direct excitation to the europium(III) at 395 nm. The low extinction coefficient, owing to the forbidden electronic transition of europium(III) ion makes **EuC3** difficult to excite directly. As a result, low emission intensities are observed when using the same concentration as in **EuC4**. The emission profile of **EuC4** has a similarity to **EuC2**, in which the intensity of the emission of the pyridyltriazole moiety (~310 – 450 nm) is lower in energy than emission from europium (~575 – 725 nm) (Fig. 3.15).

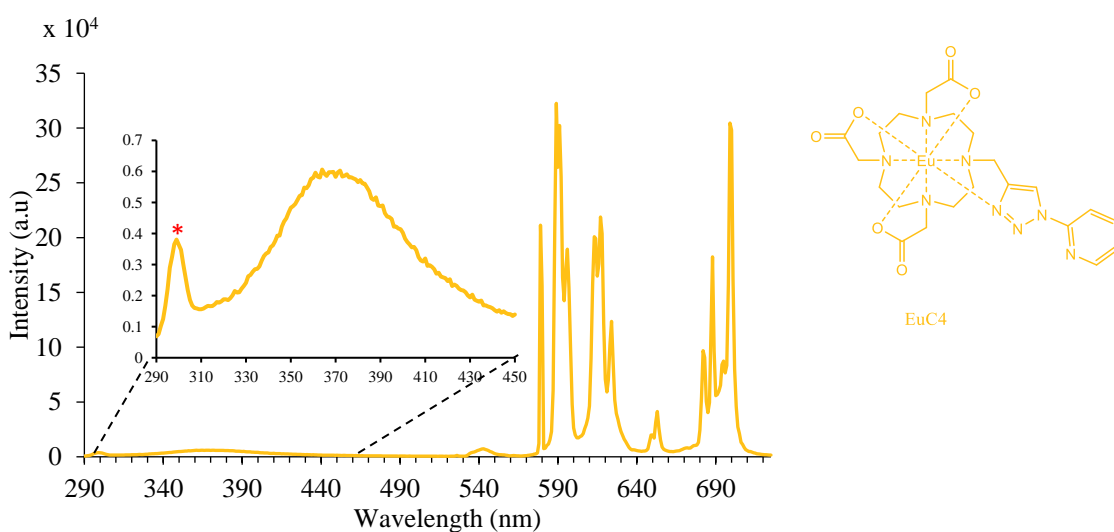


Figure 3.15: Emission spectrum of **EuC4** excited at 271 nm (in H₂O at 298K). Inset is showing expanded of the pyridyltriazole emission.

* = water raman peak.

Compared to the emission spectra of **EuC2**, the emission from the pyridyltriazole moiety was still observed in **EuC4** although in a low intensity. This is believed due to the reversed position of pyridyltriazole, (compared to **LnC2**) which prevents the pyridine moiety from coordinating to the lanthanide centre. This observation supports the assumption that the bidentate coordination *via* pyridine and triazole nitrogen atoms occur

in **EuC2**, which makes the energy transfer more efficient. In addition, it had been reported that, by ligand exchange studies and DFT calculations of metal complexes, the “regular” click pyridyltriazole ligand provides more stable complexes rather than the “inverse” click.¹⁷⁰ This is an indication that the coordination of the “inverse” click pyridyltriazole is weaker than the “regular” clicked version. The emission, which was observed at 290–450 nm, could be attributed from this monodentate coordination of “inverse” click pyridyltriazole moiety which was supported by its hydration number calculation to give $q = 1$, the hydration number calculation is summarized in Table 3.3.

Similar to **EuC2**, a comparable emission intensity at ~590 nm ($\Delta J = 1$) and ~617 nm ($\Delta J = 2$) is also presented in **EuC4**. While **EuC3** shows a distinct emission intensity for those bands. The europium emission profiles of **EuC3** and **EuC4** is presented in Fig. 3.16.

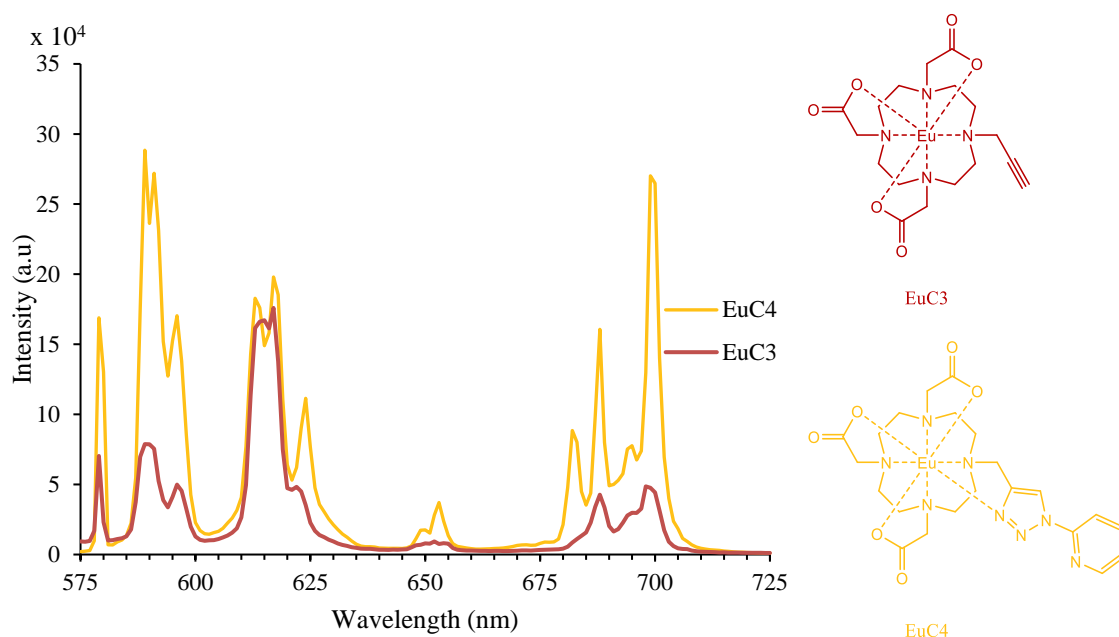


Figure 3.16: Europium emission profile of **EuC4** (orange) (excited at 271nm) and **EuC3** (brown) (excited at 395nm) (in H₂O at 298K).

Table 3.3 Hydration number calculation of **EuC3** and **EuC4**.

Compound	k_{H_2O} (ms ⁻¹)	k_{D_2O} (ms ⁻¹)	q (± 0.2)
EuC3	2.62	0.60	2.2
EuC4	1.64	0.51	1.1

A zinc(II) responsive examination was carried out on **EuC4** and its emission profile in response to zinc(II) ion was recorded (Fig. 3.17). The addition of zinc(II) did not change the emission profile significantly and the pyridyltriazole band of **EuC4** behaved similarly

to **EuC2**. There were only small changes in intensity to both pyridyltriazole and europium bands. This is an indication that zinc(II) ion does not interact with the pyridyltriazole active arm to any great extent.

The formation of **LnC4** complexes containing an inverse motif active arm pyridyltriazole was not sufficient to stimulate coordination displacement. This shows that the formation of a five-membered chelate ring as in **LnC2** and **LnC4** complexes provide a complex with high stability that is difficult to be displaced by a free metal ion such as zinc(II). Therefore, the addition of another group member to the coordination arm was intended to provide a slightly labile coordination system generally a \geq six-membered chelate. These new target complexes are discussed in the following section.

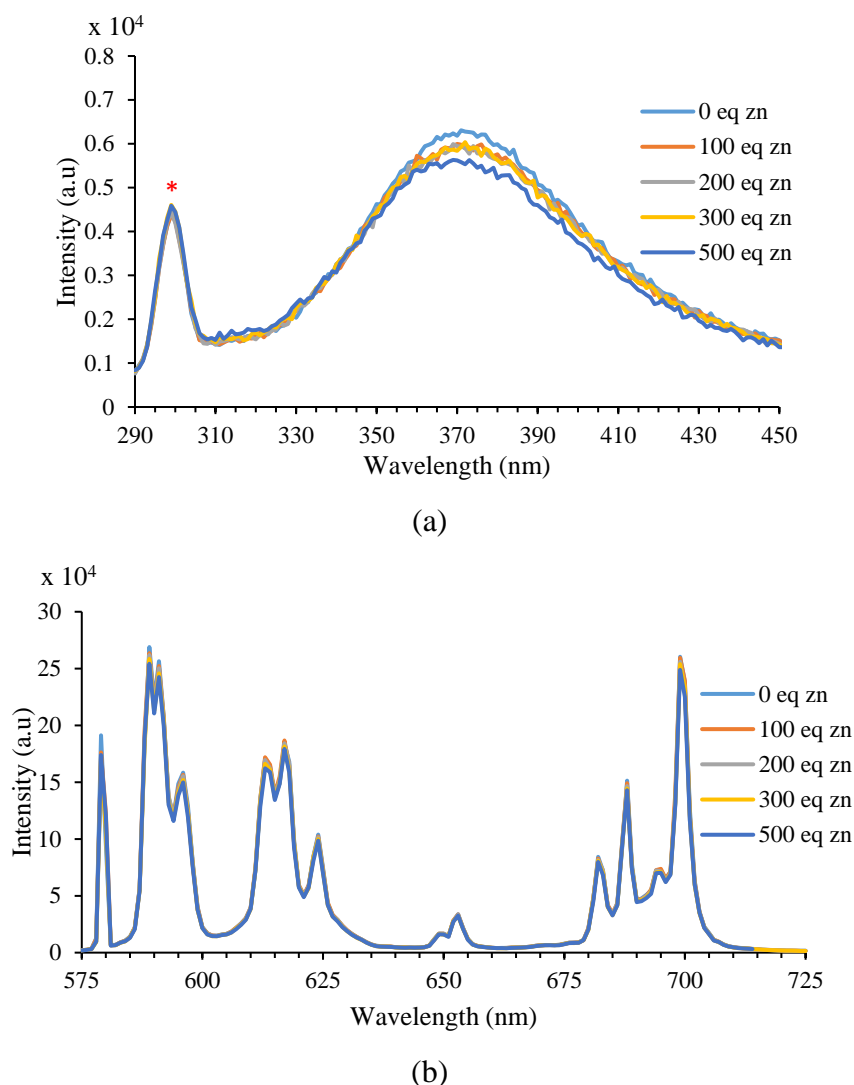


Figure 3.17: Emission profile of **EuC4** during zinc(II) addition measured in 50 mM HEPES buffer pH 7.4 and 0.1M NaCl_(aq). a) Emission of the pyridyltriazole. b) Emission of the europium(III). * = water raman peak.

3.6.3 Photophysical Properties of **LnC5** and **LnC6**

In order to solve the limitations of the previous compounds, *i.e.* the excellent stability experienced in a five-member chelate ring, led to the formation of **LnC5**. This was designed to give more carbon members in the chelate ring formed by the active arm. The use of “regular” click in the synthesis of the pyridyltriazole target compound was based on the consideration of the reaction simplicity, compared to the “inverse” click pyridyltriazole. **LnC5** was the first of these modified compounds that was synthesized, characterized and examined. The results from **LnC5** were used as a consideration to the formation of **LnC6**, which contained one less carbon atom in the linker on the pyridyltriazole active arm. The characterization and examinations were conducted in a similar manner.

Absorption spectra of **LnC5** and **LnC6** are presented in Fig. 3.18. They have a similar absorption pattern owing to the chromophore similarities. There are two main absorption bands recorded at ~ 237 nm and ~ 278 nm. As in **LnC2**, their longer absorption bands (at ~ 278 nm) are lower in intensity.

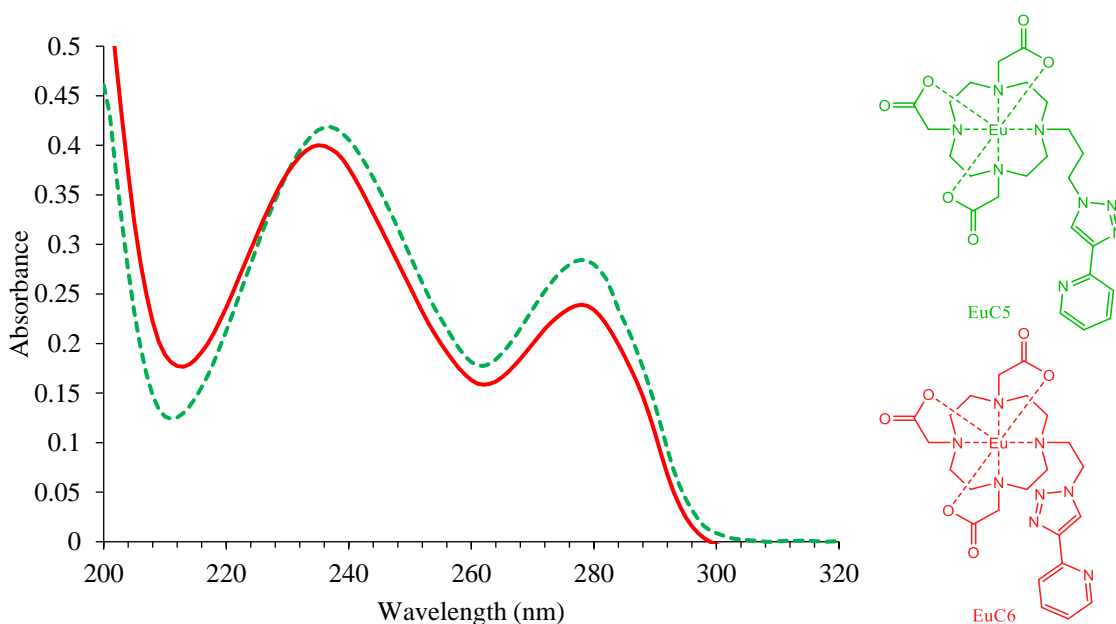


Figure 3.18: Absorption spectra of **EuC5** (dashed green line) and **EuC6** (solid red line) (in H₂O at 298K).

Through the longest absorption maximum (~ 278 nm), the luminescence properties of the two europium complexes (**EuC5** and **EuC6**) were investigated. The emission profiles of these complexes are presented at Fig. 3.19 and Fig. 3.20 respectively.

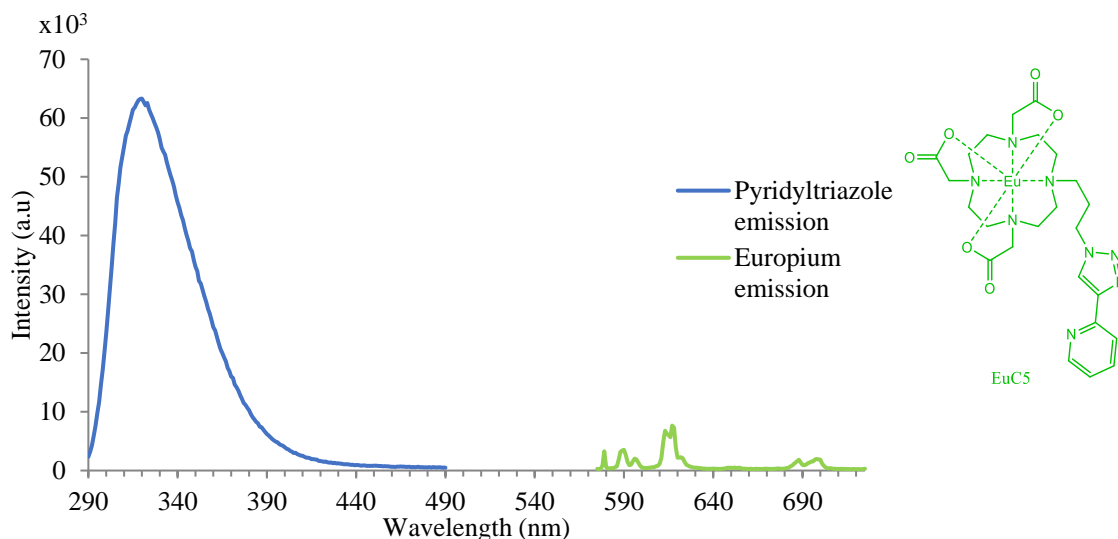


Figure 3.19: Emission profile of **EuC5** showing the pyridyltriazole emission (blue) and the europium emission (green) (excited at 278 nm in H₂O at 298K).

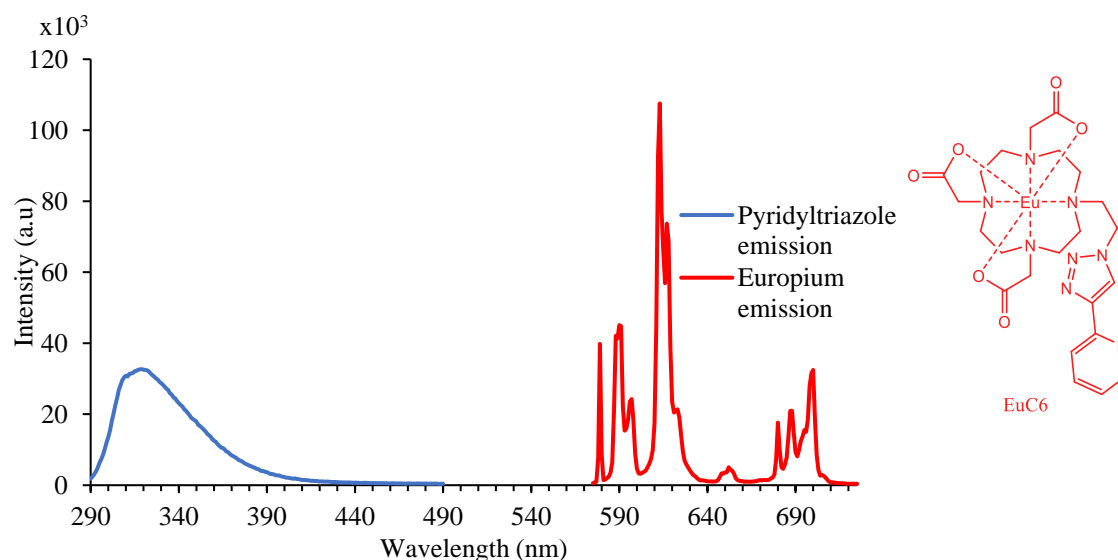


Figure 3.20: Emission profile of **EuC6** showing the pyridyltriazole emission (blue) and the europium emission (red) (excited at 278 nm in H₂O at 298K).

Compared to the previous compounds (**EuC2** and **EuC4**), the emission profiles of these complexes show some differences. Generally, they show two emission bands in two different region of the spectrum, which correspond to two different emission process of the molecule. The first emission spectrum is seen between 300 and 400 nm, corresponds to fluorescence from the pyridyltriazole moiety; the second is europium emission and is seen between 575 and 725 nm. There are two possible explanations to explain this change in behaviour. Firstly, in these two complexes, the antennae are believed to be situated more distant than in **EuC2** and **EuC4**. As a result, the energy transfer between the antenna and the lanthanide is less efficient in **LnC5** and **LnC6**. In

other words, the fluorescence rate constants of pyridyltriazole in **LnC5** and **LnC6**, are larger than the intersystem crossing/energy transfer rate constant from the pyridyltriazole to the europium centre. Thus, there are two types of emission observed from two different parts of the complex. Secondly, the coordination by a six- or seven-member ring (for **LnC5** and **LnC6** respectively) is assumed to produce a more labile coordination environment possibly resulting in an equilibrium between “opened” and “closed” structures.

The difference between these two complexes compared to the previous complexes (such as **EuC2** and **EuC4**) is in the number of carbon linkers between their antennae (pyridyltriazole) and the europium centre. **EuC6** is linked with two carbons increases the distance of the pyridyltriazole from europium. The presence of an extra carbon in **EuC5** pushes it even further away. These two complexes have a different ratio between the pyridyltriazole and the europium emission intensities. This is strongly believed to be a consequence of distance differences between antennae and their europium centres. It has been mentioned that energy transfer is a $1/r^6$ distance dependent process, thus the longer distance between the antenna (pyridyltriazole) and the lanthanide centre (europium), the less efficient in the energy transfer. This matches what appears in the **EuC5** and **EuC6** emission spectra. The europium emission of **EuC5** is less intense compared to that of **EuC6**, on the contrary, the pyridyltriazole emission in **EuC5** is more intense than in **EuC6**.

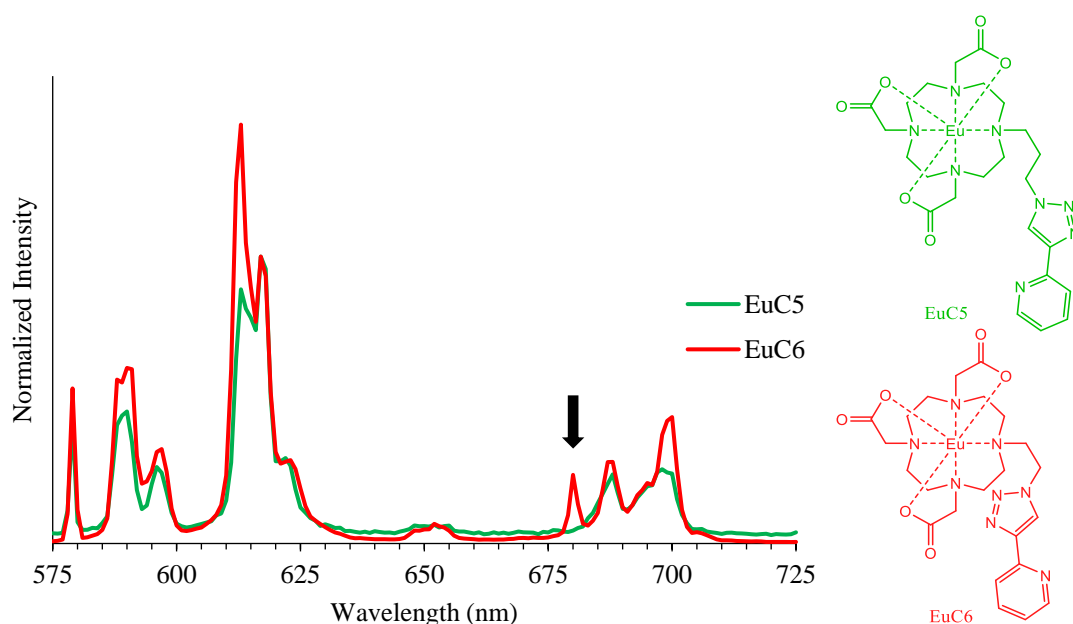


Figure 3.21: Europium emission profile of **EuC5** (green) and **EuC6** (red) (excited at 278 nm in H₂O at 298K).

EuC5 and **EuC6** present the same typical emission pattern of europium emission bands corresponding to 5D_0 to 7F_J ($\Delta J = 0, 1, 2, 3, 4$) transitions (Fig. 3.21). They share very similar emission profiles due to their structural similarities. The hydration number of **EuC5** and **EuC6** were then measured as shown in Table 3.4.

Table 3.4: The hydration number calculation of **EuC5** and **EuC6** (pH/pD 7).

Compound	$\lambda_{\text{excitation}}$ (nm)	k_{H_2O} (ms $^{-1}$)	k_{D_2O} (ms $^{-1}$)	q (± 0.2)
EuC5	278	2.58	0.61	2.1
EuC6	278	2.27	0.47	1.8

The number of inner-sphere water is relatively similar in **EuC5** and **EuC6** ($q = 2$). However, the decay rate constant of **EuC5** is slightly higher than **EuC6**, which possibly indicates the presence of equilibrium between $q = 2$ and $q = 1$ in **EuC6**. Overall, the attempts taken to keep the pyridyltriazole arm coordinated to the lanthanide centre by reducing the number of carbon linker (from three in **EuC5** to two in **EuC6**) however, only slightly affects its q number. The carbon-linker length reduction did not force the pyridyltriazole moiety to coordinate to the lanthanide centre.

Metal responsive examinations were not necessary for these two compounds due to their coordination motif. However, it is crucial to have more information about the photophysical changes as a response to the presence of free zinc(II) ions during the development of a zinc-responsive MRI contrast agent (*i.e.* for a comparison data). For this reason, the metal responsive examinations were still conducted. According to the zinc(II) binding studies performed on **EuC2** and **EuC4**, the presence of free zinc(II) ions did not show any changes to both absorption or emission (*i.e.* the ratio intensities between peaks). This is markedly different to that observed by the addition of zinc(II) to solutions of **EuC5** and **EuC6**. They showed some changes in their emission spectra as depicted at Fig. 3.22 and Fig. 3.23 for **EuC5** and **EuC6** respectively. In general, there was increased emission for the pyridyltriazole (290 – 430 nm) for both complexes during zinc(II) addition. The similar trend was also seen for the europium emission in **EuC5** bands, but not in the **EuC6**. The europium emission exhibited a decreasing trend during the addition of up to 185 equivalents zinc(II), before it started to increase gradually on further zinc(II) additions.

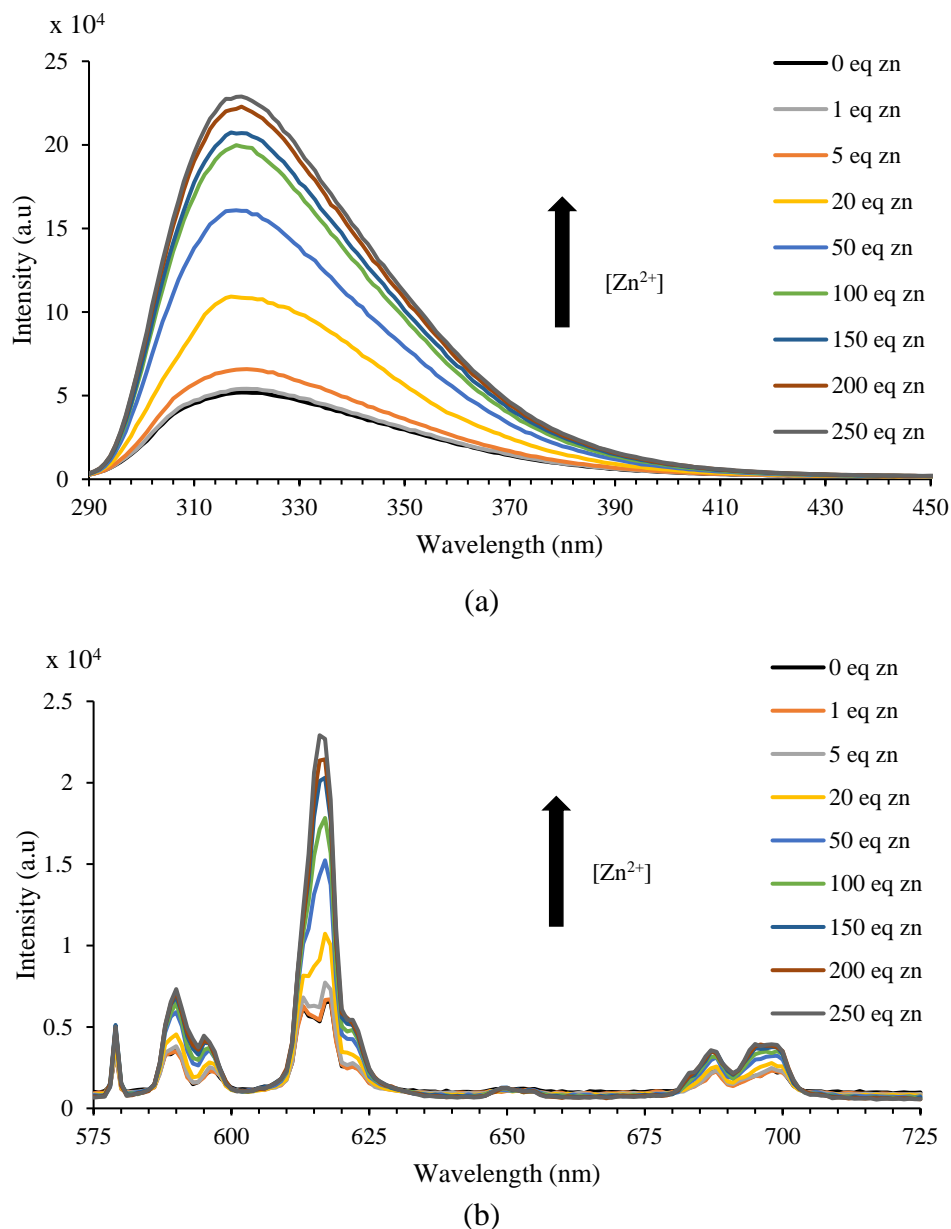


Figure 3.22: Emission profiles of **EuC5** in response to added zinc(II) in 50 mM HEPES buffer pH 7.4 and 0.1 M NaCl_(aq). a) Emission of the pyridyltriazole. b) Emission of europium(III).

The increasing fluorescence emission of the pyridyltriazole moieties in **EuC5** and **EuC6** was believed to be caused by the coordination binding of zinc(II) and pyridyltriazole. Such coordination induces the obstruction of photoinduced electron transfer deactivation processes in the pyridyltriazole moiety, thus increasing their emission intensity. This process is also believed to increase the energy transfer efficiency from the pyridyltriazole antenna to the europium centre, as in **EuC5**. This is also assumed to occur in **EuC6**. However, the presence of a partial coordination between pyridyltriazole and the europium centre, which was observed through its hydration number, provides slightly different behaviour.

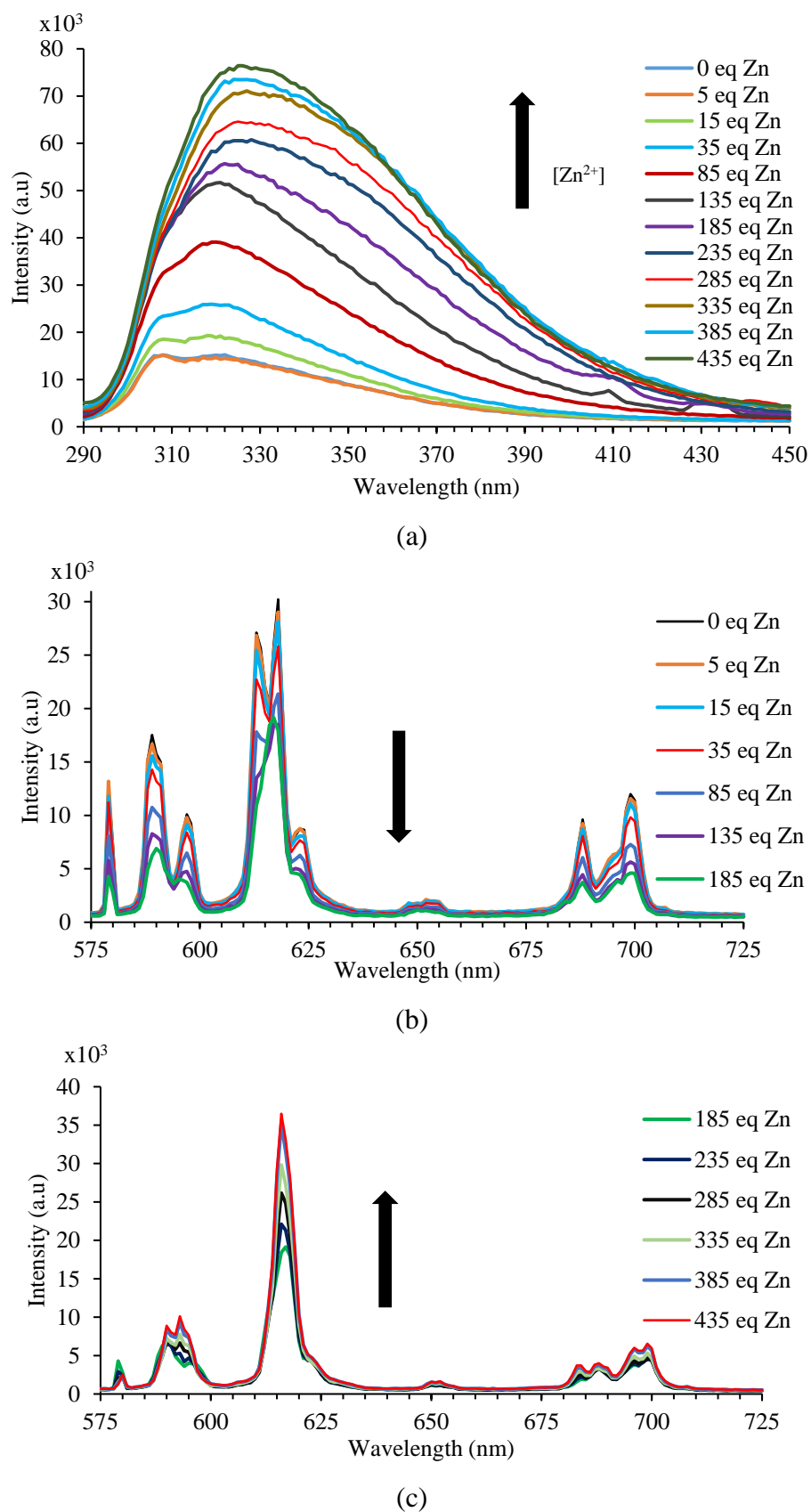


Figure 3.23: Emission profiles of **EuC6** in response to added zinc(II) in 50 mM HEPES buffer pH 7.4 and 0.1M NaCl_(aq). a) Emission of the pyridyltriazole. b-c) Emission of the europium(III).

The same zinc-responsive experiments were also conducted on the pyridyltriazole active arm (compound **17**) separately, which was intended to show the free pyridyltriazole emission intensities modulation during zinc(II) additions. As anticipated, the emission intensity of this compound increased gradually during zinc(II) additions as presented at Fig. 3.24. This emission enhancement was even higher compared to those in **EuC6**, with a relatively equal amount of added zinc(II). The lack of energy transfer between this antenna and the europium centre experienced in **EuC6** is believed to be responsible to this enhancement.

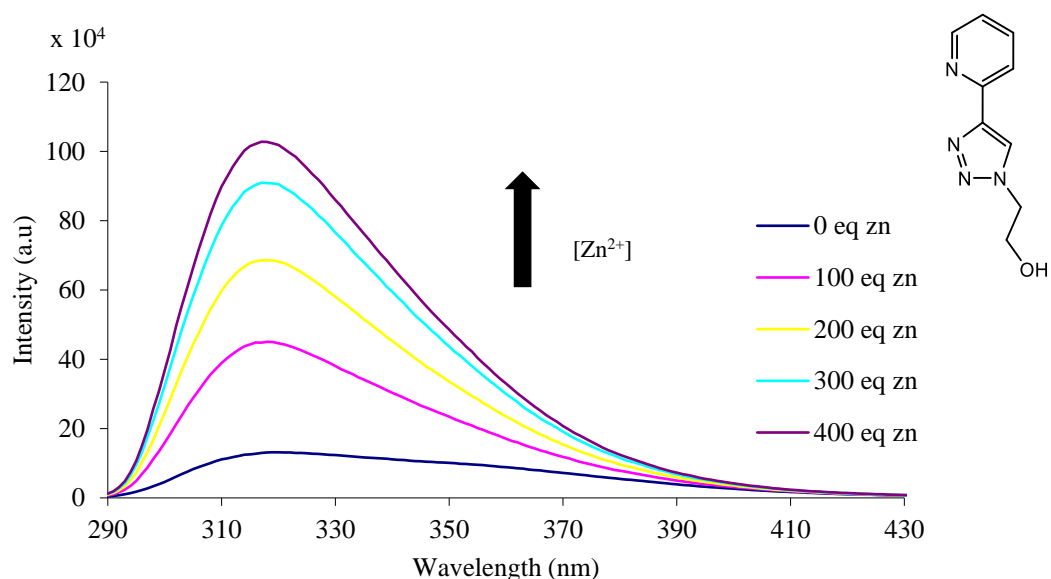


Figure 3.24: Emission profiles of the compound **17** during zinc(II) additions measured in 50 mM HEPES buffer pH 7.4 and 0.1M NaCl_(aq).

Until this point, there are more facts obtained about the photophysical properties of an “ideal” compound required as a zinc-responsive MRI contrast agent containing a pyridyltriazole active arm. Firstly, it should have no or very low ligand (pyridyltriazole) emission as a sign of coordination between this ligand and the europium centre to give switch-off effect. Secondly, it should change its ligand (pyridyltriazole) emission intensities, on coordination displacement between europium centre and zinc(II) ions has taken place.

Although they do not provide excellent properties, **LnC5** and **LnC6** succeed in providing an arm-opened form of the pyridyltriazole, leaving the europium coordination environment as presented in previous compounds (**LnC2** and **LnC4**) as illustrated at Fig. 3.25.

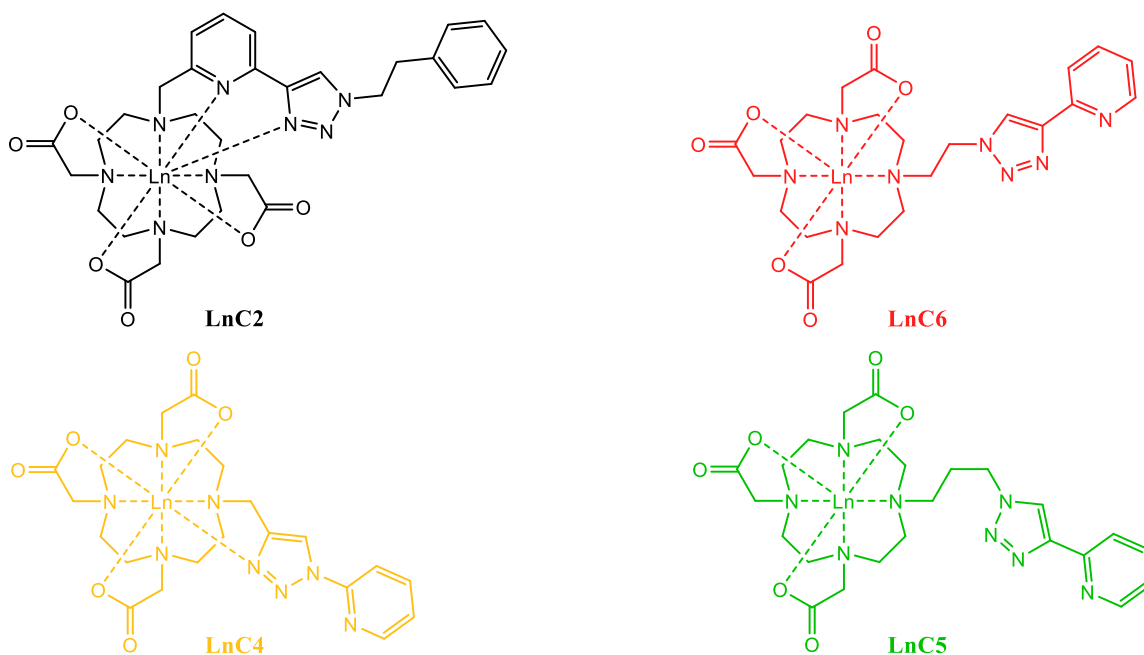


Figure 3.25: Formation of arm-closed (**LnC2** and **LnC4**) and arm-opened (**LnC5** and **LnC6**) structures by pyridyltriazole containing structures.

Clearly, further modification was required *i.e.* to the pyridine ring of **LnC5** and **LnC6**. Addition of a functional group containing certain donor atoms such as N, O or S, was hoped to transform the arm-opened to the arm-closed form. Some zinc(II) responsive compounds were discussed in the Chapter 1 which contained oxygen donors, which have tendency to coordinate to lanthanide centres. Therefore, hydroxyl and carboxylic acid groups attracted our attention as potential functional groups to be attached to the pyridine ring. The examination of these lanthanide complexes will be discussed in the following section.

3.6.4 Photophysical Properties of **LnC7** and **LnC8**

The introduction of new functional group members to the pyridyltriazole moiety were carried out by using different starting materials. The synthesis aspects are already explained in Section 2.3.3. **LnC7** was chosen due to the availability of its starting material ((3-bromophenyl)methanol) and by considering the synthetic procedure, in which this starting material is much easier to handle during the entire synthetic steps. The most efficient synthetic pathway devised for **LnC7** was then applied to the synthesis of **LnC8**, which was considered to be a more difficult synthetic process.

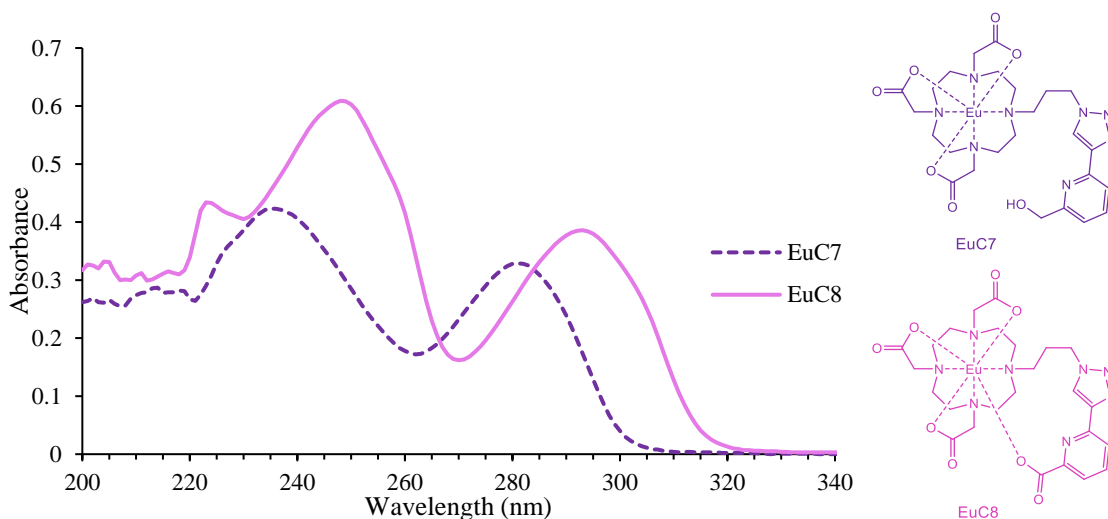


Figure 3.26: Absorption spectra of **EuC7** (purple dashed line) and **EuC8** (pink solid line) (in H₂O, 298K).

The absorption spectra (Fig. 3.26) of these two modified complexes (**EuC7** and **EuC8**) have similar patterns to their original complexes (**LnC5** or **LnC6**). They consist of two absorption maxima at 235; 281 nm and 247; 292 nm for **EuC7** and **EuC8** respectively. The absorption intensities of the shorter wavelengths (at 235 and 247 nm) for both complexes are higher than those at longer wavelengths (at 281 and 292 nm). However, the absorption maxima of **EuC8** are situated at a longer wavelength compared to those in **EuC7**. The presence of a carboxylic acid functional group in **EuC8** is responsible for this shifting. This functional group is believed to be involved in lengthening the electron delocalization on its pyridyltriazole moiety, thus lowering the energy.

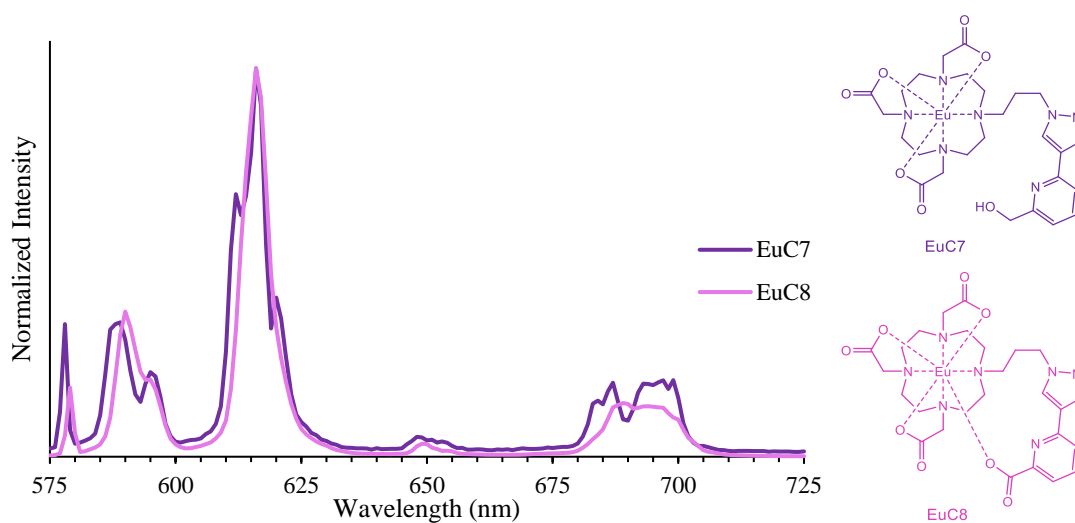


Figure 3.27: Europium emission profiles of **EuC7** (at 281 nm) and **EuC8** (at 292 nm) (in H₂O, 298K).

The emission spectra were recorded by exciting it at its absorption maxima at 281 and 292 nm for **EuC7** and **EuC8** respectively. Their emissions show characteristic bands for the europium emission, corresponding to its emissive transition between 5D_0 to 7F_J ($\Delta J = 0, 1, 2, 3, 4$) as presented in Fig. 3.27. The overall emission profile of **EuC7** has the same characteristics with **EuC5** and **EuC6**. They showed intense emission from the pyridyltriazole moiety (at 300-450 nm), while **EuC8** has emission profile similarities with the earlier model of complexes **EuC2** and **EuC4**, which do not exhibit pyridyltriazole emission, but only from europium (575-725 nm). These results will be discussed consecutively.

Compared to its pyridyltriazole emission intensity, the europium emission of **EuC7** has a lower emission intensity. This profile is indicative of the distance between the pyridyltriazole active arm and the europium centre, which lowers the energy transfer efficiency (as previously explained to compounds **EuC5** and **EuC6** in section 3.6.3). The full emission spectrum of **EuC7** is presented in Fig. 3.28.

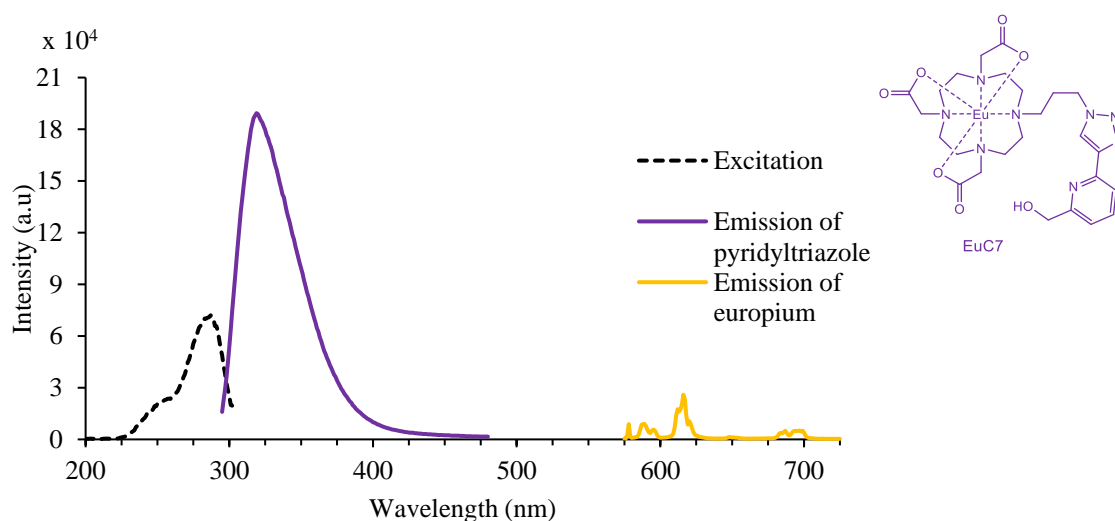
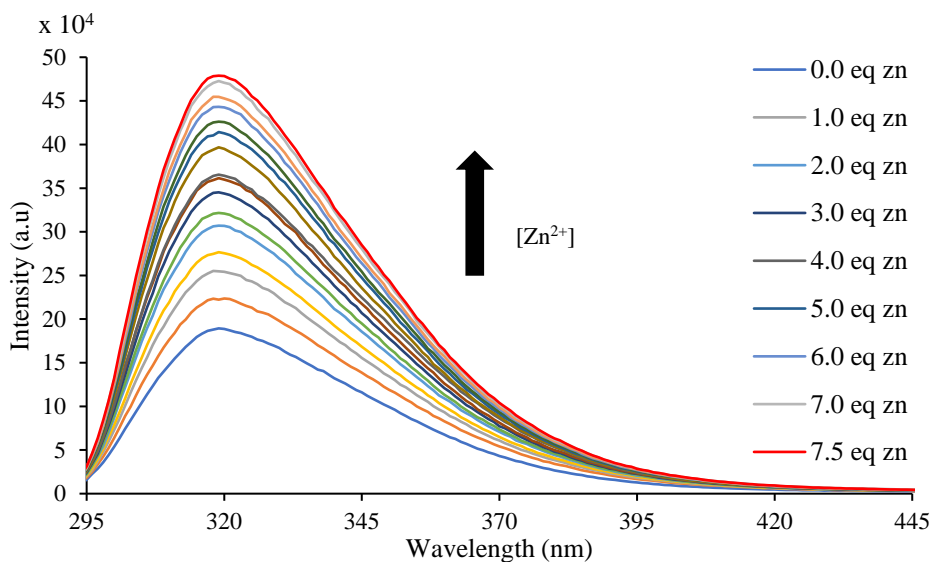


Figure 3.28: The emission profile of **EuC7** (in H_2O , 298 K) showing the excitation (at 616 nm) (black dashed), pyridyltriazole emission (at 281 nm) (purple solid) and europium emission (at 281 nm) (yellow solid) spectra.

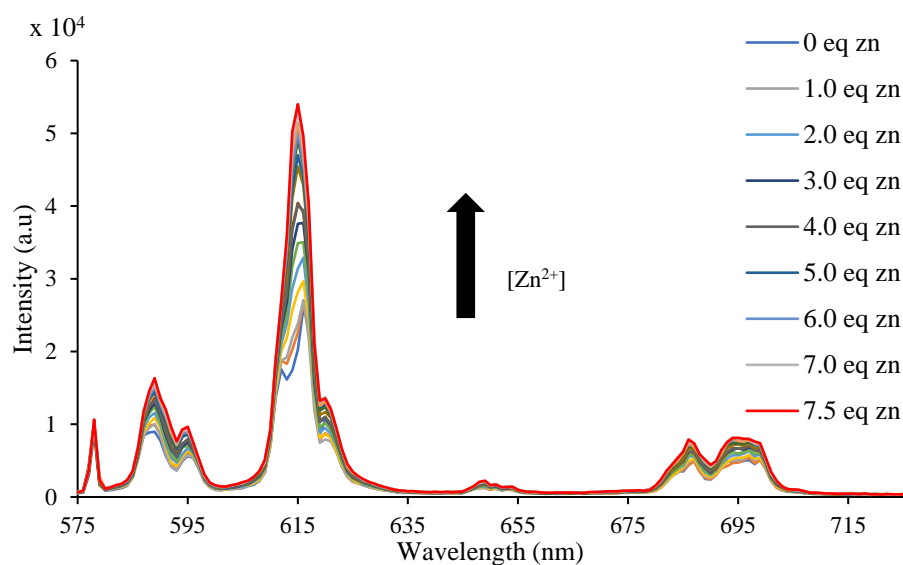
EuC7 exhibits a gloomy red emission (has a low europium emission), suggested the occurrence of an open structure as experienced in **LnC5** and **LnC6**. It was supported by its hydration number measurement, which was indicating the possession of two inner-sphere water molecules ($q = 2$) on its coordination environments as summarized at Table 3.5. This suggests little or no interactions with the hydroxyl group on the pyridyl unit.

Table 3.5: The hydration number calculation of **EuC7** and **EuC8**.

Compound	$\lambda_{\text{excitation}}$ (nm)	k_{H_2O} (ms ⁻¹)	k_{D_2O} (ms ⁻¹)	q (± 0.2)
EuC7	281	2.55	0.61	2.0
EuC8	292	1.54	0.63	0.8



(a)



(b)

Figure 3.29: Emission profiles of **EuC7** in response to added zinc(II) in 50 mM HEPES buffer pH 7.4 and 0.1M NaCl_(aq). a) Emission of the pyridyltriazole. b) Emission of the europium(III).

Although its opened-form structure is suggested by the hydration number calculation, the zinc(II) responsive examination was still performed to see how **EuC7** interacts with added zinc(II) ions (Fig. 3.29). The emission profiles of **EuC7** for both

pyridyltriazole active arm and the europium centre changed during zinc(II) addition. The emission intensity of the pyridyltriazole increased proportionally upon zinc(II) additions. There were 17%, 35%, 46% and 62% fluorescence emission enhancements experienced by the chromophore upon addition 0.5, 1.0, 1.5 and 2 equivalents of zinc(II) respectively. Further addition of zinc(II) increased the emission even further. Similarly, its europium emission bands experienced moderate enhancements (especially in the $\Delta J = 2$ band).

The coordination tendency of the pyridyltriazole active arm toward the lanthanide centre was expected to increase in **LnC8**. A carboxylate group, a negatively-charged ligand, has the potential to coordinate to europium(III). Since the lanthanide ions contain shielded *f-f* orbitals, making them interact mainly through ionic charge interactions, it was hoped that the ionized carboxylate would have tendency to coordinate to the lanthanide centre.

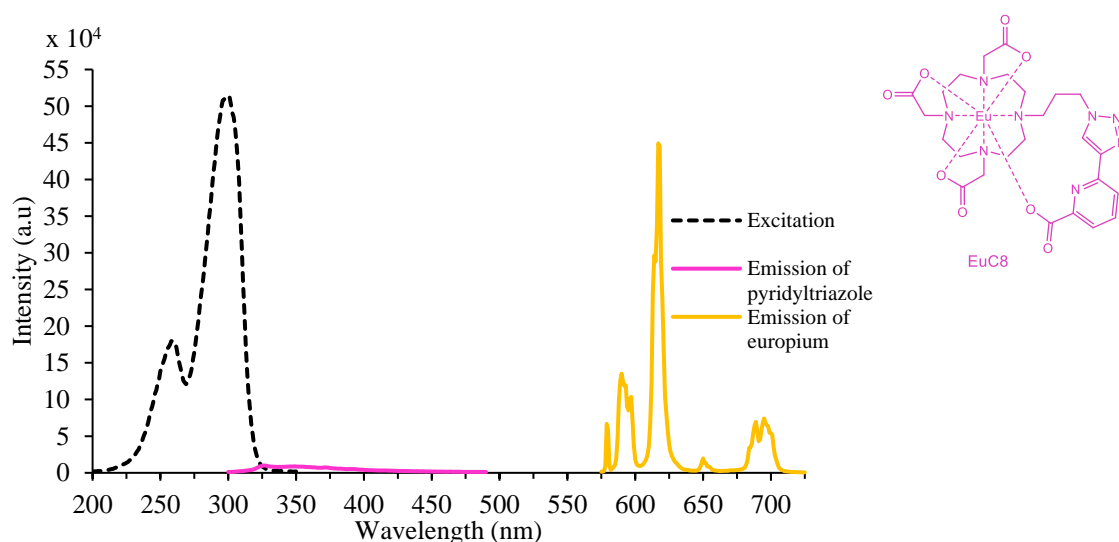


Figure 3.30: The emission profile of **EuC8** (in H₂O, pH 7.4, 298 K) showing the excitation (at 617 nm) (black dashed), pyridyltriazole emission (at 292 nm) (pink solid) and europium emission (at 292 nm) (yellow solid) spectra.

As mentioned previously, the essential point derived from the emission profile of **EuC8**, is the lack of fluorescence from the pyridyltriazole active arm. This was a primary indication of the occurrence of coordination between this active arm and the europium centre. This result was in line with its hydration number calculation result, which was showed that **EuC8** has one water as presented in Table 3.5. The coordination between the pyridyltriazole and its europium centre is expected to occur *via* the carboxylate's oxygen as in some reported compounds (explained in Section 2.1.4). Unfortunately, attempts to grow a crystal of **LnC8** complex failed.

EuC8 was examined for zinc-response in 50 mM HEPES buffer at pH 7.4 over 0.1 M NaCl ionic strength. The addition of zinc(II) to the solution of **EuC8** changed its emission profile for both the pyridyltriazole and the europium centre simultaneously; however, crucially with different trends. There was an increase in the pyridyltriazole emission band in response to zinc(II). This showed the presence of a coordination between pyridyltriazole active arm and zinc(II) ion. In contrast, the europium emission intensity decreased gradually upon zinc(II) additions. The **EuC8** emission profiles for both pyridyltriazole and europium emissions during zinc(II) addition is shown in Fig. 3.31.

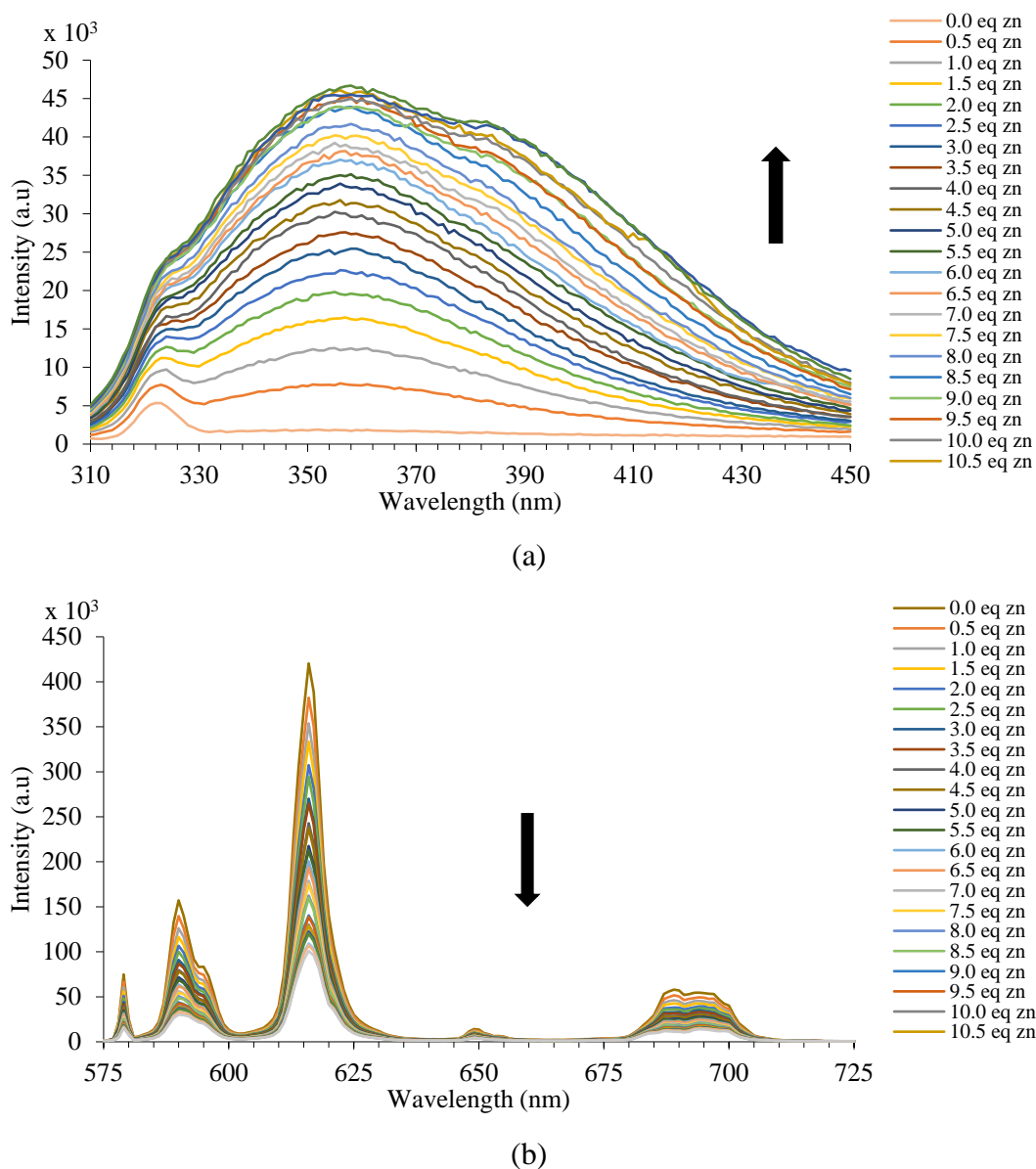


Figure 3.31: Emission spectra of **EuC8** in response to added zinc(II) in 50 mM HEPES buffer pH 7.4 and 0.1M NaCl_(aq). a) Emission of the pyridyltriazole. b) Emission of the europium(III).

The enhancement of pyridyltriazole emission can be understood by the coordination displacement occurrence from the europium central ion toward zinc(II). The complexation between pyridyltriazole and zinc(II) ion leads to the formation of an opened-structure, in which the pyridyltriazole active arm is removed from the lanthanide coordination sphere. This induces europium emission quenching owing to two factors: the change in distance between the pyridyltriazole antenna and the europium centre; and the increase in coordinated water to the empty coordination site, left by the active arm. To the gadolinium(III) complex analogue, the increasing of q value would increase its relaxivity. Hydration number monitoring during zinc(II) addition was conducted to prove this hypothesis. Indeed, there were some changes in hydration number identified upon zinc(II) addition as presented in Table 3.6.

Table 3.6: The hydration number modulation of **EuC8** as a response to added zinc(II).

Zn(II) equivalent	k_{H_2O} (ms ⁻¹)	k_{D_2O} (ms ⁻¹)	q (+0.2)
0.0	1.54	0.63	0.8
0.5	1.89	0.58	1.3
1.0	2.03	0.59	1.4
1.5	2.12	0.55	1.5
2.0	2.17	0.56	1.6
2.5	2.20	0.59	1.6

This result showed that coordination displacements of the pyridyltriazole from the europium centre in the presence of zinc(II) do occur. The hydration number increased twofold from its initial value after the addition of 2 equivalents of zinc(II), meanwhile further additions maintained its hydration number at 1.6. This result suggested the potential of this complex to be further examined as a zinc-responsive MRI contrast agent on substituting europium(III) for gadolinium(III).

The promising results of the europium complex (**EuC8**) exhibited by its photophysical properties and zinc-responsive examinations led to the further investigations with its corresponding gadolinium complex (**GdC8**). Thus, the same experiments were applied to this main target compound. Different from **EuC8**, the emission profile of **GdC8** only contains emission from the pyridyltriazole with no Gd emission as expected. The emission and the excitation profiles of **GdC8** are presented in Fig. 3.32.

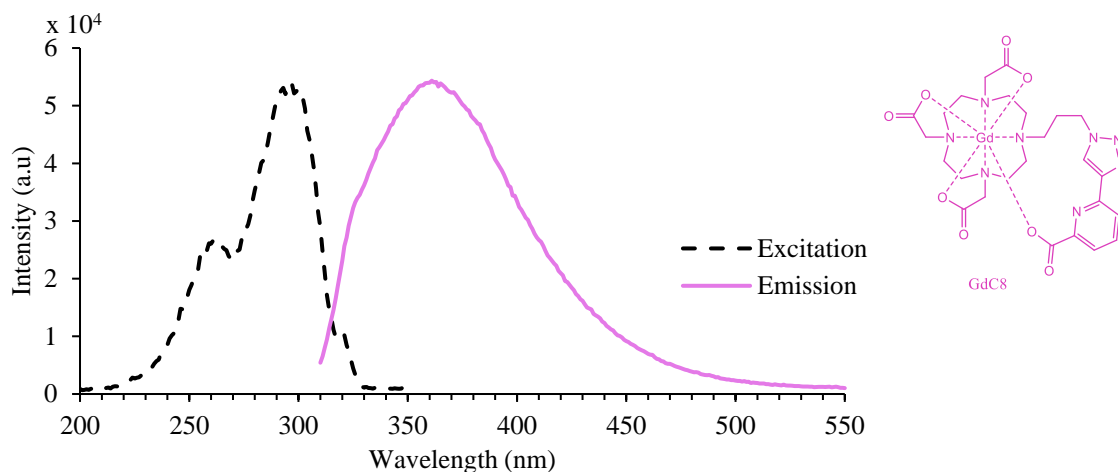


Figure 3.32: Excitation (black dashed) and emission (purple solid) spectra of **GdC8** in 50 mM HEPES Buffer pH 7.4 0.1 M NaCl_(aq).

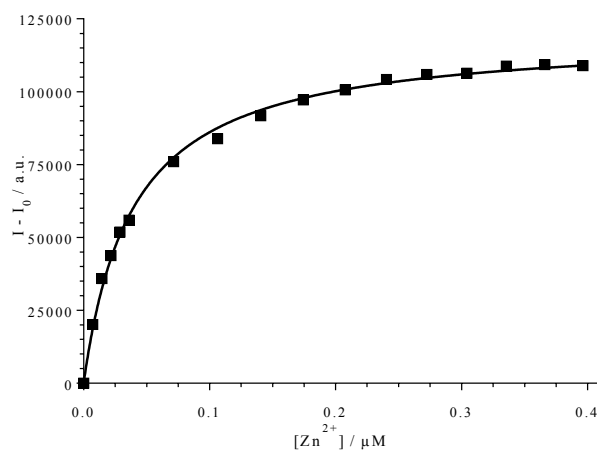
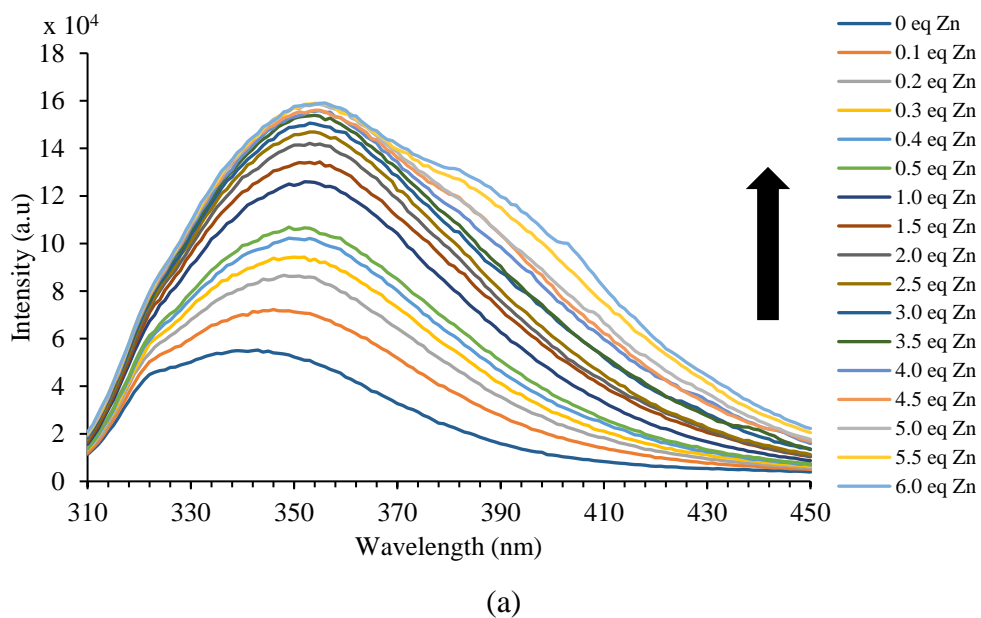


Figure 3.33: a) Emission profile of **GdC8** in response to zinc(II) addition. b) Fitting of 1:1 binding model of **GdC8** (72.7 μM, 50mM HEPES buffer pH 7.4, 0.1 M NaCl_(aq), monitored at 354 nm).

GdC8 has a broad emission ranging from 310 to 450 nm with a maximum at 361 nm when excited at 292 nm. The additional of zinc(II) to **GdC8** solution increased its emission accordingly as expected (Fig. 3.33 (a)). This titration experiment was conducted in 50 mM HEPES buffer pH 7.4 over a constant ionic strength (NaCl 0.1 M). The emission intensity increased 128% during the addition of 1 equivalent zinc(II) ion then increased even further by 188% at 6 equivalent zinc(II) ion. The binding constant calculation of **GdC8** (illustrated at Fig. 3.33 (b)) exhibited that zinc(II) is tightly bound in physiological concentration with a $K_d = 39.0 \pm 3.1 \mu\text{M}$.

Following this zinc-responsive experiment, this probe was also tested with some other biologically relevant transition metals such as calcium(II), iron(II) and copper(II). There was little response experienced by **GdC8**, in which the emission intensity revealed no significant changes in the presence of calcium(II) and iron(II); however, copper(II) showed a significant change. The emission of **GdC8** was diminished significantly by copper(II) as illustrated at Fig. 3.34.

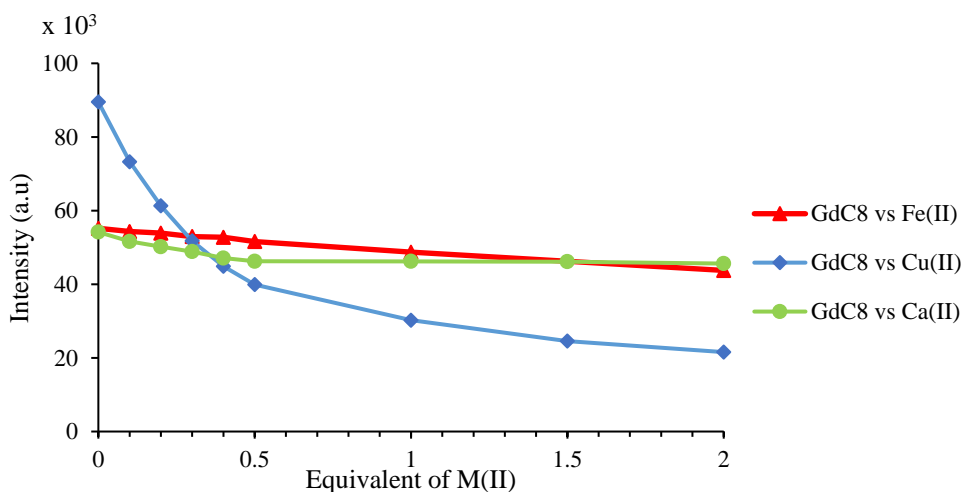


Figure 3.34: The **GdC8** emission intensity in response to some divalent transition metal ions (50 mM HEPES buffer pH 7.4, 0.1 M NaCl_(aq)), monitored at 341 nm).

The zinc(II) selectivity presented by **GdC8**, lead it to the examination as a zinc-responsive MRI contrast agent. Relaxation measurements on **GdC8** (0.072 mM) were conducted by using a 9.4T NMR probe at 400 MHz at 298K in 50 mM HEPES buffer pH 7.4 over a constant ionic strength (NaCl 0.1 M). The exact concentration of **GdC8** was measured by Evans method.¹⁷¹ Its relaxation time was then measured and calculated from 16 points generated *via* a standard inversion-recovery procedure. An unexpected relaxivity value was gained for **GdC8**. It is higher than commonly observed for $q = 1$ DOTA-based compounds. **GdC8** has relaxivity value of $6.5 \text{ mM}^{-1}\text{s}^{-1}$ in the absence of

free divalent metal ions, 54% higher than the common GdDOTA $r_1 = \sim 4.2 \text{ mM}^{-1} \text{ s}^{-1}$. The unusual relaxivity value is believed caused by ordered second-sphere water molecules around the pyridyltriazole pendant arm. Another possibility is the occurrence of dimerization of **GdC8** especially at higher concentration ($\sim 1 \text{ mM}$), which can reduce its molecular tumbling to give higher relaxivity values. Although at 400 MHz the τ_R effect is usually not significant. On addition of zinc(II) ions, its relaxivity increased to $8.4 \text{ mM}^{-1} \text{ s}^{-1}$ (29%) and $8.6 \text{ mM}^{-1} \text{ s}^{-1}$ (31%) in response to 0.5 and 1.0 equivalents of zinc(II) respectively. As expected, the relaxivity remained unchanged in the presence of calcium(II), iron(II) or iron(III) ions as presented at Table 3.7.

Table 3.7: The relaxivity values ($\text{mM}^{-1}\text{s}^{-1}$) of **GdC8** in response to several divalent metal ions.

Condition	Relaxivity (r_1) values of 0.7 mM Gd.13 on M(II)	
	0.5 equivalent	1.0 equivalent
Metal-free	6.5	
Zn ²⁺	8.4	8.6
Ca ²⁺	6.4	6.4
Fe ²⁺	6.3	n/a
Fe ³⁺	6.2	5.5
Cu ²⁺	8.4	8.3

Its excellent selectivity identified from previous experiment was substantially proved by these relaxivity values. In addition, this probe showed a considerable response to a copper(II) (28% relaxivity enhancement). Although, there was almost similar relaxivity value observed in response with copper(II), it is believed that this zinc-responsive probe would not be interfered significantly by copper(II). This is because its physiological concentration of “free” copper(II) is much lower than the concentration of zinc(II) inside the body (2 – 4 g and 250 mg for zinc(II) and copper(II) respectively),^{172,99,173} as well as in the zinc(II)-rich organs such as pancreas, prostate and amyloid plaques (several mM and μM for zinc(II) and copper(II) respectively).^{173,134,172,173}

There was a relatively constant relaxivity value observed during zinc(II) additions from 0.5 to 1.0 equivalents. Electrospray ionization (ESI) method in mass spectrometry analysis of **GdC8-Zn(II)** failed to obtain evidence about the existence of this species.

However, the complexation between a **LnC8**'s free arm and zinc(II) was observed by mass spectrometry analysis. It showed a peak at m/z 581 for $[\text{ZnL}_2+\text{Na}]^+$.

3.6.5 Photophysical Properties of **LnC9** and **LnC10**

Further modification of **LnC8** as a zinc-responsive MRI contrast agent was conducted by making changes to the linker. As explained in Chapter 2, the first modification was to elongate the pyridyltriazole linker. To do this, instead of using a hydrocarbon linker, a polyethylene glycol compound was chosen in regard to maintain the polarity of the entire complex. Polyethylene glycol is expected to maintain the water solubility of the complex at an appropriate concentration.

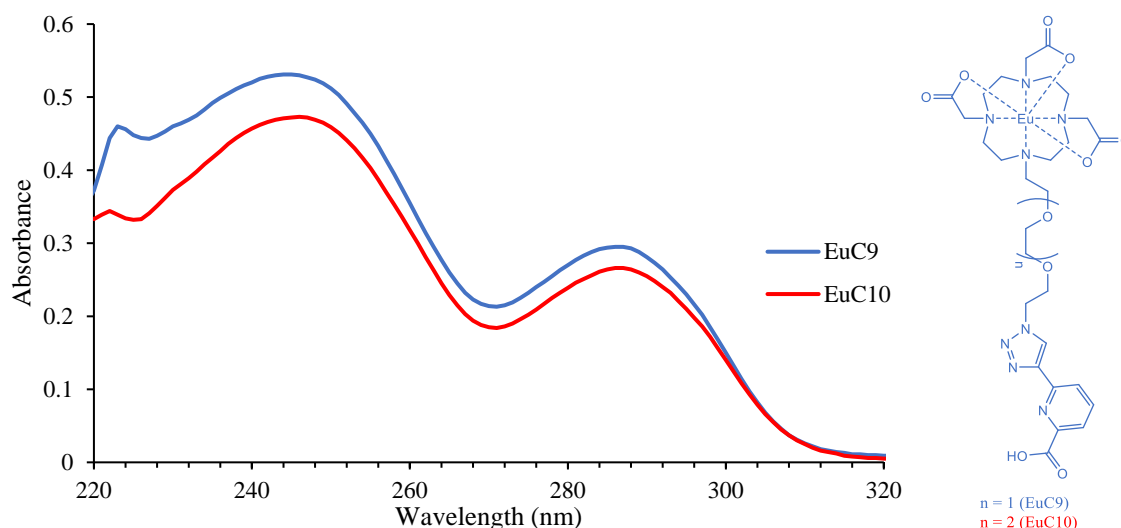


Figure 3.35: Absorption spectra of **EuC9** and **EuC10** in 50 mM HEPES Buffer pH 7.4 0.1 M $\text{NaCl}_{(\text{aq})}$.

The absorption spectra of **LnC9** and **LnC10** have a similar profile cf. the parent compound **LnC8**. It consists of two absorption maxima in which the first absorption band at ~ 245 nm has a higher intensity compared to the second absorption band at 288 nm. As expected, interaction of a polyethylene glycol linker does not significantly affect to its absorption maxima. This is because the main pyridyltriazole chromophore does not change. The absorption profile for **EuC9** and **EuC10** is presented in Fig. 3.35. The emission spectra of these two complexes were recorded by exciting it at their absorption maxima (288 nm). These complexes again exhibited the typical europium emission bands. They also exhibit a weak pyridyltriazole emission band, which would indicate that these two complexes have a similar coordination pattern to the parent complex (**EuC8**). The emission profile of **EuC10** is presented in Fig. 3.36.

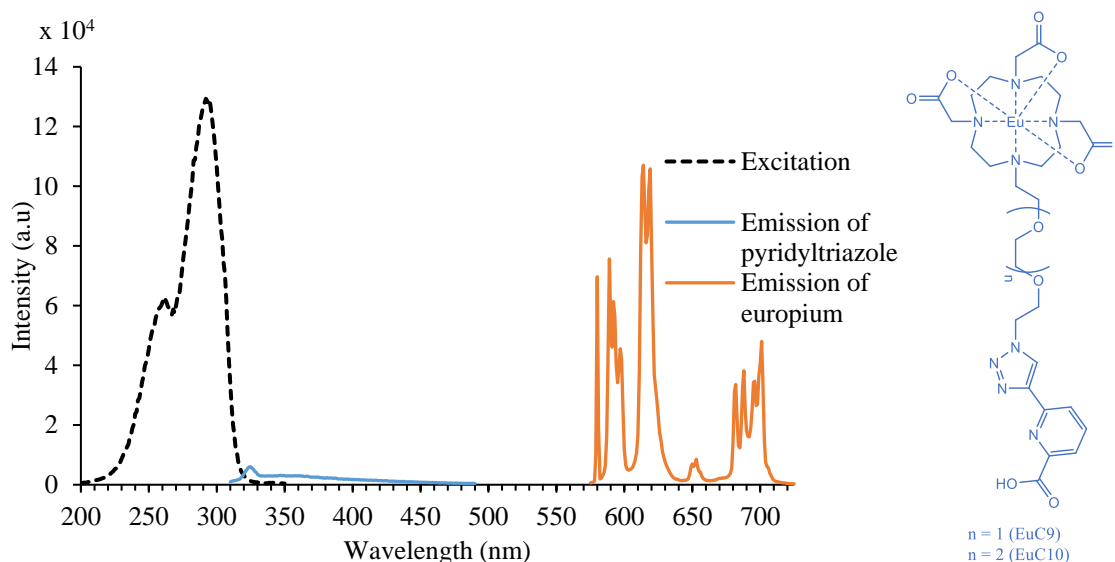


Figure 3.36: Excitation (617 nm) and emission (288 nm) profiles of **EuC10** (in H₂O, 298 K).

Due to the structural similarities of **LnC9** and **LnC10**, a zinc-responsive examination was only conducted to **EuC10** with a similar procedure to the previous complexes. Different to their parent compound **LnC8**, these complexes (**LnC9** and **LnC10**) showed similar emission trends to both pyridyltriazole (310-450 nm) and europium (575-725 nm) parts. As a response to added zinc(II) ions, the emission intensity of these two components increased simultaneously although with a different magnitude. The pyridyltriazole emission intensity increased significantly during the additional of zinc(II) (it increased by 2274% and 2706% during the addition of 0.7 and 1.0 equivalents of zinc(II) respectively). While, there were relatively small enhancements (it increased by 33% and 53% after additional 0.7 and 1.0 equivalents of zinc(II)) experienced to the europium emission as a response to added zinc(II) ions. The emission profile of **EuC10** during zinc(II) additions is presented at Fig. 3.37.

In general, the emission behaviour of this complex is similar to **EuC7** in response to added zinc(II). Both of pyridyltriazole and the europium emissions show an increase in response to zinc(II). Therefore, similar explanations were also applied to this complex. The hydration number examinations during zinc(II) additions were expected to provide valuable information about its coordination pattern. Thus, the same experiments were conducted to monitor the number of inner-sphere water during zinc(II) addition as summarized in the Table 3.8.

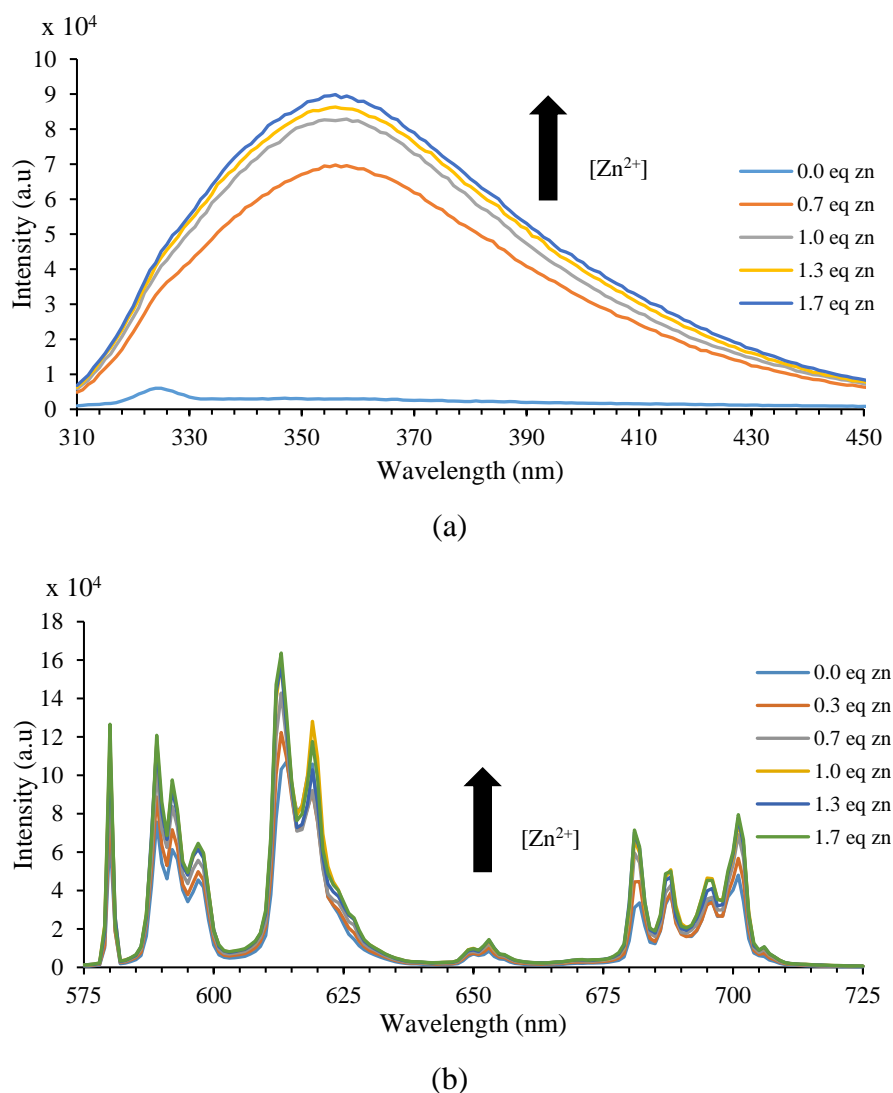


Figure 3.37: Emission spectra of **EuC10** in response to added zinc(II) in 50 mM HEPES buffer pH 7.4 and 0.1M NaCl_(aq). a) Emission of the pyridyltriazole. b) Emission of the europium(III).

Table 3.8: The hydration number calculation of **EuC10** during zinc(II) addition.

Zn(II) equivalent	$k_{H_2O}(\text{ms}^{-1})$	$k_{D_2O}(\text{ms}^{-1})$	$q (+0.20)$
0.0	1.32	0.53	0.65
0.25	1.33	0.55	0.63
0.5	1.39	0.64	0.59
0.75	1.39	0.60	0.64
1.0	1.41	0.66	0.60

It is clear that the hydration numbers remained unchanged during zinc(II) addition. The **EuC10** hydration number in the absence of zinc(II) was even lower compared to its parent **EuC8**. This indicated the presence of another binding site in the active arm. By considering the fact that there was an emission enhancement to the pyridyltriazole part

which was indicative of zinc(II) coordination, it is proposed that the possibility of the **LnC10** binding motif after zinc(II) additional as illustrated in Fig. 3.38.

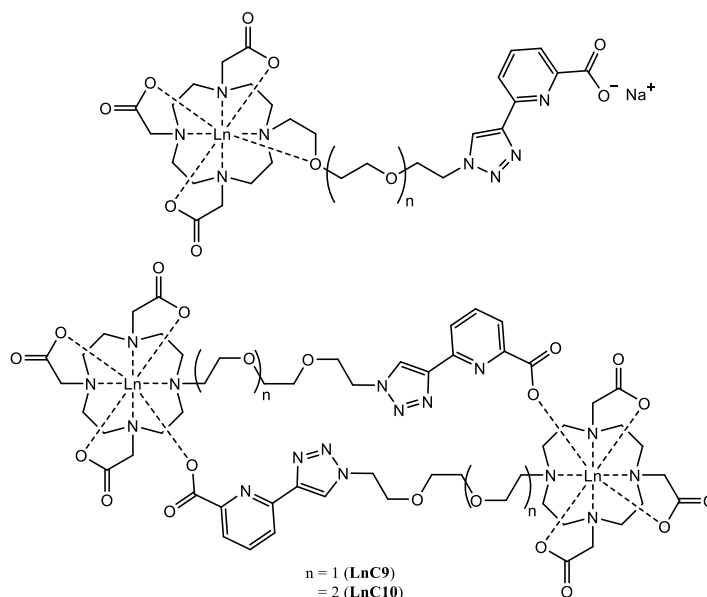


Figure 3.38: Proposed coordination motifs of **LnC9** and **LnC10**.

The relaxivity measurement of **GdC10** was conducted for further examinations. These relaxivity experiments used a similar procedure applied to their parent complex (**LnC8**). The relaxivity measurement results of **GdC10** are summarised in Table 3.9.

Table 3.9: The relaxivity values of **GdC10** in response to zinc(II) ion (400 MHz, 298 K).

Equivalent of zinc(II)	Relaxivity (r_1) values ($\text{mM}^{-1}\text{s}^{-1}$)
0.00	4.48
0.32	5.89
0.64	6.21
0.97	6.12

The relaxivity value of **GdC10** in the absence of divalent metal ion is lower than its parent complex (**GdC8**). This number is proportional to its hydration number calculated previously. The addition of zinc(II) ion increased its relaxivity, which is possibly due to the lowering molecular tumbling effect by increasing its mass during zinc(II) complexation, although it could be a result of introducing structured waters in the vicinity of the coordinated zinc(II). These would be in fairly close proximity to the gadolinium(III) and could be acting as a pool of second sphere waters.

3.6 Summary and Conclusion

The properties of a zinc-responsive MRI contrast agent designed by exploiting pyridyltriazole moiety as an active arm have successfully studied by its corresponding

europium analogues. The first model complex **LnC2**, behaved as a $q = 0$ complex which is considered as a poor MRI contrast agent. However, this model complex has an inert response toward zinc(II) ions. The presence of a five-membered chelate is believed to be responsible for its stability. Exchanging the position between pyridine and triazole rings as in **LnC4**, changed its coordination environment, allowing a water molecule to enter its coordination site; however, the triazole ring also produces a similar strong coordination pattern, which prevents its interaction with zinc(II) ions.

An attempt was made to increase the pyridyltriazole activity toward zinc(II) ions by preventing the formation of five-membered ring coordination through formation of **LnC5** and **LnC6**. The photophysical studies to their corresponding europium complexes succeed in producing an “opened-structure” allowing more water molecules in their coordination environments ($q = 2$). It also observed that, the energy transfer process between antenna and the europium centre is indeed distance dependent as observed in **EuC5** and **EuC6** emission intensities. The presence of direct coordination binding by the antenna to the europium centre, increased the energy transfer efficiency, evidenced by their high europium emission intensities (**EuC2** and **EuC4**).

The addition of a hydroxyl functional group to the pyridine ring as in **LnC7**, did not increase the coordination tendency of this pyridyltriazole moiety toward the lanthanide centre. This was observed from its weak europium emission intensities and the hydration number measurements ($q = 2$). The carboxylic acid group (as in **LnC8**) on the other hand, succeed in attracting the pyridyltriazole into the lanthanide coordination sphere which was observed by its high europium emission intensities and the hydration number calculation ($q = 1$). **EuC8** changed its emission intensity and its hydration number in response to zinc(II). The relaxation time measurement showed that **GdC8** has a high relaxivity value, which increased during zinc(II) addition. It also exhibited a good selectivity toward zinc(II) over some other biological transition metals. Further structure modification (as in **LnC9** and **LnC10**) by substituting the pyridyltriazole’s linker with a polyethylene glycol changed significantly its characteristics. Their coordination environments changed, evidenced by their lower hydration number and different response to zinc(II), which is believed to be due to the presence of a different binding motif.

Chapter 4

Highly Emissive Lanthanide Complexes in Molecular Labelling

4.1 Introduction

Lanthanide complexes have a wide range of applications from catalysts,^{174,175} lasers,^{176,177,178} molecular thermometers,^{179,180,181,182} fingerprint detection¹⁸³ and also imaging probes.^{58,62,184,8,185,186} They are developed from simple molecules into some of the most complicated structures to be used in the sophisticated instrumentation required for various purposes. One of their main applications is as optical imaging agents or luminescence probes, which are crucial elements in modern clinical applications.⁷ As luminescence probes, lanthanide complexes have a number of advantages, over organic compounds or transition metal complexes previously developed for clinical applications. As mentioned in Chapter 1, lanthanides offer high photostabilities, large Stokes shifts and long lifetimes. Their excellent photostabilities towards irradiation during subject investigation or imaging processes make these probes resistant to photobleaching. This allows repeated measurements with good reproducibility. Their substantially large Stokes shifts make it easy to differentiate lanthanide emission from any other emission such as from organic compounds or light scattering.¹⁸⁷ In addition, their non-overlapping emission bands prevents self-absorption. Some lanthanides have very long emission lifetimes (*e.g.*, Eu and Tb emissions is in the order of milliseconds),⁵⁸ which can be exploited to reduce noise or background signals from any unwanted organic chromophores.^{58,187}

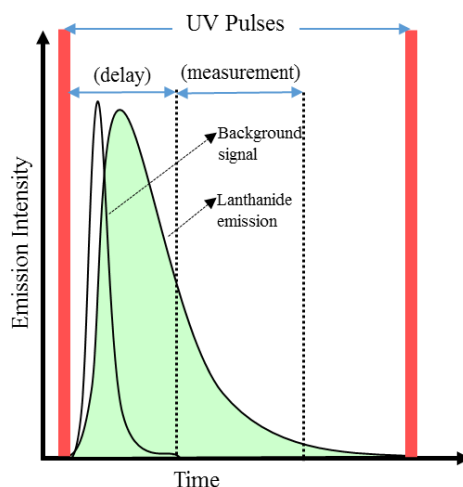


Figure 4.1: Time-gated luminescence spectrophotometry measurement.

The use of time-gated fluorescence techniques can remove any short-lived fluorescence background (ps to μ s)¹⁸⁸ from reagents and cells including the majority of organic molecules to give a good signal to noise ratio (S/N). The long-lived lanthanide emission can be selectively measured by applying a sufficient delay time between excitation and emission measurement, as illustrated in Fig. 4.1.¹⁸⁷ The final important properties of lanthanides are emission patterns which are unique to each lanthanide, as discussed in the previous chapters.

Besides their excellent properties, lanthanides also present certain difficulties. Lanthanides have very weak extinction coefficients due to their forbidden *f-f* transitions, thus they need intense radiation to excite them. The best way to populate the excited states of lanthanides, as discussed in Chapter 2, is by exploiting the energy transfer mechanisms facilitated by antennae. Another drawback is the toxicity of free lanthanide ions; their size is similar to certain biological transition metals such as calcium, which can cause problems with metabolic or signalling processes.²¹ This can be reduced by use of a suitable chelating agent such as a macrocyclic ligand, which provides good thermodynamic and kinetic stability. However, the success in designing such an emissive probe should be supported by factors such as energy transfer distance (between the antenna and the lanthanide) or the presence of a non-radiative quencher (H_2O , *etc.*). In this chapter, a number of terbium complexes will be considered as potential molecular imaging agents. Preliminary work in the development of a zinc(II) responsive MRI contrast agent revealed highly emissive luminescence terbium complexes (**TbC1** and **TbC2**). Derivatives of these complexes were then explored, followed by quantum yield measurements to assess their suitability for certain applications.

4.2 Lanthanides and Molecular Imaging

Lanthanide luminescence has attracted considerable attention for use in potential imaging agents. This group of elements has been exploited most intensively over the last three decades. Certain studies have focussed on quantitative analyses using lanthanide probes.^{189,190} For this reason, these studies encouraged the discovery of highly emissive imaging agents. Lanthanide complexes are ideal for cellular imaging giving a detectable response with lower levels of analyte. The long luminescence lifetime possessed by the lanthanides is an interesting factor that can be exploited as a luminescence probe. The combination of lanthanide luminescent probes with other imaging techniques such as

MRI, PET, or with a selective chemosensor for molecular imaging, specifically, *s*- and *d*-block metal ions, in biological systems have their own interest. This collaboration provides a powerful technique through which to gain molecular and cellular information due to their excellent fluorescence sensitivity and its multiplexed detection.⁴³

As discussed in Chapter 3, the low extinction coefficients of the lanthanides are caused by parity forbidden *4f* transitions. However, the emission state can be populated by sensitization *via* an organic chromophore or “antenna effect”. The energy transfer is mediated through Förster and Dexter mechanisms (Fig. 3.3). As mentioned, macrocyclic ligands have long been in demand due to the inherent kinetic stability of their complexes. Ligands with aromatic and chromophore antennae are vital to overcoming the problematic nature of the low extinction coefficients of lanthanide ions.⁵⁸

The luminescence quantum yield (Φ_F) is defined as the ratio of the energy absorbed and energy emitted in the form of light (photons). The quantum yields of lanthanide complexes depend heavily on the properties of the antennae (ligands) and their structural design. High values are also achieved by minimizing quenching effects from non-radiative pathways. Furthermore, sufficient energy level gaps are required to prevent any energy back-transfer ($4000 \pm 500 \text{ cm}^{-1}$ is the ideal energy gap).¹⁹¹ The occurrence of fluorescent or phosphorescent decay of the antenna also affects the overall quantum yields. A common method for luminescence quantum yield measurement is the comparative method proposed by Williams *et al.*¹⁹² The quantum yield of a given sample is calculated by comparing it to a well-known standard using Eqn. 4.1.

$$\Phi_X = \Phi_{ST} \left(\frac{\text{Grad}_X}{\text{Grad}_{ST}} \right) \left(\frac{\eta_X^2}{\eta_{ST}^2} \right) \quad (4.1)$$

Where ST and X denote the standard and sample, respectively, Φ_X is the fluorescence quantum yield of the sample, Φ_{ST} is the fluorescence quantum yield of the standard, Grad is gradient of the integrated fluorescence intensity versus the absorbance, and η is the refractive index of the solvent.

This procedure is nominally very simple; however, in practice, it is slightly complicated due to certain factors, namely the presence of self-quenching as a function of concentration, the validity of the Φ_F value of the standard, and solvent effects. There are some important factors involved in the modulation of quantum yield: the number of water molecules and other quenching groups in the lanthanide coordination sites; the

distance between the antenna and the lanthanide ion; and any change in the photophysical properties of the antennae.¹⁹³ The combination of low hydration number and highly efficient energy transfer from the antenna tends to maximize quantum yield; it can also be increased by incorporating hydrophobic moieties around the complex.⁵⁸ In general, terbium is less quenched by O–H oscillators due to a low Franck Condon overlap. Therefore, a higher quantum yield can be observed for Tb(III) complexes containing water in their coordination spheres *cf.* Eu(III) complexes.

There are several lanthanide-based sensors that have been reported in the literature, as presented in Fig. 4.2. **Tb1** and **Eu2** are DO3A-based terbium and europium complexes containing a DPA and quinolone moiety, respectively, which were reported by Aulsebrook *et al.*¹⁹⁴ to provide 210% and 340% luminescence enhancements, respectively, in response to added zinc(II) ions. Another DO3A-based complex, **Eu3**, was reported by Fang *et al.*¹⁹⁵ which contained a similar DPA moiety to the zinc(II) responsive luminescent probe. This probe increased its quantum yield by 1.55-fold from 2.74 to 4.25% during addition of an equivalence of zinc(II) ($K_d = 55$ nM). All of these complexes showed good selectivity towards zinc(II) over other metal ions (Ca^{2+} , Mg^{2+} , Fe^{3+} , Mn^{2+} , Co^{2+} , Cr^{2+} , Hg^{2+} , *etc.*). A series of azaxanthone-containing **Eu/Tb4**, **Eu/Tb5** and **Eu/Tb6** complexes were synthesized by Parker *et al.*¹⁹⁶ for the direct measurement of equilibrium bicarbonate concentrations in cellular mitochondria. Stasiuk, *et al.*¹³⁴ synthesized a dual-modal imaging probe for pancreatic β -cells, **Gd7**, which provides ratiometric fluorescence and relaxivity enhancements in response to zinc(II). **Tb8** presented a higher luminescence quantum yield (45%) than its europium analogue, **Eu8** (4%). This is caused by the energy gap between the triplet excited state of the ligand being much closer to the emissive states in terbium ($\Delta E = 5700$ cm^{-1}) than in europium ($\Delta E = 8900$ cm^{-1}). Therefore, the energy transfer processes are more efficient in terbium.¹⁹⁷ **Eu9**, a pH-responsive lanthanide luminescence probe, was reported by Rouledge *et al.*¹⁹⁸ to exhibit a high luminescence quantum yield (18%). **Eu10** was synthesized by McMahon *et al.* for the first bone imaging probe.¹⁹⁹ Picot *et al.*²⁰⁰ synthesized tricationic europium complex **Eu11** which exhibited a high luminescence quantum yield (15.6%) with a good solubility, intense emission, long luminescence lifetime, and significant two photon absorption cross-sections induced by two-photon antenna effects in the biological window. Andrews *et al.* synthesized a dimer which shows a response toward Hg(II) to both luminescence and relaxivity (from 8.3 to 10.3 $\text{mM}^{-1}\text{s}^{-1}$) for their corresponding **Eu12** and **Gd12** complexes.²⁰¹

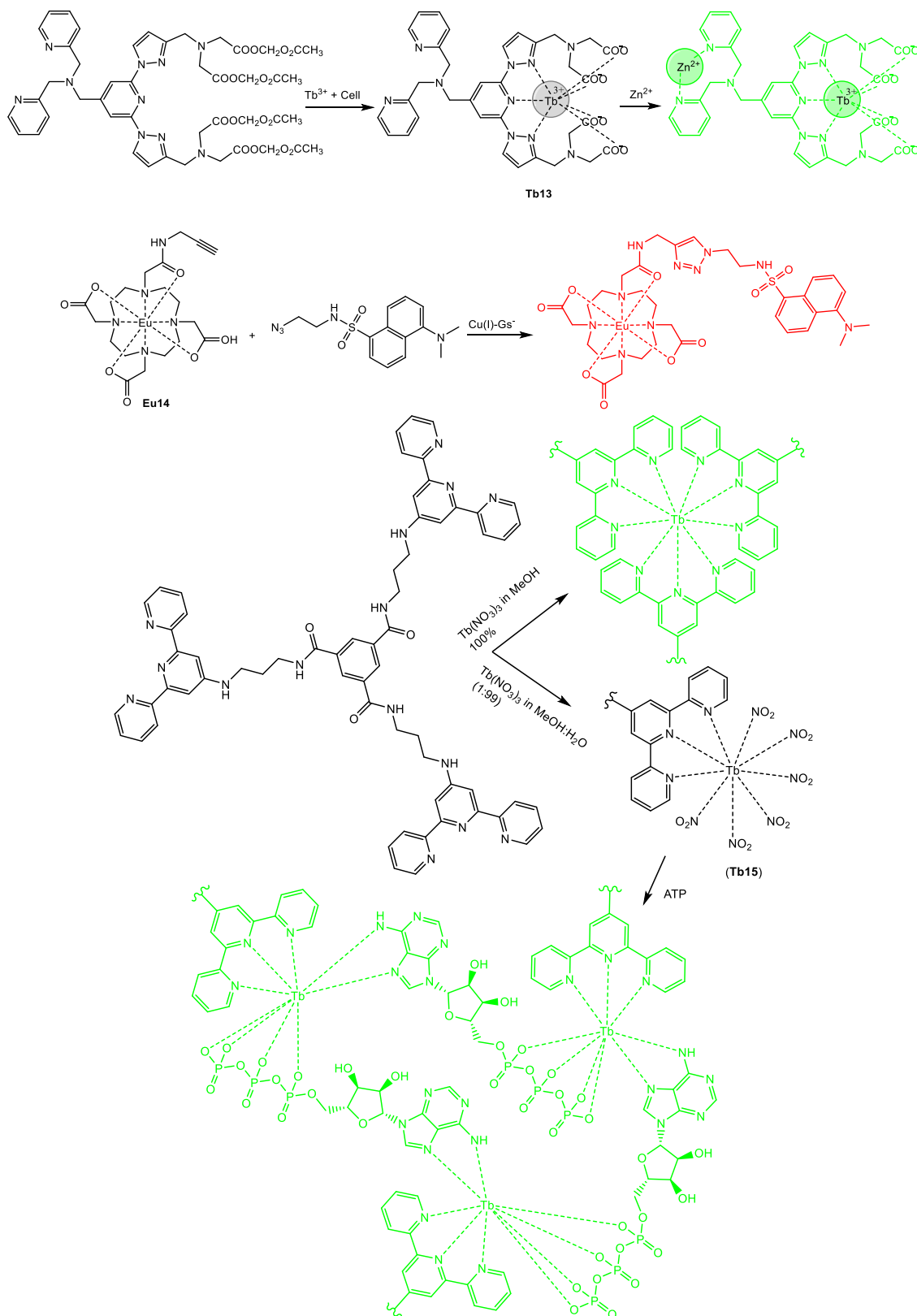


Figure 4.3: Luminescence chemosensor (**Tb13**) selective and sensitive time-resolved luminescence detection of zinc(II) ions. Luminescence enhancement of **Eu14** induced by Cu(I)-glutathione complex. Self-assembled **Tb15** for quantitative analysis of ATP.

Furthermore, unique lanthanide luminescence probes have also been reported. **Tb13**, for example, as presented in Fig. 4.3, is a polyacid containing DPA for time-resolved luminescence detection of intracellular zinc(II) ions.²⁰² In addition, **Eu14** was reported by Viguiet *et al.*²⁰³ and was used as a sensor for Cu(I) detection. Glutathione is a tripeptide that can bind to Cu(I) strongly by reducing Cu(II). Lastly, a switch-on luminescence probe (**Tb15**) used for selective ATP identification was synthesized by Jung *et al.*¹⁸⁹

4.3 Synthesis of Highly Emissive Tb Complexes

There are a number of emissive complexes that have been synthesized during the development of zinc-responsive MRI contrast agents. As mentioned in Chapter 3, terbium complexes containing pyridyltriazole moieties are generally more emissive than their europium analogues, which is beneficial in designing luminescent probes. Although the exact triplet energy level of pyridyltriazole is not measured, based on the energy of the singlet excited state, it is believed that the pyridyltriazole's triplet excited state is closer to the terbium (20400 cm^{-1}) than the europium excited state (17500 cm^{-1}), as illustrated in Fig. 4.4. This causes the energy transfer process to be more efficient in terbium as it experienced between **Tb8** and **Eu8** (Fig. 4.2).¹⁹⁷ Its efficient energy transfer is useful for applications as a sensitizer when designing luminescence probes. Thus, this chapter reports on a number of emissive terbium compounds which were synthesized utilizing ligands containing pyridyltriazole rings that were reported in Chapters 2 and 3 in zinc-responsive MRI contrast agent development. Their potential to act as imaging probes is explored.

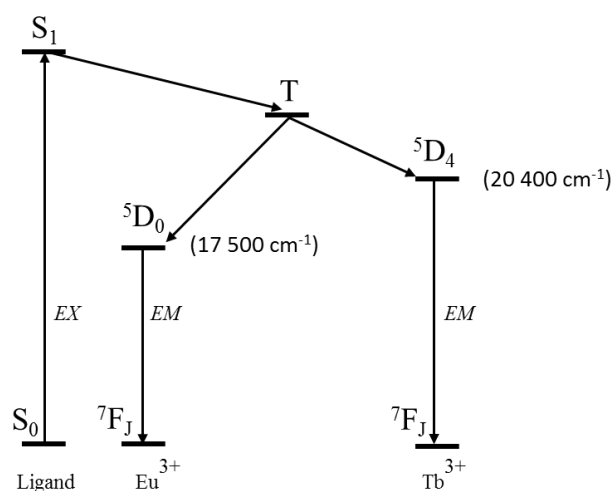


Figure 4.4: Ground and excited energy states of europium and terbium

4.3.1 Synthesis of **TbC1** and **TbC2**

C1 was described in Chapter 2, there were six synthetic steps required to produce this complex. **TbC1** absorption spectrum shows two absorption bands at 237 and 287 nm as presented in Fig. 4.5. The emission spectrum of **TbC1** shows the four typical terbium emissions bands at ~489, ~543, ~586 and 621 nm corresponding to the $^5D_4-^7F_6$, $^5D_4-^7F_5$, $^5D_4-^7F_4$ and $^5D_4-^7F_3$ transitions, respectively, with the strongest emission at ~543 nm. Its emission profile, along with its excitation spectrum, is depicted in Fig. 4.6.

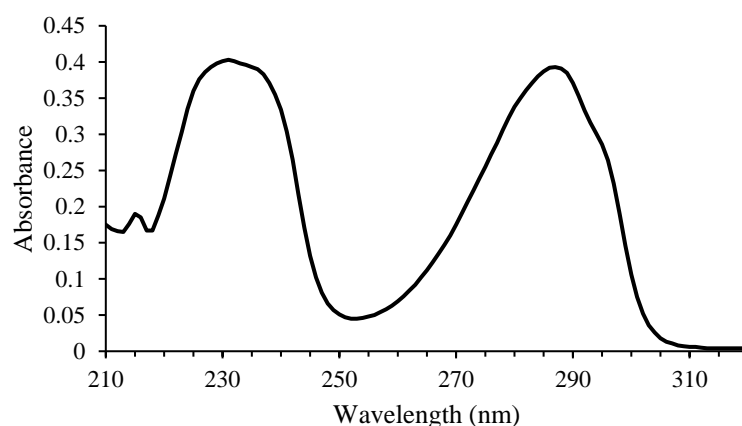


Figure 4.5: Absorption spectrum of **TbC1** in 50 mM HEPES buffer pH 7.4.

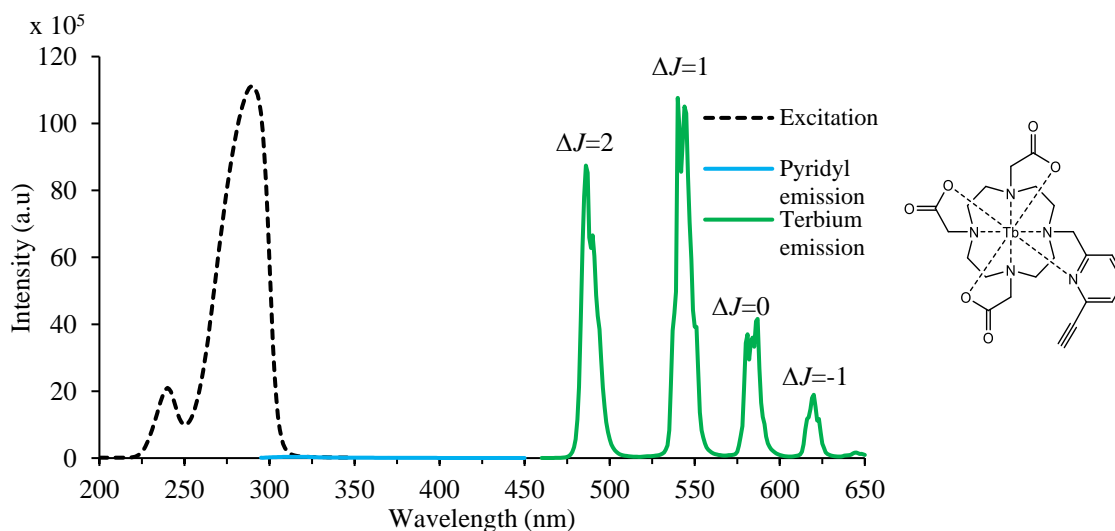


Figure 4.6: Excitation (at 540 nm) (dashed black) and emission (at 287 nm) (solid green and blue line) spectra of **TbC1** in 50 mM HEPES buffer pH 7.4.

The fluorescence quantum yield (Φ_F) measurement of this emissive compound was conducted through a comparative method, in that its emission was compared to a standard compound with a well-known Φ_F value, in this case quinine sulphate. It was chosen

because they have excitation wavelengths in similar region. The excitation and emission spectra of quinine sulphate is presented in Fig. 4.7.

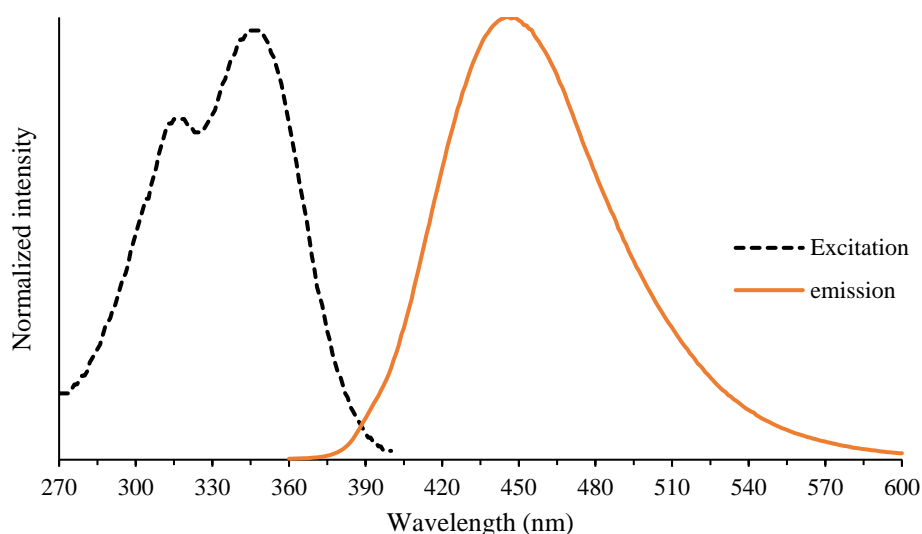


Figure 4.7: Excitation (black) and emission (orange) profile of quinine sulphate.

The fluorescence quantum yield measurement was conducted in 50 mM HEPES buffer pH 7.4 using a dilute concentration range within absorbance < 0.1 . This range was used to reduce any interference caused by certain factors, *i.e.*, high concentrations are believed to stimulate the occurrence of self-quenching.^{204,205} Figure 4.8 presents the linear plot for absorption versus integrated emission for both standard quinine sulphate and **TbC1**. The Φ_F value is determined by applying the gradient of the linear curve from both standard and sample to Eqn. 4.1 to give an Φ_F value of 19%.

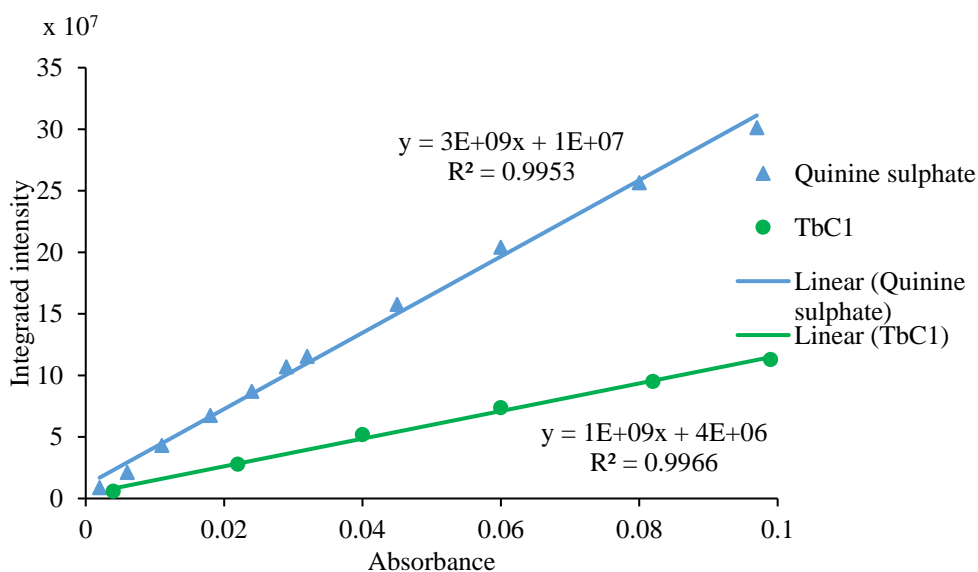


Figure 4.8: Linear plot of integrated emission vs absorbance of quinine sulphate and **TbC1**.

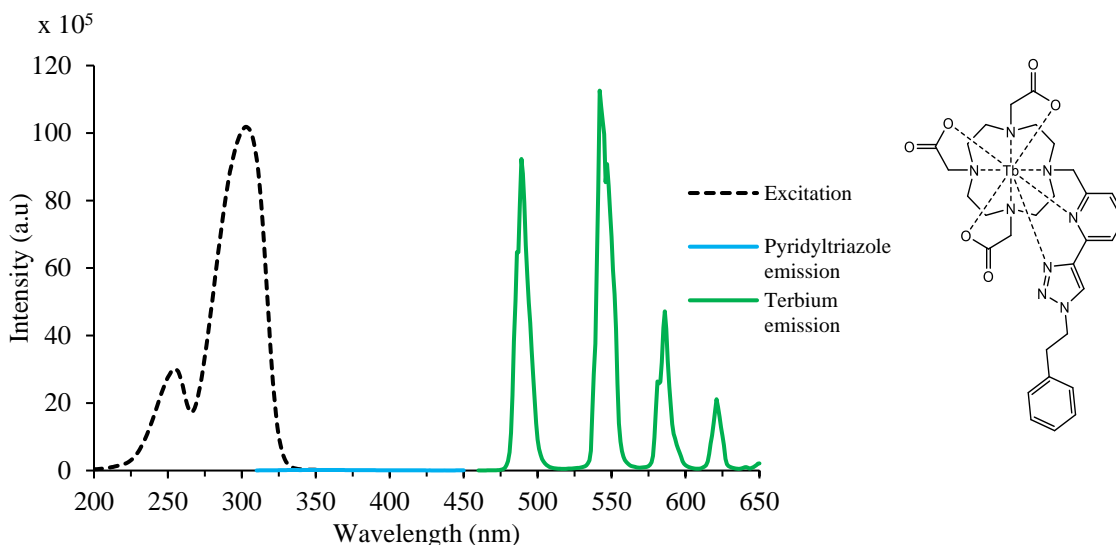


Figure 4.9: Excitation (at 542 nm) (dashed black), pyridyltriazole emission (at 292 nm) (solid blue) and terbium emission (at 292 nm) (solid green) spectra of **TbC2** in 50 mM HEPES buffer pH 7.4.

TbC2 was synthesized through the same synthetic procedures as for the **EuC2** complex presented in Scheme 2.5, in which the formation of pyridyltriazole prior to **C2** is considered to be the easiest synthetic pathway. The photophysical studies of **TbC2** revealed that it exhibited much more emissive compared to the europium complex (**EuC2**). The excitation and emission profiles of this complex are depicted in Fig. 4.9. The emission bands consist of typical terbium emission bands corresponding to the electronic transition from its emissive excited state to its ground state, as explained for **TbC1**.

The Φ_F measurement for **TbC2** resulted in an even higher value of 29%, which is approximately 50% higher than **TbC1**. As predicted, this higher Φ_F value is a consequence of the lack of inner-sphere water molecules in its coordination environment. As described in Section 2.1, by analogy to **EuC2** this compound is believed to have a closed structure by the formation of nine coordination sites or by the presence of steric hindrances which shield the lanthanide metal centre from surrounding water molecules, and as a result there is no inner-sphere water quenching. It is interesting to see that the Φ_F value of **TbC2** is ten times higher than **EuC2** (3%), which indicates that the energy transfer is more efficient to terbium (with an optimum energy gap between the pyridyltriazole triplet state and the terbium emissive state). A plot of their quantum yield measurements is presented in Fig. 4.10.

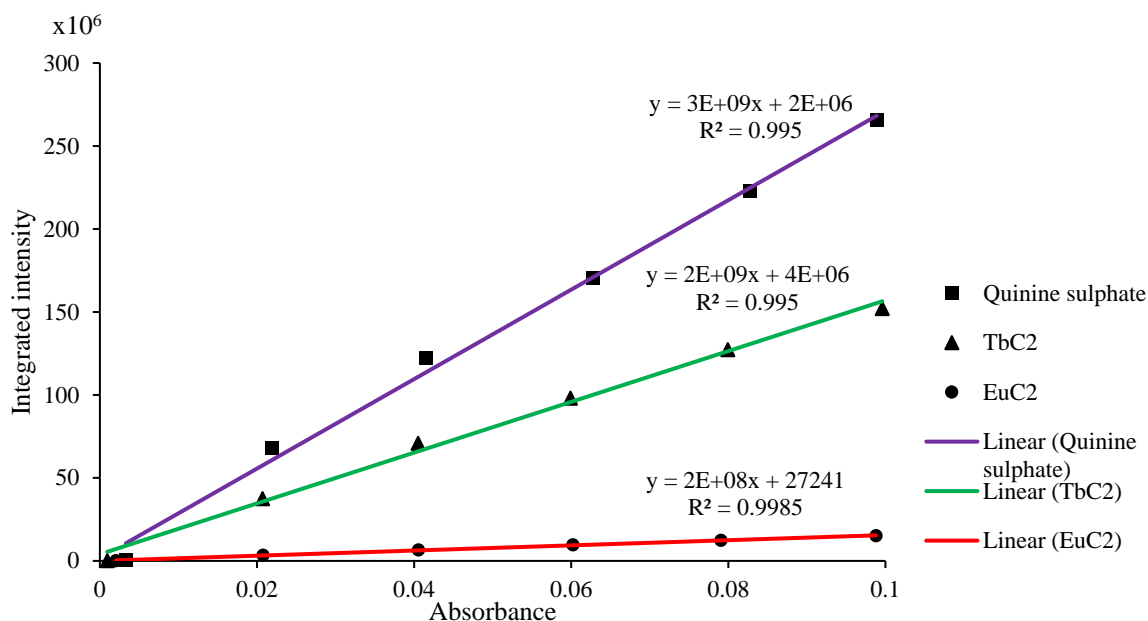
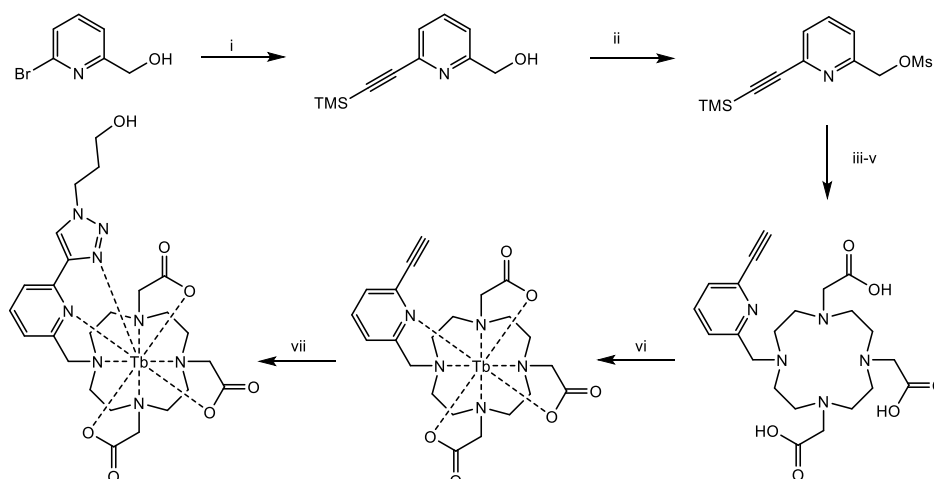


Figure 4.10: Linear plots of integrated emission vs. absorbance of standard quinoline sulphate, **TbC2** and **EuC2**.

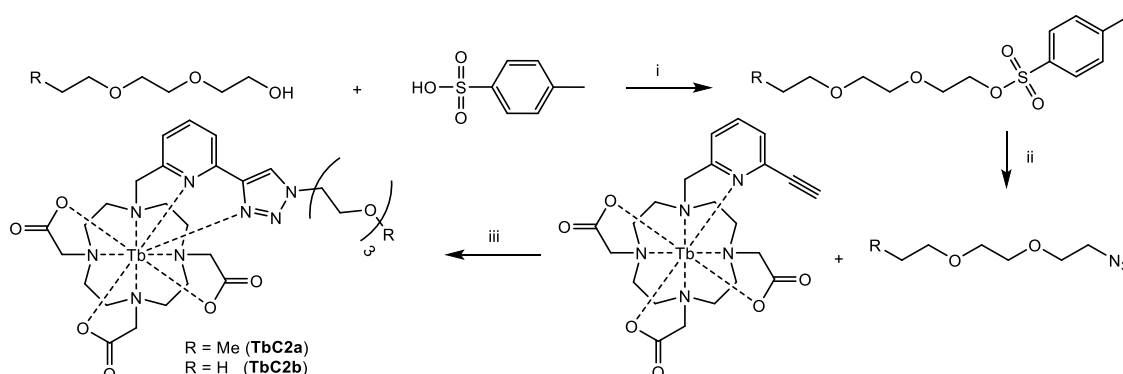
The combination of efficient energy transfer in the terbium complex compared to the europium complex and the lack of non-radiative quenching results in a highly emissive compound. In addition, the distance between the antenna and lanthanide centre is essential to increasing the energy transfer efficiency. The direct coordination that occurs between the pyridyltriazole and the lanthanide centre in **TbC2** provides a highly optimum distance between the two.

These two emissive compounds, **TbC1** and **TbC2**, have the potential to be used as luminescence probes. Their Φ_F values, combined with a highly sensitive instrument, may provide a powerful tool for bioimaging applications. In addition, **TbC1** and **TbC2** are constructed with a well-known stable ligand, DO3A, and which are believed to have similar thermodynamic and kinetic stabilities suitable for clinical applications. A modified version of **TbC2** could be used as a labelling agent by attaching it to the specific target vector. While **TbC1** can be attached to any molecular target composed of azide-containing molecules in the presence of Cu(I) catalyst, *i.e.*, as a Cu(I) sensor as in compound **Eu14** reported by Viguiet *et al.*²⁰³ Regrettably, work on a compound similar to **TbC1** was published while this study was being conducted. It was synthesized using a similar synthetic pathway, but with slightly different reagents to provide **TbC1**-like complexes to be used in protein labelling, as presented in Scheme 4.1.²⁰⁶



Scheme 4.1: The synthesis pathway of **TbC1**-like compound published by O'Malley *et al.*²⁰⁶ i) Pd(PPh₃)₂Cl₂, TMS acetylene, CuI, Et₃N, THF, N₂ atmosphere, RT, 2 h. ii) MsCl, DIPEA, DCM, 0°C to RT, 30 min. iii) *t*BuDO3A.HBr, DIPEA, MeCN, reflux, 24h. iv) KF, MeCN/H₂O, RT, 2 h. v) TFA, DCM, RT, 24h. vi) Tb(OTf)₃, H₂O, NaOH (pH 8-9), 90°C, 2 h. vii) 3-azido-1-propanol, CuSO₄, THPTA, sodium ascorbate, H₂O/MeCN, pH 7, RT, 24h.

4.3.2 Synthesis of **TbC2a**, **TbC2b** and **TbC2c**



Scheme 4.2: Synthetic route of **TbC2a** and **TbC2b**; i) Pyridine, N₂, 0°C, 24h. ii) NaN₃, H₂O:Acetone, 24h. iii) CuSO₄, NaAsc, H₂O, 75°C, 24h.

In order to study the potential applications, some **TbC2** derivatives were synthesized by tail modifications. As explained previously, the use of a benzyl group as a model complex is intended to simplify the separation process during the synthesis steps. The thing to be aware of is that the tail can also function as a molecular linker for many applications. Polyethylene glycol group compounds were chosen to act as a tail/linker to form **TbC2a** and **TbC2b**. This tail was intended to maintain the solubility of the complex in water. Water solubility is an important requirement of an imaging probe to ensure rapid distribution during molecular imaging, and furthermore to ensure ease of clearance of probe in order to avoid any long-term toxicity that might potentially cause damage to

cells. **TbC2a** and **TbC2b** were synthesized in a straightforward manner by a reaction performed using the same reaction conditions. The synthetic pathway of polyethylene glycol is described in Scheme 4.2. **TbC2a** and **TbC2b** were a white hygroscopic solid with m/z 829 $[M+Na]^+$ and 815 $[M+Na]^+$ respectively.

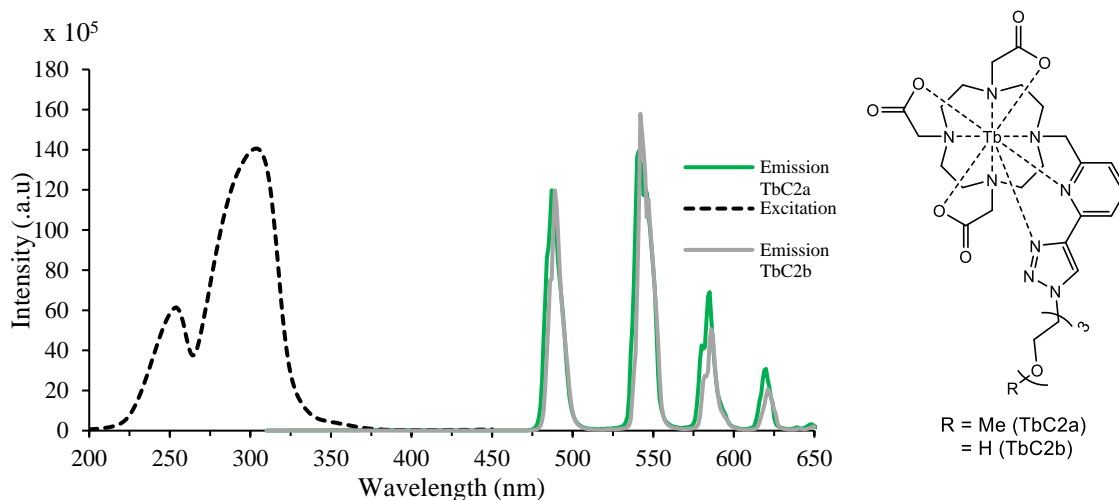


Figure 4.11: Excitation (at 541 nm) (dashed black) and emission (at 292 nm) (green solid) spectra of **TbC2a** and **TbC2b** 50 mM HEPES buffer pH 7.4.

TbC2a and **TbC2b** have the same emissive emission profile as presented in Fig. 4.11. The presence of a free hydroxyl group as in **TbC2b** was believed to further increase its polarity as has been previously noted.^{207,208,209} Their high luminescence quantum yields give bright emissive solutions at relatively low concentrations, as presented in Fig. 4.12.

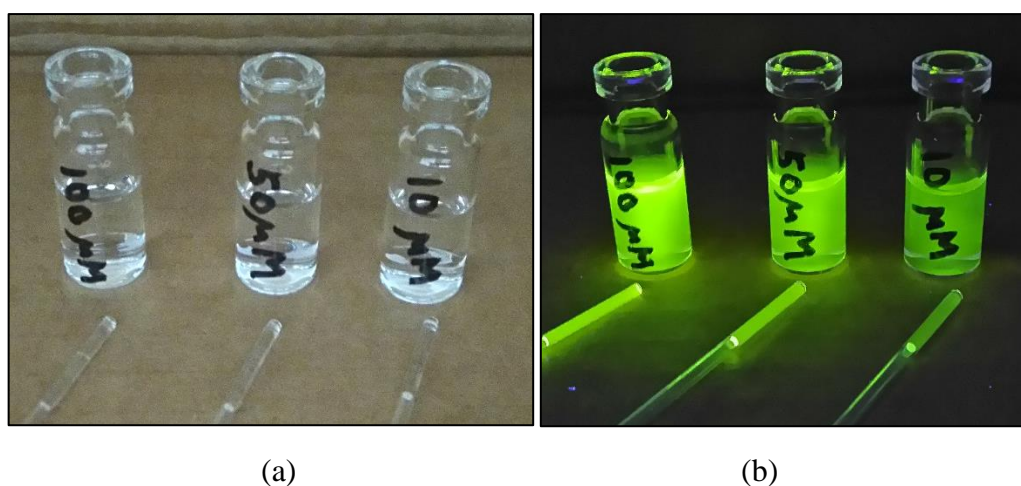
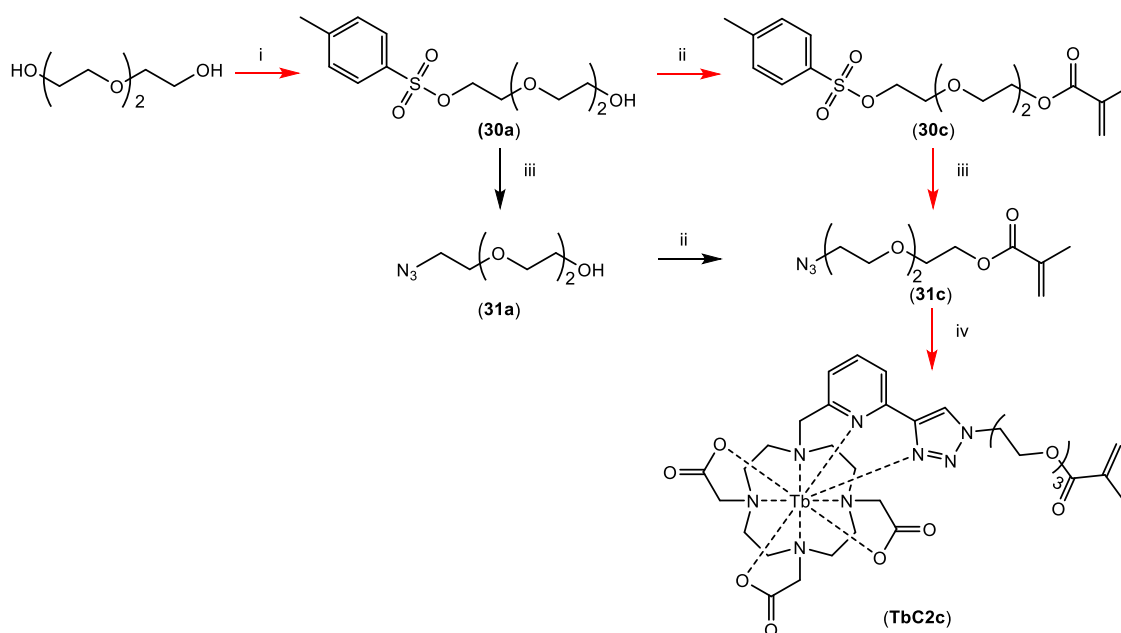


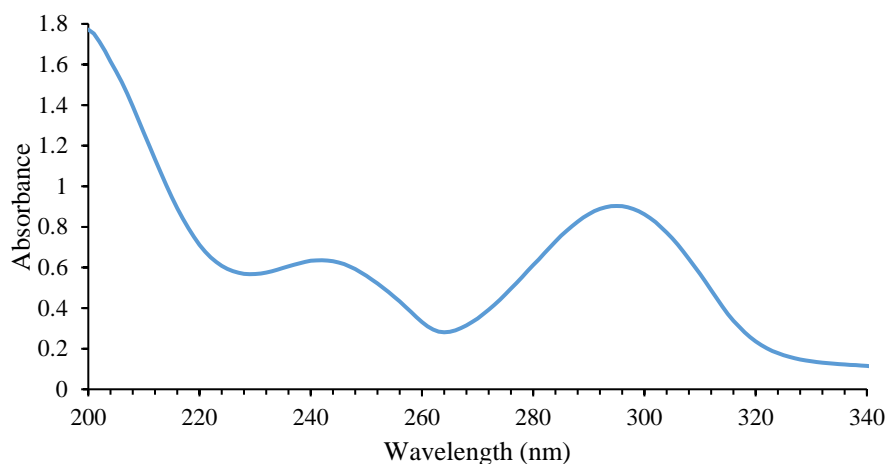
Figure 4.12: Photographs of 10, 50 and 100 μM of **TbC2a** in water, showing (a) a clear solution in normal light and (b) a bright green solution under a 300 nm UV lamp.

The use of polyethylene glycol as a tail or linker is not only intended to maintain its polarity. A hydroxyl functional group at the end of such linker can be relatively easily modified for various purposes, *i.e.*, installing a leaving group, that make it easy to combine with other compounds. **TbC2c**, for example, was synthesized to have a polyethylene glycol linker containing a polymerisable functional group. There were some attempts to give the best synthetic pathway of **TbC2c** as presented in Scheme 4.3.

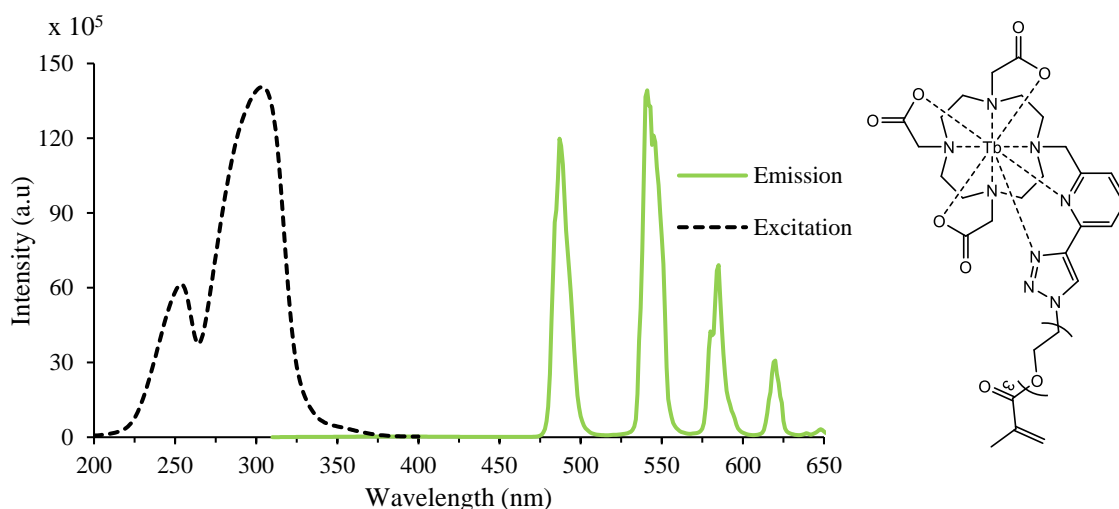


Scheme 4.3: Synthetic pathway of **TbC2c** (favoured synthetic pathway is marked in red arrows); i) Pyridine, tosylchloride, 0°C, 24h. ii) Methacryloyl chloride, pyridine, 0°C, 24h. iii) NaN₃, Acetone:H₂O (3:1), 24h. iv) **TbC1**, CuSO₄ NaAsc, H₂O, 24h.

The polymerisable linker (**31c**) was synthesized in three steps before being “clicked” onto the main lanthanide complex, **TbC1**. The first step was the synthesis of compound **30a** (Section 2.3.4). There were two routes to the following step, attaching the polymerizable group, that is, either prior or post azidification. Both routes can be applied in order to achieve **31c**. However, the second route (marked with red arrows) was preferred owing to the presence of the tosylate group which was useful for monitoring the reaction completion by TLC. The last step was the attachment of this polymerizable linker to the terbium complex (**TbC1**) through a click reaction. It was then purified by passing through a column containing Amberlite XAD 16 and lyophilized to give a white hygroscopic solid.

Figure 4.13: Absorption spectrum of **TbC2c**.

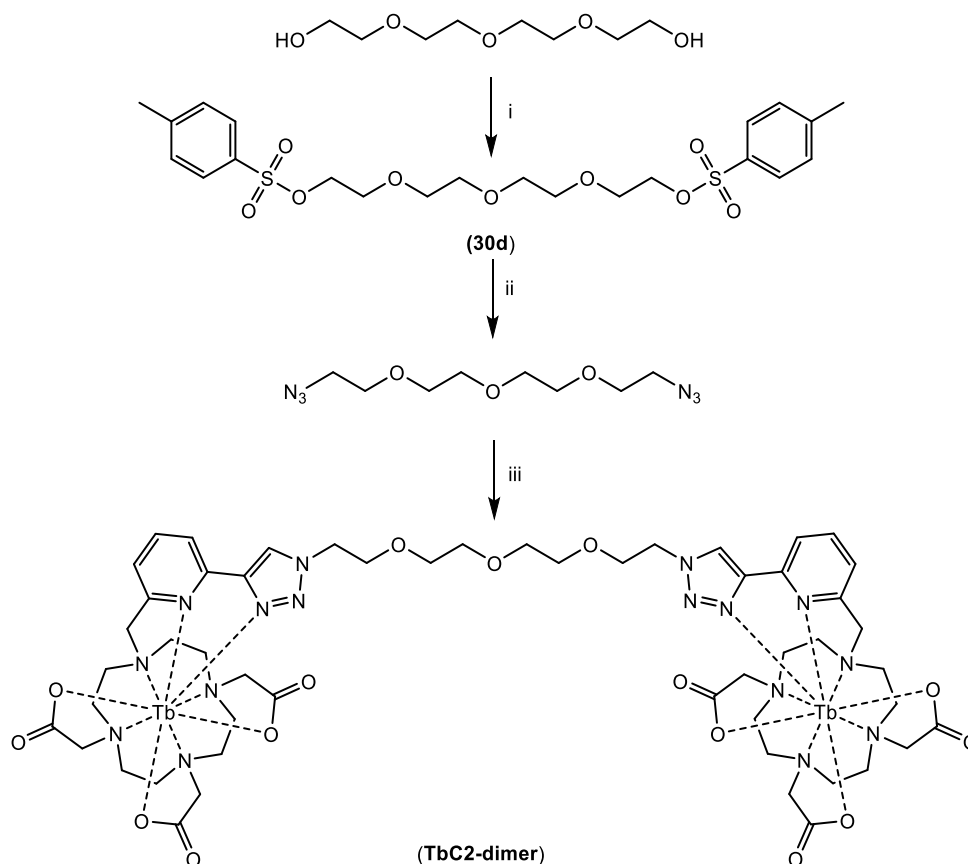
TbC2c exhibited absorption spectra, as depicted at Fig. 4.13, containing two peak maxima at 242 and 295 nm. Its emission and excitation spectra were recorded in water as presented in Fig 4.14. It also presented a maximum peak at 541 nm, similar to the previous compounds (**TbC2**, **TbC2a** and **TbC2b**). Due to time constraints, polymerization experiments have not been completed using **TbC2c**; however, this is an active research project in the Lowe group.

Figure 4.14: Excitation (at 541 nm) (dashed black) and emission (at 292 nm) (solid green) spectra of **TbC2c** in 50 mM HEPES buffer pH 7.4.

4.3.3 Synthesis of **TbC2-dimer**

Polyethylene glycol can also be used as a linker in synthesizing a dimer (**TbC2-dimer**) as presented in Scheme 4.4. Synthesis of this linker was relatively straightforward compared to all other linkers previously discussed. It took only two steps to achieve a double azide form before it was then “clicked” with **TbC1**. The double tosylation

compound (**30d**) was synthesized from tetraethylene glycol with excess tosylchloride, or was taken as a by-product from the synthesis of a mono-tosylated compound (**30b**). The ^1H NMR analysis showed two portions of hydrogen due to tosylate moieties (at 7.79 and 7.34 ppm) which indicated the presence of two tosylate groups. This was supported by MS analysis which showed a peak for the title compound at m/z 525 $[\text{M}+\text{Na}]^+$. The azidification reaction of **30d** could be accelerated by increasing the amount of sodium azide. However, considering the toxicity of the sodium azide, it was considered more desirable that its ratio was reduced, and thus the reaction time would be elongated. For safety reasons, the double azidification product was not isolated (it has $(\text{C}+\text{O})/\text{N} = 1.83$). All of organic azides which have this ratio $((\text{C}+\text{O})/\text{N})$ lower than three are potentially explosive. As well as the azidification, the click reaction was also required once more to bring the reaction to completion. The formation of the **TbC2-dimer** and the reactants' depletion were monitored *via* ESMS. The purification through Amberlite XAD-16 gave a green luminescence fractions when viewed under a UV lamp at 300 nm which were lyophilised to give a white solid.



Scheme 4.4: Synthetic pathway of **TbC2-dimer**; i) Tosylchloride, pyridine, 0°C, 24h. ii). NaN_3 , H_2O :Acetone (1:3), 75°C, 48h. iii) CuSO_4 , NaAsc, H_2O :Acetone (1:3), 65°C, 24h.

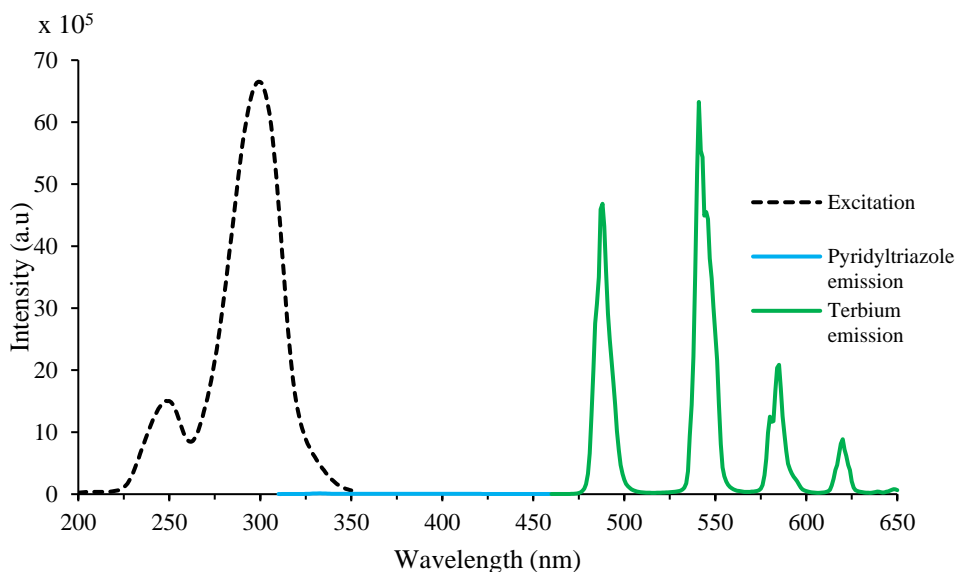


Figure 4.15: Excitation (at 541 nm) (dashed black), pyridyltriazole emission (at 292 nm) (solid blue) and terbium emission (at 292 nm) (solid green) of **TbC2-dimer** in 50 mM HEPES buffer pH 7.4.

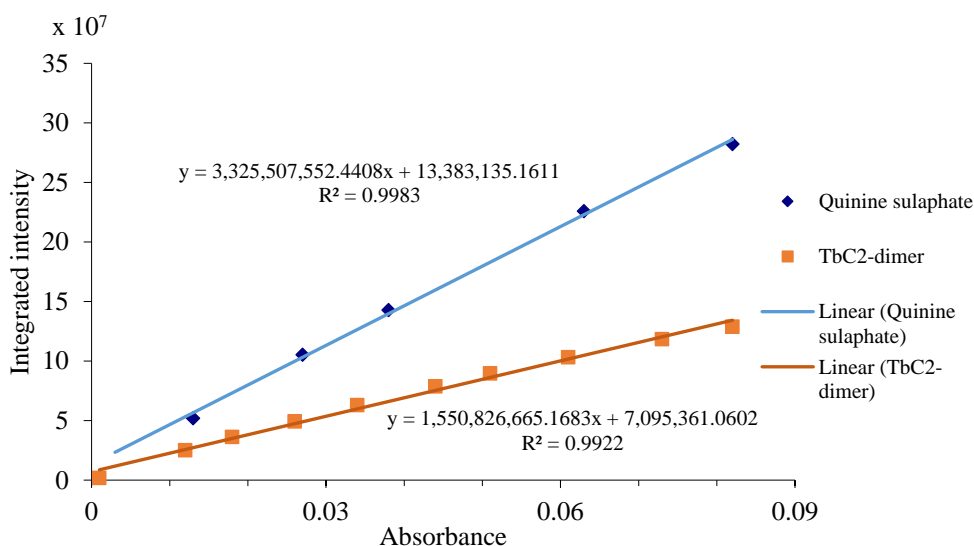


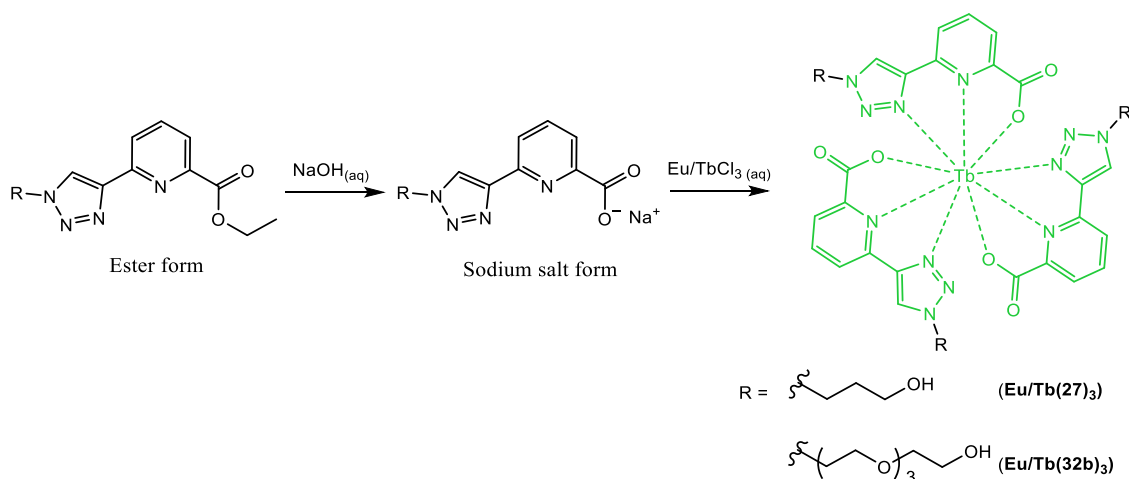
Figure 4.16: Linear plots of integrated emission vs absorbance of standard quinine sulphate and **TbC2-dimer**.

The **TbC2-dimer** exhibits almost identical excitation and emission profiles (Fig. 4.15) to other **TbC2** derivatives. Its luminescence quantum yield, however, is slightly lower than **TbC2** (Fig. 4.16), at $\Phi_F = 25\%$.

4.3.4 Synthesis of **Tb(27)**₃ and **Tb(32b)**₃

The pyridyltriazole-containing carboxylate acid group (**27** and **32b**), which was used as an active arm in **LnC8**, **LnC9** and **LnC10**, can also behave as a tridentate ligand. It was found that this ligand has the potential to be used as a chelating agent to the

emissive lanthanide to be used as a luminescence probe; the ability to capture and transfer energy (antenna) makes this ligand suitable for this purpose. Attempts were made to complex two different ligands with the emissive lanthanides terbium and europium to provide **Eu/Tb(27)**₃ and **Eu/Tb(32b)**₃, as described in Scheme 4.5.



Scheme 4.5: Synthetic pathway of **Tb/Eu(27)**₃ and **Tb/Eu(32b)**₃.

These tridentate ligands were hydrolysed with sodium hydroxide aqueous solution at pH 9 prior to the synthesis, with the excess alkali being neutralized with dilute HCl before being lyophilised to give a white hygroscopic solid (sodium salt form of **27** and **32b**). The reactions between the Ln(III) ion with these ligands were very fast. The formation of **Tb(27)**₃ and **Eu(27)**₃ was achieved spontaneously in a rapid reaction under mild reaction conditions. The complex formation can be easily observed by the appearance of a bright green (for terbium) or red (for europium) luminescence solution when viewed under a UV lamp at 300 nm during the addition of terbium (**TbCl**₃) and europium (**EuCl**₃) aqueous solutions to the aqueous solution of ligands, as presented in Fig. 4.17.

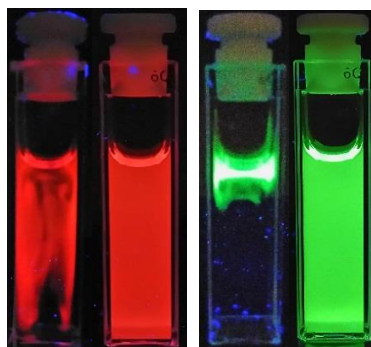


Figure 4.17: A bright red and green luminescence during **Eu(27)**₃ and **Tb(27)**₃ formation under UV lamp 300nm; a) After additional a drop **EuCl**_{3(aq)} (left) to **27** solution and after homogenization (right); b) After addition of a drop of **TbCl**_{3(aq)} (left) to **27** solution and after homogenization (right).

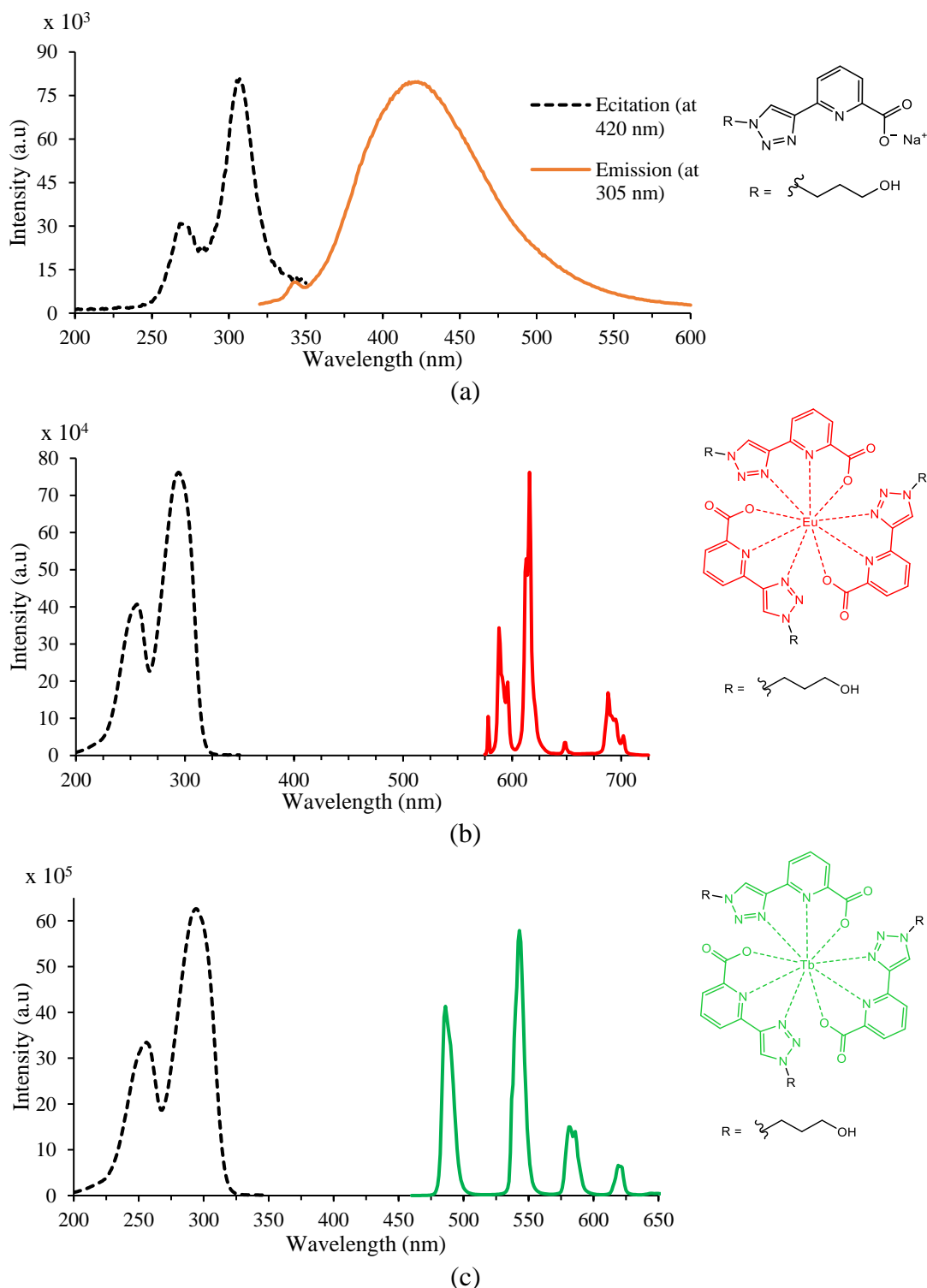


Figure 4.18: Excitation (at 420, 617 and 543 nm for **27**, $\text{Eu}(\mathbf{27})_3$ and $\text{Tb}(\mathbf{27})_3$ respectively) (dashed black) and emission (at 305, 292 and 292 nm for **27** (orange), $\text{Eu}(\mathbf{27})_3$ (red) and $\text{Tb}(\mathbf{27})_3$ (green), respectively).

Mass spectrometry analysis of $\text{Tb}(\mathbf{27})_3$ showed the presence of two main fragments at m/z 923, corresponding to $[\text{M}+\text{Na}]^+$. The emission profiles of $\text{Tb}(\mathbf{27})_3$ and $\text{Tb}(\mathbf{32b})_3$, as well as $\text{Eu}(\mathbf{27})_3$ and $\text{Eu}(\mathbf{32b})_3$, are similar to the emission profiles of the previous terbium and europium compounds (such as **TbC2c**, **EuC8**). None of them show

ligand emission. They also present the highest intensity emission band for terbium complexes at 543 nm, for the 5D_4 - 7F_5 transition, and for europium complexes at 616 nm, for the 7F_2 - 5D_0 transition. The emission and the excitation profiles of free ligand **27**, **Eu(27)**₃ and **Tb(27)**₃ are presented at Fig. 4.18.

The Φ_F measurements were conducted only for **Tb(27)**₃ and **Eu(27)**₃ in a HEPES buffer solution at pH 7.4. As presented at Fig. 4.19, the slope of **Tb(27)**₃ is much lower compared to the standard quinoline sulphate and even lower for **Eu(27)**₃. The Φ_F values were then achieved by using Eqn. 4.1, obtaining 16.3% and 1.6% for **Tb(27)**₃ and **Eu(27)**₃, respectively; these values are much lower than anticipated. The presence of three antennae in both complexes was expected to increase the Φ_F values, since they have more capability to capture energy and therefore have more energy to transfer. This is believed to be due to its structural rigidity (explained in section 3.5), which is less than that of the previous emissive compounds, such as **TbC2** which contains a macrocycle chelator. As it mentioned in section 3.3, by increasing structural rigidity the energy quenching by bond vibrations is minimized. Another possibility is the occurrence of an equilibrium between coordination of two and three ligands, since these two forms were observed in the mass spectrometry analysis. The terbium complex has an Φ_F value 10-fold higher than its analogous europium complex. This result is in accordance with the previous finding that the pyridyltriazole antenna will provide a better energy transfer efficiency to terbium than to europium.

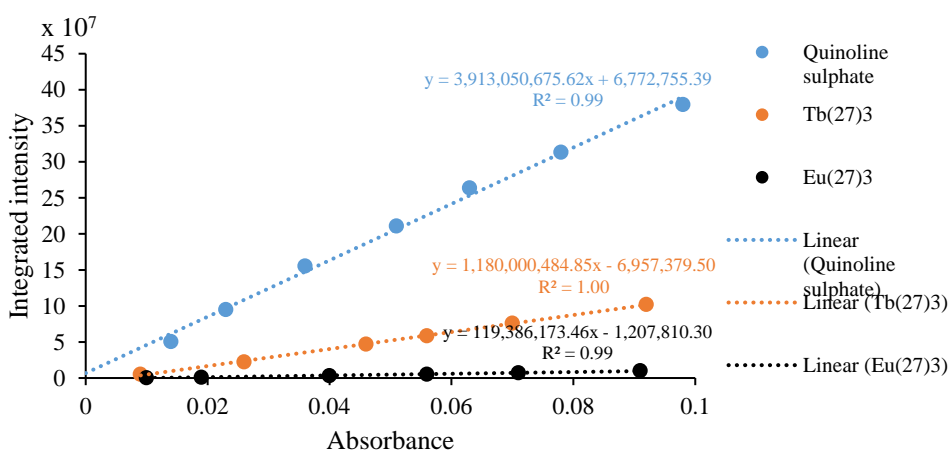


Figure 4.19: Plots of linear curve integrated emission vs absorbance of standard quinoline sulphate, **Eu(27)**₃ and **Tb(27)**₃.

To observe the binding motif (*i.e.*, how many ligands were coordinated to the lanthanide ion) of the complex formed, titration experiments were conducted with the aqueous solution of the sodium salt of **27** with **TbCl**₃ and **EuCl**₃ solutions. Their absorption and emission spectra were then examined to see if there were any changes to

their spectra. Indeed, there was a shift apparent in the absorption spectra of the sodium salt of ligand **27** during the lanthanide addition. In general, their two absorption bands transformed differently. The first absorption band (at ~245 nm) underwent hypochromic and bathochromic shifts, while the second absorption band (at ~286 nm) experienced hyperchromic and bathochromic shifts upon addition of 0 to 1.5 equivalents of Tb(III)/Eu(III), as shown in Fig. 4.20.

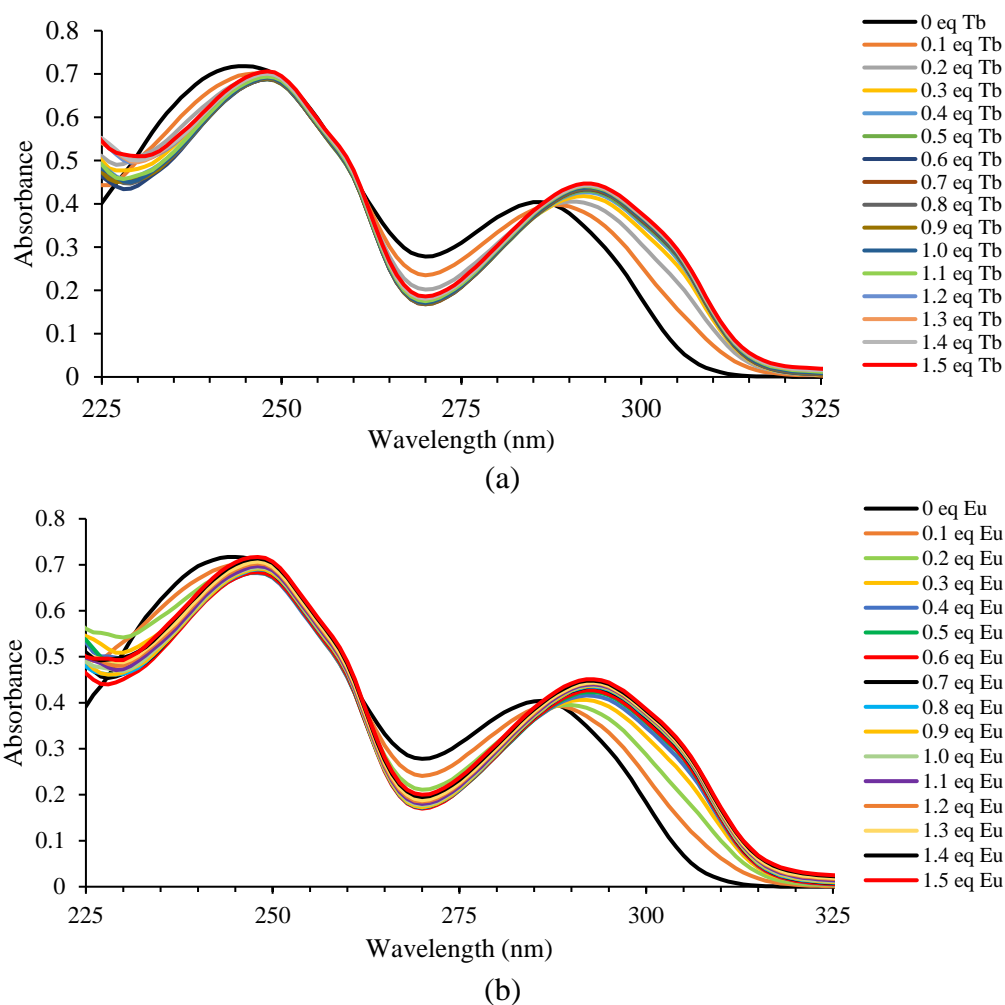


Figure 4.20: Absorption spectra of **27** (sodium salt form) during TbCl₃ (a) and EuCl₃ (b) addition in 50 mM HEPES buffer at pH 7.4.

The most significant difference observed in their absorption spectra was observed during the first 0.3 equivalents of TbCl₃/EuCl₃ added. This could be an indication of binding saturation being experienced at this point. It was expected that their emission profiles during TbCl₃/EuCl₃ addition would give more accurate information about their binding motifs since their resultant complexes were emissive. Thus, by monitoring their emission intensities, their binding motifs can be predicted. Their emission intensities were recorded during EuCl₃/TbCl₃ titrations, as shown in Fig. 4.21.

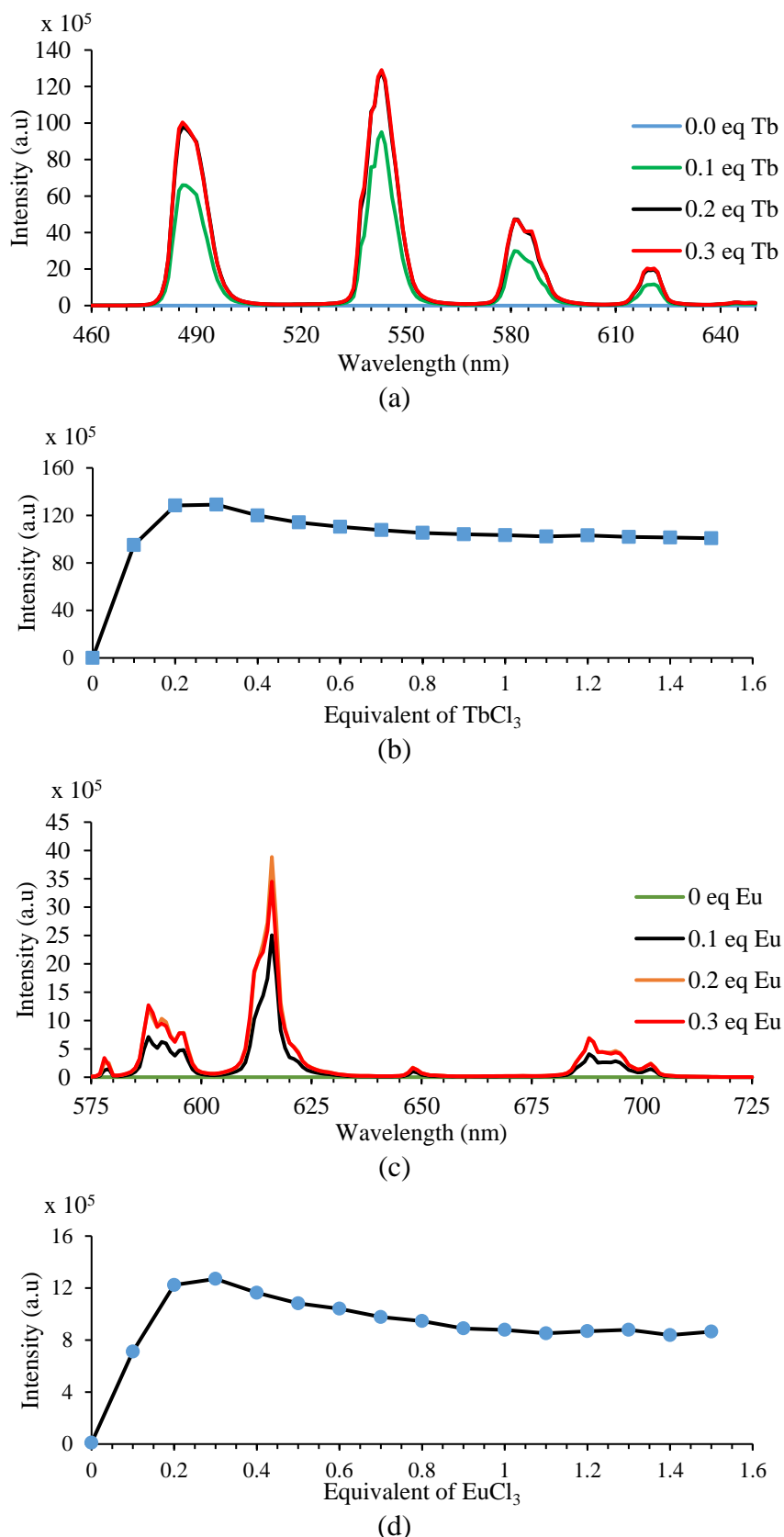
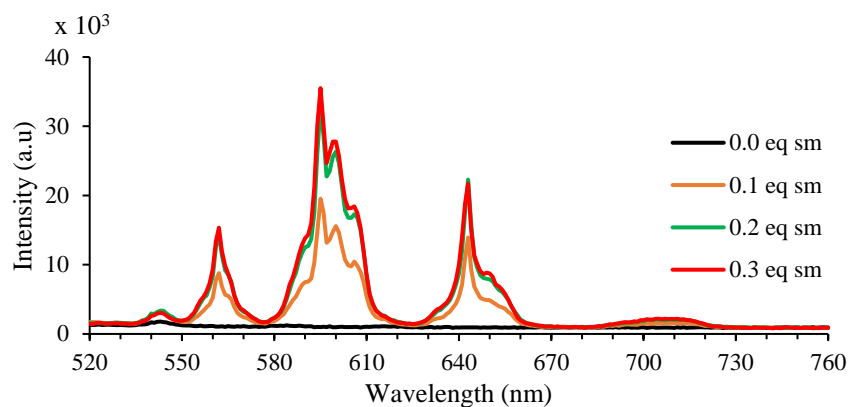
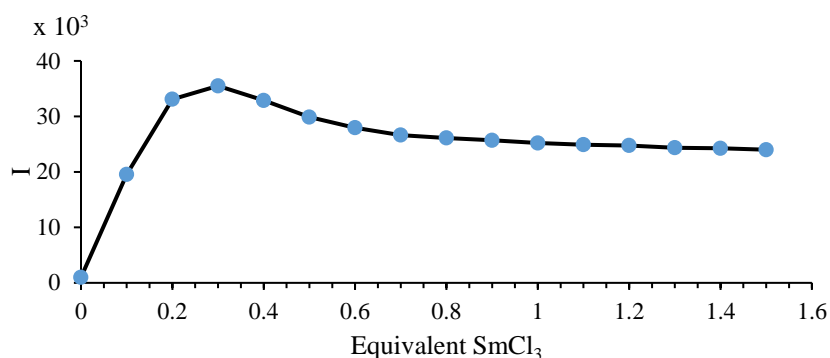


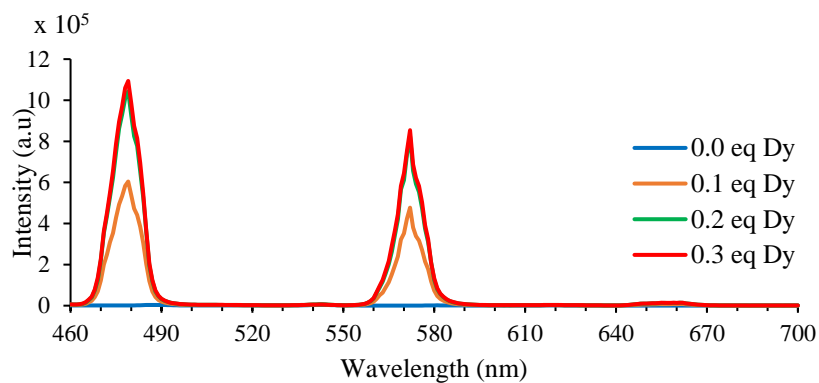
Figure 4.21: Emission profiles of **27** (sodium salt form) (excited at 287 nm) during TbCl₃ (a) and EuCl₃ (c) additions showing the emission alterations monitored at 543 nm and 588 nm for terbium (b) and europium (d) respectively, in HEPES buffer at pH 7.4.



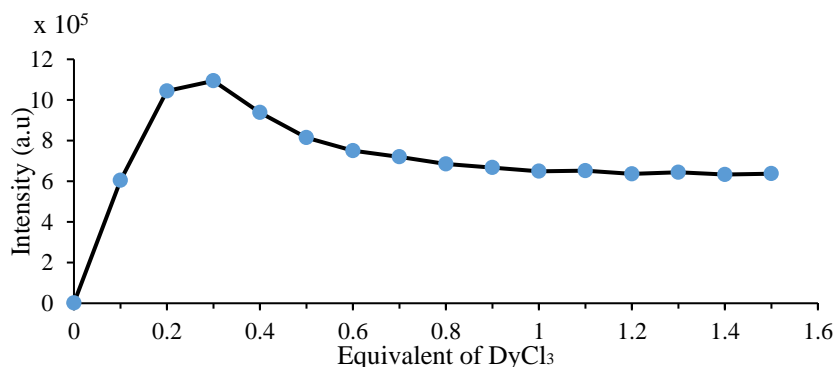
(a)



(b)



(c)



(d)

Figure 4.22: Emission profiles of **27** (sodium salt form) (excited at 287 nm) during SmCl_3 (a) and DyCl_3 (c) addition and their emission alterations monitored at 595 nm and 479 nm for samarium (b) and dysprosium (d) respectively, in 50 mM HEPES buffer at pH 7.4.

Indeed, similar to their absorption profiles, their emission intensities reached to their maxima during the addition of a 0.3 equivalent of $\text{EuCl}_3(\text{aq})/\text{TbCl}_3(\text{aq})$. Further additions decreased the intensity slightly. This result indicating the formation of a one to three ratio between the lanthanide and ligand to form nine coordination complexes as expected, which match their mass spectrometry analyses. The emission depletions on addition of further $\text{TbCl}_3/\text{EuCl}_3$ than the 0.3 equivalent are believed due to the competition between ligands and the lanthanide ions in the solution.

The capability of this ligand as a chelating agent as well as the antennae to produce emissive complexes with terbium and europium was also tested with other potential lanthanides. From the several lanthanides tested, namely samarium (Sm), dysprosium (Dy) and holmium (Ho), only Sm and Dy could be sensitized by this ligand. However, all of them exhibited relatively low emission intensities. The emission profiles of these Sm and Dy complexes during titration are presented in Fig. 4.22. The formation of $\text{Dy}(\mathbf{27})_3$ and $\text{Sm}(\mathbf{27})_3$ were observed under a 300 nm UV lamp to give pale red and a pale green solutions for samarium and dysprosium, respectively, as presented in Fig. 4.23.

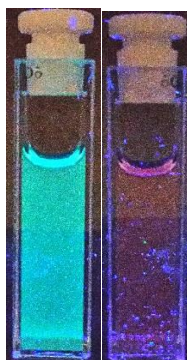
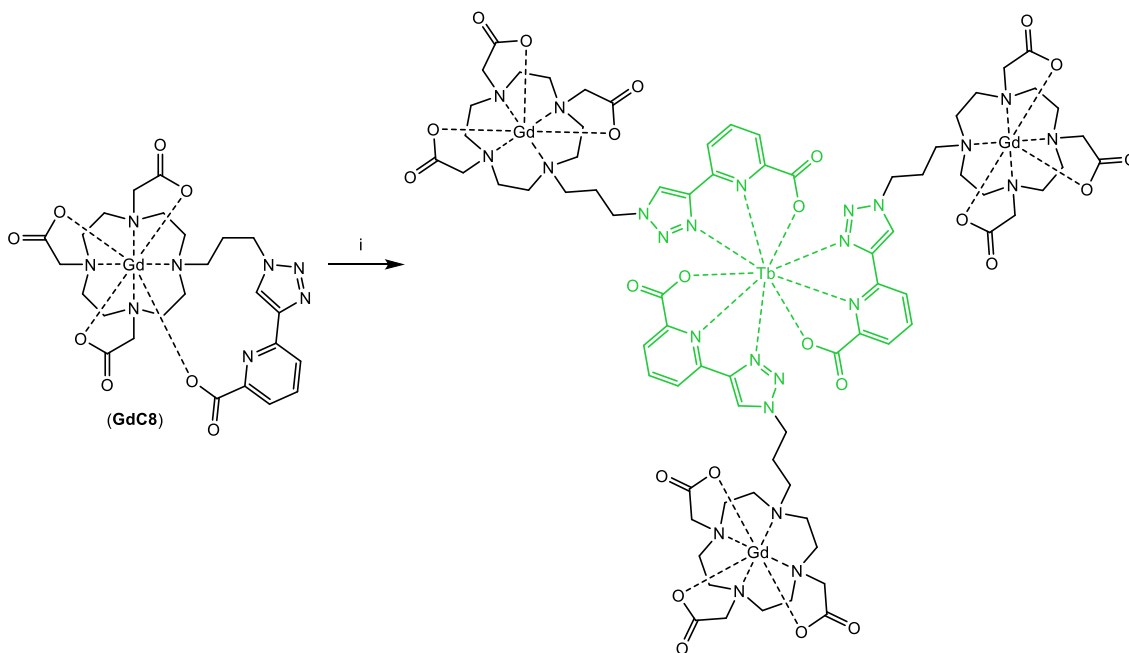


Figure 4.23: The luminescent appearance of $\text{Dy}(\mathbf{27})_3$ (left) and $\text{Sm}(\mathbf{27})_3$ (right) under UV lamp at 300 nm in 50 mM HEPES buffer at pH 7.4.

4.3.5 Synthesis of a Trimer $\text{Tb}(\text{GdC8})_3$ as a Dual Modal Fluorescence-MR Imaging Agent

The use of pyridyltriazole as a tridentate chelator in producing an emissive complex with various lanthanide trivalent ions, especially terbium, led to the synthesis of a dual functional fluorescence and MR imaging probes (Scheme 4.6), $\text{Tb}(\text{GdC8})_3$. This was synthesized as a model complex since the terbium complex exhibited a higher Φ_F value. $\text{Tb}(\text{GdC8})_3$ was synthesized using GdC8 , as explained in chapter 2, as a zinc-responsive MRI contrast agent, and TbCl_3 . Three equivalents of GdC8 were stirred along with a

single equivalent of TbCl_3 . The resulting complex exhibited a bright green emission under a UV lamp at 300 nm as presented at Fig. 4.24.



Scheme 4.6: Synthetic pathway for $\text{Tb}(\text{GdC8})_3$; i) TbCl_3 , $\text{MeOH}:\text{H}_2\text{O}$ (1:1), rt, 1h.



Figure 4.24: A potential dual-modal fluorescence/MR imaging probe $\text{Tb}(\text{GdC8})_3$ under a UV lamp at 300 nm.

The green luminescence suggest the formation of $\text{Tb}(\text{GdC8})_3$ as observed previously for $\text{Tb}(\mathbf{27})_3$ and $\text{Tb}(\mathbf{32b})_3$. It was then lyophilized in a freeze-dryer to give a white solid containing NaCl as an impurity. $\text{Tb}(\text{GdC8})_3$ was potential to be used as a dual fluorescence-MR imaging agent. Although its excitation wavelength is in the UV region and therefore not of immediate clinical use as it can potentially damage the biological system. A shift to a longer excitation wavelength can still be achieved *via* structural modification. Due to time constraints this work was not pursued any further.

4.4 Summary and Conclusion

A series of novel lanthanide luminescence probes, with the potential for use in molecular imaging, have been synthesized that contain pyridyltriazole moieties. This antenna behaved as a good sensitizer to certain lanthanides, resulting in emissive compounds which potentially could be used as molecular labelling agents in optical imaging modalities. **TbC1** is a clicked-ready luminescence probe with the potential to allow for molecular labelling. This probe has a Φ_F value (19%) which means it could be used in a relatively low concentrations. In addition, its Φ_F value was enhanced further (29%) after clicking it with azide-appended compounds. **TbC2** contains a pyridyltriazole moiety, which was found to coordinate in such a way as to form a closed structure. It had no water molecules ($q = 0$) in its coordination sphere, providing high structural stability, reducing the possibility of metal displacement. This ensures the safety aspect, which could be caused by lanthanide decomplexation during the imaging process. Several **TbC2** derivatives were synthesized to examine their potential applications, for example, as water soluble luminescence probes (**TbC2a**, **TbC2b**), polymerizable water soluble luminescence probes (**TbC2c**) and a combination of two probes giving similar luminescence intensities in lower concentrations (**TbC2-dimer**).

The tridentate chelator, pyridyltriazole, containing carboxylate acid (**27**), was found to be a good sensitizer for emissive lanthanides such as Tb and Eu, as well as for other lanthanides such as Dy and Sm. It was found to bind in a 3:1 ratio to fill the nine coordination binding sites of the corresponding lanthanides (**Ln(27)₃**). It provided a low luminescence quantum yield with Eu (1.6%), but has a sufficiently high value with Tb (16.3%) for potential use. The combination of the emissive terbium and gadolinium complex to produce **Tb(GdC8)₃** has potential as a dual-modal fluorescence/MR imaging probe.

Chapter 5

Conclusions and Future Work

5.1 Conclusions

5.1.1 Synthesis of Zinc(II)-responsive MRI Contrast Agents and Their Examination

The attempts presented in this thesis were designed to achieve the ultimate aim of synthesising a zinc(II)-responsive MRI contrast agent using the pyridyltriazole moiety as an active arm. This active arm was synthesized by exploiting the “click” reaction synthetic method. Since its inception in the late 20th century, this method is now widely used to form compounds containing the triazole unit that are utilized as ligands, chelating agents, antennae and even drugs due to their structural similarities to certain amino acids such as histidine.^{82,85,86,166} The use of pyridyltriazole as a ligand has been taken into an intensive research object in our research group through the development of potential imaging probes. Pyridyltriazole provides two coordination sites together with their typical structure allowing flexibility in the associated coordination geometry. One of the main subjects considered in this project is the potential of the pyridyltriazole as a chelating agent for one of the essential biological transition metals, zinc(II). This transition metal is important since it is involved in various biological processes including some of the severe diseases as extensively described in Chapter 1.

The challenges associated with making a perfect zinc-responsive MRI contrast agent are: the complex's structural stability with regards to minimizing gadolinium toxicity; and the reversible binding affinity of the active arm allowing different responses to the presence of targeted stimuli. These contrast agents should have a high sensitivity to allow *in vivo* application in which the concentration/binding constant should be relevant to the physiological concentration inside the body and with a high selectivity. Some additional features that can increase the quality of the probe such as possibility of its concentration to be estimated inside living organisms, ease of study during synthesis in the laboratory, and the possibility of being used with other modalities to give accurate results, should also be considered.

Various synthetic routes were attempted in order to achieve the targeted compound; however, there are two main synthetic routes that were used in synthesizing the complexes presented in this report. The first method was by synthesizing the

lanthanide complex prior to further modification by click chemistry. The second method, which was favoured with respect to purification processes and yields, was synthesis of the entire ligand (including the active arm) before lanthanide complexation.

LnC2 was the first target compound used as a model for a GdDO3A-based MRI contrast agent containing a pyridyltriazole active arm. The overall coordination binding in this complex results in a $q = 0$ complex, which is considered a good starting point from which to develop a zinc-responsive MRI contrast agent with a switch-on response. The zinc-responsive examination, which was conducted *via* its corresponding europium complex analogue, however, exhibited nonresponsive behaviour towards the zinc(II) ions. The combination of the pyridyltriazole active arm and DO3A as the main ligand *via* one carbon linker is suspected to produce a closed structure, preventing the pyridyltriazole active arm from interacting with the surrounding environment, therefore making its displacement by zinc(II) ions unlikely. This led to the formation of **LnC4**, in which the active arm was more exposed to the environment, by swapping the orientation of the pyridyltriazole which was synthesized by a “reverse” click chemistry method. It was expected that the interaction between this active arm and the zinc(II) ion would correspondingly increase. Unfortunately, this effort was not sufficient to displace the coordination binding between the lanthanide centre to the zinc(II) ion. The zinc-responsive examination *via* its corresponding europium complex analogue showed the same unresponsive behaviour experienced by **LnC4** towards the zinc(II) ion. This suggests that the coordination resulting in five-membered chelate rings in **LnC2** and **LnC4**, as illustrated in Fig. 5.1, were responsible for their inertness to coordination-displacement.

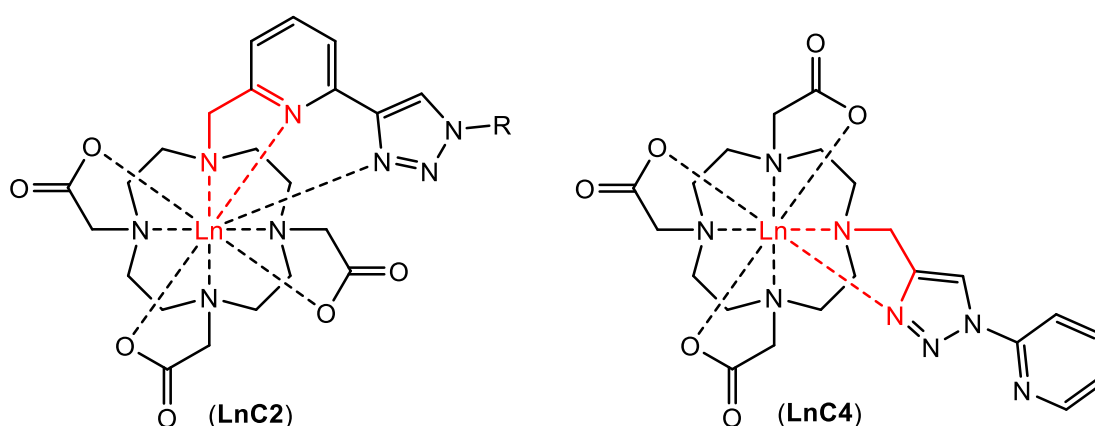


Figure 5.1: The five-membered chelate rings (marked in red) in **LnC2** and **LnC4** believed to cause stable coordination binding.

On the other hand, the presence of direct coordination, as presented in these ligands (in **LnC2** and **LnC4**), provides a relatively efficient energy-transfer that results in a high emission intensity of luminescent lanthanides such as europium and terbium.

A strategy was devised to design a complex with an additional carbon linker from one carbon in the previous compounds (**LnC2** and **LnC4**) to three and two carbon linkers to form **LnC5** and **LnC6** respectively (Fig.5.2). Instead of using a “reverse-clicked” pyridyltriazole (*via* 2-azidopyridine precursor) as in **LnC4**, the “regular-clicked” pyridyltriazole was chosen with respect to the synthetic problems associated with the formation of tetrazole, as shown in Scheme 2.10. Addition of the carbon linker increases the distance between the pyridyltriazole active arm and the lanthanide metal centre. This elongation significantly reduces the coordination binding stability. There was no indication of the formation of stable six- or seven-membered rings coordinating between the pyridyltriazole active arm and the lanthanide metal centre. As observed in the corresponding europium complexes, the europium emission intensity is significantly lower than those in **EuC2** and **EuC4**. In addition, pyridyltriazole fluorescence, which was previously absent in **EuC2** and **EuC4**, now appeared in **EuC5** and **EuC6**. Furthermore, the increasing distance affects the efficiency of the energy transfer between the pyridyltriazole active arm and the lanthanide metal centre. This was indicated by a significant decrease in the emission intensity of the corresponding europium (~ 575-725 nm) or terbium (~ 450-650 nm) complexes and by a significant increase in the pyridyltriazole active arm emission (~ 300-450 nm). By reducing the number of carbon linkers from three in **LnC5** to two in **LnC6**, the emission from the lanthanide centre (europium or terbium) was significantly increased whilst simultaneously decreasing the pyridyltriazole emission. Thus, the energy transfer process is, indeed, distance dependent.

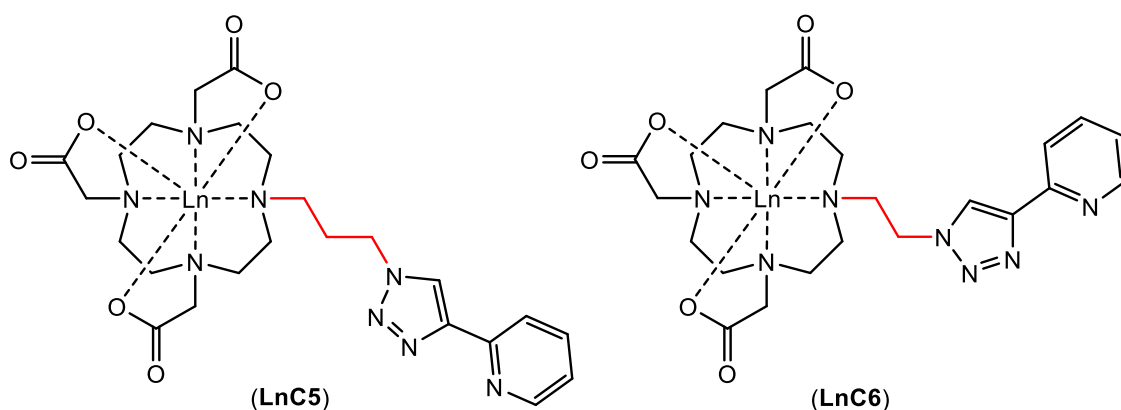


Figure 5.2: Pyridyltriazole arm containing three (**LnC5**) and two (**LnC6**) carbon linkers.

Luminescence lifetime experiments for **LnC5** confirmed the formation of a $q = 2$ complex, which means the pyridyltriazole was not involved in the lanthanide coordination sphere, whilst by shortening the linker (two-carbon), as in **LnC6**, there was no significant change in the coordination sphere with the formation of a $q = 1.8$ complex. Therefore, further structural modifications were required to attract the pyridyltriazole active arm back into the lanthanide coordination sphere. In contrast to **LnC4** in terms of synthetic processes, further structural modifications to these two complexes (**LnC5** and **LnC6**) are, relatively speaking, much more straightforward. However, owing to the competition reaction (substitution vs. elimination) experienced during the pyridyltriazole active arm attachment (to form compound **20**) during the synthesis of **LnC6**, the yields were significantly reduced (Fig. 5.3), and hence further studies to modify this complex were discontinued. The modifications then focussed on **LnC5** in order to bring the pyridyltriazole active arm into closer proximity or to be involved in the lanthanide coordination sphere. This was achieved by introducing electron rich functional groups such as a hydroxyl or carboxylic acid. The introduction of such groups was initially expected to increase the coordination affinity of pyridyltriazole towards the lanthanide metal centre due to the electrostatic interaction with the positively charged lanthanide centre.

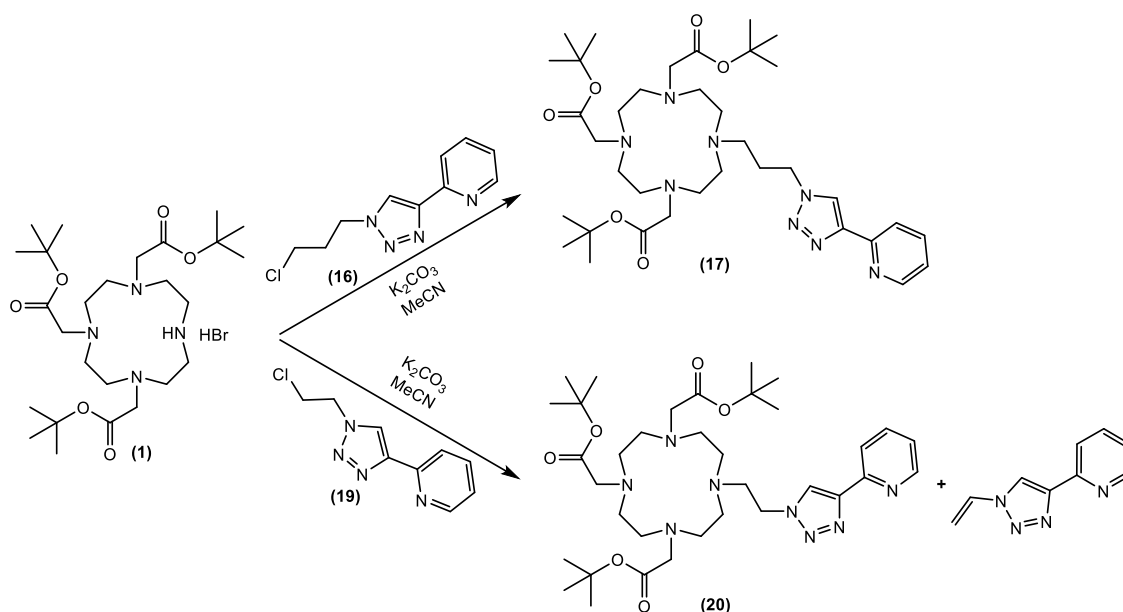


Figure 5.3: The attachment of a two-carbon linker pyridyltriazole active arm resulting in a competition reaction between substitution and elimination.

LnC7 (Fig. 5.4 (left)) is a modification of **LnC5** modified complex containing a hydroxyl functional group appended to the pyridine ring. It was synthesized using a

similar pyridine starting material to that used in the synthesis of **LnC1** and **LnC2**. The photophysical studies conducted on its corresponding europium analogue (**EuC7**) showed a similar emission pattern as presented in **EuC5**. **EuC7** also has two emission bands corresponding to the pyridyltriazole and the europium. This indicated the lack of coordination binding *via* this active arm to the lanthanide centre, this was also found for **LnC5**. This was then confirmed by lifetime studies, which indicated the occurrence of a $q = 2$ complex. **LnC8** (Fig. 5.4 (right)) was prepared containing a carboxylic acid group, which would have a negative charge at pH 7.4. This was expected to increase the coordination affinity of the pyridyltriazole towards the lanthanide centre. The photophysical studies of its corresponding europium complex exhibited a high emission intensity in the corresponding europium centre with no emission bands observed due to the pyridyltriazole moiety. This was an indication of the occurrence of coordination to europium. The lifetime studies for **EuC8** confirmed the presence of one water molecule ($q = 1$) directly coordinated to the lanthanide centre.

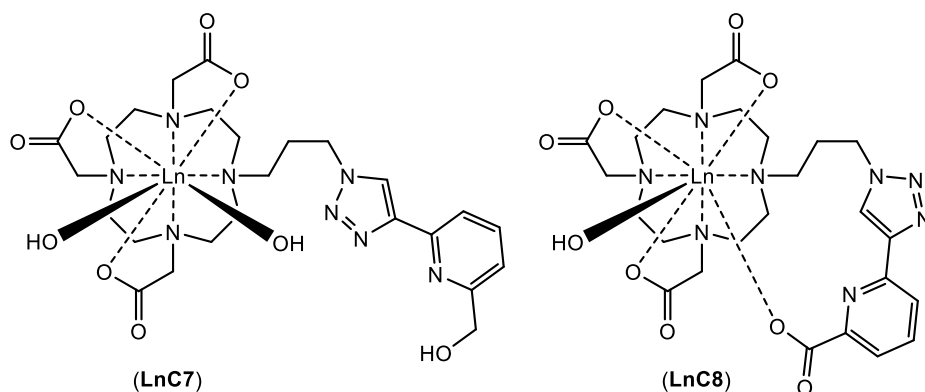


Figure 5.4: Coordination of **LnC7** ($q = 2$) and **LnC8** ($q = 1$).

As expected, the photophysical studies of **EuC8** showed significant changes in the associated emission profile in response to the addition of free zinc(II) ions. By observing the apparent change in hydration number on addition of zinc(II) ions, the probe showed responsive behaviour towards these metal ions in which the hydration number increased gradually from 0.8 to 1.6 during the addition of an equivalent amount of zinc(II) ions. Further examination indicated that **EuC8** has a good selectivity to certain other biological transition metal ions such as iron(II) and calcium(II), but not copper(II); the emission intensity was quenched significantly with copper(II), as expected. The relaxivity measurement of **GdC8** using a 400 MHz NMR probe revealed $r_1 = 6.5 \text{ mM s}^{-1}$. Although the frequency used in this probe is higher than in human clinical MRI scanner, this gives

an approximate relaxivity value for this contrast agent. As expected from the photophysical response to copper(II), this probe experienced an almost identical response to both zinc(II) and copper(II). The relaxivity increased to about 32% and 28% in response to addition of one equivalent of zinc(II) and copper(II), respectively, which should be sufficient to distinguish images during zinc investigations. However, the competition from copper(II) is unlikely to disturb the application of **GdC8** in detecting zinc(II) *in vivo* because the concentration of free copper(II) in biological systems is generally lower than for zinc(II). Moreover, in some cases, the presence of these two transition metals simultaneously can be taken as an indication of certain diseases. Therefore, both could give simultaneous responses during the investigation. **GdC8** also has a relatively good binding constant ($39.0 + 3.1 \mu\text{M}$) towards the zinc(II) ion, which is relevant to the actual concentration in several locations in the body.

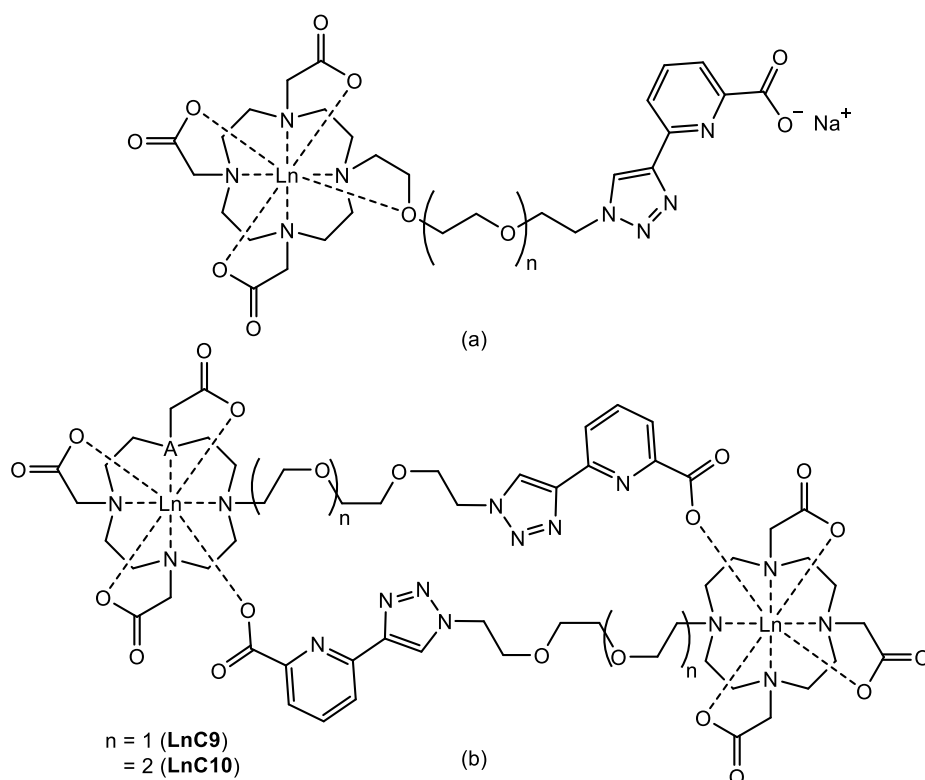


Figure 5.5: Proposed coordination of **LnC9** and **LnC10**: (a) Unimolecular coordination. (b) Formation of a dimer.

LnC8 was modified further in order to examine further potential applications by allowing more space between the active arm and the lanthanide centre *via* elongation of the carbon linker to produce **LnC9** and **LnC10**. The use of polyethylene glycol linkers rather than the hydrocarbon linkers was effectively to maintain their polarity, allowing good water solubility. **EuC9** and **EuC10** showed similar emission profile to **EuC8**, which

only consisted of europium emission bands with no emission from the corresponding pyridyltriazole. The lifetime studies of the analogous europium complex indicated a smaller hydration number ($q = 0.6 \pm 0.2$). In addition, this complex exhibited slightly different behaviour to the original compound (**EuC8**) in response to added zinc(II) ions. Their hydration numbers remained unchanged during further addition of zinc(II), whilst their emission intensities in the presence of zinc(II) ions did change. Although the actual coordination of these two complexes remains unknown due to the lack of crystal data, a hypothetical structure or manner of coordination could be determined based on photophysical data, as illustrated in Fig. 5.5.

The involvement of one of the linker's oxygen atoms to the lanthanide coordination sphere is believed to contribute to steric hindrance, preventing coordination *via* the carboxylic acid binding site, as illustrated at Fig. 5.5 (a). In addition, the formation of the dimer (Fig. 5.5 (b)) is strongly believed easy to occur since the pyridyltriazole is more independent.

5.1.2 Potential Emissive Probes for Molecular Labelling

The study of the coordination properties of **EuC1** and **EuC2** in developing a zinc(II) responsive MRI contrast agent led to further investigation in terms of potential applications that take advantage of their excellent emissive properties. Compared to the europium complexes, it was found that the formation of the terbium complex analogues (**TbC1** and **TbC2**) provided much brighter emission. This could be for several reasons: firstly, the emissive energy levels of the terbium complexes are much closer to the triplet excited energy state of the antenna (but more than 2000 cm^{-1} to prevent energy back-transfer); secondly, the emissive states of terbium experience less quenching by the surrounding water molecules compared to the europium complex. This is because the emissive state of terbium lies higher in energy than europium, and therefore overlaps with a higher vibrational energy level of water resulting in less efficient energy transfer (emission quenching). Quantum yield was determined by comparing their emissions to a standard quinine sulphate solution to give 19% and 29% for **TbC1** and **TbC2**, respectively. **TbC1** can be used as a click-ready probe that can be easily attached to various azide-appended compounds, producing a high green-emissive luminescence. On the other hand, **TbC2** can be attached to many other molecules or functional groups

depending on potential application. Some interesting **TbC2** derivatives (such as **TbC2a**, **TbC2b** and **TbC2c**) are presented in Fig. 5.6 (top left).

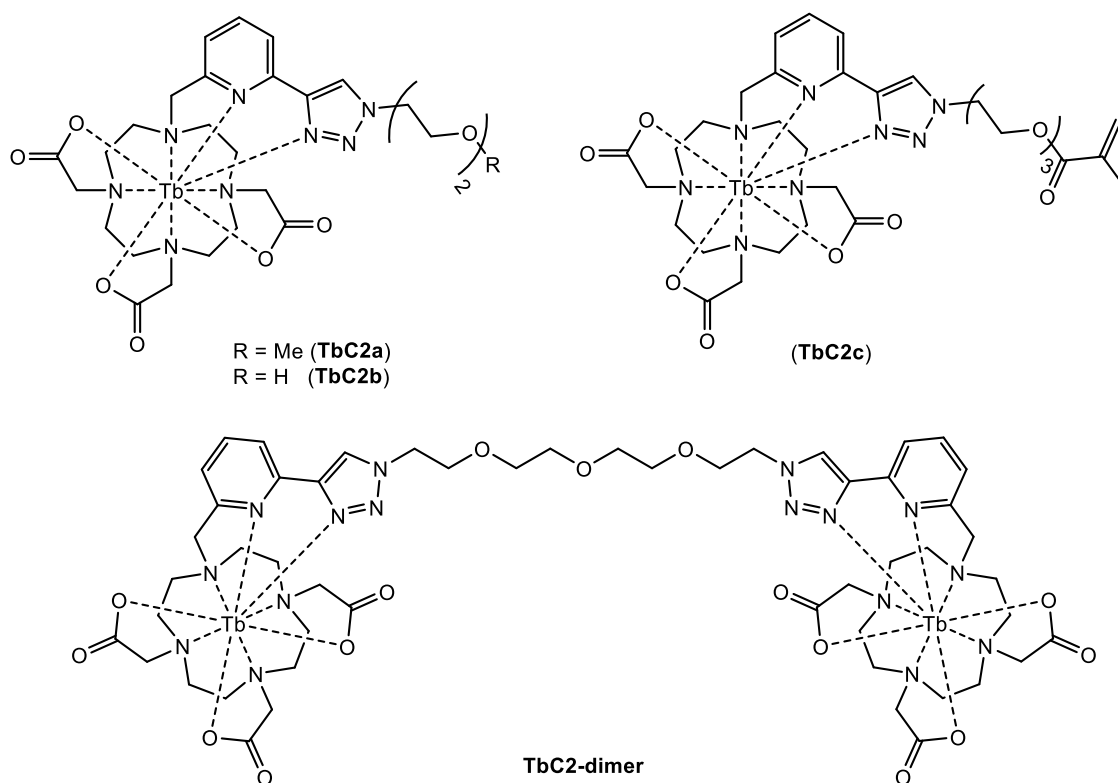


Figure 5.6: **TbC2** derivatives; Functionalization polyethylene glycol tails **TbC2a** and **TbC2b** (top left); Attaching a polymerizable functional group to form polymerize-ready **TbC2c** (top right); Combining two **TbC2** via a tetraethylene glycol resulting a dimer (**TbC2**)₂ (bottom).

The formation of the dimer (**TbC2-dimer**) (Fig. 5.6 (bottom)) would not increase the quantum yield proportionally, however, a similar emission intensity to **TbC2** was achieved with only half the concentration. The use of the polyethylene glycol linker also maintained the water solubility of this dimer. In addition, functionalization of the **TbC2**'s tail with a polymerizable linker to form **TbC2c** allowed the polymerization of this emissive probe to enable its potential use in additional applications (Fig. 5.6 (top right)). The pyridyltriazole containing carboxylic acid group also exhibited a good antenna-chelator for certain lanthanide trivalent ions. **Tb(27a)**₃/**Tb(32b1)**₃ and **Eu(27a)**₃/**Eu(32b1)**₃ show high green ($\Phi_F = 16.3\%$) and red ($\Phi_F = 1.6\%$) fluorescence emission, respectively, when viewed under a 300 nm UV lamp. This led to the formation of a potential dual-modal fluorescence/MR imaging probe, **Tb(GdC8)**₃, as presented in Fig. 5.7.

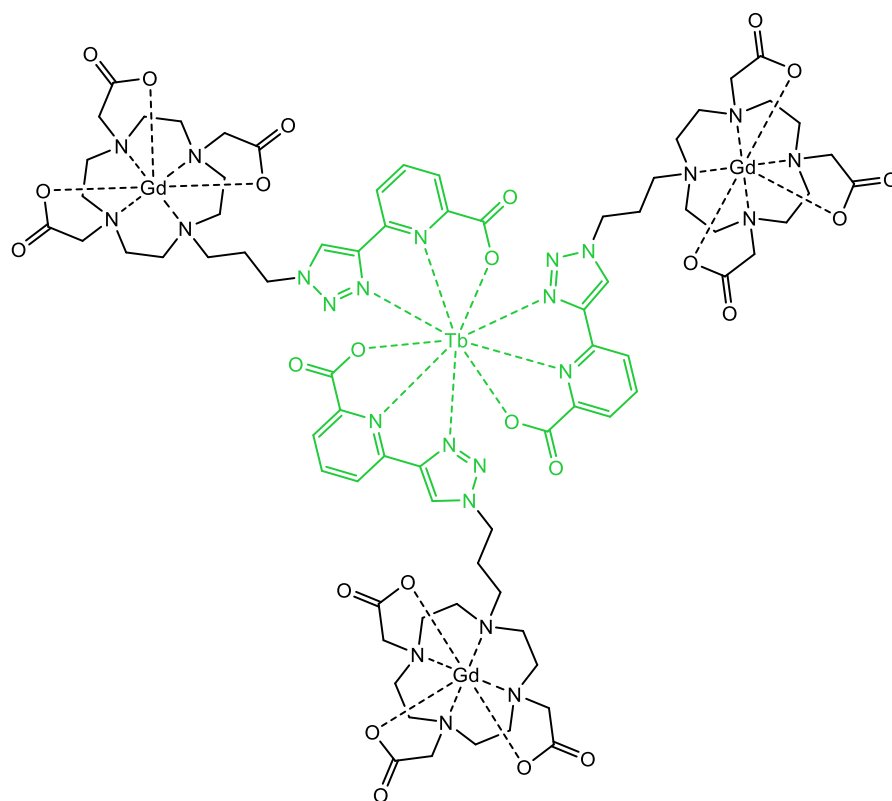


Figure 5.7: Potential dual-modal fluorescence/MR imaging probe, **Tb(GdC8)₃**.

5.2 Future Work

The next project that could be suggested is to test this new zinc(II)-responsive MRI contrast agent (**GdC8**) *in vivo*. Further development of this potential probe is also required in order to meet all requirements for *in vivo* applications. In particular, if the Tb/Eu complexes are to be used in luminescence probes, then the excitation needs to be shifted to longer wavelength. This is commonly achieved by attaching electron-withdrawing groups to the pyridine moiety or by elongation of their conjugated systems (Fig. 5.8). However, this also means that the shift in the excitation band will reduce the excited energy level of the antenna. Therefore, this shift needs to be controlled to ensure the availability of sufficient energy for transfer to the emissive state of the lanthanides centre.

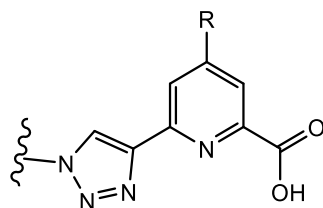


Figure 5.8: Further potential structural modification designed to shift the excitation wavelength by attaching an electron withdrawing group to 4-position of the pyridine ring.

The addition of another triazole group can be predicted to increase the stability of the complex through the formation of nine coordination sites to give a $q = 0$ complex, as illustrated in Fig. 5.9.

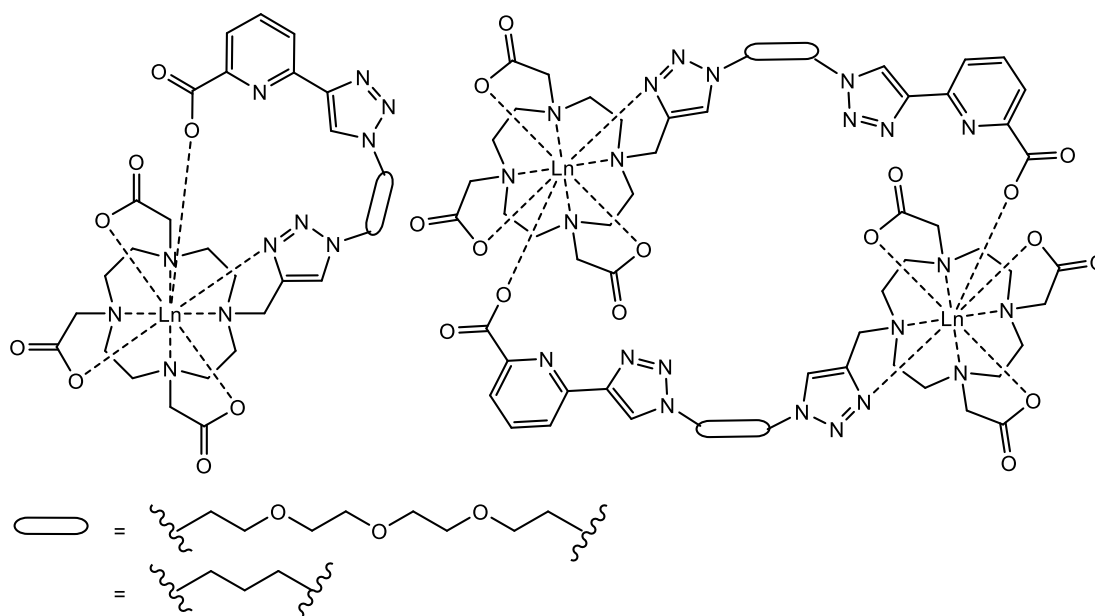


Figure 5.9: An additional triazole moiety, providing a $q = 0$ unimolecular (left) or bimolecular (right) complex.

Development of dual-modal probes could also potentially be undertaken by exploiting the pyridyltriazole in **LnC5**, **LnC6**, **LnC7**, **LnC8**, **LnC9** and **LnC10** (Fig. 5.10 (A)) as a metal chelator. Moreover, an additional triazole group would be expected to provide more stable lanthanide complexes (Fig. 5.10 (B)), as explained previously. The attachment of certain emissive transition metals, such as Ir, Re or Ru to the pyridyltriazole moiety (**LnC5** and **LnC6**), combined with other chelating ligands could potentially provide dual-modal probes that could be used in the various applications previously reported by a number of research groups.^{210,211,212,213,214} One of these (**LnC6**), had been used others in the Lowe group in combination with several transition metals, such as Fe, to produce trimeric MRI contrast agents, as well as with Re and Ir to provide dual-modal fluorescent/MR imaging agents. **LnC7**, **LnC8**, **LnC9** and **LnC10** with a hydroxyl or carboxyl group on their pyridyltriazole moieties, on the other hand, represent potential tridentate ligands for Pt(II) chelation, similar to a number of reported tridentate “NNN” ligands.^{215,216,217}

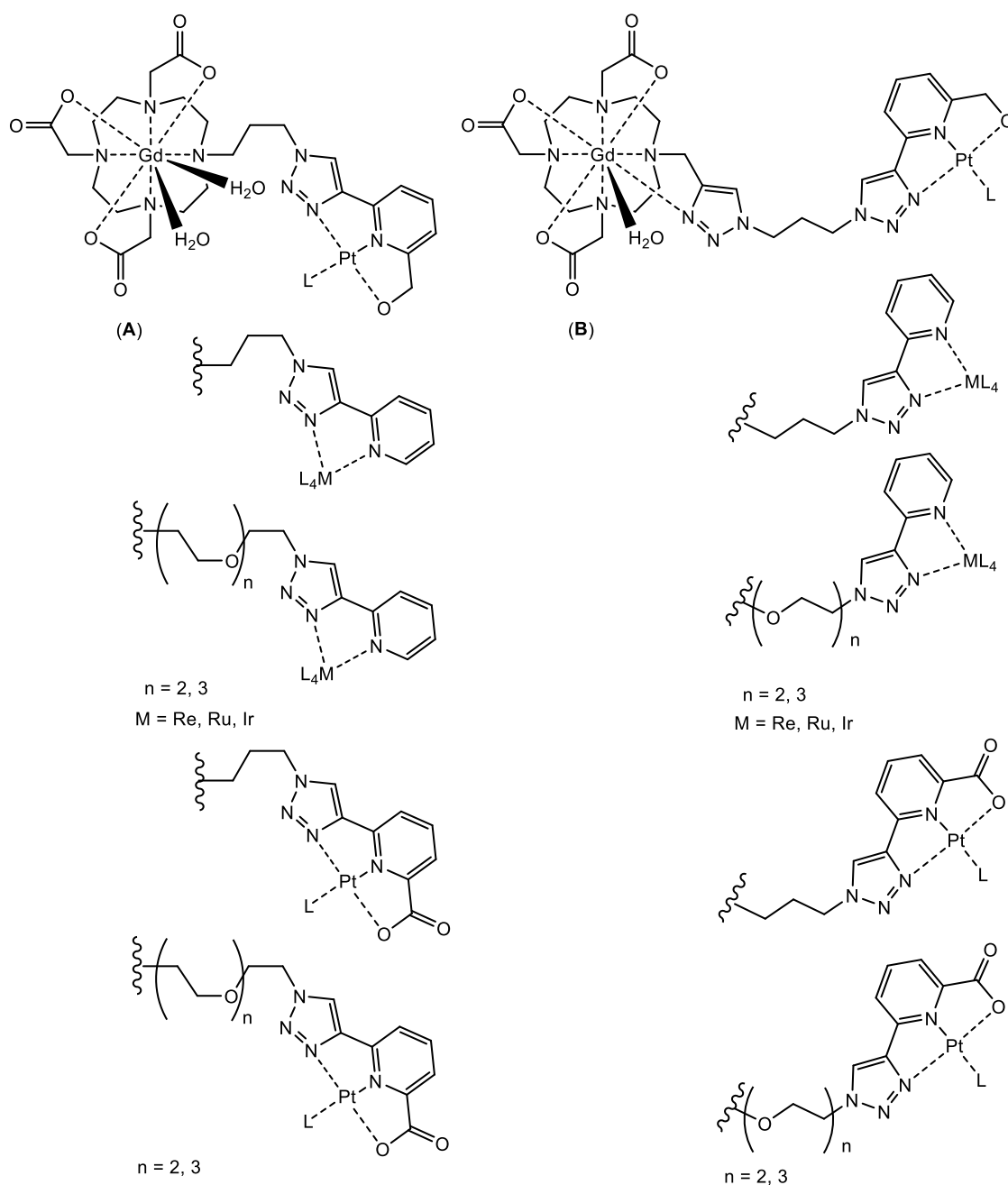


Figure 5.10: Potential dual-modal fluorescence/MR imaging probes.

It is believed that increasing the number of antenna will increase the fluorescence quantum yield of **TbC2** and its complex derivatives significantly. Furthermore, the application of polyethylene glycol should maintain its water solubility. By introducing or substituting two pyridyltriazole or just a triazol antennae to the **TbC2/GdC2** should give resulting structures that can also be polymerized, as illustrated in Fig. 5.11.

Similar attempts could also be made with the compound **Tb(GdC8)₃** as a potential dual-modal fluorescence/MR imaging probe to form a polymeric dual-modal fluorescence/MR imaging probe, **Tb(GdC8)₃-polymer**, as illustrated in Fig. 5.12. Due to

the fast response of the pyridyltriazole that contains a carboxylic acid group towards ligation with lanthanide ions, polymerization would therefore be a spontaneous process (self-assembly). These probes are predicted to have good solubility in water due to their lipophilic polyethylene linker, in contrast to some high molecular weight compounds reported in the literature, *i.e.*, multimeric agents.

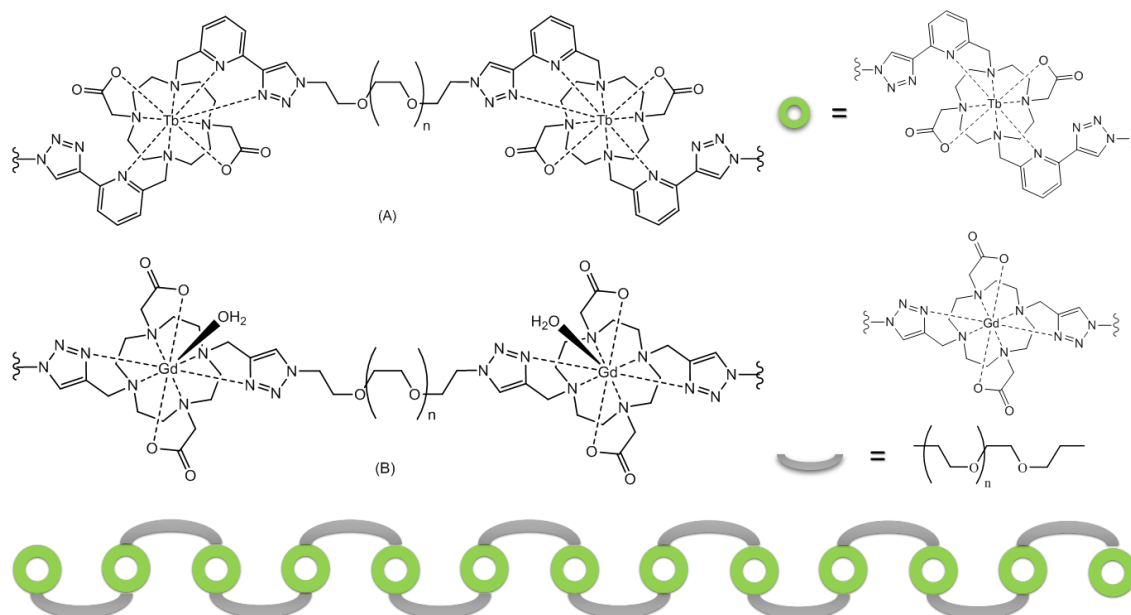


Figure 5.11: Polymeric high emissive fluorescence probe (A) and polymeric MRI probe (B).

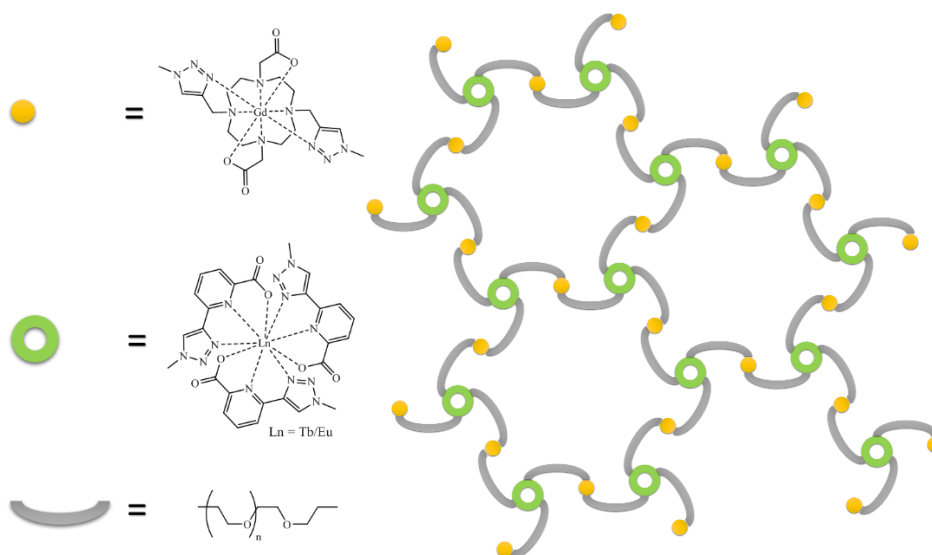


Figure 5.12: Self-assembly dual-modal polymeric probe for MR and fluorescence imaging.

Chapter 6

Experimental

6.1 Materials

All solvents used were in high purity and purchased from commercially available sources without any further purification unless otherwise stated, with the exception of water, which was obtained from a Millipore purification system, Pure Solve™. All chemicals and starting materials were purchased either from Sigma Aldrich, Acros Organics, Fisher Scientific or Alfa Aesar.

6.2 Chromatography Studies

Semi-preparative HPLC was conducted on a Thermo Fisher Ultimate 3000 with chromeleon software on Phenomenex Luna C18 column. Preparative and analytical reverse-phase HPLC were conducted by using a method as follow: 5% B for 5 min, 5-100 % B over 30 min, 100% B for 5 min, 100-5 % B over 5 min, 5 % B for 5 min. (Solvent A 0.1 % TFA in H₂O or 100% H₂O, and solvent B 0.1% TFA in MeCN or 100 % MeCN).

6.3 Spectroscopy Studies

6.3.1 NMR Spectroscopy Studies

All NMR spectra were recorded either on Bruker DRX 300 (300 MHz) DRX400 (400 MHz), AV400 (400 MHz) and AV500 (500 MHz) spectrometers at 298K unless otherwise stated, by using a variety of deuterated NMR solvents including CDCl₃, DMSO-d₆, CD₃OD and D₂O. The chemical shifts are quoted in ppm relative to tetramethylsilane. All spectra were processed with ACDLabs Spectrus Processor 2016 including the coupling constants.

6.3.2 UV-Vis and Fluorescence Spectroscopy Studies

Absorption spectra were obtained from a Shimadzu UV-1024PC spectrometer using a 1 x 1 cm quartz Hellma cuvette. Luminescence spectra were recorded using a Jobin Yvon Horiba FluorMax-3 spectrometer in a 1 x 1 cm quartz Hellma cuvette. The luminescence spectra and lifetime measurements of all complexes were recorded either in water or aqueous 50 mM HEPES buffer pH / pD 7.4 at constant ionic strength (0.1 M

NaCl). The bandpass were 5 : 1 nm for both excitation and emission. The metal titrations were conducted by addition of standard free-metal solution gradually (5 μ L aliquots) to achieve the sufficient equivalent concentration to 3000 μ L of the corresponding complex solutions. The total volume changes were no more than 5-10%.

6.3.3 Mass Spectrometry Studies

High resolution mass spectra were analysed on a Water Acquity XEVO Q ToF spectrometer or Applied Biosciences Voyager DE-STR MALDI TOF spectrometer. Instrument parameter; capillary voltage is 3 kV, cone voltage 30 V and collision energy 4 eV. The MS acquisition rate is 10 spectra per second and recorded as m/z. Mass accuracy was achieved using lock mass scan, once every 10 second. Samples are dissolved either in MeOH, EtOH or MeCN.

6.3.4 Crystallography Studies

X-ray crystallography experiments were collected on a Bruker Apex 2000 CCD diffractometer using graphite monochromated Mo-K α radiation, $\lambda = 0.7107 \text{ \AA}$. The data were corrected for Lorentz and polarisation effects and empirical absorption corrections were applied. The structure was solved by direct methods and structure refinement on F^2 employed SHELXTL version 6.10. Hydrogen atoms were included in calculated positions (C-H = 0.95-0.99 \AA) riding on the bonded atom with isotropic displacement parameters set to 1.5 U_{eq} (C) for methyl hydrogen atoms and 1.2 U_{eq} (C) for all other H atoms. All non-hydrogen atoms were refined with anisotropic displacement parameters.

6.3.5 Relaxation-time Measurements

Longitudinal relaxation time (T_1) of the corresponding gadolinium complex for both in the absence and the presence of divalent metal ions were measured at 298K, 400 MHz, 9.4 T (Bruker AV-400 NMR spectrometer). The corresponding gadolinium complex (1 mM) was prepared in 10 mL of 1 % *tert*-butyl alcohol in 50 mM HEPES buffer solution containing 0.1 M NaCl, pH 7.4. Its exact concentration was measured by Evan's method in a co-axial capillary tube placed inside the 5 mm NMR sample tube comprising 1% *tert*-butyl alcohol in D₂O.¹⁷¹ The relaxation time values were calculated from 16 points generated *via* standard inversion-recovery procedure which is fit by the Eqn 6.1 to give T_1 value and its relaxivity (r_1) were determined by using Eqn 6.2.

$$M_z = M_0 \left[1 - 2 \exp\left(\frac{-\tau}{T_1}\right) \right] \quad (6.1)$$

M_z = magnetisation
 M_0 = magnetisation
 τ = time delay
 T_1 = longitudinal relaxation (s)

$$r_1 = \frac{\left(\frac{1}{T_1}\right)^{-0.4}}{[Gd]} \quad (6.2)$$

r_1 = relaxivity ($\text{mM}^{-1} \text{s}^{-1}$)
 $[Gd]$ = concentration of the gadolinium complex (mM)
 0.4 = diamagnetic contribution of H_2O

6.4 General Synthetic Methods

6.4.1 Sonogashira Reactions

The corresponding bromide starting materials, $\text{Pd}(\text{PPh}_3)_2\text{Cl}_2$ and CuI were placed in a *schlenk* tube. After degassing, 8 mL Et_3N was then added *via* a syringe. It followed by addition of the corresponding alkyne *via* a syringe. After heating at 50°C for 1 hour the reaction was shown to be complete by TLC (SiO_2 , 100% EtOAc). The reaction mixture was allowed to cool to room temperature, then 18 mL of diethyl ether was added before being washed by 10 mL saturated NH_4Cl solution three times. The organic layer was separated, dried with MgSO_4 , filtered and concentrated under reduced pressure.

6.4.2 Chlorination Reactions

The corresponding starting material was dissolved in 10 mL DCM. It was cooled in an ice bath under an inert atmosphere. Thionyl chloride was added dropwise *via* syringe under stirring, the temperature was allowed to increase to room temperature. After stirring for 3 hours, the reaction was shown to be complete by TLC (SiO_2 , 100% EtOAc). The reaction mixture was the poured into 10 mL NaHCO_3 1M solution before 25 mL of DCM was added. The organic layer was separated, dried with MgSO_4 , filtered and concentrated under reduced pressure.

6.4.3 The DO3A's Fourth Arm Attachments

Compound **1** and potassium carbonate were placed in the *schlenk* line, which was degassed before the corresponding fourth arm was added (in 15 mL acetonitrile) *via* a syringe. After heating at reflux overnight, the reaction completion was monitored by TLC

(SiO₂, MeOH:DCM/1:9). 5 mL NaHCO₃ (1M) was then added, followed by 20 mL dichloromethane. The organic layer was separated, dried with MgSO₄, filtered and concentrated under reduced pressure.

6.4.4 *Macrocycle's tert-Bu Deprotection Reactions*

The corresponding macrocycle was dissolved in 10 mL DCM:TFA (1:1), and stirred in an open atmosphere. The reaction was monitored by TLC or MS. The reaction mixture was concentrated in reduced pressure. 30 mL DCM was added to the residue and then removed under reduced pressure. This process was repeated three times with DCM and once with diethyl ether to give a brown oily product.

6.4.5 *Trimethylsilyl (TMS) Deprotection Reactions*

6.4.5.1 *Procedure 1*

To the corresponding TMS protected compound (in 10 mL methanol) was added 5 mL potassium carbonate (1 M). It was stirred for 1 h at room temperature and monitored by TLC (SiO₂, EtOAc 100%). It was then extracted with 10 mL DCM three times. The combined organic solvent was dried with MgSO₄, filtered and concentrated under reduced pressure.

6.4.5.2 *Procedure 2*

To the corresponding TMS protected compound (in 10 mL THF) was added TBAF. The solution was then stirred at a room temperature for 1 h. The reaction completion was monitored by TLC (SiO₂, EtOAc 100%). The reaction mixture was concentrated in reduced pressure.

6.4.6 *Click Reactions*

6.4.6.1 *Procedure 1*

The corresponding bromide starting material and sodium azide were dissolved in 20 mL of EtOH:H₂O (7:3) and heated in a microwave reactor at 125°C 150psi for 1 h. The corresponding alkyne starting material, CuSO₄·5H₂O, and sodium ascorbate were then added. After microwave heating at 65°C for a further 1 h. The reaction completion was shown by TLC (SiO₂, EtOAc 100%). To the reaction mixture was added to 10 mL of saturated EDTA solution (made pH 10 by NH₄OH conc.) before being extracted with

20 mL DCM/EtOAc three times. The combined organic layer was dried with MgSO₄, filtered and concentrated under reduced pressure.

6.4.6.2 Procedure 2

The corresponding bromide starting material and sodium azide were dissolved in 10 mL EtOH : H₂O (7:3). After heated at reflux for 18 h, the mixture was cooled to room temperature. The corresponding alkyne starting material, CuSO₄.5H₂O and sodium ascorbate were then added. After stirring at a room temperature for 18 h, the reaction completion was confirmed by TLC (SiO₂, EtOAc 100%). The reaction mixture was then poured into 10 mL saturated EDTA solution (made pH 10 by NH₄OH) before been extracted by 20 mL ethyl acetate 3 times. The combined organic solvent was dried with MgSO₄, filtered and concentrated under reduced pressure.

6.4.6.3 Procedure 3

The corresponding azide, the corresponding alkyne, CuSO₄.5H₂O and sodium ascorbate were dissolved in 40 mL MeOH:H₂O (3:1). After heated at 65°C overnight the reaction was shown to be complete by TLC (SiO₂, EtOAc 100%). The reaction mixture was then poured into 10 mL saturated EDTA solution (made pH 10 by ammonia) before been extracted by 20 mL EtOAc three times. The combined organic solvent was dried with MgSO₄, filtered and concentrated in reduced pressure.

6.4.6.4 Procedure 4

The corresponding tosylate and sodium azide were dissolved in 20 mL MeOH:H₂O (3:1). After heating at reflux overnight the reaction was shown to be complete (monitored by TLC of tosylate starting material). To the reaction mixture, lanthanide complex (alkyne), CuSO₄.5H₂O and sodium ascorbate were added. It was then reheated at 65°C overnight. The reaction was showing to the completion by MS.

6.4.7 Synthesis of Azides

6.4.7.1 Procedure 1

The corresponding bromide starting material, CuI, NaAscorbate and NaN₃ were dissolved in 20 mL EtOH:H₂O (7:3) and heated in a microwave reactor at 125°C, 150psi for 1 h. The reaction completion was monitored by TLC (SiO₂, 100% EtOAc). The

reaction mixture was poured into 10 mL saturated EDTA solution (made pH 10 by NH_4OH conc.). It was extracted by 20 mL ethyl acetate 3 times. The combined organic solvent was dried with MgSO_4 , filtered and concentrated under reduced pressure.

6.4.7.2 Procedure 2

The corresponding tosylate starting material dissolved in 40 mL H_2O :acetone (1:3) was added sodium azide. After heating at reflux (75°C) overnight, it was cooled to room temperature before was poured into 50 mL H_2O . It was extracted by 20 mL DCM three times. The combined organic layer was dried with MgSO_4 , filtered and solvent was removed under reduced pressure.

6.4.8 Tosylation Reactions

The corresponding starting material was dissolved in 10 or 20 mL dry pyridine in a water bath at $\pm 0-4^\circ\text{C}$. Tosyl chloride was added stepwise. After stirring overnight, the reaction mixture was poured into 30 mL cold water in an ice bath. It was then acidified by addition of HCl conc. dropwise (monitored by pH paper), before it was then extracted with 30 mL DCM three times. The combined organic layer was washed with 20 mL HCl 0.1 M aqueous solution five times to remove any remaining pyridine. It was dried with MgSO_4 , filtered and concentrated under reduced pressure.

6.4.9 Lanthanide Complexation

6.4.9.1 Procedure 1

The corresponding ligand was dissolved in 10 mL deionized water. The corresponding lanthanide was then added ($\text{LnCl}_3 \cdot 6\text{H}_2\text{O}$). The pH of the solution was adjusted to ~ 6.4 by using 0.1 M NaOH and 0.1 M HCl . The mixture was heated at reflux for 18h. After cooling the pH was adjusted to 10 with 0.1 M NaOH to precipitate the unreacted free lanthanide(III) as $\text{Ln}(\text{OH})_3$ which was then filtered through celite. The pH of the filtrate was adjusted to ~ 7.0 using 0.1 M HCl . The absence of free lanthanide(III) ions was confirmed by xylenol orange tests. After *freeze-drying*, purification *via* reverse phase HPLC gave white hygroscopic solids.

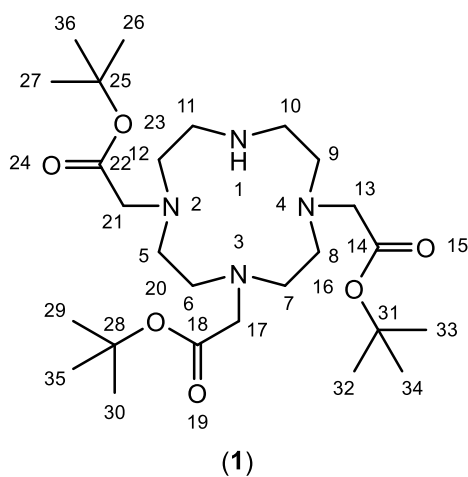
6.4.9.2 Procedure 2

The corresponding ligand was dissolved in 10 mL deionized water. The corresponding lanthanide was then added ($\text{LnCl}_3 \cdot 6\text{H}_2\text{O}$). The pH of the solution was then

adjusted to ~6.4 by using 0.1 M NaOH and 0.1 M HCl. The mixture was heated at reflux for 18h. After cooling the pH was adjusted to 10 using 0.1 M NaOH to precipitate the unreacted free lanthanide(III), which was then filtered through celite. The pH of the filtrate was adjusted to ~7.0 using 0.1 M HCl. The absence of free lanthanide(III) ions was confirmed by xylenol orange tests. The pH was increased to 9 and the solution was then heated at reflux overnight. After cooling to room temperature the pH was adjusted to 7. After *freeze-drying*, it was purified *via* reverse phase HPLC to give a white hygroscopic solid.

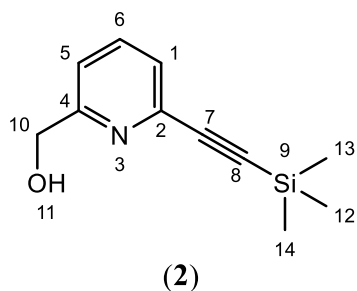
6.5 Synthetic Compounds

6.5.1 Synthesis of *tri-tert-butyl 2,2',2''-(1,4,7,10-tetraazacyclododecane-1,4,7-triyl)triacetate (1)*¹³⁸

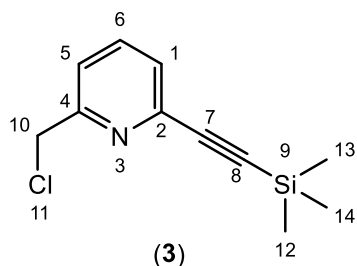


Cyclen (1.116 g, 6.48 mmol) and sodium acetate (1.594 g, 19.44 mmol) were dissolved in 15 mL dimethylacetamide at 0°C. *tert*-butylbromoacetate (3.792 g, 19.44 mmol) in 2.5 mL dimethylacetamide was added drop-wise. After completion, the temperature was allowed to increase to room temperature and the reaction mixture was closed, sealed, and stirred for 4 days.

The reaction mixture was poured into 35 mL warm water ($\pm 50^{\circ}\text{C}$) containing KBr (1.175 g, 9.721 mmol) to give a pale-yellow solution. The pH was adjusted to 9 by the additional of solid NaHCO_3 to produce white suspension. It was left without stirring for 4 h to give time for sedimentation. It was filtered and dried to give a white solid (2.145 g, 55.5%). ^1H NMR (400 MHz, CDCl_3) δ = 9.96 (2H, br s, H-1), 3.39 (4H, s, H-21, 13), 3.30 (2H, s, H-17), 3.10 (4H, br d, J = 4.7 Hz, H-11, 10), 2.79 - 3.05 (12H, m, H-12, 9, 7, 6, 8, 5), 1.44 - 1.49 (27H, m, H-35, 30, 29, 36, 34, 33, 32, 27, 26). ^{13}C NMR (101 MHz, CDCl_3) δ = 170.4 (C-22, 14), 169.6 (C-18), 81.7 (C-28), 81.5 (C-31, 25), 58.0 (C-21, 13), 51.2 (C-8, 5, 7, 6), 49.1 (C-11, 10), 48.8 (C-17), 47.4 (C-12, 9), 28.1 (C-35, 30, 29, 36, 34, 33, 32, 27, 26); m/z (ESMS⁺) found 515.3817 (calc. for $\text{C}_{26}\text{H}_{51}\text{N}_4\text{O}_6$ 515.3809) $[\text{M}+\text{H}]^+$.

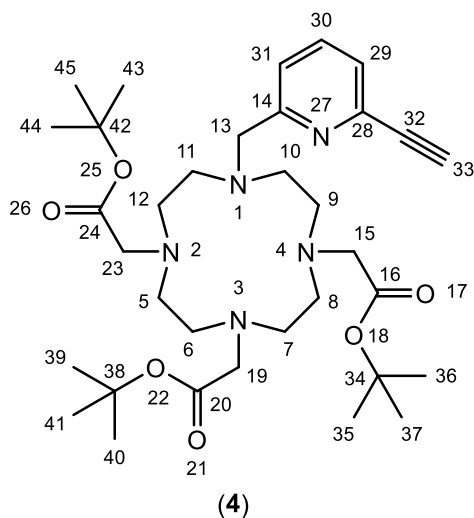
6.5.2 Synthesis of (6-((trimethylsilyl)ethynyl)pyridin-2-yl)methanol (**2**)¹⁵⁴

(6-Bromo-pyridin-2-yl) methanol (0.377 g, 2.010 mmol), Pd(PPh₃)₂Cl₂ (0.0565 g, 0.080 mmol) and CuI (0.018 g, 0.090 mmol) were used as starting materials. It followed the general procedure for Sonogashira reactions (section 6.4.1). Purification *via* flash column chromatography (SiO₂, EtOAc) gave a brown solid (0.218 g, 53%, R_f = 0.58), m.p. 73°C. ¹H NMR (400 MHz, CDCl₃) δ = 7.51 (1H, t, *J* = 7.8 Hz, H-6), 7.24 (1H, dd, *J* = 7.8 Hz, *J* = 0.8 Hz, H-5), 7.12 (1H, dd, *J* = 7.8 Hz, *J* = 1.0 Hz, H-1), 4.62 (2H, br s, H-10), 3.55 (1H, br s, H-11), 0.15 (9H, s, H-14, 13, 12); ¹³C NMR (101 MHz, CDCl₃) δ = 160.0 (C-4), 142.1 (C-2), 136.9 (C-6), 126.2 (C-1), 120.1 (C-5), 103.6 (C-7), 95.3 (C-8), 64.5 (C-10), -0.2 (C-12, 13, 14); *m/z* (ESMS⁺) found 206.1004 (calc. for C₁₁H₁₆NO²⁸Si 206.1001) [M+H]⁺.

6.5.3 Synthesis of 2-(chloromethyl)-6-((trimethylsilyl)ethynyl)pyridine (**3**)

Compound **2** (0.208 g, 1.016 mmol) and thionyl chloride (0.616 g, 5.180 mmol) were used as the starting materials. It followed the general procedure for chlorination reactions (section 6.4.2). Purification *via* flash column chromatography (SiO₂, 100% EtOAc) gave a yellow-brown solid (0.215 g, 95%, R_f = 0.74). ¹H NMR (400 MHz, CDCl₃) δ = 7.74 (1H, t, *J* = 7.8 Hz, H-6), 7.50 (1H, d, *J* = 7.8 Hz, H-5), 7.44 (1H, d, *J* = 7.8 Hz, H-1), 4.73 (2H, s, H-10), 0.27 - 0.30 (9H, m, H-14, 13, 12); ¹³C NMR (101 MHz, CDCl₃) δ = 156.9 (C-4), 142.0 (C-2), 138.0 (C-6), 127.1 (C-1), 122.6 (C-5), 102.4 (C-7), 99.4, 97.4 (C-8), 45.9 (C-10), -0.2 (C-14, 13, 12); *m/z* (ESMS⁺) found 224.0665 (calc. for C₁₁H₁₅³⁵ClN²⁸Si 224.0662) [M+H]⁺.

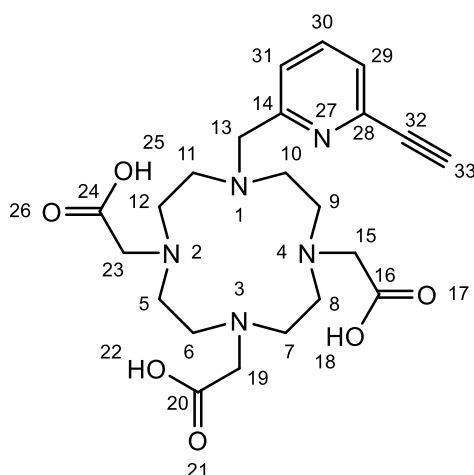
6.5.4 Synthesis of tri-tert-butyl 2,2',2''-(10-((6-ethynylpyridin-2-yl)methyl)-1,4,7,10-tetraazacyclododecane-1,4,7-triyl)triacetate (**4**).



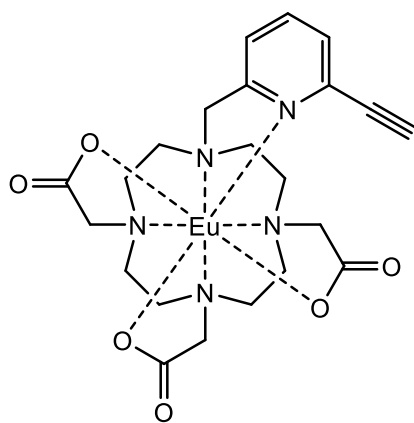
Compound **1** (0.126 g, 0.211 mmol), potassium carbonate (0.135 g, 0.973 mmol) and compound **3** (0.060 g, 0.267 mmol) were used as the starting materials. It followed the general procedure for the DO3A's fourth arm attachments (section 6.4.3). Purification *via* flash column chromatography (SiO₂, MeOH:DCM/1:9) gave viscous oily brown product (80 mg, 60%). ¹H NMR (500 MHz, CDCl₃) δ = 7.74 (1H, t, *J* = 7.8 Hz, H-30), 7.39 (2H, dd, *J* = 7.8 Hz, *J* = 3.3 Hz,

H-31, 29), 2.22 - 3.87 (26H, m, H-19, 7, 6, 13, 11, 10, 12, 9, 23, 15, 33, 8, 5), 1.49 (9H, s, H-41, 40, 39), 1.43 (17H, s, H-45, 44, 43, 37, 36, 35); ¹³C NMR (126 MHz, CDCl₃) δ = 172.2 (C-20), 171.6 (C-24, 16), 158.3 (C-14), 142.1 (C-28), 137.0 (C-30), 126.1 (C-29), 123.7 (C-31), 82.2 (C-32), 81.8 (C-42, 34, 38), 77.4 (C-33), 59.3 (C-13, 23, 15, 19), 56.0 (C-7, 6, 8, 5), 55.6 (C-12, 9), 50.1 (C-11, 10), 27.7 (C-45, 44, 43, 37, 36, 35), 27.6 (C-41, 40, 39); *m/z* (ESMS⁺) found 630.4236 (cal. for C₃₄H₅₆N₅O₆ 630.4231) [M+H]⁺.

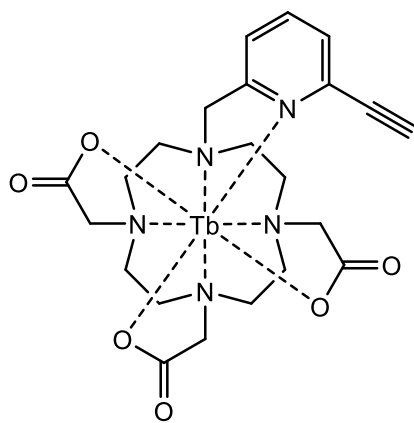
6.5.5 Synthesis of 2,2',2''-(10-((6-ethynylpyridin-2-yl)methyl)-1,4,7,10-tetraazacyclododecane-1,4,7-triyl)triacetic acid (**CI**).



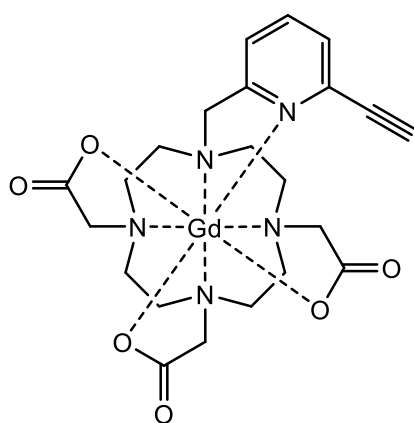
Compound **4** (0.154 mg, 0.244 mmol) was used as the starting material. It followed the general procedure for the macrocycle's tert-Bu deprotection reactions (section 6.4.4). Purification *via* a semi preparation reverse phase HPLC (*R_t* 7.2 min) gave a white hygroscopic solid 93 mg (83%). ¹H NMR (400 MHz, D₂O) δ 7.88 (1H, t, *J* = 7.8 H-30), 7.65 (1H, br, H-31), 7.49 (1H, br, H-29), 4.60-2.58 (24H, br m, H-5, 6, 7, 8, 9, 10, 11, 12, 13, 15, 19, 23), 2.14 (1H, s, H-33); *m/z* (ESMS⁺) found 462.2324 (cal. for C₂₂H₃₂N₅O₆ 462.2353) [M+H]⁺.

6.5.6 Synthesis of **EuC1****(EuC1)**

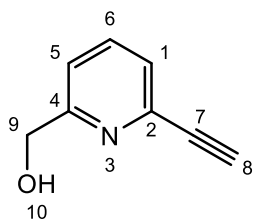
C1 (0.025 g, 0.054 mmol) and $\text{EuCl}_3 \cdot 6\text{H}_2\text{O}$ (0.022 g, 0.060 mmol) were used as starting materials. It followed the general procedure for lanthanide complexation procedure 1 (section 6.4.9.1). Purification *via* HPLC (R_t 7.2 min) gave a white hygroscopic solid 18 mg (54%); ESMS+ m/z found 634.1145 (cal. for $\text{C}_{22}\text{H}_{28}\text{N}_5\text{O}_6^{153}\text{EuNa}$ 634.1150) $[\text{M}+\text{Na}]^+$.

6.5.7 Synthesis of **TbC1****(TbC1)**

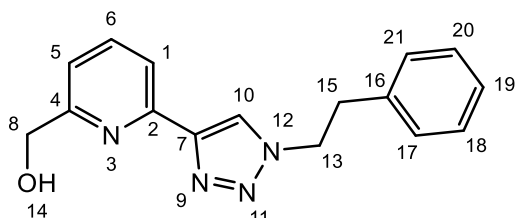
C1 (0.034 g, 0.073 mmol) and $\text{TbCl}_3 \cdot 6\text{H}_2\text{O}$ (0.031 g, 0.083 mmol) were used as starting materials. It followed the general procedure for lanthanide complexation procedure 1 (section 6.4.9.1). Purification *via* HPLC (R_t 7.2 min) gave a white hygroscopic solid 32 mg (71%); (ESMS+) m/z found 640.1199 (cal. for $\text{C}_{22}\text{H}_{28}\text{N}_5\text{O}_6^{159}\text{TbNa}$ 640.1191) $[\text{M}+\text{Na}]^+$.

6.5.8 Synthesis of **GdC1****(GdC1)**

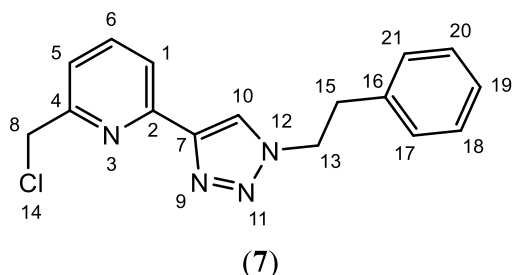
C1 (0.031 g, 0.067 mmol) and $\text{GdCl}_3 \cdot 6\text{H}_2\text{O}$ (0.027 g, 0.072 mmol) were used as starting materials. It followed the general procedure for lanthanide complexation procedure 1 (section 6.4.9.1). Purification *via* HPLC (R_t 7.2 min) gave a white hygroscopic solid 20 mg (48%); (ESMS+) m/z found 639.1198 (cal. for $\text{C}_{22}\text{H}_{28}\text{N}_5\text{O}_6^{158}\text{GdNa}$ 639.1178) $[\text{M}+\text{Na}]^+$.

6.5.9 Synthesis of (6-ethynylpyridin-2-yl)methanol (**5**).**(5)**

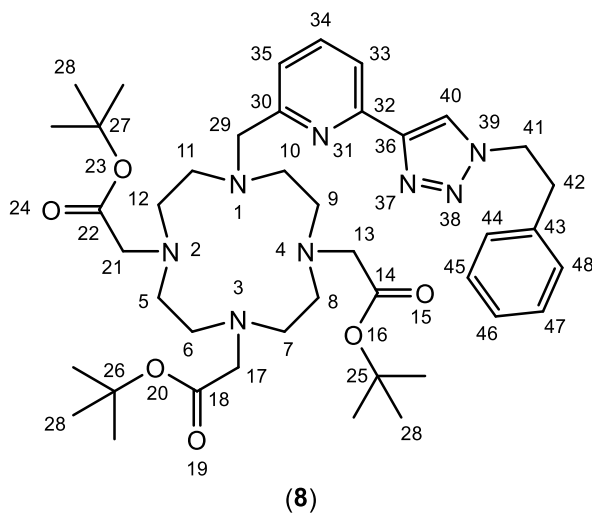
Compound **2** (0.352 g, 1.715 mmol) was used as the starting material. It followed the general procedure for TMS deprotection reactions procedure 1 (section 6.4.5.1). Purification *via* flash column chromatography (SiO₂, EtOAc 100%) gave a white-red solid (0.181 g, 79.5%, R_f = 0.5). ¹H NMR (400 MHz, CDCl₃) δ = 7.67 (1H, t, *J* = 7.8 Hz, H-6), 7.39 (1H, d, *J* = 7.8 Hz, H-1), 7.30 (1H, d, *J* = 7.8 Hz, H-5), 4.76 (2H, s, H-9), 3.79 (1H, br s, H-10), 3.18 (1H, s, H-8); ¹³C NMR (101 MHz, CDCl₃) δ = 160.3 (C-4), 141.3 (C-2), 137.0 (C-6), 126.2 (C-1), 120.6 (C-5), 82.6 (C-7), 77.6 (C-8), 64.4 (C-9); *m/z* (ESMS⁺) found 134.0602 (calc. for C₈H₈NO 134.0606) [M+H]⁺.

6.5.10 Synthesis of (6-(1-phenethyl-1H-1,2,3-triazol-4-yl)pyridin-2-yl)methanol (**6**)**(6)**

(2-bromoethyl)benzene (0.178 g, 0.962 mmol), CuSO₄·5H₂O (0.065 g, 0.262 mmol), sodium ascorbate (0.104 g, 0.525 mmol), sodium azide (0.074 g, 1.137 mmol) and compound **5** (0.117g, 0.875 mmol) were used as the starting materials. It followed the general procedure for click reactions procedure 1 (section 6.4.6.1). Purification *via* flash column chromatography (SiO₂, DCM:EtOAc/7:3) gave a white solid (0.194 g, 79%, R_f = 0.39). ¹H NMR (400 MHz, CDCl₃) δ = 8.06 (1H, dd, *J* = 7.7 Hz, *J* = 0.7 Hz, H-1), 7.92 (1H, s, H-10), 7.76 (1H, t, *J* = 7.7 Hz, H-6), 7.23 - 7.34 (3H, m, H-19, 21, 17), 7.12 - 7.18 (3H, m, H-5, 20, 18), 4.75 (2H, s, H-8), 4.66 (2H, t, *J* = 7.2 Hz, H-13), 3.82 (1H, br s, H-14), 3.28 (2H, t, *J* = 7.3 Hz, H-15); ¹³C NMR (101 MHz, CDCl₃) δ = 158.6 (C-4), 149.2 (C-2), 148.0 (C-7), 137.7 (C-6), 137.0 (C-16), 129.0 (C-21, 17), 128.8 (C-20, 18), 127.3 (C-19), 122.4 (C-10), 119.5 (C-1), 118.8 (C-5), 63.9 (C-8), 51.9 (C-13), 36.9 (C-15); *m/z* (ESMS⁺) found 281.1407 (calc. for C₁₆H₁₇N₄O 281.1402) [M+H]⁺.

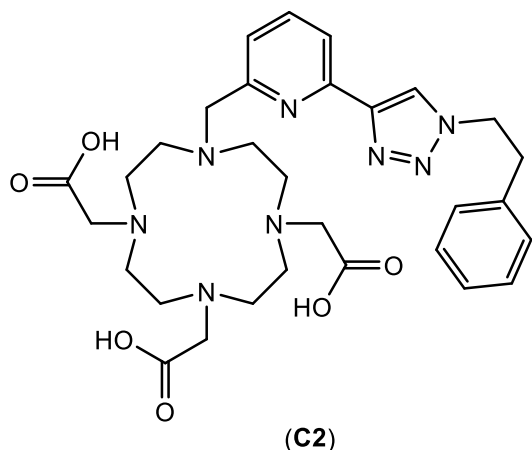
6.5.11 Synthesis of 2-(chloromethyl)-6-(1-phenethyl-1H-1,2,3-triazol-4-yl)pyridine (**7**)

6 (0.133 g, 0.475 mmol), thionyl chloride (0.283 g, 2.375 mmol) were used as the starting materials. It followed the general procedure for chlorination reactions (section 6.4.2). Purification *via* flash column chromatography (SiO₂, 100% EtOAc) gave a white solid (0.128 g, 91%, R_f = 0.62); *m/z* (ESMS⁺) found 299.1060 (calc. for C₁₆H₁₆N₄³⁵Cl 299.1063) [M+H]⁺, found 321.0901 (calc. for C₁₆H₁₅N₄³⁵ClNa 321.0883) [M+Na]⁺.

6.5.12 Synthesis of tri-tert-butyl 2,2',2''-(10-((6-(1-phenethyl-1H-1,2,3-triazol-4-yl)pyridin-2-yl)methyl)-1,4,7,10-tetraazacyclododecane-1,4,7-triyl)triacetate (**8**)

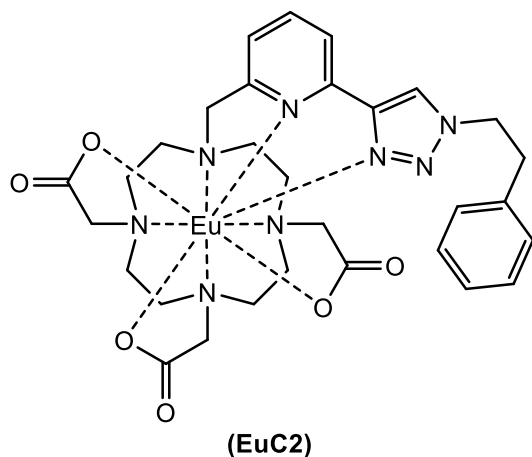
Compound **1** (0.246 g, 0.413 mmol), potassium carbonate (0.229 g, 1.657 mmol) and compound **7** (0.138 g, 0.460 mmol) were used as the starting materials. It followed the general procedure for the DO3A's fourth arm attachments (section 6.4.3). Purification *via* flash column chromatography (SiO₂, MeOH:DCM/1:9) gave viscous oily brown product (0.195 g, 61%); ¹H NMR (400 MHz, CDCl₃) δ = 8.56 (1H, s, H-40), 8.49 (1H, t, *J* = 7.7 Hz, H-34), 8.26 (1H, dd, *J* = 7.7, 0.7 Hz, H-33), 7.22-7.35 (3H, m, H-44, 46, 48), 7.13-7.20 (3H, m, H-35, 45, 47), 4.63 (2H, t, *J* = 6.4 Hz, H-41), 2.21-3.90 (26H, br m, H-5, 6, 7, 8, 9, 10, 11, 12, 13, 17, 21, 29, 42), 1.34-1.45 (27H, m, H-28); *m/z* (ESMS⁺) found 777.5065 (calc. for C₄₂H₆₅N₈O₆ 777.5027) [M+H]⁺.

6.5.13 Synthesis of 2,2',2''-(10-((6-(1-phenethyl-1H-1,2,3-triazol-4-yl)pyridin-2-yl)methyl)-1,4,7,10-tetraazacyclododecane-1,4,7-triyl)triacetic acid (**C2**)



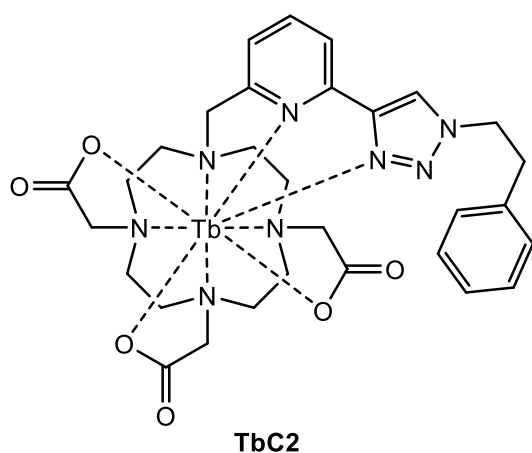
8 (0.230 g, 0.296 mmol) was used as the starting material. It followed the general procedure for macrocycle's *tert*-Bu deprotection reactions (section 6.4.4). Purification *via* HPLC (R_t 20.3 min) gave a white solid 0.134 g (74%).

6.5.14 Synthesis of **EuC2**

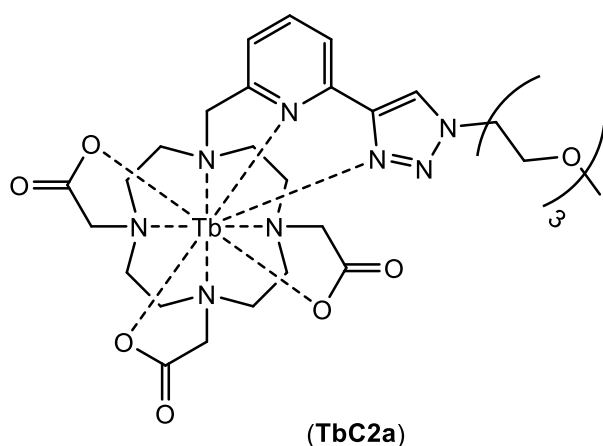


C2 (0.061 g, 0.100 mmol) and EuCl₃·6H₂O (0.041 g, 0.111 mmol) were used as starting materials. It followed the general procedure for lanthanide complexation procedure 1 (section 6.4.9.1). Purification *via* semi preparation reverse phase HPLC (R_t 18.1 min) gave a white hygroscopic solid 43 mg (55%). m/z (ESMS+) found 781.1952 [M+Na]⁺ (cal. for C₃₀H₃₇N₈O₆¹⁵³EuNa 781.1946).

6.5.15 Synthesis of **TbC2**

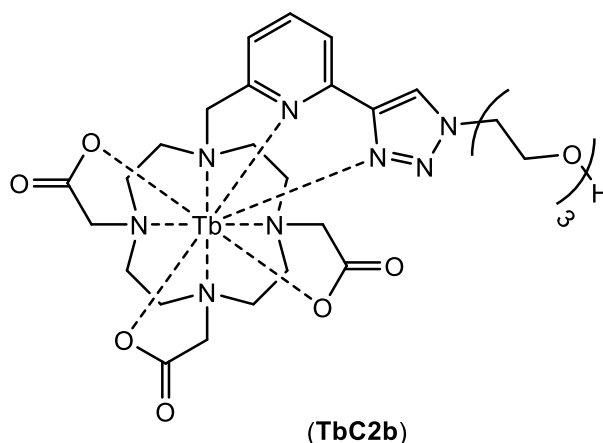


C2 (0.054 g, 0.088 mmol) and TbCl₃·6H₂O (0.037 g, 0.099 mmol) were used as starting materials. It followed the general procedure for lanthanide complexation procedure 1 (section 6.4.9.1). Purification *via* HPLC (R_t 18.1 min) gave a white hygroscopic solid 33 mg (49%); m/z (ESMS+) found 787.1997 [M+Na]⁺ (cal. for C₃₀H₃₇N₈O₆¹⁵⁹TbNa 787.1987).

6.5.16 Synthesis of **Tb2a**

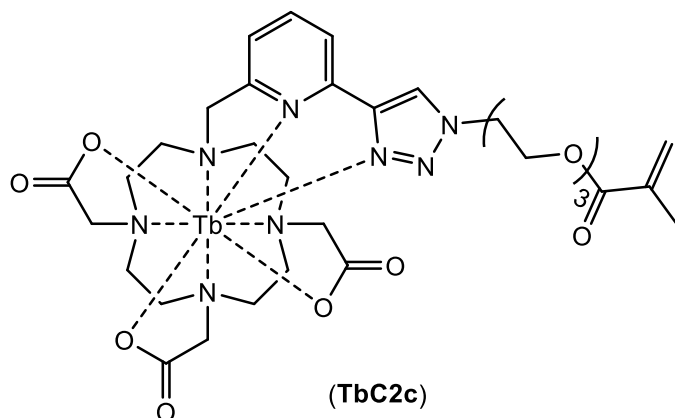
30e (0.022 g, 0.069 mmol), sodium azide (0.010 g, 0.153 mmol), **TbC1** (0.042 g, 0.068 mmol) $\text{CuSO}_4 \cdot 5\text{H}_2\text{O}$ (0.002 g, 0.008 mmol) and sodium ascorbate (0.004 g, 0.020 mmol) were used as starting materials. It followed the general procedure for click reactions procedure 4 (section 6.4.6.4). Purification *via* a column containing

Amberlite XAD 16 resin gave a white hygroscopic solid (10 mg, 18%); m/z (ESMS+) found 829.2328 $[\text{M}+\text{Na}]^+$ (cal. for $\text{C}_{29}\text{H}_{43}\text{N}_8\text{O}_9^{159}\text{TbNa}$ 829.2304).

6.5.17 Synthesis of **Tb2b**

30a (0.030 g, 0.098 mmol), sodium azide (0.013 g, 0.197 mmol), **TbC1** (0.056 g, 0.091 mmol) $\text{CuSO}_4 \cdot 5\text{H}_2\text{O}$ (0.003 g, 0.012 mmol) and sodium ascorbate (0.005 g, 0.025 mmol) were used as starting materials. It followed the general procedure for click reactions procedure 4 (section 6.4.6.4). Purification *via* a column containing

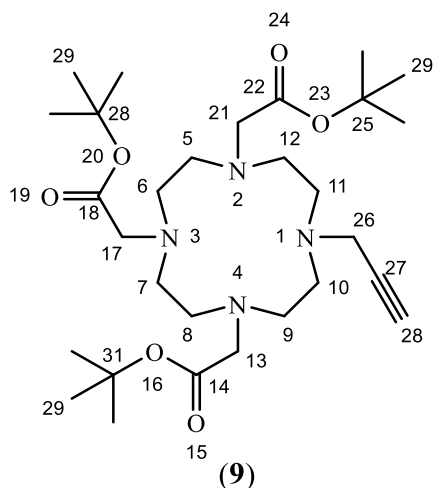
Amberlite XAD 16 resin gave a white hygroscopic solid mg (25 mg, 34%); m/z (ESMS+) found 815 for $[\text{M}+\text{Na}]^+$.

6.5.18 Synthesis of **TbC2c**

30c (0.045 g, 0.120 mmol), sodium azide (0.039 g, 0.599 mmol), **TbC1** (0.074 g, 0.119 mmol) $\text{CuSO}_4 \cdot 5\text{H}_2\text{O}$ (0.003 g, 0.012 mmol) and sodium ascorbate (0.005 g, 0.025 mmol) were used as starting materials. It followed the general procedure

for click reactions procedure 4 (section 6.4.6.4). Purification *via* a column containing Amberlite XAD 16 resin gave a white hygroscopic solid 53 mg (51%); m/z (ESMS+) found 883.2421 (cal. for $C_{32}H_{45}N_8O_{10}^{159}TbNa$ 883.2410) for $[M+Na]^+$.

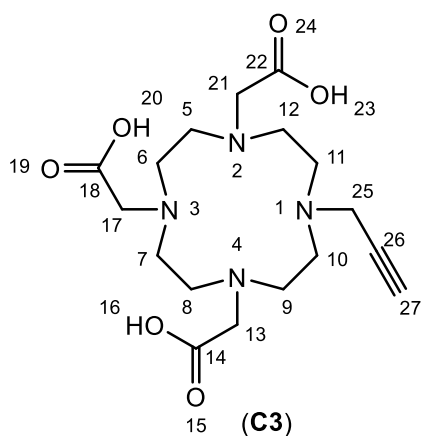
6.5.19 Synthesis of tri-tert-butyl 2,2',2''-(10-(prop-2-yn-1-yl)-1,4,7,10-tetraazacyclododecane-1,4,7-triyl)triacetate (**9**)



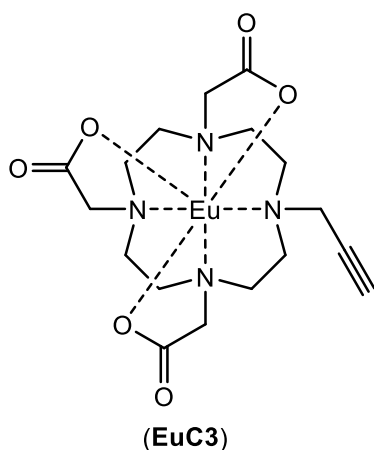
Compound **1** (0.376 g, 0.631 mmol) along with potassium carbonate (0.174 g, 1.259 mmol) were dissolved in 10 mL MeCN in an ice bath under inert atmosphere. Propargyl bromide (0.083 g, 0.697 mmol) was added *via* syringe. After stirred at room temperature overnight, the reaction was showing to complete by mass spectrophotometry analysis. The reaction mixture was filtered before concentrated in reduced pressure. 20 mL DCM was added followed

by 5 mL sodium hydrogen carbonate 1M. The organic layer was separated, dried with $MgSO_4$, filtered and concentrated in reduced pressure. Purification *via* flash column chromatography (SiO_2 , MeOH:DCM/1:9) gave viscous oily brown product 0.310 g (89%). 1H NMR (400 MHz, $CDCl_3$) δ 4.29-1.80 (24H, m, H-5, 6, 7, 8, 9, 10, 11, 12, 13, 17, 21, 26), 2.17 (1H, br t, H-28), 1.46 (27H, m, H-29); ^{13}C NMR (100 MHz, $CDCl_3$) δ 172.0, (C-14, 18, 22), 81.9, 81.6 (C-25, 28, 31), 79.2, 73.1 (C-27, 28), 58.1, 56.9, 51.3, 49.2, 47.4, 42.6 (C-5, 6, 7, 8, 9, 10, 11, 12, 13, 17, 21, 26), 28.1, 28.1 (C-29); (ESMS+) m/z found 553.3965 (cal. $C_{29}H_{53}N_4O_6$ 553.3965) for $[M+H]^+$; 575.3784 (cal. $C_{29}H_{52}N_4O_6Na$ 575.3785) for $[M+Na]^+$.

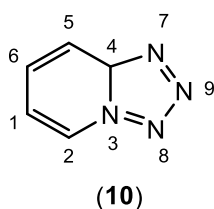
6.5.20 Synthesis of 2,2',2''-(10-(prop-2-yn-1-yl)-1,4,7,10-tetraazacyclododecane-1,4,7-triyl)triacetic acid (**C3**)



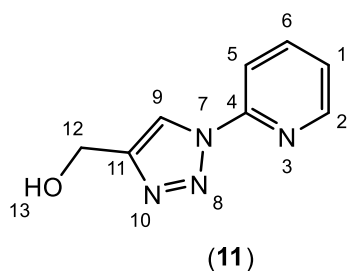
9 (0.425 g, 0.768 mmol) was used as the starting material. It followed the general procedure for macrocycle's tert-Bu deprotection reactions (section 6.4.4) to give 0.254 g (86%). 1H NMR (400 MHz, D_2O) gave broad unresolved peaks; m/z (ESMS+) found 385.2088 (calc. $C_{17}H_{29}N_4O_6$ 385.2087) for $[M+H]^+$.

6.5.21 Synthesis of **EuC3**

C3 (0.258 g, 0.671 mmol) and $\text{EuCl}_3 \cdot 6\text{H}_2\text{O}$ (0.269 g, 0.734 mmol) were used as starting materials. It followed the general procedure for lanthanide complexations procedure 1 (section 6.4.9.1) gave a hygroscopic solid 0.342 g (95%), m/z (ESMS⁺) 557.0853 (calc. $\text{C}_{17}\text{H}_{25}\text{N}_4\text{O}_6^{153}\text{EuNa}$ 557.0884) for $[\text{M}+\text{Na}]^+$.

6.5.22 Synthesis of 2-azidopyridine (**10**)

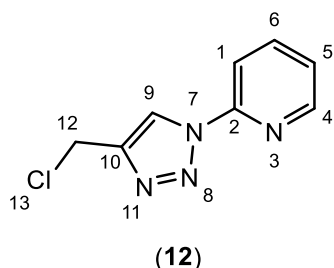
2-Bromopyridine (0.497 g, 3.146 mmol), CuI (0.060 g, 0.315 mmol), NaAscorbate (0.062 g, 0.315 mmol), NaN_3 (0.245 g, 3.775 mmol) were used as the starting materials. It followed the general procedure for synthesis of azide procedure 1 (section 6.4.7.1). Purification *via* SiO_2 column chromatography (EtOAc 100%) gave a white solid (0.220 g, 58%, $R_f = 0.40$). ^1H NMR (300 MHz, CDCl_3) $\delta = 8.93$ (1H, dt, $J = 6.9$ Hz, $J = 1.1$ Hz, H-2), 8.09 (1H, dt, $J = 9.1$ Hz, $J = 1.2$ Hz, H-5), 7.78 (1H, ddd, $J = 9.1$ Hz, $J = 6.7$ Hz, $J = 1.2$ Hz, H-6), 7.35 (1H, td, $J = 6.9$ Hz, $J = 1.2$ Hz, H-1); ^{13}C NMR (75 MHz, CDCl_3) $\delta = 148.5$ (C-4), 132.1 (C-6), 125.5 (C-2), 116.8 (C-1), 115.8 (C-5); m/z (ESMS⁺) found 121.0516 (calc. for $\text{C}_5\text{H}_5\text{N}_4$ 121.0514) for $[\text{M}+\text{H}]^+$.

6.5.23 Synthesis of (1-(pyridin-2-yl)-1H-1,2,3-triazol-4-yl)methanol (**11**)

Compound **10** (0.340 g, 2.827 mmol), CuI (0.054 g, 0.283 mmol), sodium ascorbate (0.056 g 0.283 mmol) and propargyl alcohol (0.056 g, 3.393 mmol) were dissolved in 20 mL EtOH:H₂O (7:3). The reaction mixture was heated in $\mu.w.$ at 125^oC, 150psi and was never rich to the completion even after 4 h heating when analysed by TLC (SiO_2 , 100% EtOAc, $R_f = 0.32$). The reaction mixture was then poured into 10 mL saturated EDTA solution (made pH 10 by NH_4OH conc.) before been extracted by 20 mL ethyl acetate 3 times. The combined organic solvent was dried with MgSO_4 , filtered and concentrated under reduced pressure. Separation *via* SiO_2 column chromatography (EtOAc 100%) gave a white solid (0.109 g, 22%). ^1H NMR (400 MHz, CDCl_3) $\delta = 8.57$ (1H, s, H-9), 8.50 (1H, ddd, $J = 4.9$ Hz, $J =$

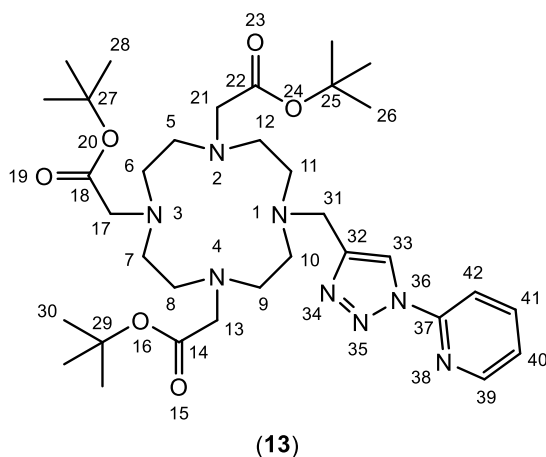
1.8 Hz, $J = 0.8$ Hz, H-2), 8.19 (1H, dt, $J = 8.2$ Hz, $J = 0.9$ Hz, H-5), 7.92 (1H, ddd, $J = 8.2$ Hz, $J = 7.4$ Hz, $J = 1.8$ Hz, H-6), 7.35 (1H, ddd, $J = 7.5$ Hz, $J = 4.8$ Hz, $J = 0.8$ Hz, H-1), 4.90 (2H, s, H-12), 2.54 (1H, br s, H-13); ^{13}C NMR (101 MHz, CDCl_3) $\delta = 149.2$ (C-4), 148.6 (C-2), 148.0 (C-10), 139.1 (C-6), 123.6 (C-1), 119.2 (C-9), 113.8 (C-5), 56.6 (C-12); m/z (ESMS $^+$) found 177.0777 (calc. for $\text{C}_8\text{H}_9\text{N}_4\text{O}$ 177.0776) for $[\text{M}+\text{Na}]^+$, m.p. 139-140 $^\circ\text{C}$.

6.5.24 Synthesis of 2-(4-(chloromethyl)-1H-1,2,3-triazol-1-yl)pyridine (**12**)



Compound **11** (0.077 g, 0.437 mmol) and thionyl chloride (0.207 g, 1.746 mmol) were used as the starting materials. It followed the general procedure for chlorination reactions (section 6.4.2). Purification *via* flash column chromatography (SiO_2 , 100% ethylacetate) gave a white solid (0.064 g, 75%, $R_f = 0.65$). ^1H NMR (400 MHz, CDCl_3) $\delta = 8.62$ (1H, s, H-9), 8.50 (1H, ddd, $J = 4.8$ Hz, $J = 1.8$ Hz, $J = 1.0$ Hz, H-4), 8.19 (1H, dt, $J = 8.2$ Hz, $J = 0.9$ Hz, H-1), 7.93 (1H, ddd, $J = 8.2$ Hz, $J = 7.4$ Hz, $J = 1.8$ Hz, H-6), 7.36 (1H, ddd, $J = 7.4$ Hz, $J = 4.9$ Hz, $J = 1.0$ Hz, H-5), 4.80 (2H, d, $J = 0.6$ Hz, H-12); ^{13}C NMR (101 MHz, CDCl_3) $\delta = 149.0$ (C-2), 148.6 (C-4), 145.1 (C-10), 139.2 (C-6), 123.8 (C-5), 120.3 (C-9), 113.8 (C-1), 36.1 (C-12); m/z (ESMS $^+$) found 195.0442 (calc. for $\text{C}_8\text{H}_8\text{N}_4^{35}\text{Cl}$ 195.0437) for $[\text{M}+\text{H}]^+$.

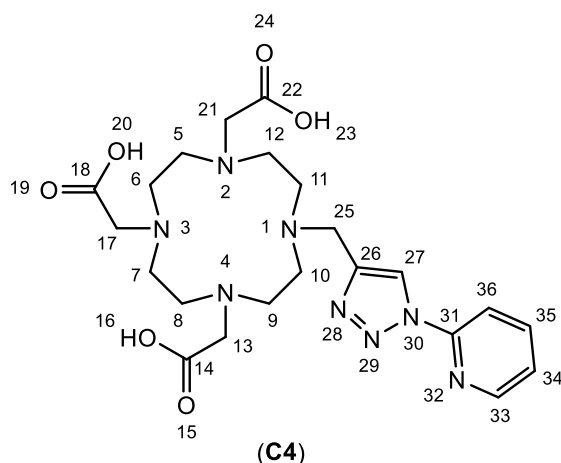
6.5.25 Synthesis of tri-tert-butyl 2,2',2''-(10-((1-(pyridin-2-yl)-1H-1,2,3-triazol-4-yl)methyl)-1,4,7,10-tetraazacyclododecane-1,4,7-triyl)triacetate (**13**)



Compound **1** (0.122 g, 0.206 mmol), potassium carbonate (0.113 g, 0.822 mmol) and compound **12** (0.048 g, 0.247 mmol) were used as the starting materials. It followed the general procedure for the DO3A's fourth arm attachments (section 6.4.3). Purification *via* flash column chromatography (SiO_2 , $\text{MeOH}:\text{DCM}/1:9$) gave viscous oily brown product (0.092 g, 66%, $R_f = 0.25$). ^1H NMR (400 MHz, CDCl_3) $\delta = 8.58$ (1H, s, H-33), 8.52 (1H, ddd, $J = 4.7$ Hz, $J = 1.8$ Hz, $J = 0.8$ Hz, H-39), 8.06 (1H, d, $J = 8.2$ Hz, H-42), 7.97 (1H, td, $J = 7.8$ Hz, $J = 1.9$ Hz, H-41), 7.42 (1H, ddd, $J = 7.3$ Hz, $J = 4.8$ Hz, $J = 1.0$ Hz, H-40), 2.00

- 3.59 (24H, m, H-31, 7, 6, 8, 5, 21, 17, 13, 12, 9, 11, 10), 1.49 (9H, s, H-28), 1.44 (18H, s, H-30, 26); ^{13}C NMR (101 MHz, CDCl_3) δ = 172.7 (C-18), 172.4 (C-14, 22), 148.9 (C-37), 148.7 (C-39), 145.3 (C-32), 139.2 (C-41), 123.9 (C-40), 119.8 (C-33), 113.3 (C-42), 82.0 (C-29, 25), 82.0 (C-27), 56.0, 55.7, 53.5, 50.1, 48.6 (C-15, 13, 14, 12, 9, 8, 5, 11, 10, 7, 6, 37), 27.9 (C-36, 35, 34, 28, 27, 26), 27.9 (C-32, 31, 30); m/z (ESMS $^+$) found 673.4405 (calc. for $\text{C}_{34}\text{H}_{57}\text{N}_8\text{O}_6$ 673.4401) for $[\text{M}+\text{H}]^+$.

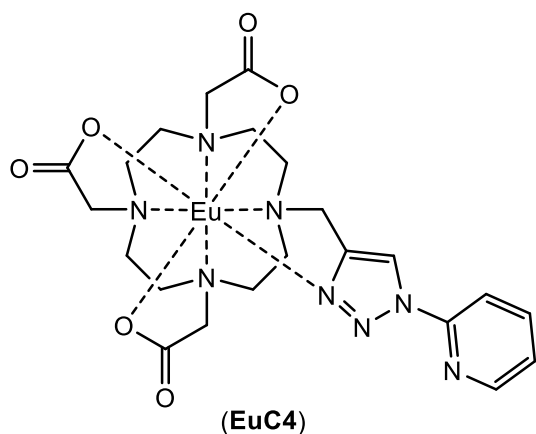
6.5.26 Synthesis of 2,2',2''-(10-((1-(pyridin-2-yl)-1H-1,2,3-triazol-4-yl)methyl)-1,4,7,10-tetraazacyclododecane-1,4,7-triyl)triacetic acid (**C4**).



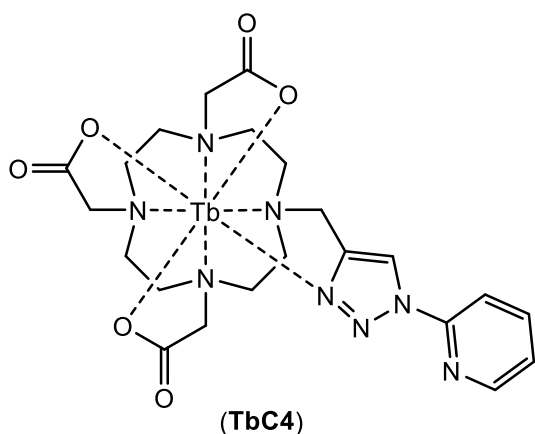
Compound **13** (0.082 g, 0.122 mmol) was used as the starting material. It followed the general procedure for macrocycle's tert-Bu deprotection reactions (section 6.4.4). Purification *via* HPLC gave a white solid 52 mg (84%). ^1H NMR (400 MHz, D_2O) δ = 8.82 (1H, br s, H-27), 8.46 (1H, d, J = 4.3 Hz, H-33), 8.04 (1H, t, J = 7.5 Hz, H-35), 7.93 (1H, d, J = 7.8 Hz, H-36),

7.51 (1H, dd, J = 6.5 Hz, J = 5.5 Hz, H-34), 2.78 - 4.63 (24H, m, H-5, 6, 7, 8, 9, 10, 11, 12, 13, 17, 21, 25); ^{13}C NMR (101 MHz, DEUTERIUM OXIDE) δ ppm 172.0 (C-14, 22); 172.1 (C-18), 148.6 (C-33), 147.7 (C-31), 140.8 (C-35), 125.3 (C-34), 125.0 (C-27), 115.1 (C-36), 53.2 - 49.2 (C-5, 6, 7, 8, 9, 10, 11, 12, 13, 17, 21; m/z (ESMS $^+$) found 505.2527 (calc. for $\text{C}_{22}\text{H}_{33}\text{N}_8\text{O}_6$ 505.2523) for $[\text{M}+\text{H}]^+$.

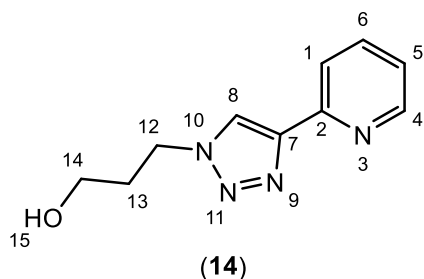
6.5.27 Synthesis of **EuC4**



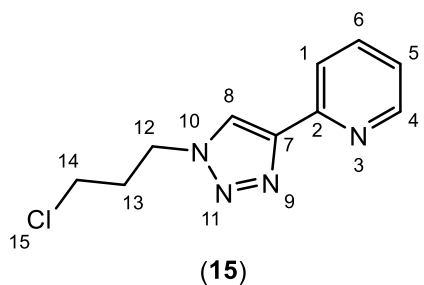
C4 (0.022 g, 0.044 mmol) and $\text{EuCl}_3 \cdot 6\text{H}_2\text{O}$ (0.018 g, 0.049 mmol) were used as starting materials. It followed the general procedure for lanthanide complexation procedure 1 (section 6.4.9.1). Purification *via* HPLC gave a white hygroscopic solid 15 mg (52%); m/z (ESMS $^+$) found 675.1311 (cal. for $\text{C}_{22}\text{H}_{29}\text{N}_8\text{O}_6^{151}\text{EuNa}$ 675.1306) for $[\text{M}+\text{Na}]^+$.

6.5.28 Synthesis of **TbC4**

C4 (0.015 g, 0.029 mmol) and $\text{TbCl}_3 \cdot 6\text{H}_2\text{O}$ (0.013 g, 0.034 mmol) were used as starting materials. It followed the general procedure for lanthanide complexation procedure 1 (section 6.4.9.1). Purification *via* HPLC gave a white hygroscopic solid 11 mg (57%); m/z (ESMS⁺) found 683.1358 (cal. for $\text{C}_{22}\text{H}_{29}\text{N}_8\text{O}_6^{159}\text{TbNa}$ 683.1361) for $[\text{M}+\text{Na}]^+$.

6.5.29 Synthesis 3-(4-(pyridin-2-yl)-1H-1,2,3-triazol-1-yl)propan-1-ol (**14**)

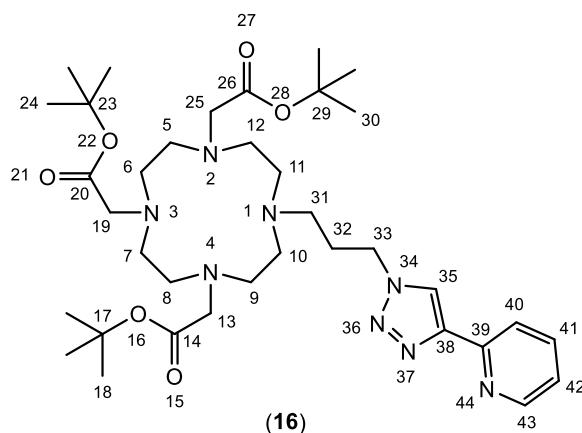
3-Bromopropanol (1.263 g, 9.019 mmol), sodium azide (0.640 g, 9.838 mmol), 2-ethynyl pyridine (0.845 g, 8.199 mmol), $\text{CuSO}_4 \cdot 5\text{H}_2\text{O}$ (0.204 g, 0.820 mmol) and sodium ascorbate (0.325 g, 1.640 mmol) were used as the starting materials. It followed the general procedure for click reactions procedure 1 (section 6.4.6.1). Purification *via* column chromatography (SiO_2 , EtOAc 100%) gave a white crystalline (1.277 g, 76 %). ^1H NMR (400 MHz, CDCl_3) δ = 8.55 (1H, dq, J = 4.9 Hz, J = 1.0 Hz, H-4), 8.24 (1H, s, H-8), 8.16 (1H, dt, J = 8.0 Hz, J = 1.0 Hz, H-1), 7.78 (1H, td, J = 7.7 Hz, J = 1.8 Hz, H-6), 7.23 (1H, ddd, J = 7.6 Hz, J = 4.9 Hz, J = 1.2 Hz, H-5), 4.62 (2H, t, J = 6.7 Hz, H-12), 3.70 (2H, br t, J = 5.7 Hz, H-14), 3.63 (1H, br s, H-15), 2.20 (2H, quin, J = 6.3 Hz, H-13); ^{13}C NMR (101 MHz, CDCl_3) δ = 150.3 (C-2), 149.3 (C-4), 148.2 (C-7), 137.2 (C-6), 123.0 (C-5), 122.7 (C-8), 120.4 (C-1), 58.5 (C-14), 47.3 (C-12), 32.8 (C-13); m/z (ESMS⁺) found 205.1094 (calc. for $\text{C}_{10}\text{H}_{12}\text{N}_4\text{O}$ 205.1089) for $[\text{M}+\text{H}]^+$.

6.5.30 Synthesis of 2-(1-(3-chloropropyl)-1H-1,2,3-triazol-4-yl)pyridine (**15**)

Compound **14** (0.137 g, 0.670 mmol) and thionyl chloride (0.399 g, 3.354 mmol) were used as the starting materials. It followed the general procedure for chlorination reactions (section 6.4.2). It was stirred for 2 days instead of 3 h. Purification *via* flash column chromatography (SiO_2 , 100% ethylacetate) gave a

white crystalline (0.112 g, 75%). ^1H NMR (400 MHz, CDCl_3) δ = 8.57 (1H, ddd, J = 4.9 Hz, J = 1.8 Hz, J = 1.0 Hz, H-4), 8.21 (1H, s, H-8), 8.16 (1H, dt, J = 8.0 Hz, J = 1.0 Hz, H-1), 7.76 (1H, td, J = 7.8 Hz, J = 1.9 Hz, H-6), 7.22 (1H, ddd, J = 7.6 Hz, J = 4.9 Hz, J = 1.2 Hz, H-5), 4.61 (2H, t, J = 6.7 Hz, H-12), 3.56 (2H, t, J = 6.2 Hz, H-14), 2.42 (2H, quin, J = 6.4 Hz, H-13); ^{13}C NMR (101 MHz, CDCl_3) δ = 149.4 (C-4), 136.9 (C-6), 122.9 (C-5), 122.6 (C-8), 120.1 (C-1), 47.2 (C-12), 41.1 (C-14), 32.5 (C-13); m/z (ESMS $^+$) found 225.0723 (calc. for $\text{C}_{10}\text{H}_{12}\text{N}_4^{37}\text{Cl}$ 225.0721) for $[\text{M}+\text{H}]^+$.

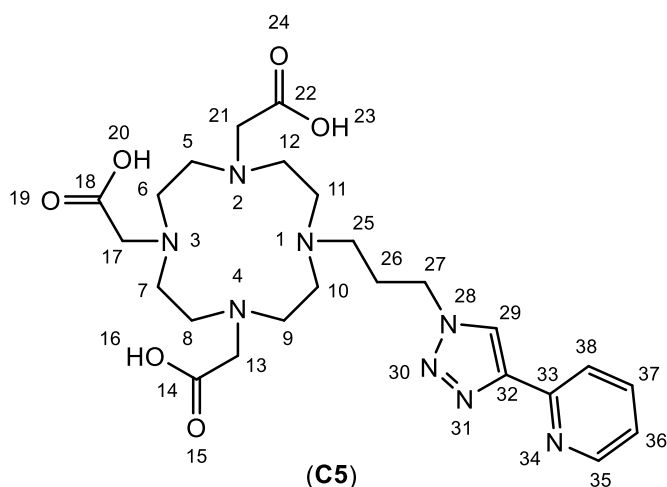
6.5.31 Synthesis of tri-tert-butyl 2,2',2''-(10-(3-(4-(pyridin-2-yl)-1H-1,2,3-triazol-1-yl)propyl)-1,4,7,10-tetraazacyclododecane-1,4,7-triyl)triacetate (**16**)



Compound (**1**) (0.254 g, 0.426 mmol) potassium carbonate (0.235 g, 1.700 mmol) and compound (**15**) (0.104 g, 0.467 mmol) were used as the starting materials. It followed the general procedure for the DO3A's fourth arm attachments (section 6.4.3). Purification *via* flash column chromatography (SiO_2 ,

$\text{MeOH}:\text{DCM}/1:9$) gave a viscous brown oily product 0.230 g (77%). ^1H NMR (400 MHz, CDCl_3) δ = 8.58 (1H, dq, J = 4.9 Hz, J = 0.8 Hz, H-43), 8.38 (1H, s, H-35), 8.13 (1H, dt, J = 7.8 Hz, J = 1.0 Hz, H-40), 7.77 (1H, td, J = 7.8 Hz, J = 1.9 Hz, H-41), 7.23 (1H, ddd, J = 7.5 Hz, J = 4.9 Hz, J = 1.1 Hz, H-42), 4.48 (2H, t, J = 7.1 Hz, H-33), 2.24 - 3.27 (24H, m, H-5, 6, 7, 8, 9, 10, 11, 12, 13, 19, 25, 31), 2.18 (2H, quin, J = 7.3 Hz, H-32), 1.39 - 1.50 (27H, m, H-18, 24, 30); ^{13}C NMR (101 MHz, CDCl_3) δ = 173.5 (C-20), 172.6 (C-14, 26), 150.2 (C-39), 149.3 (C-43), 148.1 (C-38), 136.9 (C-41), 122.8 (C-42), 122.6 (C-35), 120.2 (C-40), 82.9 (C-17, 29), 82.5 (C-23), 56.6 (C-13, 25), 55.7 (C-19), 51.2 (C-31), 50.1 (C-5, 6, 7, 8, 9, 10, 11, 12), 48.8 (C-33), 28.1, 27.9 (C-18, 30), 27.8 (C-24), 26.7 (C-32); m/z (ESMS $^+$) found 701.4734 (calc. for $\text{C}_{36}\text{H}_{61}\text{N}_8\text{O}_6$ 701.4714) for $[\text{M}+\text{H}]^+$.

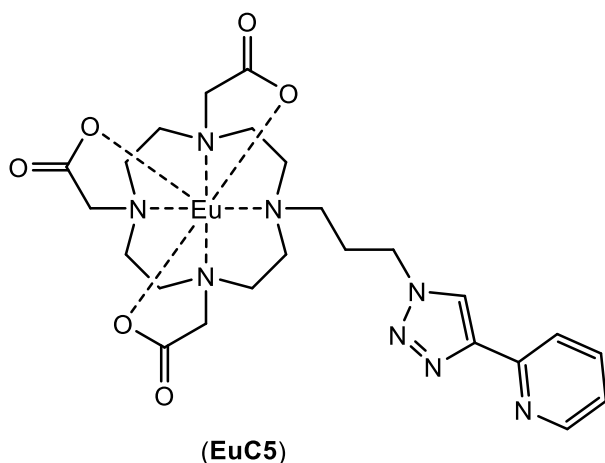
6.5.32 Synthesis of 2,2',2''-(10-(3-(4-(pyridin-2-yl)-1H-1,2,3-triazol-1-yl)propyl)-1,4,7,10-tetraazacyclododecane-1,4,7-triyl)triacetic acid (C5)



Compound **16** (0.115 g, 0.164 mmol) was used as the starting material. It followed the general procedure for macrocycle's tert-Bu deprotection reactions (section 6.4.4). Purification *via* HPLC gave a white hygroscopic solid 62 mg (71%). ¹H NMR (400 MHz, D₂O) δ = 8.80 (1H, s, H-29), 8.70 (1H,

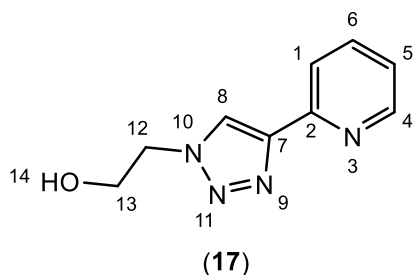
dd, J = 6.0 Hz, J = 0.9 Hz, H-35), 8.58 (1H, td, J = 8.0 Hz, J = 1.6 Hz, H-37), 8.33 (1H, d, J = 8.0 Hz, H-38), 7.94 (1H, ddd, J = 7.7 Hz, J = 6.2 Hz, J = 1.2 Hz, H-36), 4.63 (2H, t, J = 6.7 Hz, H-27), 4.04 (2H, br s, H-17), 3.24 - 3.69 (14H, m, H-5, 6, 7, 8, 12, 13, 25), 2.86 - 3.20 (8H, m, H-9, 10, 11, 12), 2.44 (2H, br quin, J = 8.0 Hz, H-26); ¹³C NMR (101 MHz, D₂O) δ = 173.9 (C-14, 18, 22), 147.5 (C-37), 142.4 (C-33), 141.1 (C-35), 139.3 (C-32), 126.9 (C-29), 126.0 (C-36), 124.6 (C-38), 54.7 (C-17), 53.0 (C-13, 21), 51.5 (C-5, 8), 51.3 (C-6, 7), 50.0 (C-25), 48.6 (C-10, 11), 48.3 (C-9, 12), 47.8 (C-27), 24.2 (C-26); m/z (ESMS⁺) found 533.2847 (calc. for C₂₄H₃₇N₈O₆ 533.2836) for [M+H]⁺.

6.5.33 Synthesis of EuC5

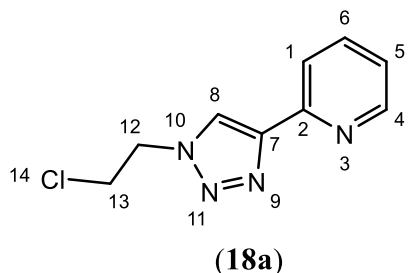


C5 (0.031 g, 0.058 mmol) and EuCl₃·6H₂O (0.024 g, 0.065 mmol) were used as starting materials. It followed the general procedure for lanthanide complexation procedure 1 (section 6.4.9.1). Purification *via* HPLC gave a white hygroscopic solid 21 mg (53%); m/z (ESMS⁺) found 703.1622 (cal. for C₂₄H₃₃N₈O₆¹⁵¹EuNa

703.1619) for [M+Na]⁺.

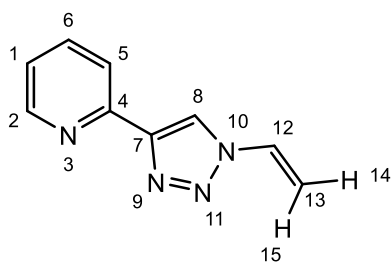
6.5.34 Synthesis of 2-(4-(pyridin-2-yl)-1H-1,2,3-triazol-1-yl)ethan-1-ol (**17**)

2-Bromoethanol (1.181 g, 9.452 mmol), sodium azide (0.726 g, 11.170 mmol), 2-ethynyl pyridine (0.103 g, 8.593 mmol), CuSO₄·5H₂O (0.215, 0.856 mmol) and sodium ascorbate (0.340 g, 1.7184 mmol) were used as the starting materials. It followed the general procedure for click reactions procedure 1 (section 6.4.6.1). Purification *via* flash column chromatography (SiO₂, EtOAc100%) gave a white crystalline (1.226 g, 75 %). ¹H NMR (400 MHz, CDCl₃) δ = 8.45 (1H, ddd, *J* = 4.9 Hz, *J* = 1.8 Hz, *J* = 1.0 Hz, H-4), 8.30 (1H, s, H-8), 8.06 (1H, dt, *J* = 8.0 Hz, *J* = 1.0 Hz, H-1), 7.75 (1H, td, *J* = 7.7 Hz, *J* = 1.8 Hz, H-6), 7.20 (1H, ddd, *J* = 7.5 Hz, *J* = 5.0 Hz, *J* = 1.2 Hz, H-5), 4.64 - 5.21 (1H, m, H-14), 4.55 (2H, t, *J* = 4.9 Hz, H-12), 4.13 (2H, t, *J* = 4.9 Hz, H-13); ¹³C NMR (101 MHz, CDCl₃) δ = 150.0 (C-2), 149.1 (C-4), 147.6 (C-7), 137.3 (C-6), 123.6 (C-8), 123.0 (C-5), 120.5 (C-1), 61.2 (C-13), 53.1 (C-12); *m/z* (ESMS⁺) found 213.0753 (calc. for C₉H₁₀N₄ONa 213.0752) for [M+Na]⁺.

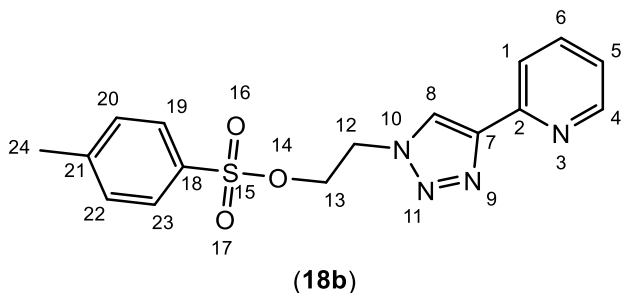
6.5.35 Synthesis of 2-(1-(2-chloroethyl)-1H-1,2,3-triazol-4-yl)pyridine (**18a**)

Compound **17** (54 mg, 0.285 mmol) and thionyl chloride (169 mg, 1.427 mmol) was used as the starting materials. It followed the general procedure for chlorination reactions (section 6.4.2). Purification *via* flash column chromatography (SiO₂, EtOAc100%) gave a white-yellow crystalline (46.9 mg, 78.8 %). ¹H NMR (400 MHz, CDCl₃) δ = 8.59 (1H, ddd, *J* = 4.9 Hz, *J* = 1.8 Hz, *J* = 1.0 Hz, H-4), 8.28 (1H, s, H-8), 8.18 (1H, dt, *J* = 8.0 Hz, *J* = 1.0 Hz, H-1), 7.78 (1H, td, *J* = 7.7 Hz, *J* = 1.8 Hz, H-6), 7.24 (1H, ddd, *J* = 7.6 Hz, *J* = 4.8 Hz, *J* = 1.1 Hz, H-5), 4.76 (2H, t, *J* = 5.9 Hz, H-12), 3.98 (2H, t, *J* = 5.9 Hz, H-13); ¹³C NMR (101 MHz, CDCl₃) δ = 150.2 (C-2), 149.6 (C-4), 148.5 (C-7), 137.0 (C-6), 123.1 (C-8), 123.1 (C-5), 120.4 (C-1), 52.0 (C-12), 42.4 (C-13); *m/z* (ESMS⁺) 209.0602 (calc. for C₉H₁₀N₄³⁵Cl 209.0594) for [M+H]⁺.

6.5.36 Formation of 2-(1-vinyl-1H-1,2,3-triazol-4-yl)pyridine (elimination by-product)



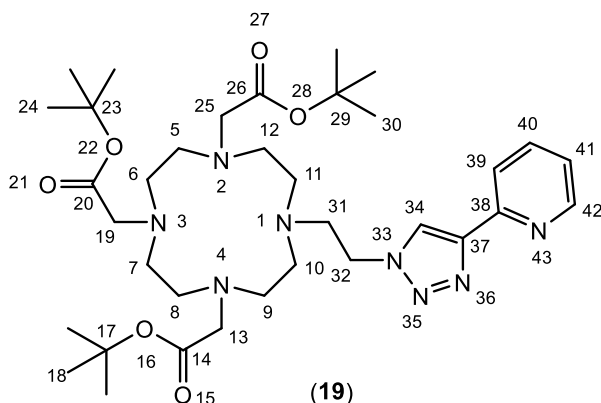
^1H NMR (400 MHz, CDCl_3) δ = 8.59 (1H, ddd, J = 4.7 Hz, J = 1.8 Hz, J = 1.0 Hz, H-2), 8.42 (1H, s, H-8), 8.20 (1H, dt, J = 7.8 Hz, J = 1.2 Hz, H-5), 7.78 (1H, td, J = 7.8 Hz, J = 1.8 Hz, H-6), 7.41 (1H, dd, J = 15.9 Hz, J = 9.0 Hz, H-12), 7.24 (1H, ddd, J = 7.6 Hz, J = 4.8 Hz, J = 1.3 Hz, H-1), 5.74 (1H, dd, J = 15.9 Hz, J = 2.1 Hz, H-13b), 5.21 (1H, dd, J = 9.0 Hz, J = 2.0 Hz, H-13a); ^{13}C NMR (101 MHz, CDCl_3) δ = 149.8 (C-4), 149.6 (C-2), 148.6 (C-7), 137.0 (C-6), 130.3 (C-12), 123.2 (C-1), 120.5 (C-5), 118.7 (C-8), 105.2 (C-13); m/z (ESMS $^+$) found 173.0825 (calc. for $\text{C}_9\text{H}_9\text{N}_4$ 173.0827) for $[\text{M}+\text{H}]^+$.

6.5.37 Synthesis of 2-(4-(pyridin-2-yl)-1H-1,2,3-triazol-1-yl)ethyl 4-methylbenzene sulfonate (**18b**)

Compound **17** (0.504 g, 2.650 mmol) and tosyl chloride (0.619 g, 3.181 mmol) were used as the starting materials. It followed the general procedure for tosylation reactions (section 6.4.8). Purification *via* flash

column chromatography (SiO_2 , EtOAc 100%) gave a white-yellow solid (0.824 g, 90 %). ^1H NMR (400 MHz, CDCl_3) δ = 8.57 - 8.61 (1H, m, H-4), 8.07 - 8.13 (2H, m, H-1, 8), 7.78 (1H, td, J = 7.7 Hz, J = 1.8 Hz, H-6), 7.65 (2H, d, J = 8.4 Hz, H-23, 19), 7.24 (1H, ddd, J = 7.6 Hz, J = 4.8 Hz, J = 1.1 Hz, H-5), 7.20 (2H, d, J = 8.6 Hz, H-22, 20), 4.68 (2H, t, J = 5.1 Hz, H-13), 4.47 (2H, t, J = 5.1 Hz, H-12), 2.30 (3H, s, H-24); ^{13}C NMR (101 MHz, CDCl_3) δ = 150.1 (C-2), 149.6 (C-4), 148.6 (C-7), 145.4 (C-21), 136.9 (C-6), 132.1 (C-18), 130.1 (C-22, 20), 127.8 (C-23, 19), 123.1 (C-8), 123.0 (C-5), 120.2 (C-1), 67.7 (C-13), 49.2 (C-12), 21.6 (C-24); m/z (ESMS $^+$) found 345.1017 (calc. for $\text{C}_{16}\text{H}_{17}\text{N}_4\text{O}_3\text{S}$ 345.1021) for $[\text{M}+\text{H}]^+$.

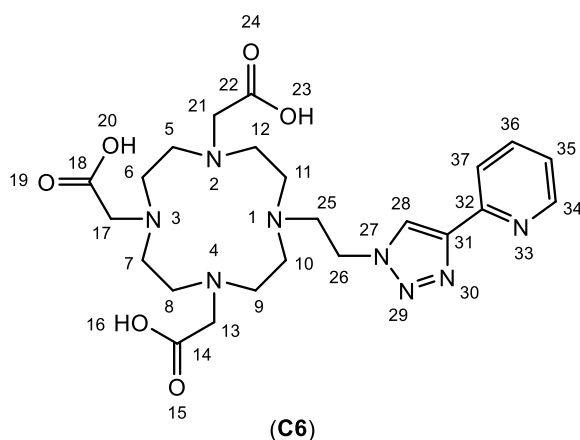
6.5.38 Synthesis of tri-tert-butyl 2,2',2''-(10-(2-(4-(pyridin-2-yl)-1H-1,2,3-triazol-1-yl)ethyl)-1,4,7,10-tetraazacyclododecane-1,4,7-triyl)triacetate (**19**)



Compound **1** (0.134 g, 0.225 mmol), potassium carbonate (0.125 g, 0.900 mmol) compound **18a** (0.052 g, 0.248 mmol) were used as the starting material. It followed the general procedure for the DO3A's fourth arm attachments (section 6.4.3) with a little modification. It was using 2-3 mL

MeCN instead of 15 mL and stirred 2 days instead of overnight. Purification *via* column chromatography (SiO₂, MeOH:DCM/1:9) gave a brown viscous oily product 31 mg (27%). ¹H NMR (400 MHz, CDCl₃) δ = 8.57 (1H, dq, *J* = 4.7 Hz, *J* = 1.0 Hz, H-42), 8.43 (1H, s, H-34), 8.03 (1H, dt, *J* = 7.8 Hz, *J* = 1.0 Hz, H-39), 7.72 (1H, td, *J* = 7.8 Hz, *J* = 1.9 Hz, H-40), 7.21 (1H, ddd, *J* = 7.4 Hz, *J* = 4.9 Hz, *J* = 1.2 Hz, H-41), 4.74 (2H, t, *J* = 6.2 Hz, H-32), 2.18 - 3.52 (24H, m, H-5, 6, 7, 8, 9, 10, 11, 12, 13, 14, 15, 37), 1.36 - 1.50 (27H, m, H-18, 24, 30); ¹³C NMR (101 MHz, CDCl₃) δ = 173.0 (C-14, 26), 172.7 (C-20), 150.4 (C-38), 149.4 (C-42), 148.2 (C-37), 136.6 (C-40), 123.5 (C-34), 122.7 (C-41), 120.1 (C-39), 82.6 (C-17, 29), 82.3 (C-23), 56.7 (C-5, 6, 7, 8), 55.6 (C-31), 55.1 (C-13, 25), 53.5 (C-19), 50.4 (C-9, 10, 11, 12), 47.3 (C-32), 28.0 (C-18, 30), 27.9 (C-24); *m/z* (ESMS⁺) found 687.4561 (calc. for C₃₅H₅₉N₈O₆ 687.4558) for [M+H]⁺.

6.5.39 Synthesis of 2,2',2''-(10-(2-(4-(pyridin-2-yl)-1H-1,2,3-triazol-1-yl)ethyl)-1,4,7,10-tetraazacyclododecane-1,4,7-triyl)triacetic acid (**C6**)

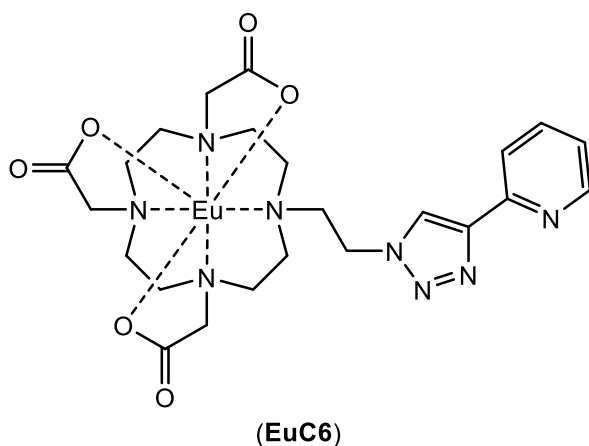


Compound **20** (0.083 g, 0.121 mmol) was used as the starting material. It followed the general procedure for macrocycle's tert-Bu deprotection reactions (section 6.4.4). Purification *via* HPLC gave a white hygroscopic solid 42 mg (66 %). ¹H NMR (400 MHz, D₂O) δ = 8.84 (1H, s, H-28), 8.65 - 8.75 (1H, m, H-34), 8.57

(1H, td, *J* = 8.0 Hz, *J* = 1.6 Hz, H-36), 8.32 (1H, d, *J* = 8.0 Hz, H-37), 7.93 (1H, ddd, *J* = 7.6 Hz, *J* = 6.1 Hz, *J* = 1.2 Hz, H-35), 4.76 (2H, br s, H-26), 2.95 - 4.31 (24H, m, H-5, 6, 7, 8, 9, 10, 11, 12, 13, 17, 21, 25); ¹³C NMR (101 MHz, D₂O) δ = 147.5 (C-36), 142.3

(C-32), 141.1 (C-34), 139.2 (C-31), 127.3 (C-28), 126.0 (C-35), 124.6 (C-37), 54.7, 53.4, 52.0, 50.2, 48.8, 46.9 (C-5, 6, 7, 8, 9, 10, 11, 12, 13, 17, 21, 25, 26); m/z (ESMS⁺) found 519.2714 (calc. for C₂₃H₃₅N₈O₆ 519.2680) for [M+H]⁺.

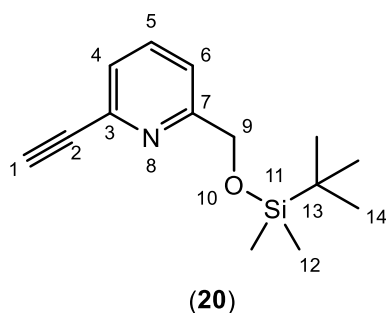
6.5.40 Synthesis of **EuC6**



C6 (0.022 g, 0.042 mmol) and EuCl₃·6H₂O (0.017 g, 0.046 mmol) were used as starting materials. It followed the general procedure for lanthanide complexation procedure 1 section (6.4.9.1). Purification *via* HPLC gave a white hygroscopic solid 15 mg (53%); m/z (ESMS⁺) found 691.1481 (cal. for C₂₃H₃₁N₈O₆¹⁵³EuNa 691.1477) for

[M+Na]⁺.

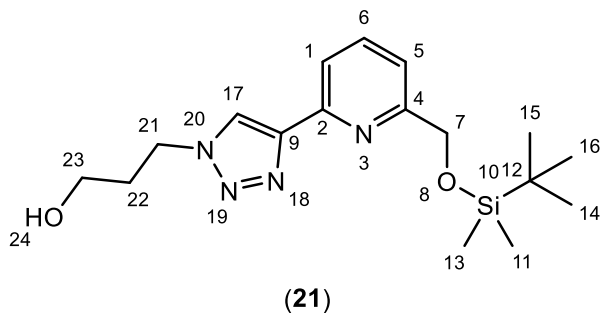
6.5.41 Synthesis 2-(((*tert*-butyldimethylsilyl)oxy)methyl)-6-ethynylpyridine (**20**)



5 (0.278 g, 2.084 mmol) was dissolved in 10 mL dry DCM in an ice bath. Imidazole (0.212 g, 3.126 mmol) was added followed by *tert*-butyldimethylsilyl chloride (0.471 g, 3.126 mmol). After stirring at room temperature for 2 h the reaction was showing to the completion by TLC (SiO₂, EtOAc 100%, R_f = 0.74). It

was filtered and washed with 10 mL brine solution three times. The organic layer was dried with MgSO₄ and solvent was removed under reduced pressure. Purification *via* flash column chromatography (SiO₂, EtOAc 100%) gave pale green liquid (0.511 g, 99 %). ¹H NMR (400 MHz, CDCl₃) δ = 7.68 (1H, t, *J* = 7.8 Hz, H-5), 7.52 (1H, dd, *J* = 7.9 Hz, *J* = 0.9 Hz, H-4), 7.35 (1H, dd, *J* = 7.6 Hz, *J* = 1.0 Hz, H-6), 4.83 (2H, s, H-9), 3.13 (1H, s, H-1), 0.96 (9H, s, H-14), 0.12 (6H, s, H-12); ¹³C NMR (101 MHz, CDCl₃) δ = 162.2 (C-7), 141.1 (C-3), 136.9 (C-5), 125.6 (C-4), 119.9 (C-6), 82.9 (C-2), 76.9 (C-1), 65.9 (C-9), 26.0 (C-14), 18.4 (C-13), -5.3 (C-12); m/z (ESMS⁺) found 248.1474 (calc. for C₁₄H₂₂NO²⁸Si 248.1471) for [M+H]⁺.

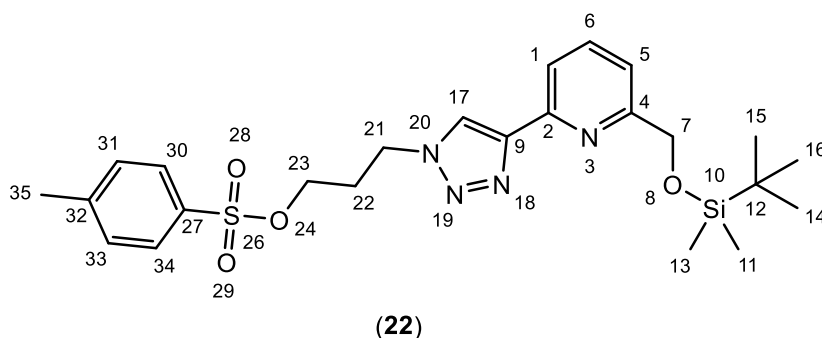
6.5.42 Synthesis of 3-(4-(6-(((tert-butyl)dimethylsilyl)oxy)methyl)pyridin-2-yl)-1H-1,2,3-triazol-1-yl)propyl 4-methylbenzenesulfonate (**21**)



3-bromopropanol (0.120 g, 0.859 mmol), sodium azide (0.065 g, 0.930 mmol), compound **20** (0.177 g, 0.716 mmol), CuSO₄·5H₂O (0.021 g, 0.086 mmol) and sodium ascorbate (0.028 g, 0.143 mmol) were used as the starting

materials. It followed the general procedure for click reaction procedure 1 (section 6.4.6.1). Purification *via* flash column chromatography (SiO₂, EtOAc 100%) gave a pale yellow jelly-like solid (0.1872 g, 75 %, R_f = 0.47). ¹H NMR (400 MHz, CDCl₃) δ = 8.17 (1H, s, H-17), 8.00 (1H, d, *J* = 7.2 Hz, H-1), 7.79 (1H, t, *J* = 7.7 Hz, H-6), 7.45 (1H, dd, *J* = 7.6 Hz, *J* = 0.8 Hz, H-5), 4.84 (2H, s, H-7), 4.59 (2H, t, *J* = 6.7 Hz, H-21), 3.68 (1H, t, *J* = 5.9 Hz, H-23), 2.46 - 3.07 (1H, m, H-24), 2.18 (2H, quin, *J* = 6.3 Hz, H-22), 0.97 (9H, s, H-16, 15, 14), 0.14 (6H, s, H-13, 11); ¹³C NMR (101 MHz, CDCl₃) δ = 161.3 (C-4), 149.2 (C-2), 148.5 (C-9), 137.6 (C-6), 122.6 (C-17), 119.3 (C-1), 118.5 (C-5), 66.2 (C-7), 58.7 (C-23), 47.2 (C-21), 32.7 (C-22), 26.0 (C-16, 15, 14), 18.5 (C-12), -5.2 (C-13, 11); *m/z* (ESMS⁺) found 349.2077 (calc. for C₁₇H₂₉NO₂²⁸Si 349.2060) for [M+H]⁺.

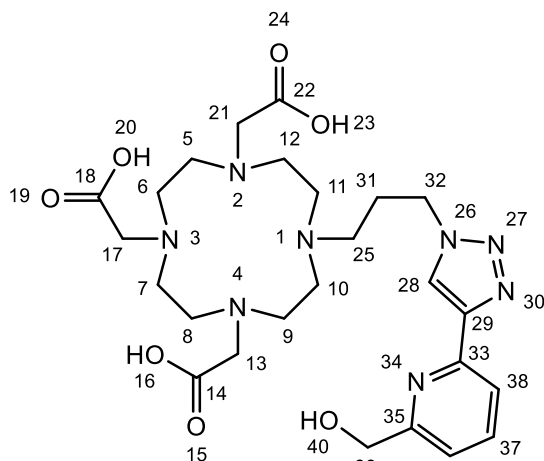
6.5.43 Synthesis of 3-(4-(6-(((tert-butyl)dimethylsilyl)oxy)methyl)pyridin-2-yl)-1H-1,2,3-triazol-1-yl)propyl 4-methylbenzenesulfonate (**22**)



Compound **21** (0.142 g, 0.409 mmol), tosyl chloride (0.159 g, 0.817 mmol) were used as the starting materials. It followed the general procedure

for tosylation reaction (section 6.4.8). Purification *via* flash column chromatography (SiO₂, EtOAc 100%) gave a white solid (0.116 g, 56 %, R_f = 0.72). ¹H NMR (400 MHz, CDCl₃) δ = 8.06 (1H, s, H-17), 7.95 (1H, d, *J* = 7.4 Hz, H-1), 7.73 - 7.81 (3H, m, H-6, 34, 30), 7.46 (1H, dd, *J* = 7.7 Hz, *J* = 0.7 Hz, H-5), 7.29 (2H, d, *J* = 8.2 Hz, H-33, 31), 4.86 (2H, s, H-7), 4.48 (2H, t, *J* = 6.7 Hz, H-21), 4.07 (2H, t, *J* = 5.9 Hz, H-23), 2.31 - 2.40 (5H, m, H-35, 22), 0.95 - 1.02 (9H, m, H-16, 15, 14), 0.13 - 0.17 (6H, m, H-13, 11); ¹³C NMR (101 MHz, CDCl₃) δ = 161.3 (C-4), 149.0 (C-2), 148.5 (C-9), 145.1 (C-32),

6.5.45 Synthesis of 2,2',2''-(10-(3-(4-(6-(hydroxymethyl)pyridin-2-yl)-1H-1,2,3-triazol-1-yl)propyl)-1,4,7,10-tetraazacyclododecane-1,4,7-triyl)triacetic acid (**C7**).

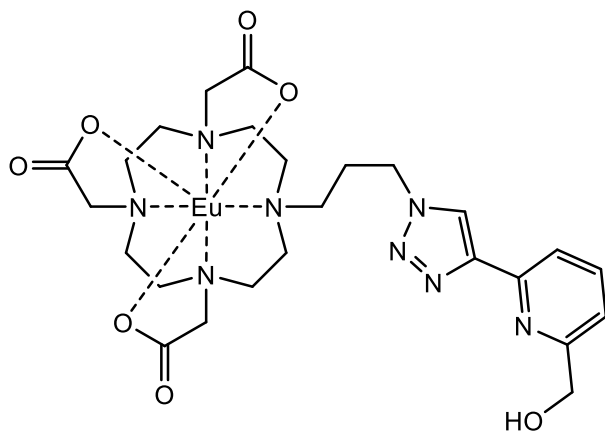


(**C7**)

Compound **23** (0.084 g, 0.099 mmol) was used as the starting material. It followed the general procedure for macrocycle's tert-Bu deprotection reactions (section 6.4.4). Purification *via* HPLC gave a white hygroscopic solid (35 mg, 63 %). ^1H NMR (400 MHz, CD_3OD) δ = 8.53 (1H, s, H-28), 7.78 - 7.92 (2H, m, H-37, 38), 7.42 (1H, dd, J = 6.8 Hz, J = 1.8 Hz, H-36), 4.71 (2H, s, H-39), 4.58 (2H, br t, J = 6.2 Hz, H-32), 3.67

(6H, br d, J = 18.4 Hz, H-13, 17, 21), 2.94 - 3.43 (18H, m, H-5, 6, 7, 8, 9, 10, 11, 12, 25), 2.25 - 2.51 (2H, m, H-31); ^{13}C NMR (101 MHz, CD_3OD) δ = 173.0 (C-14, 22), 172.3 (C-18), 162.4 (C-35), 150.3 (C-33), 148.9 (C-29), 139.1 (C-37), 124.8 (C-28), 121.1 (C-36), 119.8 (C-38), 65.6 (C-39), 56.5 (C-13, 17, 21), 52.2 (C-6, 7), 51.4 (C-5, 8, 25), 50.9 (C-9, 12), 50.6 (C-10, 11), 49.2 (C-32), 26.4 (C-31); m/z (ESMS $^+$) found 562.2864 (calc. for $\text{C}_{25}\text{H}_{38}\text{N}_8\text{O}_7$ 562.2863) for $[\text{M}+\text{H}]^+$.

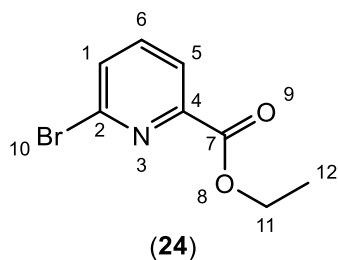
6.5.46 Synthesis of **EuC7**



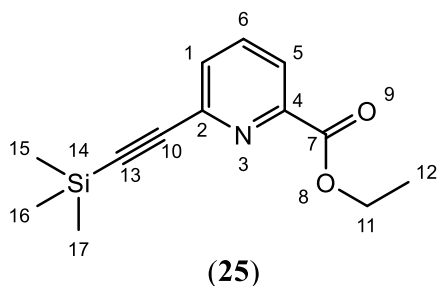
(**EuC7**)

C7 (0.023 g, 0.040 mmol) and $\text{EuCl}_3 \cdot 6\text{H}_2\text{O}$ (0.017 g, 0.046 mmol) were used as starting materials. It followed the general procedure for lanthanide complexation procedure 1 (section 6.4.9.1). Purification *via* HPLC gave a white hygroscopic solid (16 mg, 56%); m/z (ESMS $^+$) found 735.1750 (cal. for $\text{C}_{25}\text{H}_{35}\text{N}_8\text{O}_7^{153}\text{EuNa}$

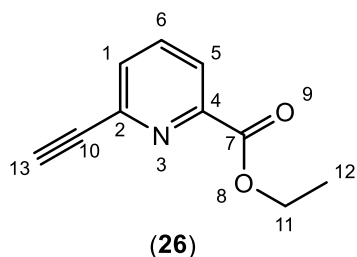
735.1739) for $[\text{M}+\text{Na}]^+$.

6.5.47 Synthesis of ethyl 6-bromopicolinate (**24**)

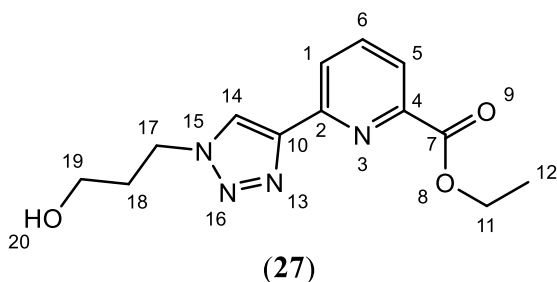
6-bromopicolinic acid (1.102 g, 5.455 mmol) in 20 mL absolute ethanol was added 4 drops concentrated H₂SO₄. The reaction mixture was heated at reflux for 18 h. The solvent was removed in reduced pressure, then the residue was dissolved in 30 mL DCM and washed with 10 mL NaHCO₃ 1 M solution two times. The organic layer was dried with MgSO₄, filtered and the solvent was removed under reduced pressure to give a white-brown solid. Purification *via* column chromatography (SiO₂ EtOAc 100%) gave a white solid (1.157 g, 92%). ¹H NMR (400 MHz, CDCl₃) δ = 8.08 (1H, dd, *J* = 7.0 Hz, *J* = 1.6 Hz, H-5), 7.64 - 7.74 (2H, m, H-1, 6), 4.47 (2H, q, *J* = 7.2 Hz, H-11), 1.43 (3H, t, *J* = 7.1 Hz, H-12); ¹³C NMR (101 MHz, CDCl₃) δ = 164.0 (C-7), 149.3 (C-4), 142.3 (C-2), 139.2 (C-6), 131.8 (C-1), 124.1 (C-5), 62.4 (C-11), 14.4 (C-12); *m/z* (ESMS⁺) 229.9809 (calc. for C₈H₉NO₂⁷⁹Br 229.9817) for [M+H]⁺.

6.5.48 Synthesis of ethyl 6-((trimethylsilyl)ethynyl)picolinate (**25**)

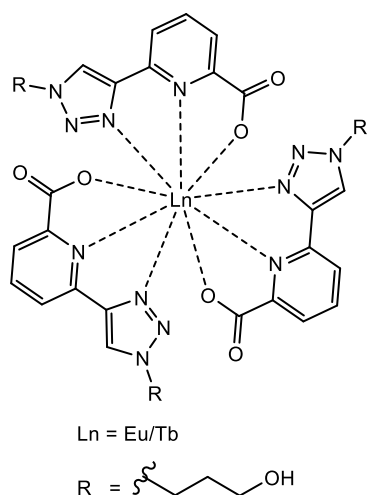
Ethyl 6-bromopicolinate (**24**) (0.089 g, 0.389 mmol), Pd(PPh₃)₂Cl₂ (10.0 mg, 150 μmol), CuI (3.0 mg, 150 μmol) and ethynyltrimethylsilane (0.152 g, 1.556 mmol) were used as the starting materials. It followed the general procedure for Sonogashira reactions (section 6.4.1). Purification *via* column chromatography (SiO₂, DCM 100%) gave a brown-black solid (72 mg, 75 %, R_f = 0.75). ¹H NMR (400 MHz, CDCl₃) δ = 8.04 (1H, dd, *J* = 7.8 Hz, *J* = 1.2 Hz, H-5), 7.79 (1H, t, *J* = 7.8 Hz, H-6), 7.61 (1H, dd, *J* = 7.8 Hz, *J* = 1.2 Hz, H-1), 4.47 (2H, q, *J* = 7.1 Hz, H-11), 1.44 (3H, t, *J* = 7.1 Hz, H-12), 0.25 - 0.28 (9H, m, H-17, 16, 15); ¹³C NMR (101 MHz, CDCl₃) δ = 164.9 (C-7), 148.8 (C-4), 143.5 (C-2), 137.2 (C-6), 130.6 (C-1), 124.3 (C-5), 103.0 (C-10), 96.4 (C-13), 62.2 (C-11), 14.4 (C-12), -0.2 (C-17, 16, 15); *m/z* (ESMS⁺) 248.1107 (calc. for C₁₃H₁₈NO₂²⁸Si 248.1107) for [M+H]⁺.

6.5.49 Synthesis of ethyl 6-ethynylpicolinate (**26**)

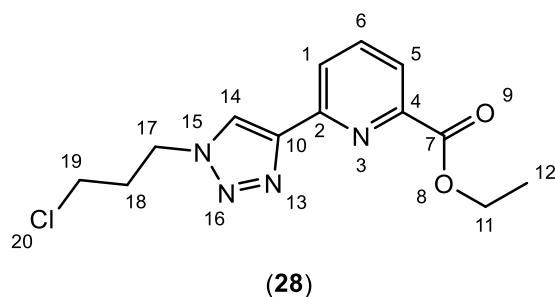
Compound **25** (0.195 g, 0.788 mmol) and TBAF (0.313 g, 1.200 mmol) were used as the starting materials. It followed the general procedure for TMS deprotection reactions procedure 2 (section 6.4.5.2). Purification *via* SiO₂ column chromatography (EtOAc 100%) gave a brown solid (0.108 g, 78%, R_f = 0.66). ¹H NMR (400 MHz, CDCl₃) δ = 8.09 (1H, dd, *J* = 7.8 Hz, *J* = 1.0 Hz, H-5), 7.82 (1H, t, *J* = 7.8 Hz, H-6), 7.64 (1H, dd, *J* = 7.8 Hz, *J* = 1.0 Hz, H-1), 4.48 (2H, q, *J* = 7.2 Hz, H-11), 3.20 (1H, s, H-13), 1.44 (3H, t, *J* = 7.1 Hz, H-12); ¹³C NMR (101 MHz, CDCl₃) δ = 164.8 (C-7), 149.0 (C-4), 142.7 (C-2), 137.4 (C-6), 130.5 (C-1), 124.7 (C-5), 82.2 (C-10), 78.6 (C-13), 62.3 (C-11), 14.4 (C-12); *m/z* (ESMS⁺) 176.0712 (calc. for C₁₀H₁₀NO₂ 176.0712) for [M+H]⁺.

6.5.50 Synthesis of ethyl 6-(1-(3-hydroxypropyl)-1H-1,2,3-triazol-4-yl)picolinate (**27**)

3-bromopropanol (0.213 g, 1.53 mmol), sodium azide (0.109 g, 1.68 mmol), compound **26** (0.267 g, 1.52 mmol), CuSO₄·5H₂O (38.0 mg, 152 μmol) and sodium ascorbate (0.151 g, 0.763 mmol) were used as the starting materials. It followed the general procedure for click reactions procedure 2 (section 6.4.6.2). Purification *via* column chromatography (SiO₂, EtOAc 100%) gave a yellow solid (0.253 g, 60%). ¹H NMR (400 MHz, CDCl₃) δ = 8.46 (1H, s, H-14), 8.36 (1H, dd, *J* = 7.9 Hz, *J* = 1.1 Hz, H-1), 8.03 (1H, dd, *J* = 7.8 Hz, *J* = 1.2 Hz, H-5), 7.92 (1H, t, *J* = 7.8 Hz, H-6), 4.62 (2H, t, *J* = 6.8 Hz, H-17), 4.48 (2H, q, *J* = 7.2 Hz, H-11), 3.71 (2H, br t, *J* = 5.5 Hz, H-19), 2.56 - 2.69 (1H, m, H-20), 2.21 (2H, quin, *J* = 6.3 Hz, H-18), 1.45 (4H, t, *J* = 7.1 Hz, H-12); ¹³C NMR (101 MHz, CDCl₃) δ = 165.2 (C-7), 151.0 (C-4), 148.0 (C-2), 147.7 (C-10), 138.0 (C-6), 124.1 (C-5), 123.7 (C-14), 123.5 (C-1), 62.1 (C-11), 58.7 (C-19), 47.3 (C-17), 32.7 (C-18), 14.4 (C-12); *m/z* (ESMS⁺) 277.1313 (calc. for C₁₃H₁₇N₄O₃ 277.1301) for [M+H]⁺.

6.5.51 Synthesis of **Eu/Tb(27)**₃

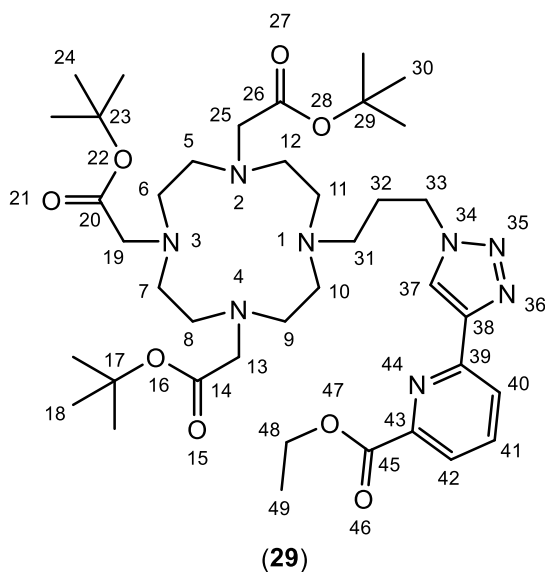
27 (0.053 g, 0.191 mmol) was dissolved in 10 mL deionised water at pH 9. It was heated at reflux for 1h. After cooling to room temperature, the pH was adjusted to 7. **Eu/TbCl₃·6H₂O** (0.023 g, 0.063 mmol / **EuCl₃·6H₂O**) was added. It was then crystallised to give a white solid (69 mg, 122% / **Eu(27)**₃) (containing NaCl); *m/z* (ESMS⁺) found 917.1624 (calc. for C₃₃H₃₃N₁₂O₉Na¹⁵³Eu 917.1603) for [M+Na]⁺ **Eu(27)**₃. Complexation with **TbCl₃·6H₂O** providing **Tb(27)**₃ with a comparable result, *m/z* (ESMS⁺) found 923.1677 (calc. C₃₃H₃₃N₁₂O₉Na¹⁵⁹Tb 923.1645) for [M+Na]⁺.

6.5.52 Synthesis of ethyl 6-(1-(3-chloropropyl)-1H-1,2,3-triazol-4-yl)picolinate (**28**)

Compound **27** (0.463 g, 1.68 mmol) and thionyl chloride (0.798 g, 6.71 mmol) was used as the starting materials. It followed the general procedure for chlorination reactions (section 6.4.2) with a longer reaction time 18 h instead of 3 h.

Purification *via* column chromatography (SiO₂, EtOAc 100%) gave a white-yellow solid (0.395 g, 80%). ¹H NMR (400 MHz, CDCl₃) δ = 8.31 - 8.44 (2H, m, H-14, 1), 8.04 (1H, d, *J* = 7.6 Hz, H-5), 7.93 (1H, t, *J* = 7.6 Hz, H-6), 4.64 (2H, t, *J* = 6.6 Hz, H-17), 4.48 (2H, q, *J* = 7.0 Hz, H-11), 3.58 (2H, t, *J* = 6.0 Hz, H-19), 2.46 (2H, quin, *J* = 6.1 Hz, H-18), 1.46 (3H, t, *J* = 7.0 Hz, H-12); ¹³C NMR (101 MHz, CDCl₃) δ = 165.2 (C-7), 150.7 (C-4), 148.1 (C-2), 147.9 (C-10), 138.0 (C-6), 124.2 (C-5), 123.5 (C-14), 123.5 (C-1), 62.0 (C-11), 47.5 (C-17), 41.1 (C-19), 32.7 (C-18), 14.4 (C-12); *m/z* (ESMS⁺) 295.0963 (calc. for C₁₃H₁₆N₄O₂³⁵Cl 295.0962) for [M+H]⁺.

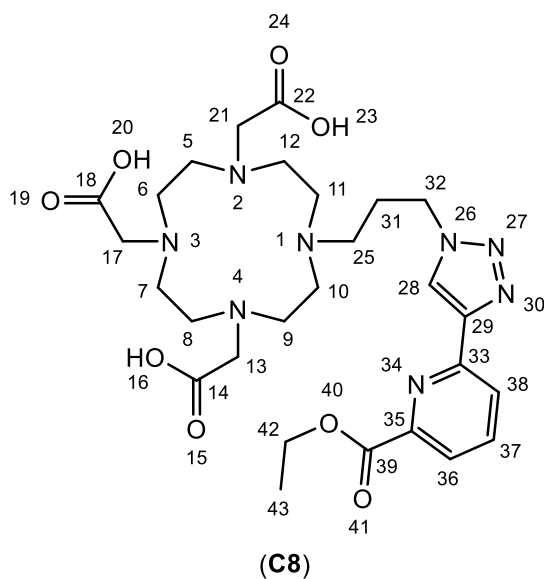
6.5.53 Synthesis of tri-tert-butyl 2,2',2''-(10-(3-(4-(6-(ethoxycarbonyl)pyridin-2-yl)-1H-1,2,3-triazol-1-yl)propyl)-1,4,7,10-tetraazacyclododecane-1,4,7-triyl)triacetate (29)



Compound **1** (0.439 g, 0.737 mmol), potassium carbonate (0.407 g, 2.945 mmol), compound **28** (0.407 g, 2.948 mmol) were used as the starting materials. It followed the general procedure for the DO3A's fourth arm attachments (section 6.4.3). Purification *via* flash column chromatography (SiO₂, DCM:MeOH 9:1) gave a light-yellow oily product (484 mg, 85 %). ¹H NMR (400 MHz, CDCl₃) δ = 8.50 (1H, s, H-37), 8.33 (1H, dd, *J* = 7.8 Hz, *J* = 1.2 Hz, H-40), 8.03

(1H, dd, *J* = 7.8 Hz, *J* = 1.0 Hz, H-42), 7.93 (1H, t, *J* = 7.8 Hz, H-41), 4.40 - 4.55 (4H, m, H-33, 48), 2.06 - 3.29 (26H, m, H-5, 6, 7, 8, 9, 10, 11, 12, 13, 19, 25, 31, 32), 1.34 - 1.56 (30H, m, H-18, 24, 30, 49); ¹³C NMR (101 MHz, CDCl₃) δ = 173.6 (C-14, 26), 172.6 (C-20), 165.1 (C-45), 150.6 (C-43), 147.9 (C-39), 147.5 (C-38), 137.8 (C-41), 124.0 (C-42), 123.3 (C-37, 40), 82.9 (C-17, 29), 82.5 (C-23), 61.9 (C-48), 58.0, 56.6, 55.7, 51.2, 50.2 (C-6, 7, 8, 9, 10, 11, 12, 13, 19, 25, 31), 48.9 (C-33), 28.1, 27.9, 27.8 (C-18, 24, 30), 26.7 (C-32), 14.3 (C-49); *m/z* (ESMS⁺) 773.4920 (calc. for C₃₉H₆₅O₈ 773.4925) for [M+H]⁺.

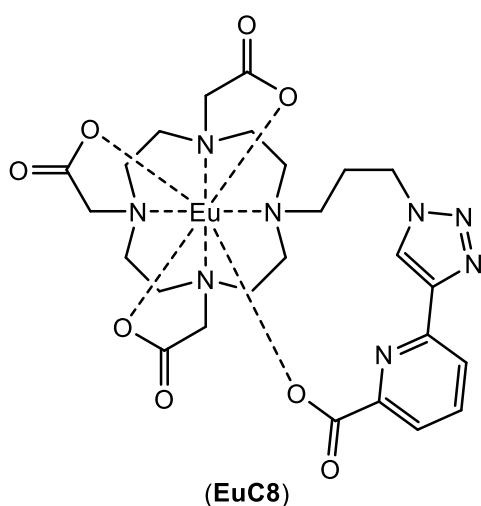
6.5.54 Synthesis of 2,2',2''-(10-(3-(4-(6-(ethoxycarbonyl)pyridin-2-yl)-1H-1,2,3-triazol-1-yl)propyl)-1,4,7,10-tetraazacyclododecane-1,4,7-triyl)triacetic acid (**C8**)



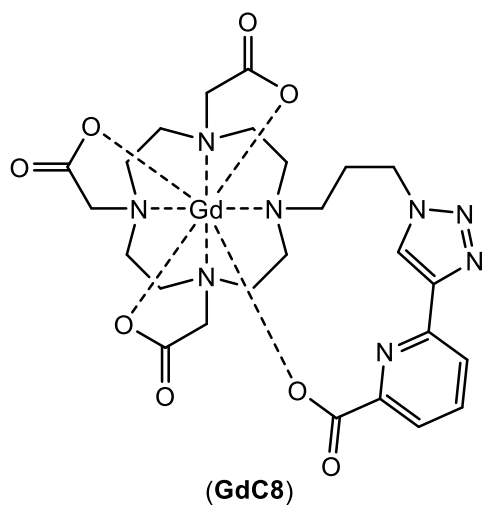
29 (0.101 g, 130.6 mmol) was used as the starting material. It followed the general procedure for the macrocycle's tert-Bu deprotection reactions (section 6.4.4). Purification *via* HPLC (R_t 20.1 min) (method see section 6.2) gave a white solid (73 mg, 92%). ^1H NMR (400 MHz, CD_3OD) δ = 8.68 (1H, s, H-28), 8.25 (1H, dd, J = 6.3 Hz, J = 2.9 Hz, H-38), 8.00 - 8.12 (2H, m, H-36, 37), 4.64 (2H, t, J = 6.8 Hz, H-32), 4.47 (2H, q, J = 7.2 Hz, H-42), 4.15

(2H, br s, H-17), 3.34 - 3.81 (14H, m, H-5, 6, 7, 8, 13, 21, 25), 2.90 - 3.27 (8H, m, H-9, 10, 11, 12), 2.46 - 2.62 (2H, m, H-31), 1.44 (3H, t, J = 7.1 Hz, H-43); ^{13}C NMR (101 MHz, CD_3OD) δ = 174.6 (C-14, 18, 22), 166.5 (C-39), 151.7 (C-35), 149.1 (C-33), 148.6 (C-29), 139.8 (C-37), 125.4 (C-28), 125.3 (C-36), 124.5 (C-38), 63.2 (C-42), 55.6 (C-17), 53.7 (C-13, 21), 53.2 (C-6, 7), 52.7 (C-5, 8), 51.3 (C-25), 50.1 (C-9, 12), 49.8 (C-10, 11), 48.8 (C-32), 25.9 (C-31), 14.5 (C-43); m/z (ESMS $^+$) 605.3069 (calc. for $\text{C}_{27}\text{H}_{41}\text{N}_8\text{O}_8$ 605.3047) for $[\text{M}+\text{H}]^+$.

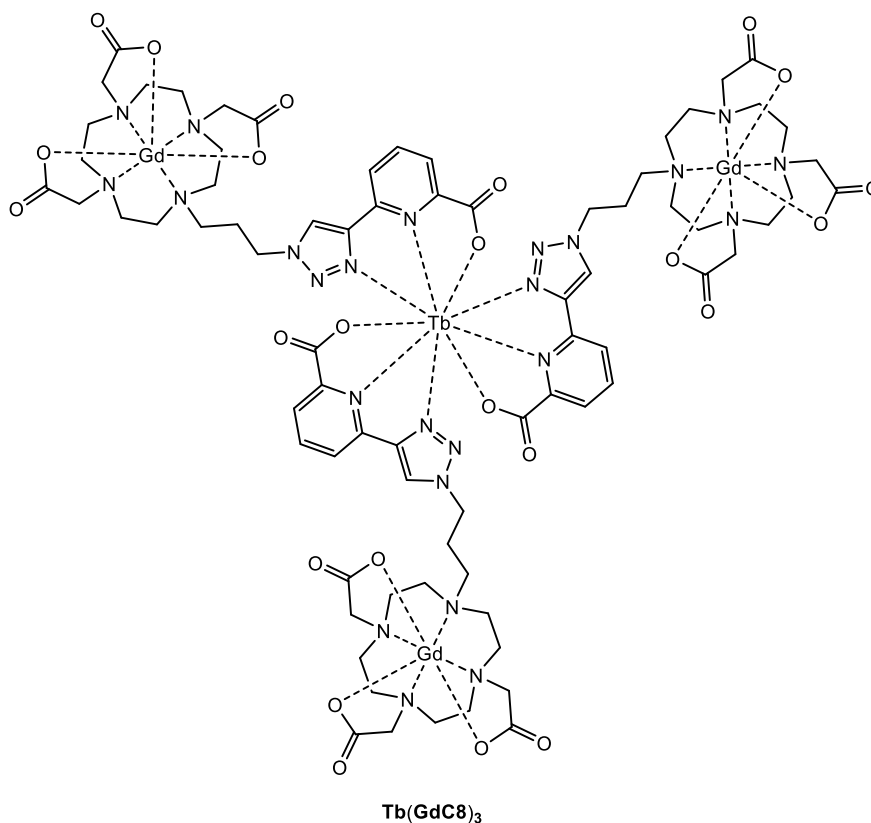
6.5.55 Synthesis of **EuC8**



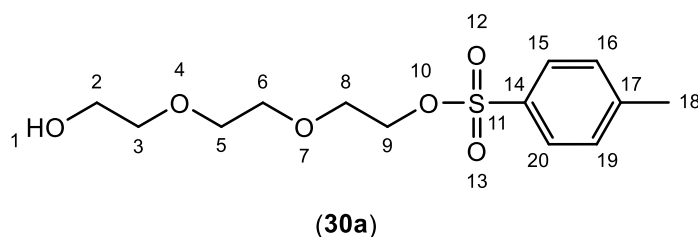
C8 (0.050 g, 0.082 mmol) and $\text{EuCl}_3 \cdot 6\text{H}_2\text{O}$ (0.030 g, 0.084 mmol) were used as starting materials. It followed the general procedure for lanthanide complexation procedure 2 (section 6.4.9.2). Purification *via* HPLC (R_t 17.6 min) gave a white hygroscopic solid (65 mg, 108 %); m/z (MALDI-TOF) found 727.2058 (calc. $\text{C}_{25}\text{H}_{34}\text{N}_8\text{O}_8^{152}\text{Eu}$ 727.1712) for **EuC8** for $[\text{M}+2\text{H}]^+$.

6.5.56 Synthesis of **GdC8**

C8 (0.050 g, 0.082 mmol) and $\text{GdCl}_3 \cdot 6\text{H}_2\text{O}$ (0.031 g, 0.083 mmol) were used as starting materials. It followed the general procedure for lanthanide complexations procedure 2. Purification *via* HPLC (R_t 17.6 min) gave a white hygroscopic solid (69 mg, 115%); m/z (ESMS+) found 732.1641 (calc. $\text{C}_{25}\text{H}_{34}\text{N}_8\text{O}_8^{157}\text{Gd}$ 732.1741) for **GdC8** for $[\text{M}+2\text{H}]^+$.

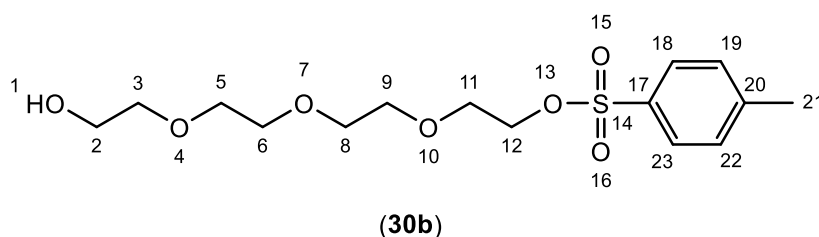
6.5.57 Synthesis of **Tb(GdC8)₃**

GdC8 (0.076 g, 0.104 mmol) and $\text{TbCl}_3 \cdot 6\text{H}_2\text{O}$ (0.013 g, 0.034 mmol) were dissolved in 5 mL deionised water. It was heated in $\mu\text{w.}$ at 75°C for 1h. It was then lyophilised to give a white solid (75 mg, 93%).

6.5.58 Synthesis of 2-(2-(2-(2-hydroxyethoxy)ethoxy)ethoxy)ethyl 4-methylbenzenesulfonate (**30a**)

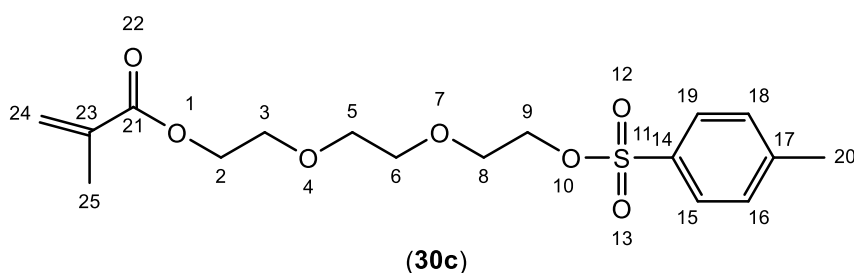
2,2'-((ethane-1,2-diylbis(oxy))bis(ethan-1-ol) (5.060 g, 33.400 mmol) and tosyl chloride (6.553 g, 33.695 mmol) were used as the starting

materials. It followed the general procedure for tosylation reactions (section 6.4.8). Purification *via* flash column chromatography (SiO₂, EtOAc 100%) gave colourless oily (4.421 g, 73%). ¹H NMR (400 MHz, CDCl₃) δ = 7.80 (1H, d, *J* = 8.4 Hz, H-20, 15), 7.35 (2H, d, *J* = 7.8 Hz, H-19, 16), 4.17 (2H, t, *J* = 4.7 Hz, H-9), 3.67 - 3.73 (4H, m, H-2, 8), 3.60 (4H, s, H-6, 5), 3.54 - 3.59 (2H, m, H-3), 2.45 (4H, s, H-1, 18); ¹³C NMR (101 MHz, CDCl₃) δ = 144.9 (C-17), 133.0 (C-14), 129.9 (C-19, 16), 128.0 (C-20, 15), 72.5 (C-3), 70.8, 70.3 (C-5, 6), 69.3 (C-9), 68.7 (C-8), 61.7 (C-2), 21.7 (C-18); *m/z* (ESMS⁺) found 327.0897 (cal. for C₁₃H₂₀O₆SNa) for [M+Na]⁺.

6.5.59 Synthesis of 2-(2-(2-(2-(2-hydroxyethoxy)ethoxy)ethoxy)ethoxy)ethyl 4-methylbenzenesulfonate (**30b**)

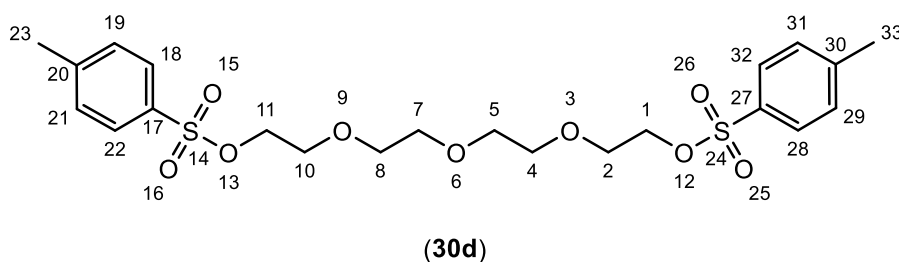
2,2'-((oxybis(ethane-2,1-diyl))bis(oxy))bis(ethan-1-ol) (3.010 g, 15.445 mmol) and tosyl chloride (1.507

g, 7.748 mmol) were used as the starting materials. It followed the general procedure for tosylation reactions (section 6.4.8). Purification *via* flash column chromatography (SiO₂, EtOAc 100%) gave colourless oily (1.753 g, 64.9 % for **30b**). ¹H NMR (400 MHz, CDCl₃) δ = 7.79 (2H, dd, *J* = 8.3 Hz, *J* = 1.5 Hz, H-23, 18), 7.34 (2H, dd, *J* = 8.0 Hz, *J* = 0.6 Hz, H-22, 19), 4.12 - 4.20 (2H, m, H-12), 3.52 - 3.75 (14H, m, H-2, 3, 5, 6, 8, 9, 11), 2.60 (1H, br s, H-1), 2.45 (3H, s, H-21); ¹³C NMR (101 MHz, CDCl₃) δ = 144.9 (C-20), 133.0 (C-17), 129.9 (C-22, 19), 128.0 (C-23, 18), 72.5 (C-3), 70.7, 70.7, 70.5, 70.4 (C-5, 6, 8, 9), 69.3 (C-12), 68.7 (C-11), 61.7 (C-2), 21.7 (C-21); *m/z* (ESMS⁺) found 349.1337 (cal. for C₁₅H₂₄O₇S 349.1321) for [M+H]⁺.

6.5.60 Synthesis of 2-(2-(2-(tosyloxy)ethoxy)ethoxy)ethyl methacrylate (**30c**)

30a (1.106 g, 3.636 mmol) was dissolved in pyridine (2.69 g, 3.636 mmol) in an

ice bath 0-4°C. Methacryloyl chloride (0.456 g, 4.363 mmol) in chilled dry DCM was then added dropwise. After stirring for 24h, the reaction mixture was poured into 50 mL water. It was acidified by HCl conc. before extracted by ethyl acetate. The organic layer was separated, dried over MgSO₄ and concentrated under reduced pressure. Purification *via* flash column chromatography (SiO₂, EtOAc 100%) gave colourless oily (0.947 g, 70%). ¹H NMR (400 MHz, CDCl₃) δ = 7.80 (2H, d, *J* = 8.2 Hz, H-19, 15), 7.34 (2H, d, *J* = 8.2 Hz, H-18, 16), 6.06 - 6.18 (1H, m, H-24), 5.52 - 5.63 (1H, m, H-24<a>), 4.28 (2H, t, *J* = 4.9 Hz, H-2), 4.16 (2H, t, *J* = 4.7 Hz, H-9), 3.67 - 3.73 (5H, m, H-3, 8), 3.54 - 3.62 (4H, m, H-5, 6), 2.45 (3H, s, H-20), 1.91 - 1.98 (3H, m, H-25); ¹³C NMR (101 MHz, CDCl₃) δ = 167.5 (C-33), 144.9 (C-27), 136.3 (C-37), 133.2 (C-26), 129.9 (C-18, 16), 128.1 (C-19, 15), 125.9 (C-24), 70.7 (C-5, 6), 69.3 (C-9), 68.9 (C-3, 8), 63.9 (C-2), 21.8 (C-20), 18.4 (C-25); *m/z* (ESMS⁺) found 372.1241 (cal. for C₁₇H₂₄O₇S 372.1234) for [M+H]⁺.

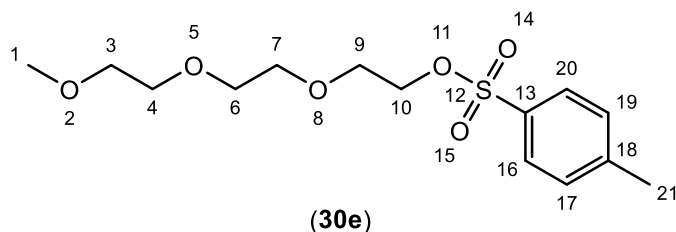
6.5.61 Synthesis of ((oxybis(ethane-2,1-diyl))bis(oxy))bis(ethane-2,1-diyl) bis(4-methylbenzenesulfonate) (**30d**)

Tetraethylene glycol (2.057 g, 10.591 mmol), *p*-toluen sulfonyl

chloride (4.943 g, 25.417 mmol) was used as the starting materials. It followed the general procedure for tosylation reactions (section 6.4.8). Purification *via* column chromatography (SiO₂, EtOAc 100%, *R_f* = 0.59) gave a colourless oil (3.422 g, 64.3%). ¹H NMR (400 MHz, CDCl₃) δ = 7.79 (4H, d, *J* = 8.2 Hz, H-32, 28, 22, 18), 7.34 (4H, d, *J* = 8.2 Hz, H-31, 29, 21, 19), 4.15 (4H, t, *J* = 4.7 Hz, H-11, 1), 3.67 (4H, t, *J* = 4.7 Hz, H-10, 2), 3.56 (8H, s, H-7, 5, 8, 4), 2.44 (6H, s, H-33, 23); ¹³C NMR (101 MHz, CDCl₃) δ = 144.9 (C-30, 20), 133.0 (C-27, 17), 129.9 (C-31, 29, 21, 19), 128.0 (C-32, 28, 22, 18),

70.7 (C-7, 5), 70.6 (C-8, 4), 69.3 (C-11, 1), 68.7 (C-10, 2), 21.7 (C-33, 23); m/z (ESMS⁺) found 525.1249 (calc. for C₂₂H₃₀O₉S₂Na 525.1229) for [M+Na]⁺.

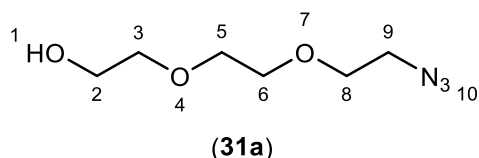
6.5.62 Synthesis of 2-(2-(2-methoxyethoxy)ethoxy)ethyl 4-methylbenzenesulfonate (**30e**)



2-(2-(2-methoxyethoxy) ethoxy) ethan-1-ol (0.453 g, 2.760 mmol) and tosyl chloride (0.580 g, 3.042 mmol) were used as the starting materials. It followed the general

procedure for tosylation reactions (section 6.4.8). Purification *via* flash column chromatography (SiO₂, EtOAc 100%) gave colourless oily (0.463 g, 52%). ¹H NMR (500 MHz, CDCl₃) δ = 7.79 (1H, d, J = 8.2 Hz, H-20, 16), 7.35 (2H, d, J = 8.2 Hz, H-19, 17), 4.16 (2H, t, J = 4.9 Hz, H-10), 3.68 (2H, t, J = 4.9 Hz, H-9), 3.57 - 3.62 (6H, m, H-7, 6, 4), 3.51 - 3.54 (2H, m, H-3), 3.36 (3H, s, H-1), 2.44 (3H, s, H-21); ¹³C NMR (126 MHz, CDCl₃) δ = 144.8 (C-18), 132.9 (C-13), 129.8 (C-19, 17), 127.9 (C-20, 16), 71.8 (C-3), 70.6 (C-7, 6, 4), 70.4, 69.2 (C-10), 68.6 (C-9), 58.9 (C-1), 21.5 (C-21)); m/z (ESMS⁺) found 319.1125 (calc. for C₁₄H₂₃O₆S 319.1215) for [M+H]⁺.

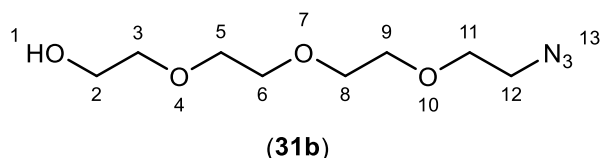
6.5.63 Synthesis of 2-(2-(2-azidoethoxy)ethoxy)ethan-1-ol (**31a**)



Compound **30a** (0.959 g, 3.152 mmol) and sodium azide (0.512 g, 7.880 mmol) was used as the starting materials. It followed the general

procedure for synthesis of azides procedure 2 (section 6.4.7.2). Purification *via* flash column chromatography (SiO₂, EtOAc 100%) gave a colourless liquid (0.425 g, 75%). ¹H NMR (400 MHz, CDCl₃) δ = 3.71 - 3.78 (2H, m, H-2), 3.65 - 3.71 (6H, m, H-5, 6, 8), 3.59 - 3.65 (2H, m, H-3), 3.40 (2H, t, J = 5.0 Hz, H-9), 2.52 (1H, t, J = 6.2 Hz, H-1); ¹³C NMR (101 MHz, CDCl₃) δ = 72.6 (C-3), 70.7 (C-5), 70.5 (C-6), 70.1 (C-8), 61.8 (C-2), 50.7 (C-9); m/z (ESMS⁺) found 198.0858 (cal. for C₆H₁₃N₃O₃Na 198.0855) for [M+Na]⁺.

6.5.64 Synthesis of 2-(2-(2-(2-azidoethoxy)ethoxy)ethoxy)ethan-1-ol (**31b**)

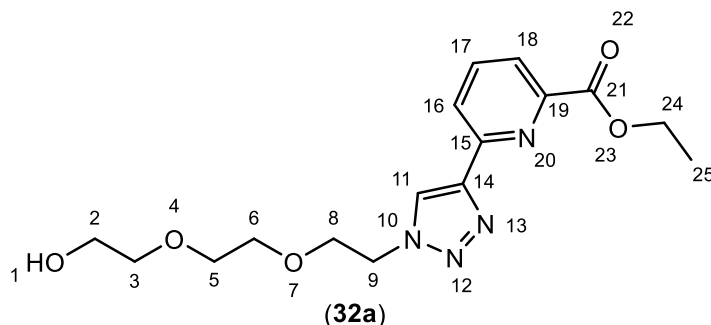


Compound **30b** (1.143 g, 3.282 mmol) and sodium azide (1.067 g, 16.413 mmol) was used as the starting

materials. It followed the general procedure for synthesis of azides procedure 2 (section 6.4.7.2). Purification *via* flash column chromatography (SiO₂, EtOAc 100%) gave a

colourless liquid (0.605 g, 84%). ^1H NMR (400 MHz, CDCl_3) δ = 3.70 - 3.75 (2H, m, H-2), 3.65 - 3.70 (10H, m, H-5, 6, 8, 9, 11), 3.58 - 3.64 (2H, m, H-3), 3.37 - 3.42 (2H, m, H-12), 2.58 - 2.85 (1H, m, H-1); ^{13}C NMR (101 MHz, CDCl_3) δ = 72.5 (C-3), 70.7 (C-5, 11), 70.6 (C-6), 70.4 (C-8), 70.0 (C-9), 61.7 (C-2), 50.7 (C-12); m/z (ESMS $^+$) found 242.1125 (cal. for $\text{C}_8\text{H}_{17}\text{N}_3\text{O}_4\text{Na}$ 242.1117) for $[\text{M}+\text{Na}]^+$.

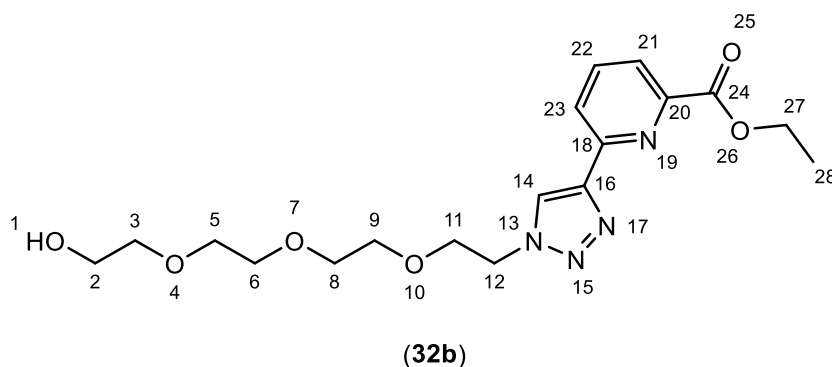
6.5.65 Synthesis of ethyl 6-(1-(2-(2-(2-hydroxyethoxy)ethoxy)ethyl)-1H-1,2,3-triazol-4-yl)picolinate (**32a**)



Compound **31a** (0.256 g, 1.464 mmol), compound **26** (0.256 g, 1.464 mmol), $\text{CuSO}_4 \cdot 5\text{H}_2\text{O}$ (18 mg, 0.073 mmol) and sodium ascorbate (29 mg, 0.146 mmol) were used as the

starting materials. It followed the general procedure for click reactions procedure 3 (section 6.4.6.3). Purification *via* flash column chromatography (SiO_2 , $\text{DCM}:\text{MeOH}/9:1$) gave a brown oily (0.450 g, 87%). ^1H NMR (400 MHz, CDCl_3) δ = 8.85 (1H, s, H-11), 8.40 (1H, dd, J = 7.8 Hz, J = 1.2 Hz, H-16), 8.01 (1H, dd, J = 7.8 Hz, J = 1.2 Hz, H-18), 7.91 (1H, t, J = 7.8 Hz, H-17), 4.63 (2H, t, J = 4.7 Hz, H-9), 4.47 (2H, q, J = 7.2 Hz, H-24), 3.97 (2H, t, J = 4.7 Hz, H-8), 3.77 - 3.88 (2H, m, H-2), 3.61 - 3.73 (6H, m, H-3, 5, 6), 1.45 (3H, t, J = 7.2 Hz, H-25); ^{13}C NMR (101 MHz, CDCl_3) δ = 165.2 (C-21), 151.3 (C-19), 147.7 (C-15), 147.3 (C-14), 137.9 (C-17), 124.7 (C-11), 123.9 (C-18), 123.6 (C-16), 72.6 (C-3), 70.3 (C-6, 5), 69.1 (C-8), 62.0 (C-24), 61.7 (C-2), 50.4 (C-9), 14.3 (C-25); m/z (ESMS $^+$) found 351.1672 (calc. for $\text{C}_{16}\text{H}_{23}\text{N}_4\text{O}_5$ 351.1668) $[\text{M}+\text{H}]^+$, found 373.1492 (calc. for $\text{C}_{16}\text{H}_{22}\text{N}_4\text{O}_5\text{Na}$ 373.1488) for $[\text{M}+\text{Na}]^+$.

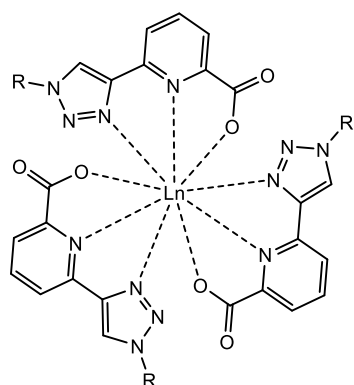
6.5.66 Synthesis of ethyl 6-(1-(2-(2-(2-(2-hydroxyethoxy)ethoxy)ethoxy)ethyl)-1H-1,2,3-triazol-4-yl)picolinate (**32b**)



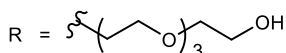
Compound **31b** (0.505 g, 2.301 mmol), compound **26** (0.403 g, 2.300 mmol), $\text{CuSO}_4 \cdot 5\text{H}_2\text{O}$ (29 mg, 0.112 mmol) and sodium

ascorbate (46 mg, 0.230 mmol) were used as the starting materials. It followed the general procedure for click reactions procedure 3 (section 6.4.6.3). Purification *via* flash column chromatography (SiO₂, DCM:MeOH/9:1) gave a brown oily (0.844 g, 93%). ¹H NMR (400 MHz, CDCl₃) δ = 8.55 (1H, s, H-14), 8.37 (1H, dd, *J* = 7.8 Hz, *J* = 1.1 Hz, H-23), 8.02 (1H, dd, *J* = 7.8 Hz, *J* = 1.1 Hz, H-21), 7.91 (1H, t, *J* = 7.8 Hz, H-22), 4.63 (2H, t, *J* = 5.3 Hz, H-12), 4.47 (2H, q, *J* = 7.2 Hz, H-27), 3.96 (2H, t, *J* = 5.3 Hz, H-11), 3.72 (2H, br d, *J* = 4.1 Hz, H-2), 3.62 - 3.67 (9H, m, H-5, 6, 8, 9), 3.56 - 3.61 (2H, m, H-3), 3.05 (1H, br t, *J* = 5.4 Hz, H-1), 1.45 (3H, t, *J* = 7.2 Hz, H-28); ¹³C NMR (101 MHz, CDCl₃) δ = 165.2 (C-24), 151.0 (C-20), 148.0 (C-18), 147.5 (C-16), 137.8 (C-22), 124.3 (C-14), 123.9 (C-21), 123.4 (C-23), 72.6 (C-3), 70.8, 70.7, 70.6, 70.3 (C-5, 6, 8, 9), 69.5 (C-11), 61.9 (C-27), 61.7 (C-2), 50.6 (C-12), 14.3 (C-28); *m/z* (ESMS⁺) found 395.1929 (calc. for C₁₈H₂₇N₄O₆ 395.1931) [M+H]⁺, found 417.1767 (calc. for C₁₈H₂₆N₄O₆Na 417.1750) for [M+Na]⁺.

6.5.67 Synthesis of **Eu/Tb(32b)**₃



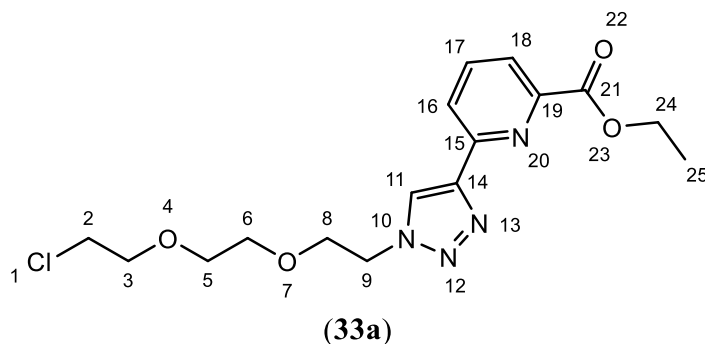
Ln = Eu/Tb



C₄₈H₆₃N₁₂O₁₈Na¹⁵⁹Tb 1277.3534) for [M+Na]⁺.

32b (0.056 g, 0.141 mmol) was dissolved in 10 mL deionised water at pH 9. It was heated at reflux for 1h. After cooling to room temperature, the pH was adjusted to 7. EuCl₃·6H₂O (0.017 g, 0.046 mmol) was added. It was then lyophilised to give a viscous liquid **Eu(32b)**₃ (65 mg, 109%). *m/z* (ESMS⁺) found 1271.3503 (calc. for C₄₈H₆₃N₁₂O₁₈¹⁵³EuNa 1271.3493) for [M+Na]⁺. Complexation with TbCl₃·6H₂O providing **Tb(32b)**₃ with a comparable result, *m/z* (ESMS⁺) found 1277.3604 (calc. for

6.5.68 Synthesis of ethyl 6-(1-(2-(2-(2-chloroethoxy)ethoxy)ethyl)-1H-1,2,3-triazol-4-yl)picolinate (**33a**)

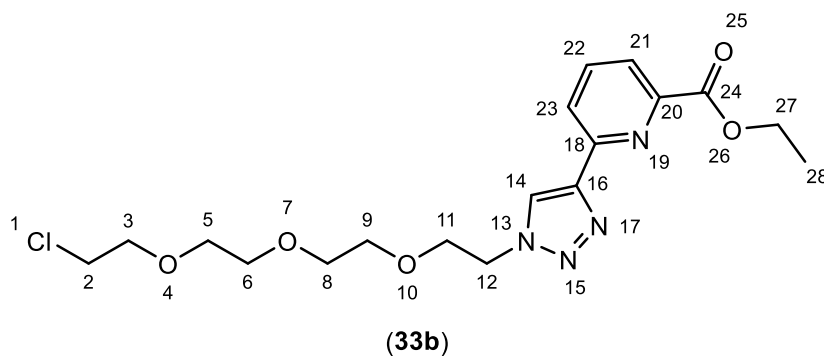


(**33a**)

Compound **32a** (0.574 g, 1.639 mmol), thionyl chloride (0.780 g, 6.554 mmol) were used as the starting materials. It followed the general procedure for chlorination reactions (section 6.4.2). Purification *via*

flash column chromatography (SiO₂, DCM:MeOH/9:1) gave a yellow oily product (0.574 g, 95%). ¹H NMR (400 MHz, CDCl₃) δ = 8.46 (1H, s, H-11), 8.36 (1H, d, *J* = 7.8 Hz, H-16), 8.02 (1H, d, *J* = 7.8 Hz, H-18), 7.92 (1H, t, *J* = 7.8 Hz, H-17), 4.63 (2H, br t, *J* = 4.6 Hz, H-9), 4.47 (2H, q, *J* = 7.1 Hz, H-24), 3.96 (2H, br t, *J* = 4.6 Hz, H-8), 3.73 (2H, t, *J* = 5.7 Hz, H-3), 3.65 (4H, s, H-5, 6), 3.61 (2H, t, *J* = 5.7 Hz, H-2), 1.45 (3H, t, *J* = 7.1 Hz, H-25); ¹³C NMR (101 MHz, CDCl₃) δ = 165.1 (C-21), 150.8 (C-19), 148.1 (C-15), 147.6 (C-14), 137.8 (C-17), 124.1 (C-18), 124.0 (C-11), 123.3 (C-16), 71.4 (C-3), 70.6, 70.5 (C-5, 6), 69.4 (C-8), 61.8 (C-24), 50.5 (C-9), 42.9 (C-2), 14.3 (C-25); *m/z* (ESMS⁺) found 369.1339 (calc. for C₁₆H₂₂N₄O₄Cl 369.1330) for [M+H]⁺, 391.1153 (calc. for C₁₆H₂₁N₄O₄ClNa 391.1149) for [M+Na]⁺.

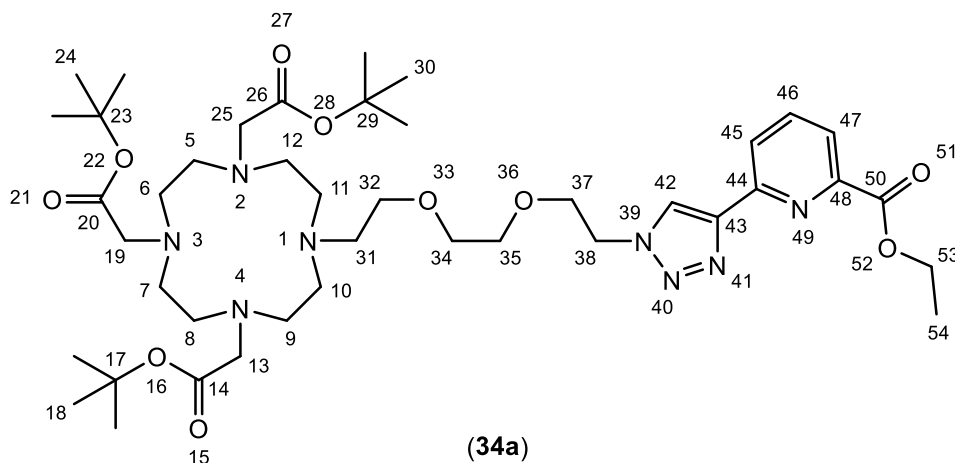
6.5.69 *Synthesis of ethyl 6-(1-(2-(2-(2-(2-chloroethoxy)ethoxy)ethoxy)ethyl)-1H-1,2,3-triazol-4-yl)picolinate (33b)*



Compound **32b**
(0.367 g, 0.930 mmol), thionyl chloride (1.107 g, 9.300 mmol) were used as the starting materials. It followed

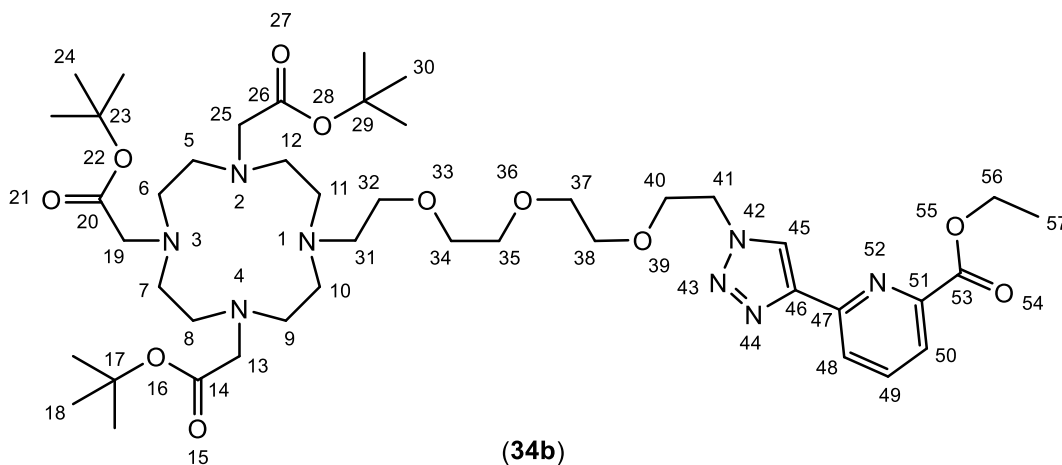
the general procedure for chlorination reactions (section 6.4.2). Purification *via* flash column chromatography (SiO₂, DCM:MeOH/9:1) gave a yellow oily product (0.331 g, 86.3%). ¹H NMR (400 MHz, CDCl₃) δ = 8.46 (1H, s, H-14), 8.36 (1H, dd, *J* = 7.8 Hz, *J* = 1.0 Hz, H-23), 8.02 (1H, dd, *J* = 7.8 Hz, *J* = 1.1 Hz, H-21), 7.91 (1H, t, *J* = 7.8 Hz, H-22), 4.62 (2H, t, *J* = 5.1 Hz, H-12), 4.47 (2H, q, *J* = 7.1 Hz, H-27), 3.95 (2H, t, *J* = 5.1 Hz, H-11), 3.67 - 3.73 (2H, m, H-3), 3.64 (8H, d, *J* = 2.5 Hz, H-5, 6, 8, 9), 3.57 - 3.62 (2H, m, H-2), 1.45 (3H, t, *J* = 7.1 Hz, H-28); ¹³C NMR (101 MHz, CDCl₃) δ = 165.1 (C-24), 151.0 (C-20), 148.1 (C-18), 147.6 (C-16), 137.8 (C-22), 124.1 (C-14), 124.0 (C-21), 123.3 (C-23), 71.3 (C-3), 70.7, 70.7, 70.6 (C-5, 6, 8, 9), 69.4 (C-11), 61.9 (C-27), 50.6 (C-12), 42.8 (C-2), 14.4 (C-28); *m/z* (ESMS⁺) found 413.1625 (calc. for C₁₈H₂₆N₄O₅Cl 413.1592) for [M+H]⁺, 435.1418 (calc. for C₁₈H₂₅N₄O₅ClNa 435.1411) for [M+Na]⁺.

6.5.70 Synthesis of tri-tert-butyl 2,2',2''-(10-(2-(2-(2-(4-(6-(ethoxycarbonyl)pyridin-2-yl)-1H-1,2,3-triazol-1-yl)ethoxy)ethoxy)ethyl)-1,4,7,10-tetraazacyclododecane-1,4,7-triyl)triacetate (**34a**)

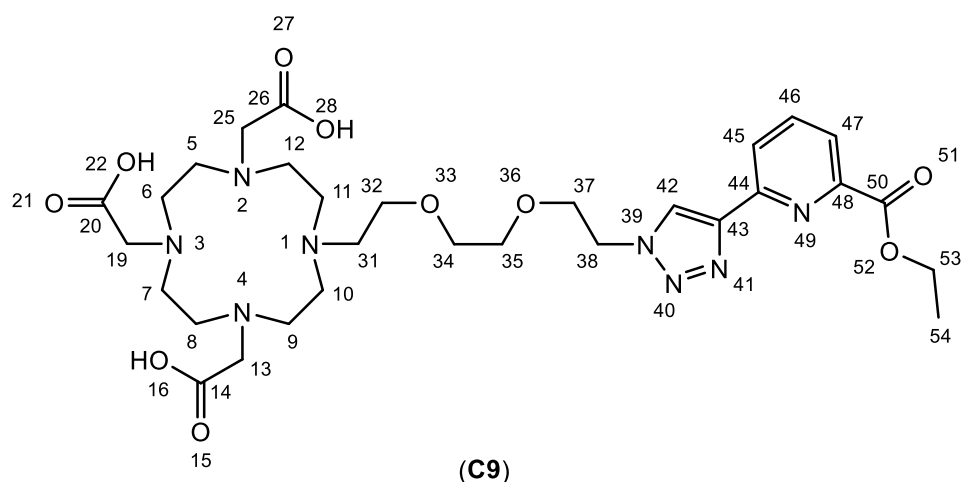


Compound **1** (0.215 g, 0.361 mmol), compound **33a** (0.133 g, 0.361 mmol) and potassium bromide (0.199 g, 1.443 mmol) were used as the starting materials. It followed the general procedure for the DO3A's fourth arm attachments (section 6.4.3). Purification *via* flash column chromatography (SiO₂, DCM : MeOH / 9:1) gave a light yellow oily (0.2154 g, 70%). ¹H NMR (400 MHz, CDCl₃) δ = 8.52 (1H, s, H-42), 8.34 (1H, dd, *J* = 7.8 Hz, *J* = 1.2 Hz, H-45), 8.03 (1H, dd, *J* = 7.8 Hz, *J* = 1.2 Hz, H-47), 7.95 (1H, t, *J* = 7.8 Hz, H-46), 4.67 (2H, t, *J* = 5.1 Hz, H-38), 4.47 (2H, q, *J* = 7.2 Hz, H-53), 3.96 (2H, t, *J* = 5.1 Hz, H-37), 3.51 - 3.70 (7H, m, H-32, 34, 35), 2.17 - 3.29 (29H, m, H-19, 31, 25, 13, 7, 6, 8, 5, 12, 9, 11, 10), 1.39 - 1.49 (33H, m, H-54, 24, 59, 56, 30, 60, 57, 18, 58, 55); ¹³C NMR (101 MHz, CDCl₃) δ = 172.7 (C-26, 14), 172.4 (C-20), 164.9 (C-50), 150.6 (C-48), 147.9 (C-44), 147.3 (C-43), 137.8 (C-46), 123.9 (C-47), 123.9 (C-42), 123.2 (C-45), 82.1 (C-29, 17), 82.1 (C-23), 70.0 (C-34), 69.6 (C-35), 69.0 (C-37), 67.2 (C-32), 61.8 (C-53), 56.2 (C-25, 13), 55.5 (C-19), 52.0, 50.3, 49.4 (C-7, 6, 8, 5, 31, 12, 9, 11, 10, 38), 27.9 (C-30, 60, 57, 18, 58, 55), 27.8 (C-24, 59, 56), 14.2 (C-54); *m/z* (ESMS⁺) found 869.5156 (calc. for C₄₂H₇₀O₁₀N₈Na 869.5113) for [M+Na]⁺.

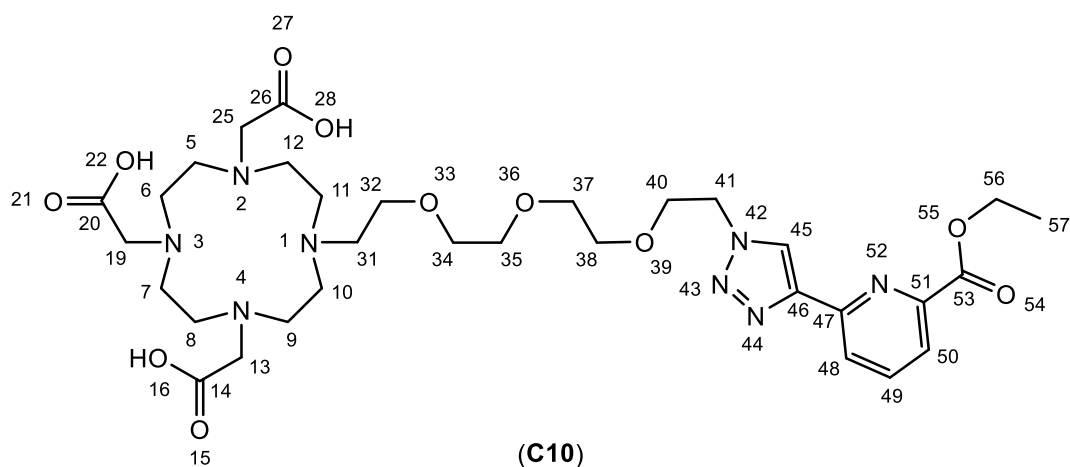
6.5.71 Synthesis of tri-*tert*-butyl 2,2',2''-(10-(2-(2-(2-(2-(4-(6-(ethoxycarbonyl)pyridin-2-yl)-1*H*-1,2,3-triazol-1-yl)ethoxy)ethoxy)ethoxy)ethyl)-1,4,7,10-tetraazacyclododecane-1,4,7-triyl)triacetate (**34b**)



Compound **1** (0.456 g, 0.767 mmol), compound **33b** (0.348 g, 0.844 mmol) and potassium bromide (0.212 g, 1.534 mmol) were used as the starting materials. It followed the general procedure for the DO3A's fourth arm attachments (section 6.4.3). Purification *via* flash column chromatography (SiO₂, DCM : MeOH / 9:1) gave a light yellow oily (0.376 g, 55%). ¹H NMR (400 MHz, CDCl₃) δ = 8.50 (1H, s, H-45), 8.34 (1H, dd, *J* = 7.8 Hz, *J* = 1.2 Hz, H-48), 8.04 (1H, dd, *J* = 7.8 Hz, *J* = 1.2 Hz, H-50), 7.97 (1H, t, *J* = 7.8 Hz, H-49), 4.67 (2H, t, *J* = 5.1 Hz, H-41), 4.47 (2H, q, *J* = 7.0 Hz, H-56), 3.99 (2H, t, *J* = 5.1 Hz, H-40), 3.48 - 3.73 (10H, m, H-32, 34, 35, 37, 38), 2.20 - 3.33 (24H, m, H-19, 25, 13, 7, 6, 8, 5, 12, 9, 11, 10, 31), 1.34 - 1.59 (30H, m, H-18, 24, 30, 57); ¹³C NMR (101 MHz, CDCl₃) δ = 172.2 (C-26, 14), 171.9 (C-20), 164.5 (C-53), 150.3 (C-51), 147.5 (C-47), 146.8 (C-46), 137.3 (C-49), 123.4 (C-45, 50), 122.7 (C-48), 81.6 (C-29, 17), 81.6 (C-23), 69.8, 69.7, 69.3 (C-34, 35, 37, 38), 68.8 (C-40), 66.7 (C-32), 61.2 (C-56), 55.8 (C-25, 13), 55.1 (C-19), 51.6, 50.1, 49.1 (C-7, 6, 8, 5, 12, 9, 11, 10, 31, 41), 27.4 (C-18, 30), 27.3 (C-24), 13.8 (C-57); *m/z* (ESMS⁺) found 891.5546 (calc. for C₄₄H₇₅O₁₁N₈ 891.5555) [M+H]⁺, 913.5365 (calc. for C₄₄H₇₄O₁₁N₈Na) for [M+Na]⁺.

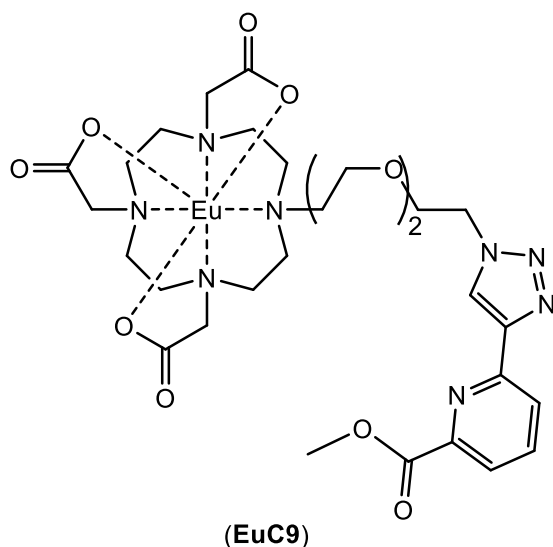
6.5.72 Synthesis of **C9**

34a (0.109 g, 0.128 mmol) was used as the starting material. It followed the general procedure for macrocycle's tert-Bu deprotection reactions (section 6.4.4). Purification via HPLC (R_t 19.9 min) gave a white solid (63 mg, 72%). $^1\text{H NMR}$ (400 MHz, D_2O) δ = 8.57 (1H, s, H-42), 7.93 - 8.16 (3H, m, H-45, 46, 47), 4.72 (2H, t, J = 5.0 Hz, H-38), 4.45 (2H, q, J = 7.2 Hz, H-53), 4.05 (2H, t, J = 5.0 Hz, H-37), 3.61 - 3.78 (12H, m, H-31, 32, 19, 25, 13), 3.46 - 3.60 (5H, m, H-34, 35), 3.24 (18H, br s, H-11, 10, 12, 9, 8, 5, 7, 6), 1.44 (3H, t, J = 7.1 Hz, H-54); $^{13}\text{C NMR}$ (101 MHz, D_2O) δ = 171.3 (C-20, 26, 14), 165.2 (C-50), 148.4 (C-48), 146.2 (C-44), 145.5 (C-43), 138.6 (C-46), 124.1 (C-42), 124.0 (C-47), 123.5 (C-45), 69.0 (C-32), 68.9 (C-34), 68.7 (C-35), 67.8 (C-37), 62.4 (C-53), 54.5 (C-25, 13, 19), 49.5 (C-38), 49.1 (C-11, 10, 12, 9, 8, 5, 7, 6, 31), 12.6 (C-54); m/z (ESMS $^+$) found 679.3424 (calc. for $\text{C}_{30}\text{H}_{47}\text{O}_{10}\text{N}_8$ 679.3415) for $[\text{M}+\text{H}]^+$.

6.5.73 Synthesis of **C10**

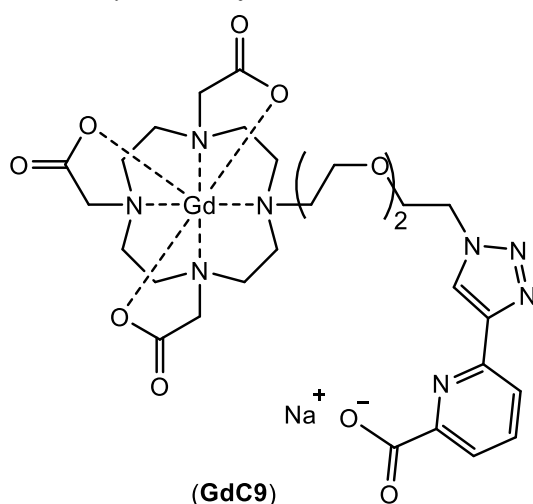
34b (0.134 g, 0.150 mmol) was used as the starting material. It followed the general procedure for macrocycle's tert-Bu deprotection reactions (section 6.4.4). Purification *via* HPLC (R_t 20.7 min) gave a white solid (55 mg, 51%). ^1H NMR (400 MHz, D_2O) δ = 8.58 (1H, s, H-45), 8.00 - 8.09 (3H, m, H-48, 49, 50), 4.73 (2H, t, J = 5.0 Hz, H-41), 4.46 (2H, q, J = 7.1 Hz, H-56), 4.06 (2H, t, J = 5.0 Hz, H-40), 3.49 - 3.77 (17H, m, H-19, 25, 13, 32, 34, 35, 37, 38), 3.25 (18H, br s, H-31, 11, 10, 12, 9, 8, 5, 7, 6), 1.45 (3H, t, J = 7.1 Hz, H-57); ^{13}C NMR (101 MHz, D_2O) δ = 171.4 (C-20, 26, 14), 165.3 (C-53), 148.4 (C-51), 146.2 (C-47), 145.6 (C-46), 138.6 (C-49), 124.2 (C-45), 124.1 (C-50), 123.5 (C-48), 69.0, 68.9, 68.8, 68.7 (C-32, 34, 35, 37, 38), 67.9 (C-40), 62.4 (C-56), 54.6 (C-19, 25, 13), 49.6 (C-41), 49.1 (C-31, 7, 6, 8, 5, 12, 9, 11, 10), 12.7 (C-57); m/z (ESMS $^+$) found 723.3665 (calc. for $\text{C}_{32}\text{H}_{51}\text{O}_{11}\text{N}_8$ 723.3677) for $[\text{M}+\text{H}]^+$.

6.5.74 Synthesis of **EuC9**

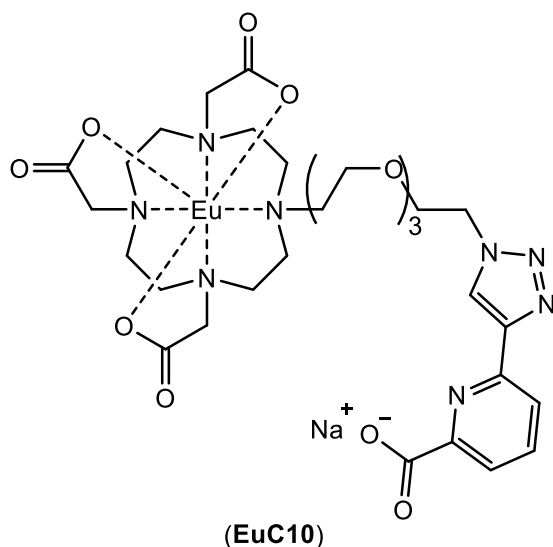


C9 (0.031 g, 0.045 mmol) and $\text{EuCl}_3 \cdot 6\text{H}_2\text{O}$ (0.018 g, 0.049 mmol) were used as starting materials. It followed the general procedure for lanthanide complexation procedure 2 (section 6.4.9.2). Purification *via* HPLC (R_t 18.1 min) gave a white hygroscopic solid (17 mg, 47%); m/z (ESMS $^+$) found 837.2217 (calc. $\text{C}_{29}\text{H}_{41}\text{N}_8\text{O}_{10}^{153}\text{EuNa}$ 837.2050) for $[\text{M}+\text{Na}]^+$.

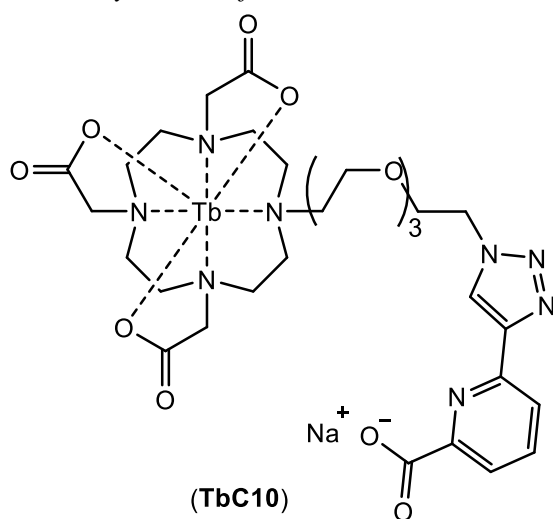
6.5.75 Synthesis of **GdC9**



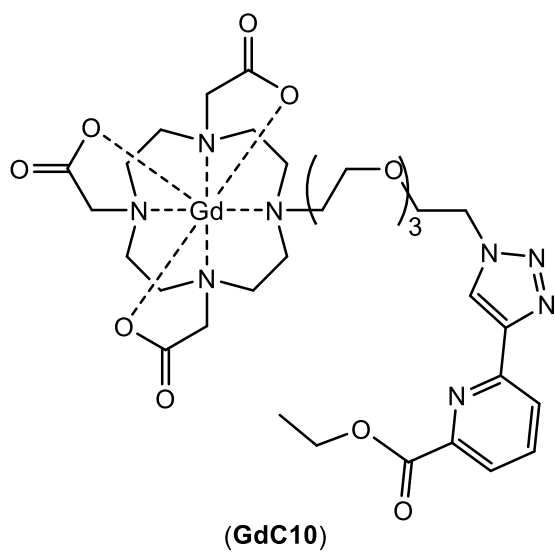
C9 (0.033 g, 0.048 mmol) and $\text{GdCl}_3 \cdot 6\text{H}_2\text{O}$ (0.020 g, 0.053 mmol) were used as starting materials. It followed the general procedure for lanthanide complexation procedure 2 (section 6.4.9.2). Purification *via* HPLC (R_t 18.1 min) gave a white hygroscopic solid (16 mg, 42 %); m/z (ESMS $^+$) found 850.1704 (calc. $\text{C}_{28}\text{H}_{38}\text{N}_8\text{O}_{10}^{158}\text{GdNa}_2$ 850.1742) for $[\text{M}+\text{Na}]^+$.

6.5.76 Synthesis of **EuC10**

C10 (0.045 g, 0.062 mmol) and $\text{EuCl}_3 \cdot 6\text{H}_2\text{O}$ (0.025 g, 0.068 mmol) were used as starting materials. It followed the general procedure for lanthanide complexation procedure 2 (section 6.4.9.2). Purification *via* HPLC (R_t 18.5 min) gave a white hygroscopic solid (27 mg, 51%); m/z (ESMS+) found 843.2183 (calc. $\text{C}_{30}\text{H}_{42}\text{N}_8\text{O}_{11}^{153}\text{Eu}$ 727.1712) for $[\text{M}-\text{H}]^-$; 889.2117 (calc. $\text{C}_{30}\text{H}_{42}\text{N}_8\text{O}_{11}^{153}\text{EuNa}_2$ 889.1986) for $[\text{M}+\text{Na}]^+$.

6.5.77 Synthesis of **TbC10**

C10 (0.036 g, 0.049 mmol) and $\text{TbCl}_3 \cdot 6\text{H}_2\text{O}$ (0.021 g, 0.056 mmol) were used as starting materials. It followed the general procedure for lanthanide complexation procedure 2 (section 6.4.9.2). Purification *via* HPLC (R_t 20.7 min) gave a white hygroscopic solid (16 mg, 38%); m/z (ESMS+) found 895.2042 (calc. $\text{C}_{30}\text{H}_{42}\text{N}_8\text{O}_{11}^{159}\text{TbNa}_2$ 895.2022) for $[\text{M}+\text{Na}]^+$.

6.5.78 Synthesis of **GdC10**

C10 (0.056 g, 0.077 mmol) and $\text{GdCl}_3 \cdot 6\text{H}_2\text{O}$ (0.032 g, 0.086 mmol) were used as starting materials. It followed the general procedure for lanthanide complexation procedure 2 (section 6.4.9.2). Purification *via* HPLC (R_t 20.7 min) gave a white hygroscopic solid (42 mg, 64%); m/z (ESMS+) found 900.2540 (calc. $\text{C}_{32}\text{H}_{47}\text{N}_8\text{O}_{11}^{158}\text{GdNa}$ 900.2503) for $[\text{M}+\text{Na}]^+$.

Chapter 7

References

- 1 M. L. James and S. S. Gambhir, *Physiol. Rev.*, 2012, **92**, 897–965.
- 2 J. C. G. Bünzli, *Chem. Rev.*, 2010, **110**, 2729–2755.
- 3 D. T. Ginat and R. Gupta, *Annu. Rev. Biomed. Eng.*, 2014, **16**, 431–453.
- 4 J. Jos and P. Kinahan, *Annu. Rev. Biomed. Eng.*, 2015, **17**, 385–414.
- 5 L. E. Jennings and N. J. Long, *Chem. Commun.*, 2009, 3511–3524.
- 6 D. G. Haralampieva, S. M. Ametamey, T. Sulser and D. Eberli, in *Cells and Biomaterials in Regenerative Medicine*, ed. D. Eberli, In Tech, 2014, pp. 175–197.
- 7 A. J. Amoroso and S. J. A. Pope, *Chem. Soc. Rev.*, 2015, **44**, 4723–4742.
- 8 E. L. Que and C. J. Chang, *Chem. Soc. Rev.*, 2010, **39**, 51–60.
- 9 P. Caravan, *Chem. Soc. Rev.*, 2006, **35**, 512–523.
- 10 H. Friebolin, *Basic One- and Two-Dimensional NMR Spectroscopy*, WILEY VCH, 2005.
- 11 A. Filler, *Nat. Preced.*, 2009, 1–69.
- 12 H. Günther, *NMR Spectroscopy: Basic Principles, Concepts and Applications in Chemistry*, John Wiley & Sons., 1992.
- 13 J. Keeler, *Understanding NMR Spectroscopy*, John Wiley & Sons, Ltd., 2010.
- 14 J. W. Hennel and J. Klinowski, *Fundamental of Nuclear Magnetic Resonance*, Longman Pub Group, 1993.
- 15 C. S. Bonnet, F. Caillé, A. Pallier, J.-F. Morfin, S. Petoud, F. Suzenet and E. Tóth, *Chem. Eur. J.*, 2014, **20**, 10959–10969.
- 16 L. M. De León-Rodríguez, A. F. Martins, M. C. Pinho, N. M. Rofsky and a. D. Sherry, *J. Magn. Reson. Imaging*, 2015, **42**, 545–565.
- 17 P. Caravan, J. J. Ellison, T. J. McMurry and R. B. Lauffer, *Chem. Rev.*, 1999, **99**, 2293–2352.
- 18 S. Aime, M. Fasano and E. Terreno, *Chem. Soc. Rev.*, 1998, **27**, 19–29.
- 19 P. Hermann, J. Kotek, V. Kubíček and I. Lukes, *Dalton Trans.*, 2008, **23**, 3027–3047.
- 20 H. U. Rashid, K. Yu and J. Zhou, *J. Struct. Chem.*, 2013, **54**, 223–249.
- 21 J. B. Lansman, *J. Gen. Physiol.*, 1990, **95**, 679–696.
- 22 M. C. Heffern, L. M. Matosziuk and T. J. Meade, *Chem. Rev.*, 2014, **114**, 4496–4539.
- 23 E. J. Werner, A. Datta, C. J. Jocher and K. N. Raymond, *Angew. Chem. Intl. Ed.*,

- 2008, **47**, 8568–8580.
- 24 C.-T. Yang and K.-H. Chuang, *Medchemcomm*, 2012, **3**, 552-565.
- 25 D. V. Hingorani, A. S. Bernstein and M. D. Pagel, *Contrast Media Mol. Imaging*, 2015, **10**, 245–265.
- 26 G.-L. Davies, I. Kramberger and J. J. Davis, *Chem. Commun.*, 2013, **49**, 9704–9721.
- 27 W.-H. Li, G. Parigi, M. Fragai, C. Luchinat and T. J. Meade, *Inorg. Chem.*, 2002, **41**, 4018–4024.
- 28 G. Liu, Y. Li and M. D. Pagel, *Magn. Reson. Med.*, 2007, **58**, 1249–1256.
- 29 R. A. Moats, S. E. Fraser and T. J. Meade, *Angew. Chem. Int. Ed.*, 1997, **36**, 725–728.
- 30 M. Giardiello, P. Lowe and M. Botta, *Chem. Commun.*, 2007, 4044–4046.
- 31 L. Zhu, Y. Yang, K. Farquhar, J. Wang, C. Tian, J. Ranville and S. G. Boyes, *ACS Appl. Mater. Interfaces*, 2016, **8**, 5040–5050.
- 32 F. K. Kálmán, M. Woods, P. Caravan, P. Jurek, M. Spiller, G. Tirscó, R. Király, E. Brúcher and A. D. Sherry, *Inorg. Chem.*, 2007, **46**, 5260–5270.
- 33 A. Y. Louie, M. M. Huber, E. T. Ahrens, U. Rothbacher, R. Moats, R. E. Jacobs, S. E. Fraser and T. J. Meade, *Nat. Biotechnol.*, 2000, **18**, 321–325.
- 34 Y.-T. Chang, C.-M. Cheng, Y.-Z. Su, W.-T. Lee, J.-S. Hsu, G.-C. Liu, T.-L. Cheng and Y.-M. Wang, *Bioconjugate Chem.*, 2007, **18**, 1716–1727.
- 35 S. Iwaki, K. Hanaoka, W. Piao, T. Komatsu, T. Ueno, T. Terai and T. Nagano, *Bioorganic Med. Chem. Lett.*, 2012, **22**, 2798–2802.
- 36 W. Xu and Y. Lu, *Chem. Commun.*, 2011, **47**, 4998-5000.
- 37 M. de Smet, S. Langereis, S. van den Bosch and H. Grüll, *J. Control. Release*, 2010, **143**, 120–127.
- 38 E. L. Que and C. J. Chang, *J. Am. Chem. Soc.*, 2006, **128**, 15942–15943.
- 39 K. Hanaoka, K. Kikuchi, Y. Urano and T. Nagano, *J. Chem. Soc. Perkin Trans. 2*, 2001, **25**, 1840–1843.
- 40 C. S. Bonnet and É. Tóth, *Am. J. Neuroradiol.*, 2010, **31**, 401–409.
- 41 J. Luo, W.-S. Li, P. Xu, L.-Y. Zhang and Z.-N. Chen, *Inorg. Chem.*, 2012, **51**, 9508–9516.
- 42 J.-A. Park, Y. J. Lee, I. O. Ko, T.-J. Kim, Y. Chang, S. M. Lim, K. M. Kim and J. Y. Kim, *Biochem. Biophys. Res. Commun.*, 2014, **455**, 246–250.
- 43 X. Zhang, X. Jing, T. Liu, G. Han, H. Li and C. Duan, *Inorg. Chem.*, 2012, **51**, 2325–2331.
- 44 M. Moon, R. G. Thomas, S.-U. Heo, M.-S. Park, W. K. Bae, S. H. Heo, N. Y. Yim and Y. Y. Jeong, *Mol. Imaging Biol.*, 2015, **17**, 497-503.

- 45 J.-K. Kim, D. Kim, M.-S. Kang, H.-K. Kim, J.-S. Kim, E.-K. Yu and J.-H. Jeong, *Arch. Pharm. Res.*, 2006, **29**, 188–190.
- 46 W.-Y. Chai, P.-C. Chu, M.-Y. Tsai, Y.-C. Lin, J.-J. Wang, K.-C. Wei, Y.-Y. Wai and H.-L. Liu, *J. Controlled Release*, 2014, **192**, 1–9.
- 47 J. Luo, X.-F. Zhu and Z.-N. Chen, *Eur. J. Inorg. Chem.*, 2015, 3087–3093.
- 48 P. Kadjane, C. Platas-Iglesias, P. Boehm-Sturm, V. Truffault, G. E. Hagberg, M. Hoehn, N. K. Logothetis and G. Angelovski, *Chem. Eur. J.*, 2014, **20**, 7351–7362.
- 49 A. Mishra, N. K. Logothetis and D. Parker, *Chem. Eur. J.*, 2011, **17**, 1529–1537.
- 50 W.-S. Li, J. Luo and Z.-N. Chen, *Dalton Trans.*, 2011, **40**, 484–488.
- 51 S. Gündüz, N. Nitta, S. Vibhute, S. Shibata, M. E. Mayer, N. K. Logothetis, I. Aoki and G. Angelovski, *Chem. Commun.*, 2015, **51**, 2782–2785.
- 52 S. S. Deshpande, *Crit. Rev. Food Sci. Nutr.*, 2001, **41**, 155–224.
- 53 J.-C. G. Bünzli and C. Piguet, *Chem. Soc. Rev.*, 2005, **34**, 1048–1077.
- 54 J. R. Lakowicz, *Principles of Fluorescence Spectroscopy*, Springer, USA, Third Ed., 2010.
- 55 J. R. Albani, *Principles and Applications of Fluorescence Spectroscopy*, John Wiley & Sons, Inc., 2007.
- 56 M. H. V. Werts, *Sci. Prog.*, 2005, **88**, 101–131.
- 57 J. C. G. Bünzli, *J. Coord. Chem.*, 2014, **67**, 3706–3733.
- 58 S. Faulkner, S. J. A. Pope and B. P. Burton-Pye, *Appl. Spectrosc. Rev.*, 2005, **40**, 1–31.
- 59 C. Turro, P. K. L. Fu and P. M. Bradley, *Met. Ions Biol. Syst.*, 2003, **40**, 323–353.
- 60 I. Nasso, N. Geum, G. Bechara, B. Mestre-Voegtli, C. Galaup and C. Picard, *J. Photochem. Photobiol. A.*, 2014, **274**, 124–132.
- 61 D. Parker, *Chem. Soc. Rev.*, 2004, **33**, 156–165.
- 62 J. C. G. Bünzli, *Chem. Rev.*, 2010, **110**, 2729–2755.
- 63 F. Himo, T. Lovell, R. Hilgraf, V. V. Rostovtsev, L. Noodleman, K. B. Sharpless and V. V. Fokin, *J. Am. Chem. Soc.*, 2005, **127**, 210–216.
- 64 H. C. Kolb, M. G. Finn and K. B. Sharpless, *Angew. Chemie - Int. Ed.*, 2001, **40**, 2004–2021.
- 65 V. K. Tiwari, B. B. Mishra, K. B. Mishra, N. Mishra, A. S. Singh and X. Chen, *Chem. Rev.*, 2016, **116**, 3086–3240.
- 66 C. W. Tornøe, C. Christensen and M. Meldal, *J. Org. Chem.*, 2002, **67**, 3057–3064.
- 67 V. V. Rostovtsev, L. G. Green, V. V. Fokin and K. B. Sharpless, *Angew. Chem. Int. Ed.*, 2002, **41**, 2596–2599.
- 68 M. Ahlquist and V. V. Fokin, *Organometallics*, 2007, **26**, 4389–4391.

- 69 C. Nolte, P. Mayer and B. F. Straub, *Angew. Chem. Int. Ed.*, 2007, **46**, 2101–2103.
- 70 C. Iacobucci, S. Reale, J. F. Gal and F. De Angelis, *Angew. Chem. Int. Ed.*, 2015, **54**, 3065–3068.
- 71 L. Jin, D. R. Tolentino, M. Melaimi and G. Bertrand, *Sci. Adv.*, 2015, 1–5.
- 72 B. T. Worrell, J. A. Malik and V. V. Fokin, *Science*, 2013, **340**, 457–460.
- 73 C. Wang, D. Ikhlef, S. Kahlal, J. Y. Saillard and D. Astruc, *Coord. Chem. Rev.*, 2016, **316**, 1–20.
- 74 W. G. Kim, M. E. Kang, J. Bin Lee, M. H. Jeon, S. Lee, J. Lee, B. Choi, P. M. S. D. Cal, S. Kang, J. M. Kee, G. J. L. Bernardes, J. U. Rohde, W. Choe and S. Y. Hong, *J. Am. Chem. Soc.*, 2017, **139**, 12121–12124.
- 75 P. Appukkuttan, W. Dehaen, V. V. Fokin and E. Van Der Eycken, *Org. Lett.*, 2004, **6**, 4223–4225.
- 76 T. N. Glasnov and C. O. Kappe, *QSAR Comb. Sci.*, 2007, **26**, 1261–1265.
- 77 N. P. Tu, J. E. Hochlowski and S. W. Djuric, *Mol. Divers.*, 2012, **16**, 53–58.
- 78 F. Friscourt and G. J. Boons, *Org. Lett.*, 2010, **12**, 4936–4939.
- 79 A. Anand, M. V. Kulkarni, S. D. Joshi and S. R. Dixit, *Bioorg. Med. Chem. Lett.*, 2016, **26**, 4709–4713.
- 80 S. Wang and B. Cheng, *Sci. Rep.*, 2017, **7**, 1–9.
- 81 J. M. Baskin, J. a Prescher, S. T. Laughlin, N. J. Agard, P. V Chang, I. a Miller, A. Lo, J. a Codelli and C. R. Bertozzi, *Proc. Natl. Acad. Sci. U. S. A.*, 2007, **104**, 16793–16797.
- 82 A. Bernardin, A. Cazet, L. Guyon, P. Delannoy, F. Vinet, D. Bonnaffé and I. Texier, *Bioconjugate Chem.*, 2010, **21**, 583–588.
- 83 J. Hong, Q. Luo and B. K. Shah, *Biomacromolecules*, 2010, **11**, 2960–2965.
- 84 M. Tireli, S. Maračić, S. Lukin, M. J. Kulcsár, D. Žilić, M. Cetina, I. Halasz, S. Raić-Malić and K. Užarević, *Beilstein J. Org. Chem.*, 2017, **13**, 2352–2363.
- 85 K. Nwe and M. W. Brechbiel, *Cancer Biother. Radiopharm.*, 2009, **24**, 289–302.
- 86 A. Qin, J. W. Y. Lam and B. Z. Tang, *Macromolecules*, 2010, **43**, 8693–8702.
- 87 W. Xi, T. F. Scott, C. J. Kloxin and C. N. Bowman, *Adv. Funct. Mater.*, 2014, **24**, 2572–2590.
- 88 S. Verma, *Int. J. Drug Dev. Res.*, 2015, **7**, 18–26.
- 89 H. C. Kolb and K. B. Sharpless, *Drug Discov. Today*, 2003, **8**, 1128–1137.
- 90 E. Bonandi, M. S. Christodoulou, G. Fumagalli, D. Perdicchia, G. Rastelli and D. Passarella, *Drug Discov. Today*, 2017, **22**, 1572–1581.
- 91 P. Thirumurugan, D. Matosiuk and K. Jozwiak, *Chem. Rev.*, 2013, **113**, 4905–4979.
- 92 T. Ishizuka, H. S. Liu, K. Ito and Y. Xu, *Sci. Rep.*, 2016, **6**, 1–10.

- 93 A. Raulf, C. K. Spahn, P. J. M. Zessin, K. Finan, S. Bernhardt, A. Heckel and M. Heilemann, *RSC Adv.*, 2014, **4**, 30462–30466.
- 94 H. Fu, Y. Li, L. Sun, P. He and X. Duan, *Anal. Chem.*, 2015, **87**, 11332–11336.
- 95 C. Y. Jao and A. Salic, *Proc. Natl. Acad. Sci. U. S. A.*, 2008, **105**, 15779–15784.
- 96 Y. Su, L. Li, H. Wang, X. Wang and Z. Zhang, *Chem. Commun.*, 2016, **52**, 2185–2188.
- 97 A. S. Prasad, *Adv. Nutr.*, 2013, **4**, 176–190.
- 98 W. Maret and H. H. Sandstead, *J. Trace Elem. Med. Biol.*, 2006, **20**, 3–18.
- 99 P. Jiang and Z. Guo, *Coord. Chem. Rev.*, 2004, **248**, 205–229.
- 100 E. John, T. C. Laskow, W. J. Buchser, B. R. Pitt, P. H. Basse, L. H. Butterfield, P. Kalinski and M. T. Lotze, *J. Transl. Med.*, 2010, **8**, 1-16.
- 101 H. Tapiero and K. D. Tew, *Biomed. Pharmacother.*, 2003, **57**, 399–411.
- 102 J. E. Coleman, *Curr. Opin. Chem. Biol.*, 1998, **2**, 222–234.
- 103 A. I. Bush, *Curr. Opin. Chem. Biol.*, 2000, **4**, 184–191.
- 104 P. Ranasinghe, S. Pigera, P. Galappathy, P. Katulanda and G. R. Constantine, *DARU J. Pharm. Sci.*, 2015, **23**, 44.
- 105 J. C. King, D. M. Shames and L. R. Woodhouse, *J. Nutr.*, 2000, **130**, 1360–1366.
- 106 M. Maares and H. Haase, *Arch. Biochem. Biophys.*, 2016, **611**, 58–65.
- 107 D. K. Dhawan and V. D. Chadha, *Indian J. Med. Res.*, 2010, **132**, 676–682.
- 108 M. P. Cuajungco and G. J. Lees, *Neurobiol. Dis.*, 1997, **4**, 137–169.
- 109 K. J. Barnham and A. I. Bush, *Curr. Opin. Chem. Biol.*, 2008, **12**, 222–228.
- 110 N. M. Hooper, *FEBS Lett.*, 1994, **354**, 1–6.
- 111 C. Y. Wang, T. Wang, W. Zheng, B. L. Zhao, G. Danscher, Y. H. Chen and Z. Y. Wang, *PLoS One*, 2010, **5**, 1–12.
- 112 P. J. Little, R. Bhattacharya, A. E. Moreyra and I. L. Korichneva, *Nutrition*, 2010, **26**, 1050–1057.
- 113 E. Kimura, S. Aoki, E. Kikuta and T. Koike, *Proc. Natl. Acad. Sci. U. S. A.*, 2003, **100**, 3731–3736.
- 114 Sun, Qi, R. M. van Dam, W. C. Willett and F. B. Hu, *Diabetes Care*, 2009, **32**, 629–634.
- 115 G. Dodson and D. Steiner, *Curr. Opin. Struct. Biol.*, 1998, **8**, 189–194.
- 116 A. C. Esqueda, J. a. López, G. Andreu-de-Riquer, J. C. Alvarado-Monzón, J. Ratnakar, A. J. M. Lubag, a. D. Sherry and L. M. De León-Rodríguez, *J. Am. Chem. Soc.*, 2009, **131**, 11387–11391.
- 117 R. G. Pearson, *J. Chem. Educ.*, 1968, **45**, 581–587.
- 118 R. G. Pearson, *J. Am. Chem. Soc.*, 1963, **85**, 3533–3539.

- 119 A. Krezel, Q. Hao and W. Maret, *Arch. Biochem. Biophys.*, 2007, **463**, 188–200.
- 120 A. Krężel and W. Maret, *Arch. Biochem. Biophys.*, 2016, **611**, 3–19.
- 121 J. Tang, H.-Y. Yin and J.-L. Zhang, in *Inorganic and Organometallic Transition Metal Complexes with Biological Molecules and Living Cells*, Elsevier Inc., 2017, pp. 1–53.
- 122 W. Maret, *J. Inorg. Biochem.*, 2012, **111**, 110–116.
- 123 R. J. P. Williams, *J. Inorg. Biochem.*, 2002, **88**, 241–250.
- 124 B. Czaplinska, E. Spaczynska and R. Musiol, *Med. Chem.*, 2018, **14**, 19–33.
- 125 X. Li, J. Chen, Z. Niu and E. Wang, *Indian J. Chem.*, 2014, **53A**, 1349–1352.
- 126 B. A. Wong, S. Friedle and S. J. Lippard, *Inorg. Chem.*, 2009, **48**, 7009–7011.
- 127 K. Komatsu, Y. Urano, H. Kojima and T. Nagano, *J. Am. Chem. Soc.*, 2007, **129**, 13447–13454.
- 128 S. Mizukami, S. Okada, S. Kimura and K. Kikuchi, *Inorg. Chem.*, 2009, **48**, 7630–7638.
- 129 L. Xue, C. Liu and H. Jiang, *Chem. Commun.*, 2009, 1061–1063.
- 130 E. Roussakis, S. Voutsadaki, E. Pinakoulaki, D. P. Sideris, K. Tokatlidis and H. E. Katerinopoulos, *Cell Calcium*, 2008, **44**, 270–275.
- 131 Y. Zhang, X. Guo, W. Si, L. Jia and X. Qian, *Org. Lett.*, 2008, **10**, 473–476.
- 132 E. Tomat and S. J. Lippard, *Curr. Opin. Chem. Biol.*, 2010, **14**, 225–230.
- 133 L. M. De León-Rodríguez, A. J. M. Lubag, J. a. López, G. Andreu-de-Riquer, J. C. Alvarado-Monzón and a. D. Sherry, *Medchemcomm*, 2012, **3**, 480–483.
- 134 G. J. Stasiuk, F. Minuzzi, M. Sae-Heng, C. Rivas, H. P. Juretschke, L. Piemonti, P. R. Allegrini, D. Laurent, A. R. Duckworth, A. Beeby, G. A. Rutter and N. J. Long, *Chem. - A Eur. J.*, 2015, **21**, 5023–5033.
- 135 J. L. Major, G. Parigi, C. Luchinat and T. J. Meade, *Proc. Natl. Acad. Sci. U. S. A.*, 2007, **104**, 13881–13886.
- 136 J. L. Major, R. M. Boiteau and T. J. Meade, *Inorg. Chem.*, 2012, **29**, 997–1003.
- 137 C. S. Bonnet, *Coord. Chem. Rev.*, 2018, **369**, 91–104.
- 138 L. M. De León-Rodríguez, A. F. Martins, M. C. Pinho, N. M. Rofsky and A. D. Sherry, *J. Magn. Reson. Imaging*, 2015, **42**, 545–565.
- 139 O. Axelsson and A. Olsson, Synthesis of Cyclen Derivatives, US. Patent 8. 138, 332 B2, 2012.
- 140 R. Chinchilla and C. Nájera, *Chem. Rev.*, 2007, **107**, 874–922.
- 141 S. Thorand and N. Krause, *J. Org. Chem.*, 1998, **63**, 8551–8553.
- 142 B. L. Gupta, *Talanta*, 1974, **21**, 683–684.
- 143 G. J. Stasiuk and M. P. Lowe, *Dalton Trans.*, 2009, 9725–9727.

- 144 S. H. Park, *Bull. Korean Chem. Soc.*, 2003, **24**, 253–255.
- 145 J. I. Sarmiento-sánchez, A. Ochoa-terán and I. A. Rivero, *Arkivoc*, **2011**, 177–188.
- 146 S. Kale, S. Kahandal, S. Disale and R. Jayaram, *Curr. Chem. Lett.*, 2012, **1**, 69–80.
- 147 J. Andersen, U. Madsen, F. Björkling and X. Liang, *Synlett*, 2005, 2209–2213.
- 148 I. Stengel, A. Mishra, N. Pootrakulchote, S.-J. Moon, S. M. Zakeeruddin, M. Grätzel and P. Bäuerle, *J. Mater. Chem.*, 2011, **21**, 3726–3734.
- 149 B. Chattopadhyay, C. I. R. Vera, S. Chuprakov and V. Gevorgyan, *Org. Lett.*, 2010, **12**, 2166–2169.
- 150 G. Colombano, C. Travelli, U. Galli, A. Caldarelli, M. G. Chini, P. L. Canonico, G. Sorba, G. Bifulco, G. C. Tron and A. a. Genazzani, *J. Med. Chem.*, 2010, **53**, 616–623.
- 151 M. Pizzotti, S. Cenini, F. Porta, W. Beck and J. Erbe, *J. Chem. Soc. Dalton Trans.*, 1978, 1155–1160.
- 152 Q. Zhang, X. Wang, C. Cheng, R. Zhu, N. Liu and Y. Hu, *Org. Biomol. Chem.*, 2012, **10**, 2847.
- 153 M. K. Elmkaddem, C. Fischmeister, C. M. Thomas and J.-L. Renaud, *Chem. Commun.*, 2010, **46**, 925–927.
- 154 E. Sugawara and H. Nikaido, *Antimicrob. Agents Chemother.*, 2014, **58**, 7250–7.
- 155 R. Brückner, *Advanced organic chemistry: reaction mechanisms*, Harcourt/Academic Press, 2002.
- 156 A. D’Amora, L. Fanfoni, D. Cozzula, N. Guidolin, E. Zangrando, F. Felluga, S. Gladioli, F. Benedetti and B. Milani, *Organometallics*, 2010, **29**, 4472–4485.
- 157 L. Lattuada, A. Barge, G. Cravotto, G. B. Giovenzana and L. Tei, *Chem. Soc. Rev.*, 2011, **40**, 3019–3049.
- 158 A. Mattarei, M. Azzolini, M. Zoratti, L. Biasutto and C. Paradisi, *Molecules*, 2015, **20**, 16085–16102.
- 159 G. E. Buono-core, H. Li and B. Marciniak, *Coord. Chem. Rev.*, 1990, **99**, 55–87.
- 160 L. Armelao, S. Quici, F. Barigelletti, G. Accorsi, G. Bottaro, M. Cavazzini and E. Tondello, *Coord. Chem. Rev.*, 2010, **254**, 487–505.
- 161 J. C. G. Bünzli, A. S. Chauvin, H. K. Kim, E. Deiters and S. V. Eliseeva, *Coord. Chem. Rev.*, 2010, **254**, 2623–2633.
- 162 A. Beeby, I. M. Clarkson, R. S. Dickins, S. Faulkner, D. Parker, L. Royle, A. S. de Sousa, J. A. G. Williams and M. Woods, *J. Chem. Soc. Perkin Trans. 2*, 1999, **2**, 493–504.
- 163 M. P. Coogan and S. J. A. Pope, in *The Chemistry of Molecular Imaging*, John Wiley & Sons, Inc, Hoboken, NJ, 2014, 275–298.
- 164 M. Latva, H. Takalo, V.-M. Mikkala, C. Matachescu, J. C. Rodríguez-Ubis and J. Kankare, *J. Lumin.*, 1997, **75**, 149–169.

- 165 E. G. Moore, A. P. S. Samuel and K. N. Raymond, *Acc. Chem. Res.*, 2009, **42**, 542–552.
- 166 C. M. G. dos Santos, A. J. Harte, S. J. Quinn and T. Gunnlaugsson, *Coord. Chem. Rev.*, 2008, **252**, 2512–2527.
- 167 S. C. Burdette, G. K. Walkup, B. Spingler, R. Y. Tsien and S. J. Lippard, *J. Am. Chem. Soc.*, 2001, **123**, 7831–7841.
- 168 R. Parkesh, T. Clive Lee and T. Gunnlaugsson, *Org. Biomol. Chem.*, 2007, **5**, 310–317.
- 169 J. Jayabharathi, P. Ramanathan, V. Thanikachalam and A. Arunpandiyam, *J. Fluoresc.*, 2014, **24**, 827–834.
- 170 W. K. C. Lo, G. S. Huff, J. R. Cubanski, A. D. W. Kennedy, C. J. McAdam, D. A. McMorran, K. C. Gordon and J. D. Crowley, *Inorg. Chem.*, 2015, **54**, 1572–1587.
- 171 D. M. Corsi, C. Platas-Iglesias, H. Van Bekkum and J. A. Peters, *Magn. Reson. Chem.*, 2001, **39**, 723–726.
- 172 L. De Leon-Rodriguez, A. J. M. Lubag and A. Dean Sherry, *Inorg. Chim. Acta*, 2012, **393**, 12–23.
- 173 P. Faller and C. Hureau, *Dalton Trans.*, 2009, 1080–1094.
- 174 K. Mikami, M. Terada and H. Matsuzawa, *Angew. Chem. Int. Ed.*, 2002, **41**, 3554–3571.
- 175 J. Inanaga, H. Furuno and T. Hayano, *Chem. Rev.*, 2002, **102**, 2211–2225.
- 176 P. K. Shahi, A. K. Singh, S. B. Rai and B. Ullrich, *Sens. Actuators, A Phys.*, 2015, **222**, 255–261.
- 177 K. Kuriki, Y. Koike and Y. Okamoto, *Chem. Rev.*, 2002, **102**, 2347–2356.
- 178 D. D. Van Der Voort, N. C. J. Maes, T. Lamberts, A. M. Sweep, W. Van De Water, R. P. J. Kunnen, H. J. H. Clercx, G. J. F. Van Heijst and N. J. Dam, *Rev. Sci. Instrum.*, 2016, **87**, 1–8.
- 179 C. D. S. Brites, P. P. Lima and L. D. Carlos, *J. Lumin.*, 2016, **169**, 497–502.
- 180 D. Yue, J. Zhang, D. Zhao, X. Lian, Y. Cui, Y. Yang and G. Qian, *J. Solid State Chem.*, 2016, **241**, 99–104.
- 181 O. A. Savchuk, J. J. Carvajal, M. C. Pujol, J. Massons, P. Haro-González, O. Martínez, J. Jiménez, M. Aguiló and F. Díaz, *J. Lumin.*, 2016, **169**, 711–716.
- 182 H. Liang, F. Xie, X. Ren, Y. Chen, B. Chen and F. Guo, *Spectrochim. Acta A*, 2013, **116**, 317–320.
- 183 P. K. Shahi, P. Singh, A. K. Singh, S. K. Singh, S. B. Rai and R. Prakash, *J. Colloid Interface Sci.*, 2017, **491**, 199–206.
- 184 S. Lacerda and É. Tóth, *Chem. Med. Chem.*, 2017, **12**, 883–894.
- 185 K. Hanaoka, K. Kikuchi, H. Kojima, Y. Urano and T. Nagano, *J. Am. Chem. Soc.*, 2004, **126**, 12470–12476.

- 186 S. Faulkner, S. J. A. Pope and B. P. Burton-Pye, *Appl. Spectrosc. Rev.*, 2005, **40**, 1–31.
- 187 A. Thibon and V. C. Pierre, *Anal. Bioanal. Chem.*, 2009, **394**, 107–120.
- 188 E. F. Gudgin Dickson, A. Pollak and E. P. Diamandis, *J. Photochem. Photobiol. B: Biol.*, 1995, **27**, 3–19.
- 189 S. H. Jung, K. Y. Kim, J. H. Lee, C. J. Moon, N. S. Han, S.-J. Park, D. Kang, J. K. Song, S. S. Lee, M. Y. Choi, J. Jaworski and J. H. Jung, *ACS Appl. Mater. Interfaces*, 2017, **9**, 722–729.
- 190 J. Nurmi, T. Wikman, M. Karp and T. Lövgren, *Anal. Chem.*, 2002, **74**, 3525–3532.
- 191 M. L. Cable, D. J. Levine, J. P. Kirby, H. B. Gray and A. Ponce, in *Advances in Inorg. Chem.*, 2011, **63**, 1–45.
- 192 A. T. R. Williams, S. A. Winfield and J. N. Miller, *Analyst*, 1983, **108**, 1067–1071.
- 193 M. L. Aulsebrook, B. Graham, M. R. Grace and K. L. Tuck, *Coord. Chem. Rev.*, 2017, 1–30.
- 194 M. L. Aulsebrook, B. Graham, M. R. Grace and K. L. Tuck, *Tetrahedron*, 2014, **70**, 4367–4372.
- 195 X. Fang, G. Zhao, Y. Xiao, J. Xu and W. Yang, *Tetrahedron Lett.*, 2013, **54**, 806–810.
- 196 D. G. Smith, R. Pal and D. Parker, *Chem. Eur. J.*, 2012, **18**, 11604–11613.
- 197 I. Nasso, N. Geum, G. Bechara and B. Mestre-voegtlié, *J. Photochem. Photobiol. A.*, 2014, **274**, 124–132.
- 198 J. D. Routledge, M. W. Jones, S. Faulkner and M. Tropicano, *Inorg. Chem.*, 2015, **54**, 3337–3345.
- 199 B. McMahon, P. Mauer, C. P. McCoy, T. C. Lee and T. Gunnlaugsson, *J. Am. Chem. Soc.*, 2009, **131**, 17542–17543.
- 200 A. Picot, A. D'Aléo, P. L. Baldeck, A. Grichine, A. Duperray, C. Andraud and O. Maury, *J. Am. Chem. Soc.*, 2008, **130**, 1532–1533.
- 201 M. Andrews, A. J. Amoroso, L. P. Harding and S. J. A. Pope, *Dalton Trans.*, 2010, **39**, 3407–3411.
- 202 Z. Ye, G. Wang, J. Chen, X. Fu, W. Zhang and J. Yuan, *Biosens. Bioelectron.*, 2010, **26**, 1043–1048.
- 203 R. F. H. Viguier and A. N. Hulme, *J. Am. Chem. Soc.*, 2006, **128**, 11370–11371.
- 204 W. H. Melhuish, *J. Phys. Chem.*, 1961, **65**, 229–235.
- 205 G. A. Crosby and J. N. Demas, *J. Phys. Chem.*, 1971, **75**, 991–1024.
- 206 W. I. O'Malley, E. H. Abdelkader, M. L. Aulsebrook, R. Rubbiani, C. T. Loh, M. R. Grace, L. Spiccia, G. Gasser, G. Otting, K. L. Tuck and B. Graham, *Inorg. Chem.*, 2016, **55**, 1674–1682.

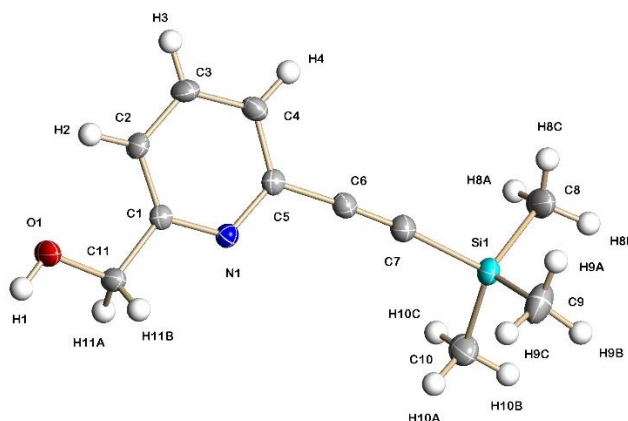
- 207 D. M. J. Doble, M. Botta, J. Wang, S. Aime, A. Barge and K. N. Raymond, *J. Am. Chem. Soc.*, 2001, **123**, 10758–10759.
- 208 A. G. Kanaras, F. S. Kamounah, K. Schaumburg, C. J. Kiely and M. Brust, *Chem. Commun.*, 2002, **20**, 2294–2295.
- 209 S. Zalipsky, *Adv. Drug Deliv. Rev.*, 1995, **16**, 157–182.
- 210 H. Yang, L. Ding, L. An, Z. Xiang, M. Chen, J. Zhou, F. Li, D. Wu and S. Yang, *Biomaterials*, 2012, **33**, 8591–8599.
- 211 G. Dehaen, P. Verwilst, S. V. Eliseeva, S. Laurent, L. Vander Elst, R. N. Muller, W. M. De Borggraeve, K. Binnemans and T. N. Parac-Vogt, *Inorg. Chem.*, 2011, **50**, 10005–10014.
- 212 P. Verwilst, S. V. Eliseeva, L. Vander Elst, C. Burtea, S. Laurent, S. Petoud, R. N. Muller, T. N. Parac-Vogt and W. M. De Borggraeve, *Inorg. Chem.*, 2012, **51**, 6405–6411.
- 213 T. Koullourou, L. S. Natrajan, H. Bhavsar, S. J. A. Pope, J. Feng, J. Narvainen, R. Shaw, E. Scales, R. Kauppinen, A. M. Kenwright and S. Faulkner, *J. Am. Chem. Soc.*, 2008, **130**, 2178–2179.
- 214 M. Tropiano, C. J. Record, E. Morris, H. S. Rai, C. Allain and S. Faulkner, *Organometallics*, 2012, **31**, 5673–5676.
- 215 P. Shi, B. J. Coe, S. Sánchez, D. Wang, Y. Tian, M. Nyk and M. Samoc, *Inorg. Chem.*, 2015, **54**, 11450–11456.
- 216 S. Banerjee, J. A. Kitchen, S. A. Bright, J. E. O'Brien, D. C. Williams, J. M. Kelly and T. Gunnlaugsson, *Chem. Commun.*, 2013, **49**, 8522–8524.
- 217 A. Shaira, D. Reddy and D. Jaganyi, *Dalton Trans.*, 2013, **42**, 8426–8436.

Chapter 8

Appendix

8.1 X-ray Crystallography

Compound 2



Figures show 50% displacement ellipsoids. There is intermolecular hydrogen bonding; Hydrogen bonds with $H..A < r(A) + 2.000$ Angstroms and $\langle DHA \rangle > 110$ deg.

D-H	d(D-H)	d(H..A)	$\langle DHA \rangle$	d(D..A)	A
O1-H1	0.840	2.073	172.32	2.908	N1 [-x+1, -y+1, z+1/2]

$R1 = 0.0304$, $wR2 = 0.0798$.

Crystal data and structure refinement for compound 2.

Identification code	15073	
Empirical formula	C11 H15 N O Si	
Formula weight	205.33	
Temperature	150(2) K	
Wavelength	0.71073 Å	
Crystal system	Orthorhombic	
Space group	Pna2(1)	
Unit cell dimensions	a = 11.336(3) Å	$\alpha = 90^\circ$.
	b = 10.908(3) Å	$\beta = 90^\circ$.
	c = 9.515(2) Å	$\gamma = 90^\circ$.
Volume	1176.6(5) Å ³	
Z	4	
Density (calculated)	1.159 Mg/m ³	
Absorption coefficient	0.169 mm ⁻¹	
F(000)	440	
Crystal size	0.38 x 0.27 x 0.24 mm ³	
Theta range for data collection	2.59 to 27.00°.	
Index ranges	-14 ≤ h ≤ 14, -13 ≤ k ≤ 13, -12 ≤ l ≤ 11	
Reflections collected	9240	
Independent reflections	2503 [R(int) = 0.0289]	
Completeness to theta = 27.00°	99.9 %	

Absorption correction	Empirical
Max. and min. transmission	0.928 and 0.782
Refinement method	Full-matrix least-squares on F ²
Data / restraints / parameters	2503 / 1 / 130
Goodness-of-fit on F ²	1.050
Final R indices [I>2sigma(I)]	R1 = 0.0304, wR2 = 0.0798
R indices (all data)	R1 = 0.0315, wR2 = 0.0809
Absolute structure parameter	0.10(10)
Largest diff. peak and hole	0.271 and -0.168 e.Å ⁻³

Atomic coordinates ($\times 10^4$) and equivalent isotropic displacement parameters ($\text{\AA}^2 \times 10^3$) for compound **2**. U(eq) is defined as one third of the trace of the orthogonalized U^{ij} tensor.

	x	y	z	U(eq)
Si(1)	4186(1)	1558(1)	-653(1)	28(1)
O(1)	5964(1)	4976(1)	7291(1)	36(1)
N(1)	5649(1)	3520(1)	3926(1)	20(1)
C(1)	6157(1)	3951(1)	5091(1)	20(1)
C(2)	7340(1)	3777(1)	5389(2)	25(1)
C(3)	8020(1)	3104(1)	4451(2)	29(1)
C(4)	7502(1)	2623(1)	3257(2)	26(1)
C(5)	6309(1)	2852(1)	3032(1)	21(1)
C(6)	5699(1)	2376(1)	1821(2)	25(1)
C(7)	5137(1)	2007(1)	834(2)	28(1)
C(8)	5153(2)	1090(2)	-2134(2)	45(1)
C(9)	3201(2)	293(2)	-80(2)	46(1)
C(10)	3303(2)	2921(2)	-1140(2)	38(1)
C(11)	5353(1)	4649(1)	6059(1)	25(1)

Bond lengths [\AA] and angles [$^\circ$] for compound **2**.

Si(1)-C(7)	1.8447(16)	C(2)-C(1)-C(11)	122.17(12)
Si(1)-C(10)	1.8516(18)	C(1)-C(2)-C(3)	118.64(12)
Si(1)-C(8)	1.8568(17)	C(1)-C(2)-H(2)	120.7
Si(1)-C(9)	1.8575(19)	C(3)-C(2)-H(2)	120.7
O(1)-C(11)	1.4081(17)	C(4)-C(3)-C(2)	119.52(12)
O(1)-H(1)	0.8400	C(4)-C(3)-H(3)	120.2
N(1)-C(1)	1.3343(18)	C(2)-C(3)-H(3)	120.2
N(1)-C(5)	1.3473(18)	C(3)-C(4)-C(5)	118.08(13)
C(1)-C(2)	1.384(2)	C(3)-C(4)-H(4)	121.0
C(1)-C(11)	1.5027(18)	C(5)-C(4)-H(4)	121.0
C(2)-C(3)	1.388(2)	N(1)-C(5)-C(4)	122.68(12)
C(2)-H(2)	0.9500	N(1)-C(5)-C(6)	115.67(12)
C(3)-C(4)	1.383(2)	C(4)-C(5)-C(6)	121.65(13)
C(3)-H(3)	0.9500	C(7)-C(6)-C(5)	176.65(15)
C(4)-C(5)	1.3914(19)	C(6)-C(7)-Si(1)	174.88(14)
C(4)-H(4)	0.9500	Si(1)-C(8)-H(8A)	109.5
C(5)-C(6)	1.441(2)	Si(1)-C(8)-H(8B)	109.5
C(6)-C(7)	1.204(2)	H(8A)-C(8)-H(8B)	109.5
C(8)-H(8A)	0.9800	Si(1)-C(8)-H(8C)	109.5
C(8)-H(8B)	0.9800	H(8A)-C(8)-H(8C)	109.5
C(8)-H(8C)	0.9800	H(8B)-C(8)-H(8C)	109.5
C(9)-H(9A)	0.9800	Si(1)-C(9)-H(9A)	109.5
C(9)-H(9B)	0.9800	Si(1)-C(9)-H(9B)	109.5
C(9)-H(9C)	0.9800	H(9A)-C(9)-H(9B)	109.5

C(10)-H(10A)	0.9800	Si(1)-C(9)-H(9C)	109.5
C(10)-H(10B)	0.9800	H(9A)-C(9)-H(9C)	109.5
C(10)-H(10C)	0.9800	H(9B)-C(9)-H(9C)	109.5
C(11)-H(11A)	0.9900	Si(1)-C(10)-H(10A)	109.5
C(11)-H(11B)	0.9900	Si(1)-C(10)-H(10B)	109.5
C(7)-Si(1)-C(10)	107.15(7)	H(10A)-C(10)-H(10B)	109.5
C(7)-Si(1)-C(8)	108.08(7)	Si(1)-C(10)-H(10C)	109.5
C(10)-Si(1)-C(8)	110.51(10)	H(10A)-C(10)-H(10C)	109.5
C(7)-Si(1)-C(9)	108.88(8)	H(10B)-C(10)-H(10C)	109.5
C(10)-Si(1)-C(9)	110.15(9)	O(1)-C(11)-C(1)	109.87(10)
C(8)-Si(1)-C(9)	111.92(10)	O(1)-C(11)-H(11A)	109.7
C(11)-O(1)-H(1)	109.5	C(1)-C(11)-H(11A)	109.7
C(1)-N(1)-C(5)	118.40(12)	O(1)-C(11)-H(11B)	109.7
N(1)-C(1)-C(2)	122.64(13)	C(1)-C(11)-H(11B)	109.7
N(1)-C(1)-C(11)	115.19(12)	H(11A)-C(11)-H(11B)	108.2

Anisotropic displacement parameters ($\text{\AA}^2 \times 10^3$) for compound **2**. The anisotropic displacement factor exponent takes the form: $-2\pi^2[h^2 a^*2U^{11} + \dots + 2 h k a^* b^* U^{12}]$

	U ¹¹	U ²²	U ³³	U ²³	U ¹³	U ¹²
Si(1)	28(1)	33(1)	23(1)	-8(1)	-7(1)	2(1)
O(1)	30(1)	55(1)	24(1)	-18(1)	-6(1)	12(1)
N(1)	21(1)	22(1)	18(1)	0(1)	-1(1)	-1(1)
C(1)	23(1)	20(1)	17(1)	2(1)	1(1)	-1(1)
C(2)	25(1)	31(1)	20(1)	-4(1)	-6(1)	1(1)
C(3)	21(1)	38(1)	29(1)	-3(1)	-4(1)	7(1)
C(4)	25(1)	29(1)	23(1)	-3(1)	2(1)	5(1)
C(5)	25(1)	21(1)	19(1)	1(1)	-1(1)	-1(1)
C(6)	26(1)	25(1)	23(1)	-3(1)	0(1)	2(1)
C(7)	28(1)	30(1)	26(1)	-4(1)	-2(1)	2(1)
C(8)	35(1)	68(1)	31(1)	-22(1)	-6(1)	11(1)
C(9)	52(1)	43(1)	43(1)	-2(1)	-17(1)	-13(1)
C(10)	41(1)	43(1)	31(1)	-4(1)	-8(1)	7(1)
C(11)	22(1)	33(1)	22(1)	-5(1)	-2(1)	4(1)

Hydrogen coordinates ($\times 10^4$) and isotropic displacement parameters ($\text{\AA}^2 \times 10^3$) for compound **2**.

	x	y	z	U(eq)
H(1)	5510	5365	7828	54
H(2)	7681	4111	6217	30
H(3)	8835	2974	4630	35
H(4)	7947	2149	2608	31
H(8A)	5608	1799	-2460	67
H(8B)	4667	776	-2906	67
H(8C)	5695	446	-1817	67
H(9A)	3670	-448	86	69
H(9B)	2614	131	-813	69
H(9C)	2798	529	791	69
H(10A)	2829	3182	-332	57
H(10B)	2779	2714	-1925	57
H(10C)	3832	3588	-1421	57
H(11A)	5064	5397	5580	30
H(11B)	4662	4136	6303	30

Torsion angles [°] for compound **2**.

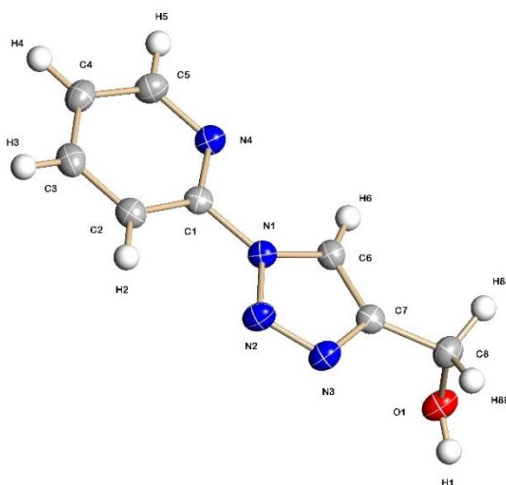
C(5)-N(1)-C(1)-C(2)	2.48(19)
C(5)-N(1)-C(1)-C(11)	-177.93(12)
N(1)-C(1)-C(2)-C(3)	-1.5(2)
C(11)-C(1)-C(2)-C(3)	178.97(13)
C(1)-C(2)-C(3)-C(4)	-0.3(2)
C(2)-C(3)-C(4)-C(5)	0.9(2)
C(1)-N(1)-C(5)-C(4)	-1.79(19)
C(1)-N(1)-C(5)-C(6)	177.79(11)
C(3)-C(4)-C(5)-N(1)	0.1(2)
C(3)-C(4)-C(5)-C(6)	-179.45(13)
N(1)-C(1)-C(11)-O(1)	175.67(11)
C(2)-C(1)-C(11)-O(1)	-4.74(19)

Hydrogen bonds for compound **2** [Å and °].

D-H...A	d(D-H)	d(H...A)	d(D...A)	<(DHA)
O(1)-H(1)...N(1)#1	0.84	2.07	2.9079(16)	172.3

Symmetry transformations used to generate equivalent atoms:

#1 -x+1,-y+1,z+1/2

Compound 11

Figures show 50% displacement ellipsoids. There is intermolecular hydrogen bonding; Hydrogen bonds with $H..A < r(A) + 2.000$ Angstroms and $<DHA > 110$ deg.

D-H	d(D-H)	d(H..A)	<DHA	d(D..A)	A
O1-H1	0.840	2.019	169.38	2.849	N3 [-x+1, -y+1, -z+2]

R1 = 0.0545, wR2 = 0.1465.

Crystal data and structure refinement for compound **11**.

Empirical formula	C8 H8 N4 O
Formula weight	176.18
Temperature	150(2) K

Wavelength	0.71073 Å	
Crystal system	Triclinic	
Space group	P-1	
Unit cell dimensions	a = 6.060(4) Å	$\alpha = 80.559(9)^\circ$.
	b = 7.458(5) Å	$\beta = 87.934(9)^\circ$.
	c = 9.626(6) Å	$\gamma = 66.519(9)^\circ$.
Volume	393.4(4) Å ³	
Z	2	
Density (calculated)	1.487 Mg/m ³	
Absorption coefficient	0.106 mm ⁻¹	
F(000)	184	
Crystal size	0.36 x 0.27 x 0.16 mm ³	
Theta range for data collection	2.15 to 25.00°	
Index ranges	-7<=h<=7, -8<=k<=8, -11<=l<=11	
Reflections collected	2765	
Independent reflections	1367 [R(int) = 0.0423]	
Completeness to theta = 25.00°	98.5 %	
Absorption correction	Empirical	
Max. and min. transmission	0.969 and 0.196	
Refinement method	Full-matrix least-squares on F ²	
Data / restraints / parameters	1367 / 0 / 119	
Goodness-of-fit on F ²	1.031	
Final R indices [I>2sigma(I)]	R1 = 0.0545, wR2 = 0.1465	
R indices (all data)	R1 = 0.0601, wR2 = 0.1522	
Largest diff. peak and hole	0.278 and -0.293 e.Å ⁻³	

Atomic coordinates ($\times 10^4$) and equivalent isotropic displacement parameters ($\text{Å}^2 \times 10^3$) for compound **11**. U(eq) is defined as one third of the trace of the orthogonalized U_{ij} tensor.

	x	y	z	U(eq)
O(1)	1342(2)	7098(2)	9743(1)	31(1)
N(1)	4863(2)	6976(2)	5755(1)	22(1)
N(2)	6757(3)	5742(2)	6626(1)	27(1)
N(3)	5848(3)	5162(2)	7779(1)	27(1)
N(4)	3264(3)	8991(2)	3629(1)	26(1)
C(1)	5248(3)	7892(2)	4402(2)	22(1)
C(2)	7567(3)	7598(2)	3990(2)	25(1)
C(3)	7831(3)	8540(3)	2691(2)	29(1)
C(4)	5794(3)	9723(3)	1844(2)	30(1)
C(5)	3570(3)	9873(3)	2355(2)	29(1)
C(6)	2763(3)	7156(2)	6382(2)	23(1)
C(7)	3402(3)	5994(2)	7663(2)	23(1)
C(8)	1881(3)	5651(3)	8846(2)	29(1)

Bond lengths [Å] and angles [°] for compound **11**.

O(1)-C(8)	1.422(2)	C(1)-N(4)-C(5)	116.09(16)
O(1)-H(1)	0.8400	N(4)-C(1)-C(2)	125.16(17)
N(1)-C(6)	1.355(2)	N(4)-C(1)-N(1)	114.77(16)
N(1)-N(2)	1.357(2)	C(2)-C(1)-N(1)	120.07(15)
N(1)-C(1)	1.425(2)	C(3)-C(2)-C(1)	117.66(16)
N(2)-N(3)	1.308(2)	C(3)-C(2)-H(2)	121.2
N(3)-C(7)	1.360(2)	C(1)-C(2)-H(2)	121.2

N(4)-C(1)	1.323(2)	C(2)-C(3)-C(4)	119.21(16)
N(4)-C(5)	1.337(2)	C(2)-C(3)-H(3)	120.4
C(1)-C(2)	1.387(3)	C(4)-C(3)-H(3)	120.4
C(2)-C(3)	1.367(2)	C(5)-C(4)-C(3)	118.07(17)
C(2)-H(2)	0.9500	C(5)-C(4)-H(4)	121.0
C(3)-C(4)	1.391(3)	C(3)-C(4)-H(4)	121.0
C(3)-H(3)	0.9500	N(4)-C(5)-C(4)	123.78(17)
C(4)-C(5)	1.386(3)	N(4)-C(5)-H(5)	118.1
C(4)-H(4)	0.9500	C(4)-C(5)-H(5)	118.1
C(5)-H(5)	0.9500	C(7)-C(6)-N(1)	105.40(15)
C(6)-C(7)	1.355(3)	C(7)-C(6)-H(6)	127.3
C(6)-H(6)	0.9500	N(1)-C(6)-H(6)	127.3
C(7)-C(8)	1.493(2)	C(6)-C(7)-N(3)	107.96(15)
C(8)-H(8A)	0.9900	C(6)-C(7)-C(8)	130.30(16)
C(8)-H(8B)	0.9900	N(3)-C(7)-C(8)	121.67(15)
C(8)-O(1)-H(1)	109.5	O(1)-C(8)-C(7)	111.25(14)
C(6)-N(1)-N(2)	110.25(15)	O(1)-C(8)-H(8A)	109.4
C(6)-N(1)-C(1)	129.23(15)	C(7)-C(8)-H(8A)	109.4
N(2)-N(1)-C(1)	120.52(15)	O(1)-C(8)-H(8B)	109.4
N(3)-N(2)-N(1)	106.45(14)	C(7)-C(8)-H(8B)	109.4
N(2)-N(3)-C(7)	109.94(13)	H(8A)-C(8)-H(8B)	108.0

Anisotropic displacement parameters ($\text{\AA}^2 \times 10^3$) for compound **11**. The anisotropic displacement factor exponent takes the form: $-2\pi^2 [h^2 a^{*2} U^{11} + \dots + 2hk a^* b^* U^{12}]$

	U ¹¹	U ²²	U ³³	U ²³	U ¹³	U ¹²
O(1)	32(1)	27(1)	25(1)	-3(1)	2(1)	-2(1)
N(1)	19(1)	19(1)	24(1)	-5(1)	1(1)	-3(1)
N(2)	23(1)	25(1)	25(1)	-1(1)	-2(1)	-1(1)
N(3)	26(1)	24(1)	24(1)	-3(1)	2(1)	-4(1)
N(4)	22(1)	24(1)	26(1)	-5(1)	1(1)	-4(1)
C(1)	22(1)	17(1)	25(1)	-8(1)	2(1)	-5(1)
C(2)	21(1)	22(1)	30(1)	-9(1)	2(1)	-4(1)
C(3)	27(1)	29(1)	34(1)	-14(1)	8(1)	-12(1)
C(4)	36(1)	26(1)	26(1)	-6(1)	7(1)	-12(1)
C(5)	28(1)	26(1)	27(1)	-2(1)	-2(1)	-5(1)
C(6)	19(1)	20(1)	27(1)	-7(1)	3(1)	-4(1)
C(7)	23(1)	17(1)	26(1)	-7(1)	2(1)	-5(1)
C(8)	31(1)	24(1)	28(1)	-3(1)	3(1)	-10(1)

Hydrogen coordinates ($\times 10^4$) and isotropic displacement parameters ($\text{\AA}^2 \times 10^3$) for compound **11**.

	x	y	z	U(eq)
H(1)	2077	6564	10523	47
H(2)	8924	6772	4589	30
H(3)	9387	8389	2371	35
H(4)	5924	10409	943	35
H(5)	2182	10646	1765	35
H(6)	1178	7932	6004	28
H(8A)	363	5701	8458	34
H(8B)	2741	4316	9400	34

Torsion angles [°] for compound **11**.

C(6)-N(1)-N(2)-N(3)	-0.02(18)
C(1)-N(1)-N(2)-N(3)	179.23(13)
N(1)-N(2)-N(3)-C(7)	0.29(18)
C(5)-N(4)-C(1)-C(2)	0.0(3)
C(5)-N(4)-C(1)-N(1)	179.86(13)
C(6)-N(1)-C(1)-N(4)	-3.8(3)
N(2)-N(1)-C(1)-N(4)	177.14(13)
C(6)-N(1)-C(1)-C(2)	176.10(14)
N(2)-N(1)-C(1)-C(2)	-3.0(2)
N(4)-C(1)-C(2)-C(3)	1.0(3)
N(1)-C(1)-C(2)-C(3)	-178.83(14)
C(1)-C(2)-C(3)-C(4)	-0.5(2)
C(2)-C(3)-C(4)-C(5)	-0.8(3)
C(1)-N(4)-C(5)-C(4)	-1.5(3)
C(3)-C(4)-C(5)-N(4)	2.0(3)
N(2)-N(1)-C(6)-C(7)	-0.25(18)
C(1)-N(1)-C(6)-C(7)	-179.42(16)
N(1)-C(6)-C(7)-N(3)	0.41(17)
N(1)-C(6)-C(7)-C(8)	177.38(16)
N(2)-N(3)-C(7)-C(6)	-0.45(19)
N(2)-N(3)-C(7)-C(8)	-177.73(14)
C(6)-C(7)-C(8)-O(1)	-86.8(2)
N(3)-C(7)-C(8)-O(1)	89.80(19)

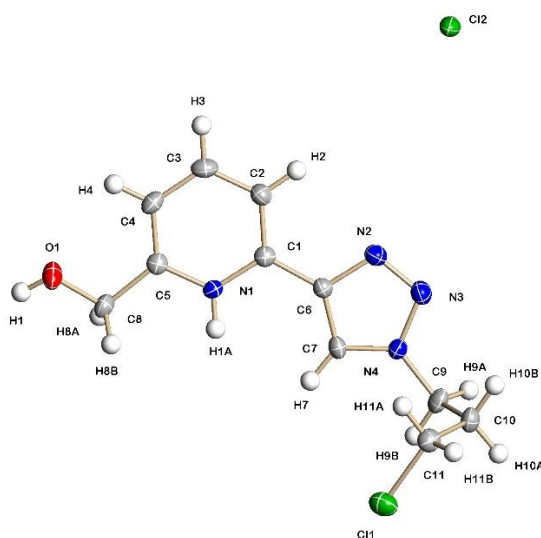
Symmetry transformations used to generate equivalent atoms:

Hydrogen bonds for compound **11** [Å and °].

D-H...A	d(D-H)	d(H...A)	d(D...A)	<(DHA)
O(1)-H(1)...N(3)#1	0.84	2.02	2.849(2)	169.4

Symmetry transformations used to generate equivalent atoms:

#1 -x+1,-y+1,-z+2

Compound 21 derivative

Figures show 50% displacement ellipsoids. There is intermolecular hydrogen bonding;

Hydrogen bonds with H..A < r(A) + 2.000 Angstroms and <DHA > 110 deg.

D-H	d(D-H)	d(H..A)	<DHA	d(D..A)	A
O1-H1	0.840	2.247	176.89	3.087	Cl2 [-x+2, -y, -z+1]
N1-H1A	0.880	2.220	171.47	3.093	Cl2 [x+1, y, z-1]

R1 = 0.0446, wR2 = 0.0759.

Crystal data and structure refinement for compound **21** derivative.

Empirical formula	C11 H14 Cl2 N4 O	
Formula weight	289.16	
Temperature	150(2) K	
Wavelength	0.71073 Å	
Crystal system	Monoclinic	
Space group	P2(1)/n	
Unit cell dimensions	a = 5.0942(19) Å b = 30.070(11) Å c = 8.768(3) Å	$\alpha = 90^\circ$. $\beta = 106.182(7)^\circ$. $\gamma = 90^\circ$.
Volume	1289.9(8) Å ³	
Z	4	
Density (calculated)	1.489 Mg/m ³	
Absorption coefficient	0.497 mm ⁻¹	
F(000)	600	
Crystal size	0.26 x 0.17 x 0.05 mm ³	
Theta range for data collection	1.35 to 26.00°.	
Index ranges	-6<=h<=6, -37<=k<=37, -10<=l<=10	
Reflections collected	9983	
Independent reflections	2531 [R(int) = 0.0900]	
Completeness to theta = 26.00°	100.0 %	
Absorption correction	Empirical	
Max. and min. transmission	0.894 and 0.616	
Refinement method	Full-matrix least-squares on F ²	
Data / restraints / parameters	2531 / 0 / 164	
Goodness-of-fit on F ²	0.840	
Final R indices [I>2sigma(I)]	R1 = 0.0446, wR2 = 0.0759	
R indices (all data)	R1 = 0.0778, wR2 = 0.0829	
Largest diff. peak and hole	0.320 and -0.258 e.Å ⁻³	

Atomic coordinates (x 10⁴) and equivalent isotropic displacement parameters (Å²x 10³) for compound **21** derivative. U(eq) is defined as one third of the trace of the orthogonalized U^{ij} tensor.

	x	y	z	U(eq)
Cl(1)	6174(2)	2008(1)	-3223(1)	37(1)
O(1)	17977(4)	108(1)	2904(2)	33(1)
N(1)	12080(4)	803(1)	2410(2)	20(1)
N(2)	7166(4)	1607(1)	3178(3)	26(1)
N(3)	5075(5)	1794(1)	2155(3)	28(1)
N(4)	5018(4)	1641(1)	694(3)	21(1)
C(1)	10817(5)	1072(1)	3228(3)	21(1)
C(2)	11825(5)	1091(1)	4857(3)	24(1)
C(3)	14110(6)	843(1)	5599(3)	28(1)
C(4)	15345(5)	571(1)	4728(3)	24(1)

C(5)	14274(5)	548(1)	3118(3)	21(1)
C(6)	8441(5)	1330(1)	2359(3)	20(1)
C(7)	7054(5)	1352(1)	780(3)	21(1)
C(8)	15324(5)	249(1)	2045(3)	26(1)
C(9)	2911(5)	1798(1)	-697(3)	27(1)
C(10)	3397(5)	2276(1)	-1133(3)	26(1)
C(11)	6022(5)	2351(1)	-1563(3)	27(1)
Cl(2)	382(1)	710(1)	8753(1)	29(1)

Bond lengths [Å] and angles [°] for compound **21** derivative.

Cl(1)-C(11)	1.803(3)	C(5)-C(4)-H(4)	120.4
O(1)-C(8)	1.416(3)	C(3)-C(4)-H(4)	120.4
O(1)-H(1)	0.8400	N(1)-C(5)-C(4)	119.1(2)
N(1)-C(5)	1.355(3)	N(1)-C(5)-C(8)	116.4(2)
N(1)-C(1)	1.356(3)	C(4)-C(5)-C(8)	124.6(2)
N(1)-H(1A)	0.8800	C(7)-C(6)-N(2)	108.2(2)
N(2)-N(3)	1.312(3)	C(7)-C(6)-C(1)	132.3(2)
N(2)-C(6)	1.376(3)	N(2)-C(6)-C(1)	119.5(2)
N(3)-N(4)	1.354(3)	N(4)-C(7)-C(6)	105.2(2)
N(4)-C(7)	1.338(3)	N(4)-C(7)-H(7)	127.4
N(4)-C(9)	1.461(3)	C(6)-C(7)-H(7)	127.4
C(1)-C(2)	1.377(4)	O(1)-C(8)-C(5)	107.4(2)
C(1)-C(6)	1.460(3)	O(1)-C(8)-H(8A)	110.2
C(2)-C(3)	1.384(4)	C(5)-C(8)-H(8A)	110.2
C(2)-H(2)	0.9500	O(1)-C(8)-H(8B)	110.2
C(3)-C(4)	1.383(4)	C(5)-C(8)-H(8B)	110.2
C(3)-H(3)	0.9500	C(2)-C(1)-C(6)	122.3(2)
C(4)-C(5)	1.365(3)	C(1)-C(2)-C(3)	119.2(3)
C(4)-H(4)	0.9500	C(1)-C(2)-H(2)	120.4
C(5)-C(8)	1.505(3)	C(3)-C(2)-H(2)	120.4
C(6)-C(7)	1.370(3)	C(4)-C(3)-C(2)	120.7(3)
C(7)-H(7)	0.9500	C(4)-C(3)-H(3)	119.6
C(8)-H(8A)	0.9900	C(2)-C(3)-H(3)	119.6
C(8)-H(8B)	0.9900	C(5)-C(4)-C(3)	119.2(3)
C(9)-C(10)	1.524(3)	H(8A)-C(8)-H(8B)	108.5
C(9)-H(9A)	0.9900	N(4)-C(9)-C(10)	112.5(2)
C(9)-H(9B)	0.9900	N(4)-C(9)-H(9A)	109.1
C(10)-C(11)	1.504(3)	C(10)-C(9)-H(9A)	109.1
C(10)-H(10A)	0.9900	N(4)-C(9)-H(9B)	109.1
C(10)-H(10B)	0.9900	C(10)-C(9)-H(9B)	109.1
C(11)-H(11A)	0.9900	H(9A)-C(9)-H(9B)	107.8
C(11)-H(11B)	0.9900	C(11)-C(10)-C(9)	114.9(2)
C(8)-O(1)-H(1)	109.5	C(11)-C(10)-H(10A)	108.5
C(5)-N(1)-C(1)	123.2(2)	C(9)-C(10)-H(10A)	108.5
C(5)-N(1)-H(1A)	118.4	C(11)-C(10)-H(10B)	108.5
C(1)-N(1)-H(1A)	118.4	C(9)-C(10)-H(10B)	108.5
N(3)-N(2)-C(6)	108.3(2)	H(10A)-C(10)-H(10B)	107.5
N(2)-N(3)-N(4)	107.5(2)	C(10)-C(11)-Cl(1)	111.01(19)
C(7)-N(4)-N(3)	110.8(2)	C(10)-C(11)-H(11A)	109.4
C(7)-N(4)-C(9)	129.4(2)	Cl(1)-C(11)-H(11A)	109.4
N(3)-N(4)-C(9)	119.8(2)	C(10)-C(11)-H(11B)	109.4
N(1)-C(1)-C(2)	118.6(2)	Cl(1)-C(11)-H(11B)	109.4
N(1)-C(1)-C(6)	119.1(2)	H(11A)-C(11)-H(11B)	108.0

Anisotropic displacement parameters ($\text{\AA}^2 \times 10^3$) for compound **21** derivative. The anisotropic displacement factor exponent takes the form: $-2\pi^2 [h^2 a^{*2} U^{11} + \dots + 2 h k a^* b^* U^{12}]$

	U11	U22	U33	U23	U13	U12
Cl(1)	36(1)	45(1)	31(1)	-3(1)	13(1)	-5(1)
O(1)	25(1)	30(1)	39(1)	-10(1)	1(1)	6(1)
N(1)	20(1)	21(1)	17(1)	1(1)	3(1)	0(1)
N(2)	27(1)	29(2)	24(1)	-3(1)	8(1)	1(1)
N(3)	28(1)	27(2)	30(2)	-3(1)	9(1)	3(1)
N(4)	19(1)	21(1)	22(1)	2(1)	5(1)	2(1)
C(1)	21(1)	19(2)	23(2)	1(1)	7(1)	-4(1)
C(2)	25(2)	24(2)	25(2)	-3(1)	8(1)	-1(1)
C(3)	32(2)	29(2)	20(2)	-1(1)	4(1)	-7(1)
C(4)	21(2)	21(2)	26(2)	4(1)	0(1)	-2(1)
C(5)	20(2)	18(2)	25(2)	0(1)	7(1)	-4(1)
C(6)	21(1)	18(2)	22(2)	0(1)	8(1)	-1(1)
C(7)	19(1)	19(2)	27(2)	-1(1)	10(1)	1(1)
C(8)	24(2)	20(2)	29(2)	3(1)	2(1)	3(1)
C(9)	20(2)	30(2)	31(2)	8(1)	5(1)	4(1)
C(10)	23(2)	23(2)	34(2)	4(1)	9(1)	4(1)
C(11)	30(2)	23(2)	29(2)	-1(1)	7(1)	-2(1)
Cl(2)	31(1)	31(1)	22(1)	-3(1)	4(1)	8(1)

Hydrogen coordinates ($\times 10^4$) and isotropic displacement parameters ($\text{\AA}^2 \times 10^3$) for compound **21** derivative.

	x	y	z	U(eq)
H(1)	18400	-121	2477	50
H(1A)	11444	794	1369	24
H(2)	10962	1272	5462	29
H(3)	14840	859	6720	33
H(4)	16920	403	5243	29
H(7)	7452	1197	-71	25
H(8A)	14103	-12	1725	31
H(8B)	15395	411	1076	31
H(9A)	1106	1779	-483	33
H(9B)	2869	1602	-1610	33
H(10A)	1855	2368	-2042	32
H(10B)	3387	2471	-225	32
H(11A)	7589	2280	-638	33
H(11B)	6160	2667	-1837	33

Table 6. Torsion angles [$^\circ$] for compound **21** derivative.

C(6)-N(2)-N(3)-N(4)	-0.4(3)
N(2)-N(3)-N(4)-C(7)	0.6(3)
N(2)-N(3)-N(4)-C(9)	-179.0(2)
C(5)-N(1)-C(1)-C(2)	0.7(4)
C(5)-N(1)-C(1)-C(6)	-179.1(2)
N(1)-C(1)-C(2)-C(3)	1.1(4)
C(6)-C(1)-C(2)-C(3)	-179.0(2)
C(1)-C(2)-C(3)-C(4)	-1.3(4)
C(2)-C(3)-C(4)-C(5)	-0.4(4)
C(1)-N(1)-C(5)-C(4)	-2.4(4)
C(1)-N(1)-C(5)-C(8)	176.4(2)

C(3)-C(4)-C(5)-N(1)	2.2(4)
C(3)-C(4)-C(5)-C(8)	-176.6(2)
N(3)-N(2)-C(6)-C(7)	0.1(3)
N(3)-N(2)-C(6)-C(1)	-178.7(2)
N(1)-C(1)-C(6)-C(7)	2.2(4)
C(2)-C(1)-C(6)-C(7)	-177.6(3)
N(1)-C(1)-C(6)-N(2)	-179.2(2)
C(2)-C(1)-C(6)-N(2)	0.9(4)
N(3)-N(4)-C(7)-C(6)	-0.5(3)
C(9)-N(4)-C(7)-C(6)	179.1(2)
N(2)-C(6)-C(7)-N(4)	0.3(3)
C(1)-C(6)-C(7)-N(4)	178.9(3)
N(1)-C(5)-C(8)-O(1)	164.2(2)
C(4)-C(5)-C(8)-O(1)	-17.0(4)
C(7)-N(4)-C(9)-C(10)	-106.7(3)
N(3)-N(4)-C(9)-C(10)	72.9(3)
N(4)-C(9)-C(10)-C(11)	61.4(3)
C(9)-C(10)-C(11)-Cl(1)	58.6(3)

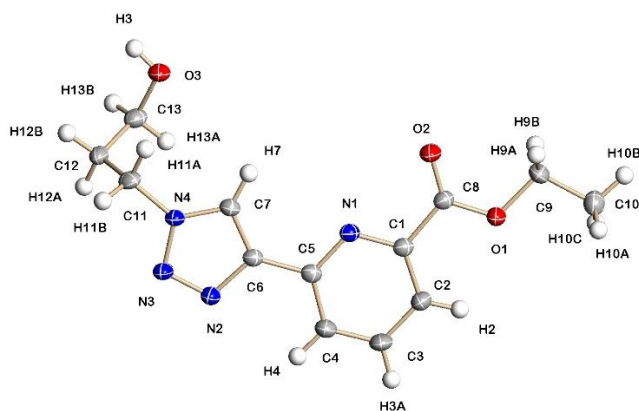
Table 7. Hydrogen bonds for compound **21** derivative [\AA and $^\circ$].

D-H...A	d(D-H)	d(H...A)	d(D...A)	$\angle(\text{DHA})$
N(1)-H(1A)...Cl(2)#1	0.88	2.22	3.093(2)	171.5
O(1)-H(1)...Cl(2)#2	0.84	2.25	3.087(2)	176.9

Symmetry transformations used to generate equivalent atoms:

#1 $x+1, y, z-1$ #2 $-x+2, -y, -z+1$

Compound 27



Figures show 50% displacement ellipsoids. There is intermolecular hydrogen bonding;

Hydrogen bonds with $\text{H}\dots\text{A} < r(\text{A}) + 2.000$ Angstroms and $\angle(\text{DHA}) > 110$ deg.

D-H	d(D-H)	d(H..A)	$\angle(\text{DHA})$	d(D..A)	A
O3-H3	0.840	2.182	149.29	2.936	O2 [$-x+1, -y+1, -z$]
O3-H3	0.840	2.478	139.09	3.161	N1 [$-x+1, -y+1, -z$]

$R1 = 0.0529$, $wR2 = 0.1439$

Crystal data and structure refinement for compound **27**.

Empirical formula	C13 H16 N4 O3	
Formula weight	276.30	
Temperature	150(2) K	
Wavelength	0.71073 Å	
Crystal system	Triclinic	
Space group	P-1	
Unit cell dimensions	a = 5.7969(12) Å	$\alpha = 102.516(3)^\circ$.
	b = 8.5508(18) Å	$\beta = 90.924(3)^\circ$.
	c = 13.937(3) Å	$\gamma = 92.119(4)^\circ$.
Volume	673.7(2) Å ³	
Z	2	
Density (calculated)	1.362 Mg/m ³	
Absorption coefficient	0.100 mm ⁻¹	
F(000)	292	
Crystal size	0.30 x 0.24 x 0.20 mm ³	
Theta range for data collection	1.50 to 26.00°.	
Index ranges	-7<=h<=7, -10<=k<=10, -17<=l<=17	
Reflections collected	5227	
Independent reflections	2610 [R(int) = 0.0479]	
Completeness to theta = 26.00°	98.6 %	
Absorption correction	Empirical	
Max. and min. transmission	0.981 and 0.443	
Refinement method	Full-matrix least-squares on F ²	
Data / restraints / parameters	2610 / 0 / 184	
Goodness-of-fit on F ²	1.058	
Final R indices [I>2sigma(I)]	R1 = 0.0529, wR2 = 0.1439	
R indices (all data)	R1 = 0.0576, wR2 = 0.1488	
Extinction coefficient	0.030(8)	
Largest diff. peak and hole	0.311 and -0.367 e.Å ⁻³	

Atomic coordinates ($\times 10^4$) and equivalent isotropic displacement parameters ($\text{Å}^2 \times 10^3$) for compound **27**. U(eq) is defined as one third of the trace of the orthogonalized U_{ij} tensor.

	x	y	z	U(eq)
O(1)	13220(2)	9569(1)	3100(1)	28(1)
O(2)	10837(2)	8764(1)	1788(1)	34(1)
O(3)	3041(2)	3012(1)	-606(1)	34(1)
N(1)	8113(2)	7106(1)	2846(1)	23(1)
N(2)	3319(2)	4588(1)	3405(1)	25(1)
N(3)	1572(2)	3966(2)	2821(1)	26(1)
N(4)	1871(2)	4416(1)	1961(1)	23(1)
C(1)	10003(2)	7926(2)	3285(1)	24(1)
C(2)	10672(3)	8016(2)	4258(1)	28(1)
C(3)	9303(3)	7199(2)	4809(1)	33(1)
C(4)	7359(3)	6352(2)	4378(1)	31(1)
C(5)	6814(2)	6324(2)	3395(1)	24(1)
C(6)	4743(2)	5440(2)	2915(1)	23(1)
C(7)	3820(2)	5324(2)	1984(1)	24(1)
C(8)	11365(3)	8782(2)	2634(1)	24(1)
C(9)	14724(3)	10398(2)	2529(1)	30(1)
C(10)	16523(3)	11320(2)	3232(1)	34(1)
C(11)	166(3)	3899(2)	1161(1)	29(1)

C(12)	480(3)	2196(2)	591(1)	29(1)
C(13)	2757(3)	1987(2)	64(1)	30(1)

Bond lengths [Å] and angles [°] for compound **27**.

O(1)-C(8)	1.3291(18)	C(4)-C(3)-H(3A)	120.5
O(1)-C(9)	1.4546(17)	C(2)-C(3)-H(3A)	120.5
O(2)-C(8)	1.2090(18)	C(3)-C(4)-C(5)	119.40(14)
O(3)-C(13)	1.4207(17)	C(3)-C(4)-H(4)	120.3
O(3)-H(3)	0.8400	C(5)-C(4)-H(4)	120.3
N(1)-C(5)	1.3419(19)	N(1)-C(5)-C(4)	122.59(14)
N(1)-C(1)	1.3420(19)	N(1)-C(5)-C(6)	116.72(13)
N(2)-N(3)	1.3103(17)	C(4)-C(5)-C(6)	120.68(13)
N(2)-C(6)	1.3661(18)	N(2)-C(6)-C(7)	108.28(13)
N(3)-N(4)	1.3476(17)	N(2)-C(6)-C(5)	121.35(13)
N(4)-C(7)	1.3431(18)	C(7)-C(6)-C(5)	130.34(13)
N(4)-C(11)	1.4612(19)	N(4)-C(7)-C(6)	104.42(12)
C(1)-C(2)	1.389(2)	N(4)-C(7)-H(7)	127.8
C(1)-C(8)	1.501(2)	C(6)-C(7)-H(7)	127.8
C(2)-C(3)	1.385(2)	O(2)-C(8)-O(1)	124.05(14)
C(2)-H(2)	0.9500	O(2)-C(8)-C(1)	124.20(14)
C(3)-C(4)	1.373(2)	O(1)-C(8)-C(1)	111.75(12)
C(3)-H(3A)	0.9500	C(1)-C(2)-H(2)	121.1
C(4)-C(5)	1.396(2)	C(4)-C(3)-C(2)	119.04(14)
C(4)-H(4)	0.9500	O(1)-C(9)-C(10)	106.61(12)
C(5)-C(6)	1.465(2)	O(1)-C(9)-H(9A)	110.4
C(6)-C(7)	1.378(2)	C(10)-C(9)-H(9A)	110.4
C(7)-H(7)	0.9500	O(1)-C(9)-H(9B)	110.4
C(9)-C(10)	1.496(2)	C(10)-C(9)-H(9B)	110.4
C(9)-H(9A)	0.9900	H(9A)-C(9)-H(9B)	108.6
C(9)-H(9B)	0.9900	C(9)-C(10)-H(10A)	109.5
C(10)-H(10A)	0.9800	C(9)-C(10)-H(10B)	109.5
C(10)-H(10B)	0.9800	H(10A)-C(10)-H(10B)	109.5
C(10)-H(10C)	0.9800	C(9)-C(10)-H(10C)	109.5
C(11)-C(12)	1.519(2)	H(10A)-C(10)-H(10C)	109.5
C(11)-H(11A)	0.9900	H(10B)-C(10)-H(10C)	109.5
C(11)-H(11B)	0.9900	N(4)-C(11)-C(12)	112.81(12)
C(12)-C(13)	1.518(2)	N(4)-C(11)-H(11A)	109.0
C(12)-H(12A)	0.9900	C(12)-C(11)-H(11A)	109.0
C(12)-H(12B)	0.9900	N(4)-C(11)-H(11B)	109.0
C(13)-H(13A)	0.9900	C(12)-C(11)-H(11B)	109.0
C(13)-H(13B)	0.9900	H(11A)-C(11)-H(11B)	107.8
C(8)-O(1)-C(9)	116.68(12)	C(13)-C(12)-C(11)	113.30(12)
C(13)-O(3)-H(3)	109.5	C(13)-C(12)-H(12A)	108.9
C(5)-N(1)-C(1)	116.88(13)	C(11)-C(12)-H(12A)	108.9
N(3)-N(2)-C(6)	108.76(12)	C(13)-C(12)-H(12B)	108.9
N(2)-N(3)-N(4)	107.29(11)	C(11)-C(12)-H(12B)	108.9
C(7)-N(4)-N(3)	111.25(11)	H(12A)-C(12)-H(12B)	107.7
C(7)-N(4)-C(11)	129.07(12)	O(3)-C(13)-C(12)	112.66(13)
N(3)-N(4)-C(11)	119.68(11)	O(3)-C(13)-H(13A)	109.1
N(1)-C(1)-C(2)	124.26(14)	C(12)-C(13)-H(13A)	109.1
N(1)-C(1)-C(8)	114.10(13)	O(3)-C(13)-H(13B)	109.1
C(2)-C(1)-C(8)	121.63(14)	C(12)-C(13)-H(13B)	109.1
C(3)-C(2)-C(1)	117.83(14)	H(13A)-C(13)-H(13B)	107.8
C(3)-C(2)-H(2)	121.1		

Anisotropic displacement parameters ($\text{\AA}^2 \times 10^3$) for compound **27**. The anisotropic displacement factor exponent takes the form: $-2\pi^2 [h^2 a^{*2} U^{11} + \dots + 2 h k a^* b^* U^{12}]$

	U11	U22	U33	U23	U13	U12
O(1)	30(1)	32(1)	22(1)	9(1)	-2(1)	-7(1)
O(2)	39(1)	42(1)	21(1)	12(1)	-5(1)	-10(1)
O(3)	40(1)	41(1)	21(1)	11(1)	-1(1)	-8(1)
N(1)	26(1)	24(1)	20(1)	5(1)	1(1)	1(1)
N(2)	29(1)	27(1)	21(1)	7(1)	-1(1)	-3(1)
N(3)	31(1)	29(1)	19(1)	8(1)	-2(1)	-2(1)
N(4)	27(1)	26(1)	17(1)	7(1)	0(1)	0(1)
C(1)	27(1)	23(1)	21(1)	5(1)	1(1)	1(1)
C(2)	30(1)	32(1)	22(1)	5(1)	-3(1)	-4(1)
C(3)	39(1)	43(1)	19(1)	9(1)	-2(1)	-5(1)
C(4)	34(1)	36(1)	22(1)	9(1)	2(1)	-5(1)
C(5)	27(1)	23(1)	22(1)	5(1)	3(1)	3(1)
C(6)	27(1)	23(1)	19(1)	5(1)	2(1)	2(1)
C(7)	26(1)	26(1)	20(1)	7(1)	2(1)	1(1)
C(8)	28(1)	24(1)	21(1)	4(1)	-1(1)	1(1)
C(9)	31(1)	33(1)	26(1)	11(1)	3(1)	-6(1)
C(10)	33(1)	33(1)	37(1)	9(1)	-4(1)	-4(1)
C(11)	29(1)	38(1)	20(1)	8(1)	-4(1)	1(1)
C(12)	35(1)	31(1)	21(1)	8(1)	-5(1)	-9(1)
C(13)	39(1)	30(1)	22(1)	6(1)	-2(1)	-1(1)

Hydrogen coordinates ($\times 10^4$) and isotropic displacement parameters ($\text{\AA}^2 \times 10^3$) for compound **27**.

	x	y	z	U(eq)
H(3)	2184	2672	-1105	51
H(2)	12023	8617	4536	34
H(3A)	9703	7225	5476	40
H(4)	6393	5789	4745	37
H(7)	4426	5783	1474	28
H(9A)	13832	11133	2222	36
H(9B)	15454	9617	2004	36
H(10A)	15783	12120	3730	52
H(10B)	17624	11860	2872	52
H(10C)	17342	10583	3553	52
H(11A)	285	4636	703	34
H(11B)	-1400	3972	1435	34
H(12A)	390	1463	1051	35
H(12B)	-802	1884	101	35
H(13A)	4042	2211	557	36
H(13B)	2838	859	-298	36

Torsion angles [$^\circ$] for compound **27**.

C(6)-N(2)-N(3)-N(4)	0.00(15)
N(2)-N(3)-N(4)-C(7)	0.30(15)
N(2)-N(3)-N(4)-C(11)	-179.74(12)
C(5)-N(1)-C(1)-C(2)	-0.3(2)
C(5)-N(1)-C(1)-C(8)	-179.52(11)
N(1)-C(1)-C(2)-C(3)	0.3(2)
C(8)-C(1)-C(2)-C(3)	179.45(13)
C(1)-C(2)-C(3)-C(4)	-0.3(2)
C(2)-C(3)-C(4)-C(5)	0.4(2)

C(1)-N(1)-C(5)-C(4)	0.3(2)
C(1)-N(1)-C(5)-C(6)	179.56(11)
C(3)-C(4)-C(5)-N(1)	-0.4(2)
C(3)-C(4)-C(5)-C(6)	-179.58(13)
N(3)-N(2)-C(6)-C(7)	-0.29(16)
N(3)-N(2)-C(6)-C(5)	177.81(12)
N(1)-C(5)-C(6)-N(2)	179.19(11)
C(4)-C(5)-C(6)-N(2)	-1.6(2)
N(1)-C(5)-C(6)-C(7)	-3.2(2)
C(4)-C(5)-C(6)-C(7)	176.07(14)
N(3)-N(4)-C(7)-C(6)	-0.46(15)
C(11)-N(4)-C(7)-C(6)	179.58(13)
N(2)-C(6)-C(7)-N(4)	0.45(15)
C(5)-C(6)-C(7)-N(4)	-177.42(13)
C(9)-O(1)-C(8)-O(2)	-2.4(2)
C(9)-O(1)-C(8)-C(1)	177.78(11)
N(1)-C(1)-C(8)-O(2)	0.5(2)
C(2)-C(1)-C(8)-O(2)	-178.78(14)
N(1)-C(1)-C(8)-O(1)	-179.73(11)
C(2)-C(1)-C(8)-O(1)	1.0(2)
C(8)-O(1)-C(9)-C(10)	174.25(12)
C(7)-N(4)-C(11)-C(12)	99.41(17)
N(3)-N(4)-C(11)-C(12)	-80.54(16)
N(4)-C(11)-C(12)-C(13)	-63.68(17)
C(11)-C(12)-C(13)-O(3)	-57.96(17)

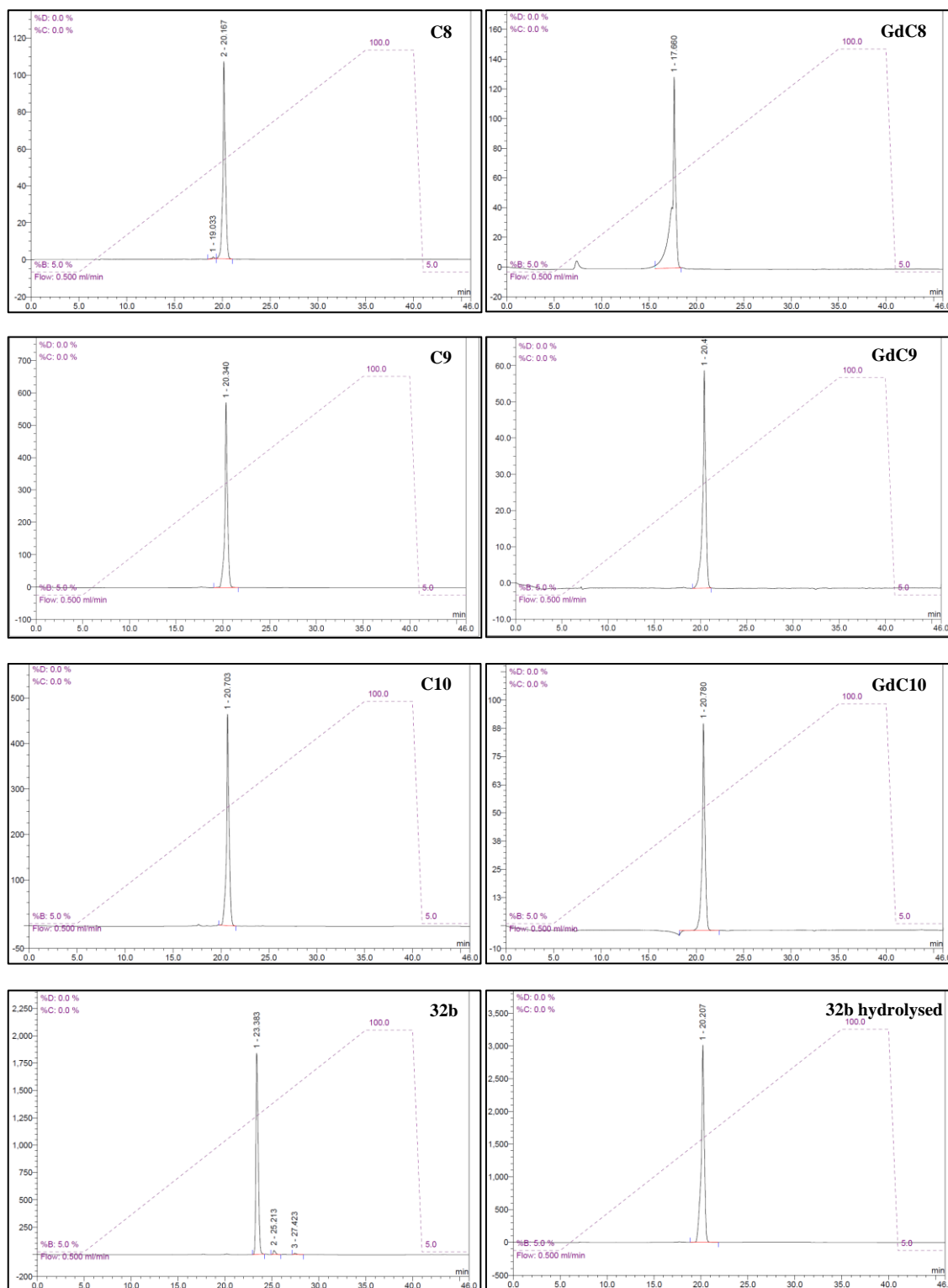
Hydrogen bonds for compound **27** [Å and °].

D-H...A	d(D-H)	d(H...A)	d(D...A)	<(DHA)
O(3)-H(3)...O(2)#1	0.84	2.18	2.9357(16)	149.3
O(3)-H(3)...N(1)#1	0.84	2.48	3.1613(17)	139.1

Symmetry transformations used to generate equivalent atoms:

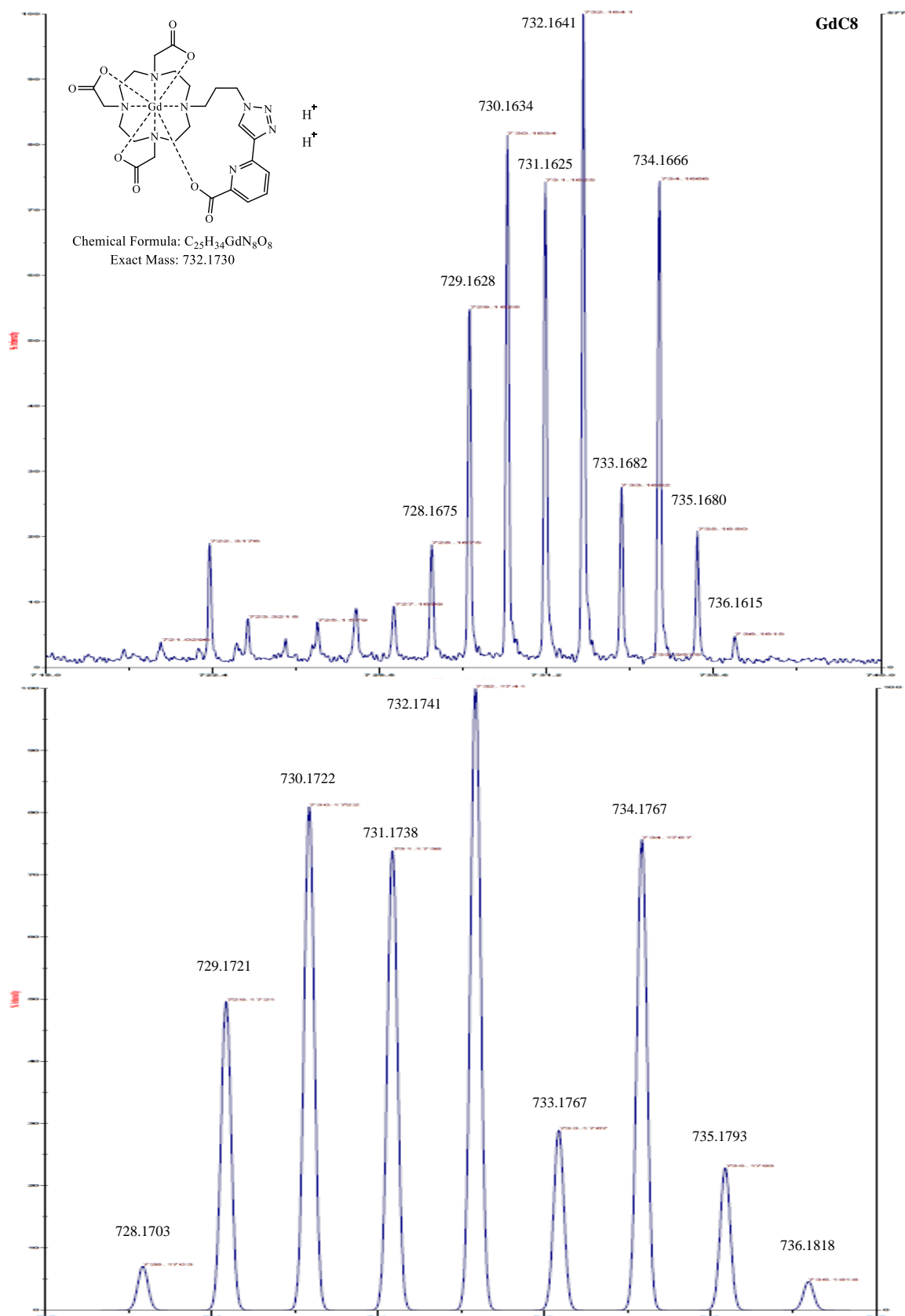
#1 -x+1,-y+1,-z

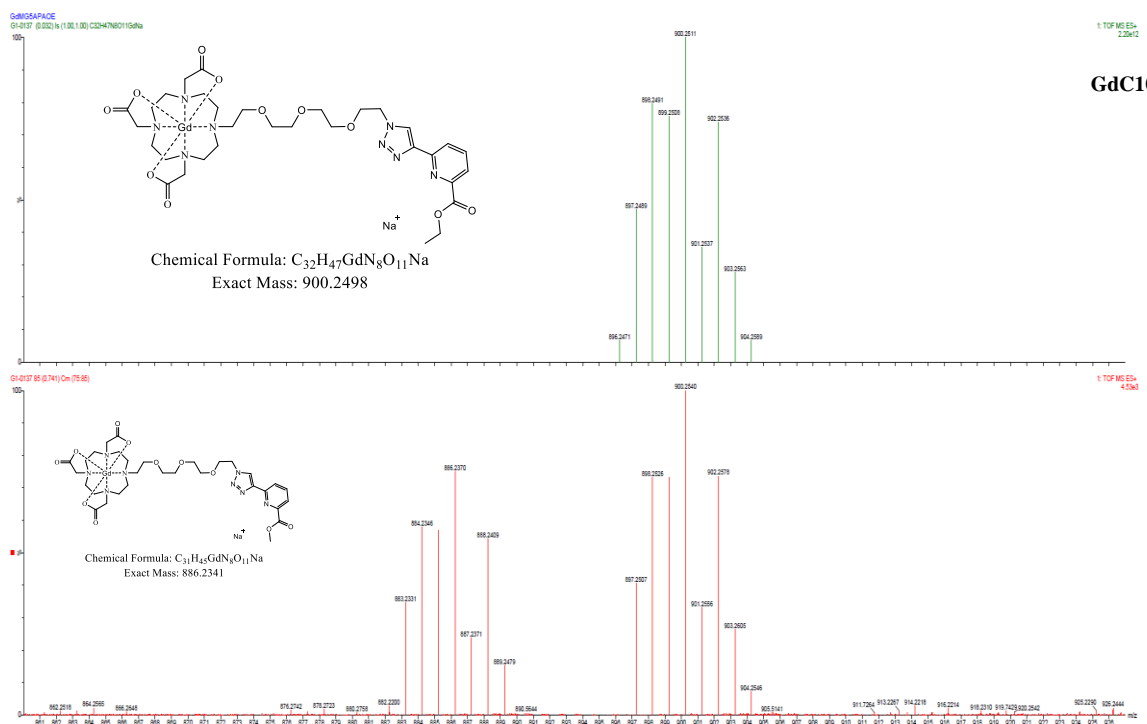
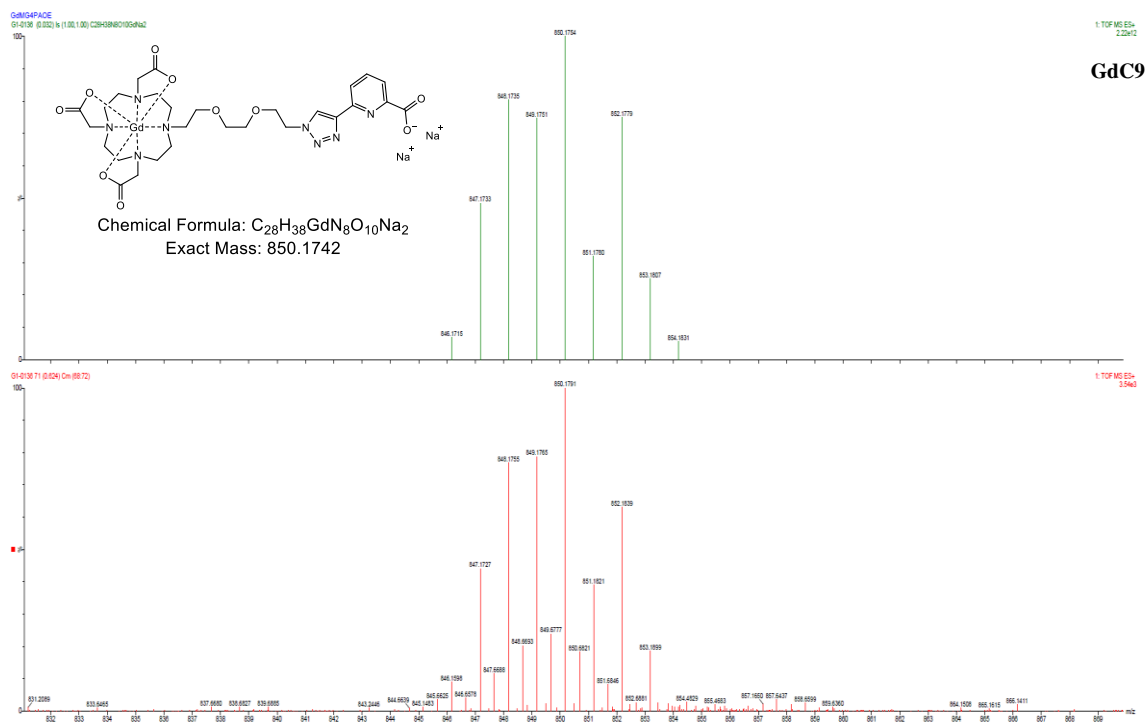
8.2 HPLC Analyses

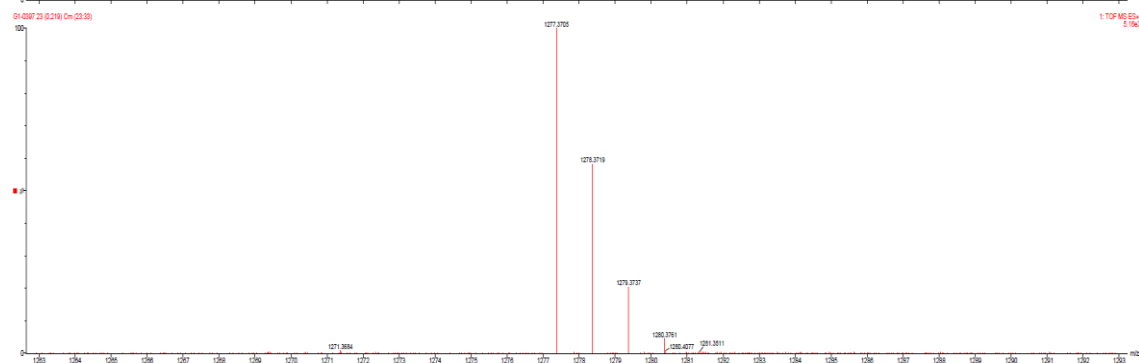
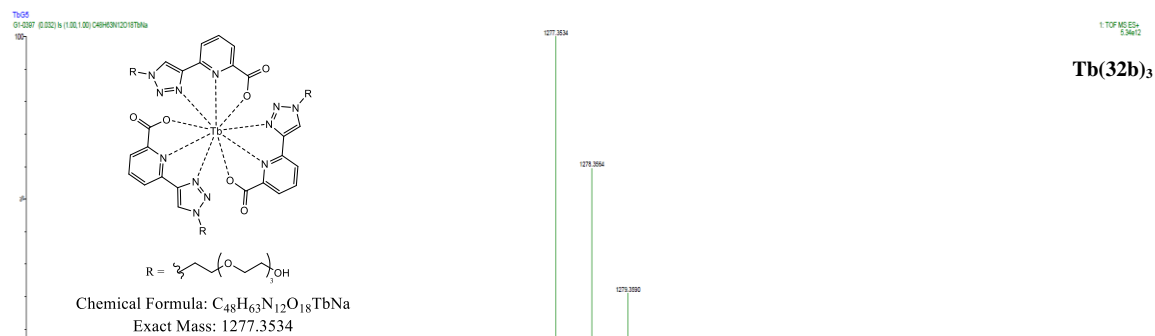
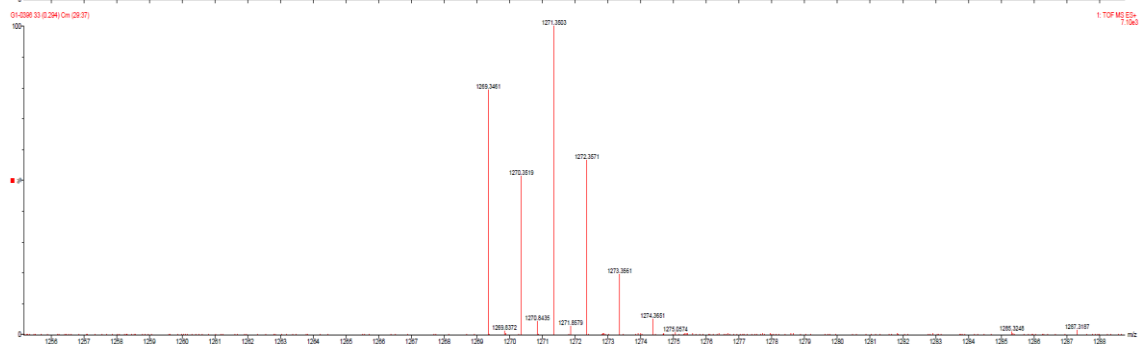
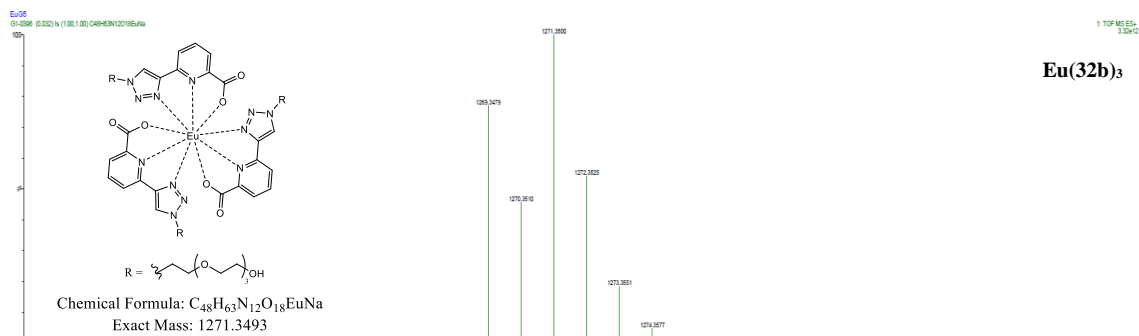


Analytical HPLC analysis of **C8**, **GdC8**, **C9**, **GdC9**, **C10**, **GdC10**, **32b** and **32b hydrolysed**. Method: 5% MeCH for 5 min, 5-100% MeCN over 30 min, 100% MeCN for 5 min, 100-5% MeCN over 5 min, 5% MeCN for 5 min.

8.3 Mass Spectrometry Analyses







8.4 Courses and Conferences

Lecture Course

Chemistry research skills

Training Courses

Fine-tuning your Research Questions	21/11/2014
Effective Reading and Note-taking	21/11/2014
Making your research information come to you	25/11/2014
CSE – The Literature Review	26/11/2014
CSE – Design a Poster	03/12/2014
Finding your Academic Voice	10/12/2014
Induction Library	02/02/2015
Induction IT Services	02/02/2015
Induction: Managing Expectations: You, Your Supervisors and the Institution	02/02/2015
Induction: Project Managing the Research Degree	02/02/2015
Induction: Personal and Professional Development Planning	06/02/2015
(CSE Training Day 2) Preparing for the Probation Review	25/03/2015
Fundamentals for an Effective Presentation	14/04/2015

Conferences Attended

Oral Communication

“A New Zinc(II) Responsive MRI Contrast Agent, Adhitiyawarman and Mark P. Lowe, *September 2017*, The 4th International Seminar on Chemistry, Bandung, Indonesia.

Poster Presentations

“Lanthanide Complexes as MRI Contrast Agent and Luminescent Probes”, Adhitiyawarman and Mark P. Lowe, *February 2015*, ELTU Postgraduate Research Festival 2015, University of Leicester, UK.

“A Potential Zinc Responsive MRI Contrast Agent”, Adhitiyawarman and Mark P. Lowe, *March 2017*, Challenges for Chemistry in Molecular Imaging, The Royal Society London, UK.

“A Potential Zinc Responsive MRI Contrast Agent”, Adhitiyarwarman and Mark P. Lowe, *April 2017*, The RSC Organic Division Midlands Meeting, University of Leicester, UK.

“A Potential Zinc Responsive MRI Contrast Agent”, Adhitiyarwarman and Mark P. Lowe, *July 2017*, Departmental Research Day, University of Leicester, UK.

Publication

Adhitiyarwarman and M. P. Lowe, *Res. J. Chem. Environ.*, 2018, **22**, 22-3